Charge Carrier Generation and Dynamics in Organic Semiconductor Systems

Dissertation

zur
Erlangung des akademischen Grades
Doktor der Naturwissenschaften
(Dr. rer. nat.)
der Naturwissenschaftlichen Fakultät
der Universität Paderborn

vorgelegt von

Fabian Bauch

Paderborn, 26. Februar 2026

Kurzfassung

Mit der steigenden globalen Energienachfrage und der zunehmenden Komplexität elektronischer Geräte haben organische Halbleiter große wissenschaftliche und gesellschaftliche Aufmerksamkeit gewonnen. Trotz rascher Fortschritte und deutlicher Vorteile gegenüber anorganischen Materialien begrenzen ihre amorphe Morphologie und schwache intermolekulare Wechselwirkungen weiterhin ihr Potenzial, da sie die Ladungsträgermobilität reduzieren und eine effiziente photoinduzierte Ladungserzeugung erschweren.

In dieser Arbeit werden elektronische Strukturmethoden eingesetzt, um Ladungsträgererzeugung durch molekulare Dotierung, photoinduzierte Ladungsbildung sowie Transportmechanismen zu untersuchen. Im Fokus stehen grundlegende elektronische Prozesse und ihre Verbindung zu geräterelevanten Eigenschaften. Simulationen der Ladungsträgerdynamik identifizieren das Polaron-Energieniveau als zentralen Deskriptor für Ladungstransfer. Eine zeitaufgelöste Analyse von Exziton-Dipolmomenten und Coulomb-Wechselwirkungen über verschiedene Polymerarchitekturen zeigt eine starke Korrelation mit der Ladungsträgerausbeute. Zudem werden Exzitonen-Dissoziation und Ladungstransport in einer Mischung aus dem trifluoromethyl-substituierten Nicht-Fulleren-Akzeptor Y_2CF_3 und PM6 untersucht, wobei effiziente Dissoziation und perkolierende Transportpfade nachgewiesen werden. Abschließend werden kleinstmolekulare Donorarchitekturen systematisch auf ihre Eignung für All-Small-Molecule-Photovoltaik geprüft.

Abstract

With the increasing global demand for energy and the growing complexity of electronic devices, organic semiconductors have attracted significant scientific and societal attention. Although their performance has advanced rapidly and they offer distinct advantages over inorganic materials, their amorphous morphology and relatively weak intermolecular interactions continue to limit their potential by reducing charge-carrier mobility and hindering efficient photoinduced charge generation.

In this work, electronic-structure methods are employed to investigate charge-carrier generation via molecular doping, photoinduced charge formation, and charge-transport mechanisms. The focus is on elucidating the fundamental electronic processes and connecting them to device-relevant properties. Simulations of charge-carrier dynamics identify the polaron energy level as a key descriptor of charge-transfer processes. A time-resolved analysis of exciton dipole moments and Coulomb interactions across various polymer architectures reveals a strong correlation with charge-carrier yield. Moreover, exciton dissociation and charge transport are examined in a blend of the novel trifluoromethyl-substituted non-fullerene acceptor Y_2CF_3 and PM6, demonstrating efficient dissociation and percolating charge-transport pathways. Finally, small-molecule donor architectures are systematically screened to evaluate their suitability for application in all-small-molecule photovoltaic devices.

Scientific Contributions

Main publications

[P1] **Fabian Bauch**, Chuan-Ding Dong, and Stefan Schumacher. *Dynamics-induced charge transfer in semiconducting conjugated polymers*. Journal of Materials Chemistry C **11**, 12992-12998 (2023).
I developed the initial concept and methodological framework, including preliminary quantum-chemical calculations serving as a proof of concept, some of which were incorporated into the supplementary material of the paper. The quantum-chemical calculations discussed in the main text were performed by Dr. Chuan-Ding Dong, who also wrote the manuscript, which I subsequently revised. The results presented in the paper were discussed in close collaboration between Dr. Chuan-Ding Dong and myself.

[P2] **Fabian Bauch**, Chuan-Ding Dong, and Stefan Schumacher. *Dynamics of Electron–Hole Coulomb Attractive Energy and Dipole Moment of Hot Excitons in Donor–Acceptor Polymers*. The Journal of Physical Chemistry C **128**, 3525-3532 (2024).
I developed the methodological framework, performed and analysed all quantum-chemical calculations presented in the paper, and wrote the initial draft of the manuscript.

[P3] Chuan-Ding Dong, **Fabian Bauch**, Yuanyuan Hu, and Stefan Schumacher. *Charge transfer in superbase n-type doping of PCBM induced by deprotonation*. Physical Chemistry Chemical Physics **26**, 4194-4199 (2024).
The methodological framework was developed primarily by Dr. Chuan-Ding Dong, with partial contributions from me, including preliminary quantum-chemical calculations that were not incorporated into the paper or its supplementary material. The quantum-chemical calculations presented in the paper were performed by Dr. Chuan-Ding Dong, who also wrote the manuscript, which I subsequently revised.

[P4] **Fabian Bauch**, Chuan-Ding Dong, and Stefan Schumacher. *Designing high performance organic donor molecules for photovoltaics*. Advanced Theory and Simulations, e01560 (2025).
I developed the methodological framework, performed and analysed all quantum-chemical calculations presented in the paper, and wrote the initial draft of the manuscript.

[P5] **Fabian Bauch**, Xiaojuan Ni, Saied Md Pratik, Sadisha Nanayakkara, Tonghui Wang, Jean-Luc Brédas, Stefan Schumacher, and Veaceslav Coropceanu. *Electronic Properties of Organic Solar Cells based on CF_3-Functionalized Non-Fullerene Acceptors*. ACS Applied Materials & Interfaces **18**, 2200-2211 (2026).
The methodology was developed by Dr. Veaceslav Coropceanu. The molecular dynamics simulations were performed by Dr. Xiaojuan Ni. I carried out all quantum-chemical calculations presented in the paper and performed the majority of the analysis, with a minor portion of the analysis contributed by Dr. Xiaojuan Ni. I was primarily responsible for writing the manuscript, with the molecular dynamics section written by Dr. Xiaojuan Ni. The manuscript was revised by Dr. Saied Md Pratik and Dr. Tonghui Wang, and the writing process was supervised by Dr. Veaceslav Coropceanu.

Other publications

Fabian Bauch, Chuan-Ding Dong, and Stefan Schumacher. *Protonation-induced charge transfer and polaron formation in organic semiconductors doped by Lewis acids*. RSC Advances **12**, 13999-14006 (2022).
I developed the methodological framework, performed and analysed all quantum-chemical calculations presented in the paper, and wrote the initial draft of the manuscript. The results reported in this work were generated exclusively during my Master's studies and form part of my Master's thesis submitted to Paderborn University. The manuscript itself was written during the early phase of my doctoral studies.

Research stay

From 1 September 2024 to 15 December 2024, I had the opportunity to conduct research as a visiting scholar under the supervision of Prof. Dr. Jean-Luc Brédas in the Department of Chemistry and Biochemistry at the University of Arizona, Tucson, Arizona, USA. I am grateful for the generous hospitality and fruitful collaboration, which culminated in a joint publication in *ACS Applied Materials & Interfaces*.

Conferences

[C1] **Fabian Bauch**, Chuan-Ding Dong, and Stefan Schumacher. *Protonation-Induced Charge Transfer and Polaron Formation in Organic Semiconductors Doped by Lewis Acids* (Talk). DPG conference in Regensburg, Regensburg, Germany (8. September 2022).

[C2] **Fabian Bauch**, Chuan-Ding Dong, and Stefan Schumacher. *Theoretical Insights into Charge Carrier Generation and Dynamics in Organic Semiconductors through Density Functional Theory* (Poster). XVI International Conference on Organic Electronics, Madrid, Spain (5. July 2023).

[C3] **Fabian Bauch**, Chuan-Ding Dong, and Stefan Schumacher. *Engineering Small-Molecule Donors for Organic Photovoltaics: a Theoretical Investigation* (Poster). XVII International Conference on Organic Electronics, Coimbra, Portugal (7. July 2025).

Contents

Introduction 1

The surging demand for opto-electronic technologies in everyday life is driving an urgent search for materials that are inexpensive, scalable, lightweight, flexible, and capable of highly tunable functionality. Since the seminal discovery in the 1970s that simple conjugated polymers can exhibit dramatically enhanced conductivity upon halogen doping [1], a new era of electronics has unfolded. This breakthrough opened the door to conjugated molecular systems – organic semiconductors (OSCs) – which have rapidly become foundational materials for organic photovoltaics (OPVs) [2–9], organic light-emitting diodes (OLEDs) [10–16], organic field-effect transistors (OFETs) [17–20], sensors [21, 22], and photoswitches [23, 24], including a wide range of charge-transport applications [25–27].

The structurally versatile framework of conjugated molecules provides a uniquely adaptable platform, enabling fine control over electronic structure and responses to external stimuli, such as visible light. Yet, their molecular nature introduces inherent disadvantageous compared to inorganic semiconductors: OSCs are typically amorphous and held together by weak van der Waals forces. As a consequence, this results in pronounced structural and energetic disorder, leading to comparably low charge mobility, limited exciton diffusion length and dissociation, larger energy losses, and strong charge recombination [28–34]. Moreover, pronounced electron-phonon coupling imposes fundamental constraints on device performance.

Beyond energetic disorder and its associated limitations, OSCs face additional stability challenges. In particular, they are highly susceptible to degradation upon exposure to air and moisture. Oxygen and water can diffuse into the device, triggering chemical processes such as oxidation, as well as physical deterioration of device components [35, 36]. In addition, OSCs exhibit limited thermal stability. Elevated temperatures, for example during prolonged illumination, increase molecular mobility and thereby accelerate degradation pathways, leading to morphological evolution and potential chemical modifications [35–37].

To overcome these limitations and unlock new capabilities, intense research activities have focused on untangling the interplay between chemical design, opto-electronic properties, molecular packing, nanoscale morphology, and ultimately device functionality [30, 38–41], as depicted in Figure 1.1. Advances in OSC synthesis and structural control have propelled

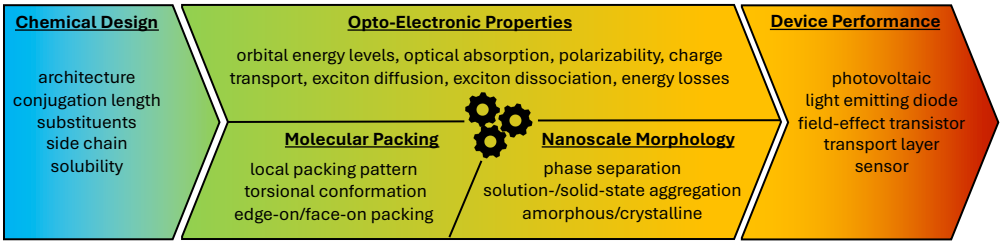

Figure 1.1: Pathway from molecular design to device functionality. The chemical design of organic semiconductors defines their intrinsic opto-electronic and molecular properties, which both govern and are influenced by molecular packing and nanoscale morphology. These structure-property relationships ultimately govern the performance and versatility of organic semiconductors in diverse applications.

the power conversion efficiencies (PCE) of OPV devices from just a few percent to an impressive 21% [42], alongside the widespread commercialization of OLEDs, clear evidence of the remarkable pace of innovation in organic materials science.

Modeling organic materials in its entirety remains challenging. Their molecular properties demand a quantum-mechanical description, yet applying such methods to the full morphological landscape is computationally unfeasible. The current state-of-the-art solution relies on a multiscale strategy: classical simulations capture the behavior of assemblies containing hundreds of molecules, while quantum-mechanical calculations resolve the electronic structure of small molecular clusters as well as the underlying parametrization [43, 44]. This combined approach has yielded crucial insights into structural and energetic disorder, exciton dissociation, and charge-transport processes [39, 45–49]. Nevertheless, the immense diversity of molecular architectures and processing conditions continues to make accurate predictions of device performance a challenge.

In this thesis, quantum-chemical calculations are employed to probe the electronic structure and key mechanisms in OSCs, aiming to advance understanding and help bridge existing knowledge-gaps. Specifically, this thesis contains two contributions related to charge-carrier injection and transport [50, 51], and three contributions addressing OPV performance and exciton dynamics [52–54]. Table of contents figures from the publications joined with this thesis are shown in Figure 1.2 to provide a brief overview.

The electronic mechanisms underlying emerging molecular doping strategies, specifically the use of superbases [P3] to enhance charge-carrier density, were systematically investigated. Charge-transport events between polymer chains were captured using *ab initio* molecular dynamics simulations, revealing correlations between interchain hopping and

the polaron energy level, proposed here as a charge-transport descriptor [P1]. Dynamic simulations of excitons along polymer backbones linked the excited-state dipole moment and the Coulomb attraction between the electron and hole to the formation of polaron-pairs [P2]. In addition, the interface formation and exciton dissociation behavior of the novel trifluoromethyl-substituted non-fullerene acceptor Y_2CF_3 in combination with the donor polymer PM6 were analyzed [P5]. Finally, systematic molecular modifications of molecular donor systems were performed to study charge dissociation when paired with the state-of-the-art non-fullerene acceptor Y6 [P4].

The first part in this thesis introduces the fundamental concepts of OSCs, beginning with intrinsic electronic structure, vibrational states, and light absorption, and progressing to intermolecular interactions and energetic disorder. Building on this foundation, electronic-state transitions are described from a static and dynamic perspective.

In the second part of this thesis, a discussion of charge-carrier injection and transport is provided, building on the foundations and including the contributions of this thesis to these topics. Moreover, the manifold of excited-states and device principles of OPVs are then elaborated, along with the associated contributions from this thesis. Finally, this thesis concludes with a summary and an outlook on future research directions building on the results from this thesis.

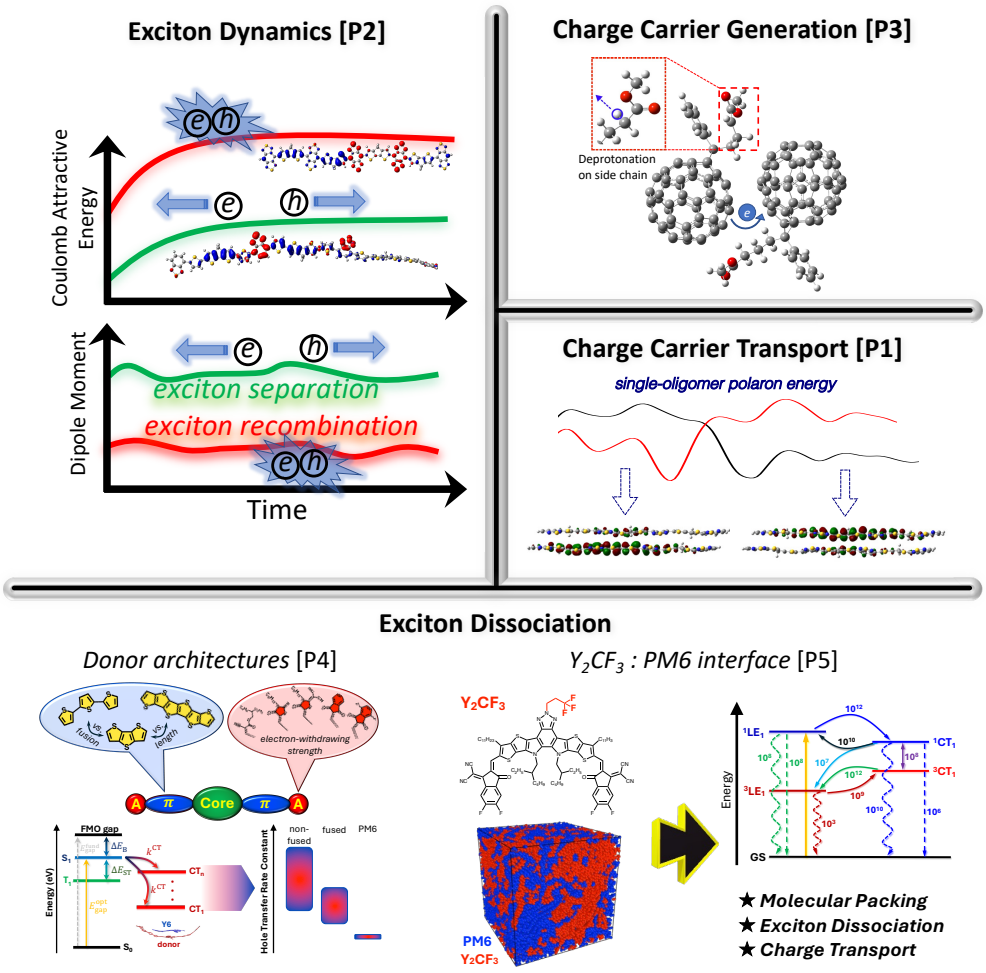

Figure 1.2: Overview of TOC graphics from my publications [P1–P5] contributing to this thesis. TOC graphics reproduced from References [50–54]. Copyright © respective rights holders. Reproduced in accordance with applicable publisher policies and Creative Commons licenses.

Part I

Fundamentals of Organic Semiconductors

Chemical Background 2

In the first part of this thesis, the fundamental properties of organic semiconductors are presented. The discussion begins with the chemical structure and electronic characteristics of isolated molecular systems, including their response to incident light (optical absorption) and their vibrational motion. Subsequently, interactions between molecular systems and their impact on the electronic landscape at a larger scale are examined. This is followed by a presentation of both static and dynamic approaches to model the coupling between electrons and nuclei as well as transitions between electronic states. This part provides the essential framework for understanding the opto-electronic properties that are later employed to analyze the phenomena investigated in this work, particularly in relation to organic semiconductor applications discussed in Part II of the thesis.

Unlike conventional inorganic semiconductors such as silicon and gallium arsenide, organic semiconductors (OSCs) are molecular materials primarily composed of carbon and hydrogen atoms. Their molecular nature gives rise to advantageous properties, including low mass density, mechanical flexibility, cost-efficient fabrication, and wide applicability. Within the framework of quantum-mechanical molecular orbital theory, the sp^2-hybridized orbitals of carbon atoms form σ-bonds that establish the carbon backbone. Each carbon atom further retains one non-hybridized p-orbital (commonly denoted as the p_z-orbital), which overlaps with neighboring p_z orbitals to form π-orbitals, as illustrated in Figure 2.1(a). These π-bonds are weaker and energetically higher than the corresponding σ-bonds. Their alternating arrangement along the backbone leads to a sequence of alternating single and double bonds, forming a conjugated system. [1] The overlap of adjacent p_z-orbitals along the conjugated backbone leads to the formation of extended π-orbitals that span multiple carbon–carbon bonds, i.e., they form delocalized π-orbitals rather than being confined to individual double bonds. As with the formation of π-bonds, they can form antibonding patterns, typically referred to as π^*. For a more comprehensive description the reader is referred to References [56–59].

From the perspective of molecular orbital theory, electrons reside in a set of discrete molecular orbitals (MOs), which describe the spatial probability distribution of electrons and are

[1] In an infinite one-dimensional conjugated chain, bond-length alternation into single and double bonds emerges via spontaneous symmetry breaking, known as *Peierls distortion* [55].

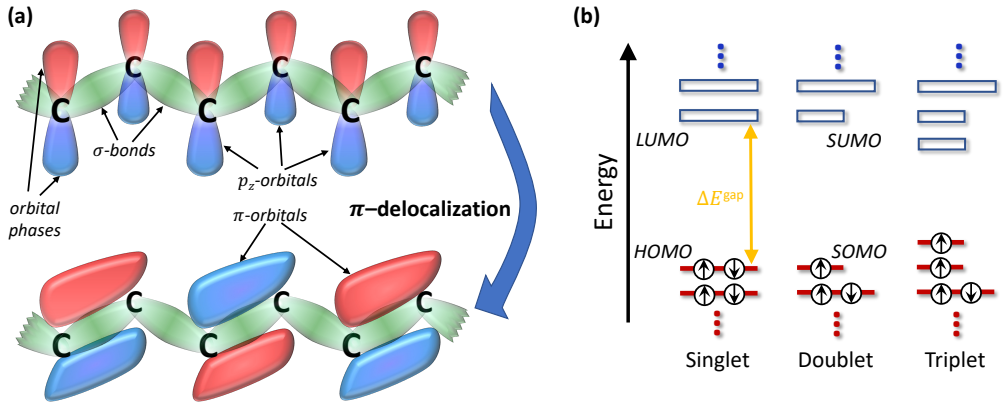

Figure 2.1: Molecular π-orbitals and spin multiplicity. (a) Formation of π-bonds from atomic p_z-orbitals in a linear organic chain of carbon atoms (C). Hydrogen atoms are not represented in this illustration. The shape of the orbitals is for illustrative purposes only. (b) Electronic structure of singlet, doublet, and triplet states in an energy level diagram. The spin of the electrons is indicated.

characterized by discrete energy levels. The collection of occupied and unoccupied molecular orbitals constitutes the electronic structure, commonly depicted in a single-particle energy-level diagram, as shown in Figure 2.1(b). The spatial extension of the conjugated system increases the effective overlap between neighboring p_z-orbitals, which in turn stabilizes the bonding π-orbitals and destabilizes the antibonding π^*-orbitals. As a consequence, the highest occupied molecular orbital (HOMO), derived from bonding π-orbitals and occupied by π-electrons, shifts to higher energy, while the lowest unoccupied molecular orbital (LUMO), derived from antibonding π^*-orbitals, shifts to lower energy.

The combined effect of these energy shifts establishes a well-defined energy separation between the HOMO and LUMO. This separation, typically on the order of a few electron volts (eV), defines the band-gap (ΔE^{gap}), analogous to the band-gap in inorganic semiconductors, and underpins the semiconducting behavior of OSCs. This trend saturates beyond a critical conjugation length, limiting further band-gap narrowing. By convention, since molecular orbitals energetically close to the HOMO and LUMO constitute the key microscopic origin of the distinctive optical and charge-transport properties of organic semiconductors, discussions of the electronic structure typically focus on these frontier orbitals. Accordingly, an occupied molecular orbital located n energy levels below the HOMO is denoted HOMO$-n$, while an unoccupied molecular orbital located m energy levels above the LUMO is labeled LUMO$+m$.

Organic semiconductors can be categorized according to molecular architecture, ranging from finite molecules to extended polymers, and intermediate oligomers, all of which can have linear, quasi-two-dimensional, and quasi-three-dimensional shapes. A polymer consists of an (effectively) infinite repetition of structural units, enabling enhanced π-delocalization and typically a smaller band-gap compared to finite molecules. Oligomers represent finite, shorter segments of such polymeric structures, bridging molecular and polymeric regimes. The extended conjugated backbone defines the primary electronic structure of the OSC, but it is not the only component that significantly influences the functionality of OSCs in devices.

Besides the linear chain of alternating single and double bonds, typical structural units usually incorporate aromatic ring structures, which promote increased π-electron delocalization and thus orbital energy shifts, and often enhance backbone planarity. Non-aromatic rings may also be used to fuse aromatic rings, further stabilizing backbone planarity. These ring-structures alone can define the backbone architecture, as in ladder-type polymers, however, they might also be connected via single or double bonds [60].

In addition to carbon, OSCs commonly incorporate heteroatoms such as sulfur, oxygen, nitrogen, and fluorine, among others, which substantially influence the electronic structure. These effects arise not only from participation of the heteroatom-associated orbitals in π-electron delocalization, but also from their inductive and resonance interactions with the conjugated system. Such electronic modulation shifts the energies of the molecular orbitals: electron-donation motifs raises the occupied orbital energies, while electron-withdrawal motifs lowers the unoccupied orbital energies, which often leads to an overall reduction in the band-gap. Structural units that preferentially stabilize and contribute to the LUMO character are commonly referred to as acceptor (A) units, whereas those that preferentially stabilize and contribute to the HOMO character are referred to as donor (D) units. In many conjugated systems, sulfur- and oxygen-containing units exhibit electron-donating character, while nitrogen- and fluorine-containing units often display electron-withdrawing behavior, depending on their bonding configuration and integration into the backbone.

Moreover, beyond their electronic effects, the heterotaoms may also influence the molecular conformation. Noncovalent interactions between heteroatoms can hinder rotational freedom between adjacent structural units, thereby promoting backbone planarity [60]. Such conformational locking is associated with interactions between atom pairs that possess opposing partial charges, such as F–S or F–H contacts. Such interaction may also affect the molecular packing.

As a result, integrating electron-rich and electron-deficient units into the conjugated backbone has been demonstrated to be a particularly powerful molecular design strategy, as such modifications critically impact the response of the electronic structure to external perturbations, including intermolecular interactions and light absorption, which govern the nature of electronic excitations [61, 62]. In its simplest form, this approach employs an alternating sequence of donor (D) and acceptor (A) units giving rise to donor-acceptor (DA) polymers; however, more complex conjugated architectures can, in principle, integrate an arbitrary number of chemically distinct building blocks, showcasing finite molecules with well-defined D-A configurations.

A further critical design element lies in the choice of side chains appended to the OSC backbone and components [63]. Although side chains typically exert only a minor influence on the intrinsic electronic structure of OSCs, such as the orbital energies, band-gap, and light-absorption characteristics, they play a decisive role in governing molecular packing, the morphology on the nanoscale, and solubility of the organic compound. These structural factors, in turn, can indirectly modulate opto-electronic properties by controlling intermolecular interactions, which will be turned to in Section 4.2. Such interactions are crucial for charge-carrier injection and transport, as well as for the exciton dissociation into free charges after photo-excitation. Consequently, systematic tailoring of side chains has become a central strategy in optimizing OSC performance in targeted devices. Common examples include linear and branched alkyl chains, oligo(ethylene glycol) chains, and fluoroalkyl chains.

The progression from the chemical design of OSCs to their integration into diverse device architectures – such as organic solar cells and organic photovoltaics (OPVs), organic light-emitting diodes (OLEDs), organic field-effect transistors (OFETs), biosensors, and transport layers – is schematically depicted in Figure 1.1. While chemical design dictates the intrinsic opto-electronic properties, these properties are further modulated by local molecular packing (Å to a few nm), which in turn feedbacks into the opto-electronic response. At the nanoscale (a few nm to several hundred nm), the resulting morphology becomes a detrimental factor for device performance. Consequently, predicting the functionality of OSC devices cannot rely exclusively on the intrinsic opto-electronic characteristics of the materials; instead, it also requires accurate prediction of morphology. However, such predictions are often computationally unfeasible at the quantum-mechanical level of theory, necessitating compromises in the quantum-chemical description of material properties.

In the following Section 3, the opto-electronic properties of OSCs are elucidated, spanning

from the intrinsic electronic structure to their perturbations induced by light-absorption and vibrational dynamics. Building upon this foundation, the next Section 4 extends the discussion toward intermolecular interactions, addressing the role of molecular packing, solvent effects, and their collective impact on the opto-electronic properties.

Opto-electronic Properties of Organic Semiconductors 3

To establish the conceptual foundation for this thesis, this section introduces the key physical quantities associated with the electronic structure of organic semiconductors. It starts with a discussion of the fundamental quantum-mechanical properties of electrons and their associated observables, followed by a quantum-mechanical description within the framework of potential energy surfaces. Subsequently, the vibrational modes of the system are introduced, and the section ends with a discussion of the interaction with light.

3.1 Electronic Structure Properties

Starting from a description of physical properties of the electronic system, a key quantum-mechanical property of electrons is their spin, which, according to Pauli's exclusion principle, prohibits two electrons with the same spin from occupying the same molecular orbital. Consistent with the previously introduced single-particle picture, the electronic structure is therefore described by spin-resolved molecular orbitals, as illustrated in Figure 2.1(b). Although this representation is a simplification of the true many-particle system, it remains a powerful framework for analyzing molecular interactions and their response to external perturbations.

Besides possessing the quantum-mechanical property of spin, the molecular orbitals occupied by electrons are also characterized by their orbital angular momentum, which is described by the quantum number l (with $l = 1$ for p- and thus for π-orbitals). The orbital angular momentum can be interpreted as the motion of an electron around the nucleus, or, in quantum-mechanical terms, as a descriptor of the orbital's spatial distribution and shape. This angular momentum can be projected onto a specific spatial axis, giving rise to the magnetic quantum number m of the orbitals ($m \in -l, \ldots, +l$). In molecular systems, the orbital angular momentum of electrons plays a significant role, particularly in cases where the electron-spin is flipped during electronic transitions. Such processes can lead to

transitions that are formally forbidden by the conservation of total angular momentum but are allowed by spin-orbit coupling, which is discussed in more detail in Section 5.2.

A fundamental characteristic of the electronic structure is the spin multiplicity of a quantum state, which is determined by its total spin angular momentum S and expressed as $2S + 1$. Accordingly, states are classified as singlet ($S = 0$), doublet ($S = \frac{1}{2}$), triplet ($S = 1$), and so on, with the multiplicity reflecting the number of unpaired electrons, as depicted in Figure 2.1(b). In OSCs, the total number of electrons is fixed by the atomic composition and generally equals the number of protons, meaning that most OSCs are overall charge-neutral. Typically, such systems contain an even number of electrons, evenly distributed between α- (spin up) and β- (spin down) electrons. In this case, the electronic system is a neutral singlet, where each orbital is doubly occupied in accordance with Pauli's exclusion principle. However, if the number of α- and β-electrons is not balanced, e.g., by missing an electron, the electronic system becomes a doublet. In some cases, even triplet electronic systems can be energetically preferred despite an even total electron count. From now on, general references to OSCs refer to a neutral electronic state.

Although OSCs most commonly exist in a neutral configuration, electrons can be removed or added, a process referred to as ionization. This alters the electronic distribution, spin multiplicity, and corresponding geometry. The resulting charged species are termed cation in the case of electron removal and anion in the case of electron addition. Such processes may occur, for instance, via intermolecular charge transfer (Section 7.1), leading to energetically stabilized doublet states in both donor and acceptor molecules, or through chemical doping. The energies associated with these processes are the (vertical) ionization potential (IP) and (vertical) electron affinity (EA), respectively.

The electronic structure gives rise to electrostatic properties. A central quantity are the multipole moments, or more relevant in this work the second order, i.e., the permanent dipole moment $\boldsymbol{\mu}$,[1] [2] which quantifies the net separation of localized positive and negative charges within the OSC. It can be rigorously expressed in terms of the total charge density $\rho(\mathbf{r})$, comprising both electronic and nuclear contributions, as

$$\boldsymbol{\mu} = \int \rho(\mathbf{r}) \cdot \mathbf{r} \, \mathrm{d}^3 r \, . \tag{3.1}$$

[1] Throughout this thesis, bold notation indicates vector quantities.

[2] To complete the picture, it should be noted that higher-order poles are present in organic semiconductors following the multipole expansion. Particularly noteworthy here is the quadrupole moment, which has been shown to have a significant influence on OSC and corresponding components [64, 65]. However, this lies outside the scope of this thesis.

The magnitude and orientation of $\boldsymbol{\mu}$ are determined not only by the presence of electron-rich or electron-poor moieties but also by the overall asymmetry of the molecular system.

Complementary to the dipole moment, the polarizability characterizes the linear response of the electron distribution to external electric fields (without introducing electronic transitions), such as those originating from neighboring molecules as elucidated in Section 4, or an applied electric field. Physically, it describes how easily the charge distribution can be distorted by such perturbations. Molecules with high polarizability have a greater ability to redistribute their charge density, facilitating charge separation, and shielding Coulomb interactions between localized charges.

3.2 From the Schrödinger Equation to Potential Energy Surfaces: Adiabatic and Diabatic Descriptions

Moving beyond the discussion of the system's physical properties, a fully quantum-mechanical description is now introduced. For a comprehensive and detailed treatment, the reader is referred to References [66, 67].

Any quantum-mechanical state of a many-particle system – in the present case, an OSC composed of nuclei and electrons – is fully characterized by a wave function $\Psi(\mathbf{r}, \mathbf{R}; t)$ evolving under the molecular Hamiltonian $\hat{\mathcal{H}}(\mathbf{r}, \mathbf{R})$ according to the time-dependent Schrödinger equation:

$$i\hbar \frac{\mathrm{d}\Psi(\mathbf{r}, \mathbf{R}; t)}{\mathrm{d}t} = \hat{\mathcal{H}}(\mathbf{r}, \mathbf{R})\Psi(\mathbf{r}, \mathbf{R}; t) \tag{3.2}$$

$$\hat{\mathcal{H}}(\mathbf{r}, \mathbf{R}) = \hat{\mathcal{T}}_\mathrm{n} + \underbrace{\hat{\mathcal{T}}_\mathrm{e} + \hat{\mathcal{V}}_\mathrm{ee} + \hat{\mathcal{V}}_\mathrm{ne} + \hat{\mathcal{V}}_\mathrm{nn}}_{\hat{\mathcal{H}}_\mathrm{e}(\mathbf{r},\mathbf{R})} . \tag{3.3}$$

The Hamiltonian can be decomposed into a nuclear kinetic energy operator ($\hat{\mathcal{T}}_\mathrm{n}$) and an electronic part ($\hat{\mathcal{H}}_\mathrm{e}(\mathbf{r}, \mathbf{R})$), which accounts for the electronic kinetic energy ($\hat{\mathcal{T}}_\mathrm{e}$), electron-electron ($\hat{\mathcal{V}}_\mathrm{ee}$) and electron-nuclei ($\hat{\mathcal{V}}_\mathrm{ne}$) interactions, as well as the nuclei-nuclei interaction ($\hat{\mathcal{V}}_\mathrm{nn}$) as an effective potential.

The wave function contains the complete information about the molecular system, including the geometry of the OSC (nuclear coordinates $\mathbf{R}$), the electronic structure (electronic coordinates $\mathbf{r}$, including the spin and orbital angular momentum), and their correlated

dynamics. In the absence of external perturbations, the Hamiltonian is time-independent. The wave function, however, retains an explicit parametric dependence on time t.

Formally, the exact molecular wave function can be expanded in the Born–Huang representation [68, 69]:

$$\Psi(\mathbf{r},\mathbf{R};t) = \sum_k \phi_k(\mathbf{r};\mathbf{R})\chi_k(\mathbf{R};t)\,, \tag{3.4}$$

where the electronic wave functions $\phi_k(\mathbf{r};\mathbf{R})$ form a complete orthonormal set in the electronic Hilbert space for fixed nuclear geometry and satisfy the stationary electronic Schrödinger equation:

$$\hat{\mathcal{H}}_\mathrm{e}(\mathbf{r},\mathbf{R})\phi_k(\mathbf{r};\mathbf{R}) = E_k(\mathbf{R})\phi_k(\mathbf{r};\mathbf{R})\,. \tag{3.5}$$

Here, $E_k(\mathbf{R})$ denotes the electronic energy associated with the k-th electronic state. The nuclear wave functions $\chi_k(\mathbf{R};t)$ carry the explicit time dependence.

Turning to the time-dependent Schrödinger equation to describe nuclear dynamics, inserting Equation 3.4 into Equation 3.2 and multiplying $|\phi_j(\mathbf{r};\mathbf{R})\rangle$ from left, one obtains the following coupled equations for the dynamics of the nuclear wave functions [70]:

$$\begin{aligned} i\hbar\frac{\partial\chi_k(\mathbf{R};t)}{\partial t} &= \hat{\mathcal{T}}_\mathrm{n}\chi_k(\mathbf{R};t) + E_k(\mathbf{R})\chi_k(\mathbf{R};t) \\ &\quad - \sum_{\alpha,j}\left(\frac{\hbar^2}{M_\alpha}\underbrace{\langle\phi_k|\,\partial/\partial\mathbf{R}_\alpha\,|\phi_j\rangle}_{\mathbf{d}^\alpha_{kj}}\cdot\frac{\partial\chi_j(\mathbf{R};t)}{\partial\mathbf{R}_\alpha} + \frac{\hbar^2}{2M_\alpha}\underbrace{\langle\phi_k|\,\partial^2/\partial\mathbf{R}_\alpha^2\,|\phi_j\rangle}_{D^\alpha_{kj}}\chi_j(\mathbf{R};t)\right). \end{aligned} \tag{3.6}$$

Here, α stands for the individual nuclei with mass M_α. In the third term, the quantity $\mathbf{d}^\alpha_{kj}$ is known as the non-adiabatic coupling vector [71], which will be elucidated within the next paragraphs, and in the last term, the quantity D^α_{kj} is the second-derivative coupling. These terms mediate transitions between different electronic states and therefore couple nuclear motion of distinct electronic states. Note that the diagonal elements $\mathbf{d}^\alpha_{kk}$ vanish, and D^α_{kk} typically constitutes only a small correction to nuclear motion.

A key physical insight arises from the large mass difference between nuclei and electrons. Because nuclei are much heavier than electrons, their motion is significantly slower, leading to a separation of electronic and nuclear time scales. This separation forms the basis of the Born–Oppenheimer approximation [72]. Within this approximation, electrons are

assumed to adjust instantaneously to changes in nuclear positions, allowing the electronic and nuclear problems to be treated separately. Moreover, within the Born–Oppenheimer approximation, the derivative coupling terms $\mathbf{d}^{\alpha}_{kj}$ and D^{α}_{kj} are neglected to leading order in the small parameter $\sqrt{m_e/M_\alpha}$, where m_e is the mass of the electron. The nuclear equations thereby decouple, and nuclear dynamics proceed on a single electronic state.

In this limit, the Born–Huang expansion effectively reduces to the single dominant term corresponding to state k:

$$\Psi(\mathbf{r}, \mathbf{R}; t) \approx \phi_k(\mathbf{r}; \mathbf{R})\chi_k(\mathbf{R}; t)\,, \tag{3.7}$$

Consequently, it is appropriate to first focus on the electronic problem defined by the stationary Schrödinger equation of a single electronic state that governs nuclear motion. The lowest-energy electronic state of the system is referred to as the ground state and is uniquely characterized by its ground-state energy $E_0(\mathbf{R})$ and the corresponding electronic wave function $\phi_0(\mathbf{r}; \mathbf{R})$

For any particular state, any displacement of the nuclei and the accompanying redistribution of the electronic density increases the total potential energy of the system in this state. This dependence of the total energy on the nuclear configuration defines the potential energy surface (PES) of this state. The molecular geometry associated with the lowest energy of any particular electronic state (such as the ground state) is referred to as the equilibrium geometry of that state, it corresponds to the configuration in which all forces between nuclei and electrons are balanced. Owing to the large number of nuclear degrees of freedom, the PES of a real molecular system is inherently high-dimensional and cannot be visualized directly. For illustrative purposes, it is common to consider a diatomic system, where the PES reduces to a one-dimensional curve. In this simplified case, the potential is well approximated by a harmonic form for small displacements around equilibrium, whereas larger displacements require an anharmonic description, typically represented by the Morse potential, as illustrated in Figure 3.1(a).

In every type of device functionality, OSCs undergo various transitions between electronic states, for instance, during charge transport and light absorption. When describing such electronic transitions between two states based on nuclear coordinates, it is useful to distinguish between diabatic and adiabatic representations of the PES. In the diabatic picture, the PESs of the individual states are treated as independent, non-interacting surfaces that may cross. In contrast, the adiabatic PES accounts for the mutual electronic interaction of the states, resulting in avoided crossings, as illustrated in Figure 3.1(b). Interpretation-wise,

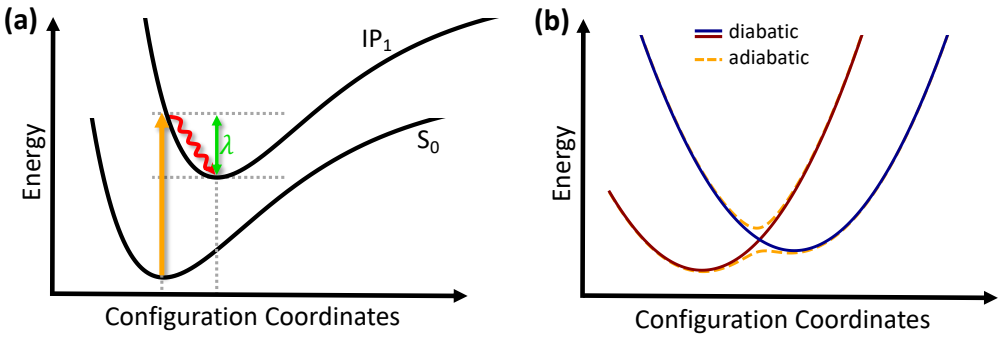

Figure 3.1: Potential energy surfaces. (a) Potential energy surface (PES) of a neutral ground state (S_0) and an ionized state (IP_1). The orange arrow indicates vertical ionization from the ground state equilibrium position; the red waved arrow indicates the relaxation to the equilibrium position of the ionized state; the green arrow denotes the reorganization energy λ. (b) Illustration of diabatic (solid) and adiabatic (dashed) PESs. The shape of the PESs is for illustration purpose only.

this means that the system does not undergo jumps between distinct electronic states; instead, the electronic character is deformed continuously as a function of the nuclear coordinates.

For many chemical processes, describing the electronic state and its dynamics within a single Born–Oppenheimer adiabatic state is an adequate and accurate approximation. This is valid when the energy separation between electronic states is large compared to the nuclear kinetic energy, so that nuclear motion can be treated as evolving on a single PES. However, in situations where two or more adiabatic states come close in energy, this approximation breaks down. In such cases, the nuclear motion can induce transitions between adiabatic states, and several PESs must be considered simultaneously.

These non-adiabatic effects become particularly important in regions such as avoided crossings (in one-dimensional systems) and conical intersections (in multidimensional systems) where adiabatic PESs cross [69, 73]. In these regions, the coupling between nuclear and electronic motion, known as non-adiabatic coupling, becomes significant. It arises from the dependence of the electronic wavefunction $\phi_i(\mathbf{r}, \mathbf{R})$ on the nuclear coordinates, and appears as additional derivative terms in the nuclear Schrödinger equation when the nuclear kinetic energy is non-negligible ($\mathbf{d}_{kj}$ and the often neglected D_{kj} in Equation 3.6), allowing population transfer between adiabatic states. Such couplings play a central role in many important phenomena, including photochemical reactions, internal conversion, intersystem crossing, and excited-state relaxation and will be discussed further in Sections 5

and 6.

A change in the electronic state generally triggers a structural relaxation of the nuclei toward the equilibrium geometry corresponding to the new electronic configuration. Because electronic rearrangements occur on time scales that are much shorter than those of nuclear motion, the electronic transition can be considered effectively instantaneous. Such transitions are therefore referred to as vertical transitions, in accordance with the *Franck–Condon principle* [74–76] in the case of vertical excitation induced by photon absorption. The *Franck–Condon principle* follows directly from the Born–Oppenheimer approximation. Immediately after a vertical transition, the nuclear configuration is not in equilibrium with the new electronic state. The subsequent nuclear relaxation leads to the dissipation of energy and gives rise to the reorganization energy λ [45, 77, 78], which is defined as the energy difference between the vertically accessed electronic state and its relaxed equilibrium configuration (Figure 3.1(a), green arrow).

For completeness, it is noted that the probability of an electronic transition is partially determined by the overlap of the nuclear vibrational wave functions in the initial and final states, while the relaxation process itself is mediated by phonon emission that will be discussed in more detail in this chapter. The reorganization energy plays a central role in charge-carrier dynamics, as it governs the energetic cost associated with charge localization and transport, and it also strongly influences optical absorption and emission processes, as will be addressed throughout this thesis. An essential contribution to the nuclear reorganization and motion arises from the vibrational modes of the OSC, which will be elucidated in detail in the following section.

3.3 Vibrational Modes

In OSCs, the motion of nuclei modulates the electronic distribution, and *vice versa*. Consequently, OSCs can be vibrationally excited by the absorption of thermal energy (e.g., through molecular collisions) or by low-energy electromagnetic radiation, among other processes. A molecular vibrational mode corresponds to a characteristic collective periodic motion of atoms around their equilibrium positions. Each OSC with N_A atoms possesses $3N_A - 6$ distinct vibrational modes (for non-linear molecules), where the total number of vibrational degrees of freedom arises from the $3N_A$ cartesian coordinates, reduced by three translational and three rotational degrees of freedom that can be eliminated [79–81].

Each normal mode can be expressed as a linear combination of atomic displacements with specific weighting factors.

Since these vibrational modes correspond to small displacements around equilibrium geometries, the PES $E_k(\mathbf{R})$ for each electronic state k can be approximated by a Taylor expansion around the equilibrium nuclear configuration $\mathbf{R}_{\text{eq}}$. At equilibrium, the first derivatives vanish, so the linear term in the expansion is zero. Keeping only the quadratic contribution and neglecting higher terms, which become negligible for sufficiently small displacements, the expansion becomes [79, 80]:

$$E_k(\mathbf{R}) \approx E_k(\mathbf{R}_{\text{eq}}) + \frac{1}{2} \sum_{i,j}^{3N_A} \underbrace{\frac{\partial^2 E_k(\mathbf{R})}{\partial R_i \partial R_j}\bigg|_{\mathbf{R}_{\text{eq}}}}_{H_{\text{ij}}} \Delta R_i \, \Delta R_j \,, \tag{3.8}$$

where $\Delta\mathbf{R} = \mathbf{R} - \mathbf{R}_{\text{eq}}$; H_{ij} denotes the Hessian matrix, which couples the nuclear motions. Because vibrational motion typically probes only a small region around equilibrium, this harmonic approximation is often well justified. However, anharmonic corrections are sometimes important depending on the system and physical quantity under interest.

By transforming to the normal mode coordinates $\{Q_\alpha\}$, which diagonalize the Hessian, the nuclear Hamiltonian separates into a sum of independent harmonic oscillators [79]:

$$\hat{\mathcal{H}}_{\text{vib}} = \frac{1}{2} \sum_{\alpha=1}^{3N_A-6} \left(-\frac{\partial^2}{\partial Q_\alpha^2} + \omega_\alpha^2 Q_\alpha^2 \right) , \tag{3.9}$$

with normal mode frequencies ω_α. Inserting this Hamiltonian into the nuclear stationary Schrödinger equation, one obtains solutions in the form of products of single-mode harmonic oscillator wave functions χ_ν^{har}:

$$\chi_\nu^{(k)}(\mathbf{Q}) = \prod_{\alpha=1}^{3N_A-6} \chi_{\nu_\alpha}^{\text{har},(k)}(Q_\alpha^{(k)}) \,, \tag{3.10}$$

with corresponding vibrational energies

$$E_k^{\text{vib}} = \sum_{\alpha=1}^{3N_A-6} \hbar\omega_\alpha^{(k)} \left(\nu_\alpha + \frac{1}{2} \right) , \tag{3.11}$$

where $\nu_\alpha \in \{0, 1, 2, \dots\}$ are the vibrational quantum numbers of each oscillator. The superscript (k) indicates that the normal modes are defined on the electronic PES k, while

the subscript ν labels the set of occupied vibrational quanta. Transitions between vibrational wave functions correspond to changes in these occupation numbers driven by thermal fluctuations and interactions with the environment, resulting in time-dependent nuclear motion and concomitant fluctuations of the electronic structure.

The vibrational modes expressed along the normal coordinates are referred to as phonons, in analogy to the quasi-particle description of lattice vibrations in crystalline solids. For each electronic state k of the OSC, a corresponding set of quantized phonon excitations can be defined, that can be both absorbed from or emitted into the surrounding environment. As a result, every electronic state possesses a discrete vibrational energy spectrum with characteristic wave functions and transition energies, which can be illustrated, for instance, through the Morse potential depicted in Figure 3.2(a). In particular, phonon emission plays a crucial role in facilitating the relaxation of vibrationally excited electronic states back toward equilibrium, such as after photon absorption or charge-carrier injection. Even at zero temperature, the presence of zero-point energy ($\nu = 0$) ensures that nuclei retain residual vibrational motion.

Organic semiconductors possess a strong electron-phonon coupling (EPC) [25], i.e., a strong electronic distortion (electron motion) leads to strong nuclear relaxation (nuclear motion) and *vice versa* that arise due to the comparably weak bonding of the conjugated system. Note, that the electron distribution changes quasi-instantaneously in comparison to the timescale of nuclear movements due to the low mass of electrons. This feature is especially prominent for cationic or anionic OSCs. The disturbed conjugation due to a missing or excess electron creates a strong electronic disturbance and thus a strong nuclear distortion, which coupled deformation forms a quasiparticle known as polaron.

The strong electron-phonon coupling in charged systems, i.e., the polaron, leads to a spatial modulation of the electron density along the conjugate system, resulting in oscillatory behavior of both charge density and dipole moment along the conjugate system. This oscillating dipole moment interacts with infrared radiation, leading to intense absorption of radiation with characteristic frequencies above 400 cm^{-1}, so-called intense vibrational modes (IVMs) [82, 83], that are not present in the undisturbed, neutral conjugated system, as exemplarily shown in Figure 3.2(b). Thus, infrared radiation can be used as experimental and theoretical tool to identify the presence of an excess charge. Moreover, different bonding patterns, such as triple bonds between carbon and nitrogen, posses specific excitation energies. As a consequence, these excitation energies can be used as experimental descriptor of the chemical constitutions of the OSCs.

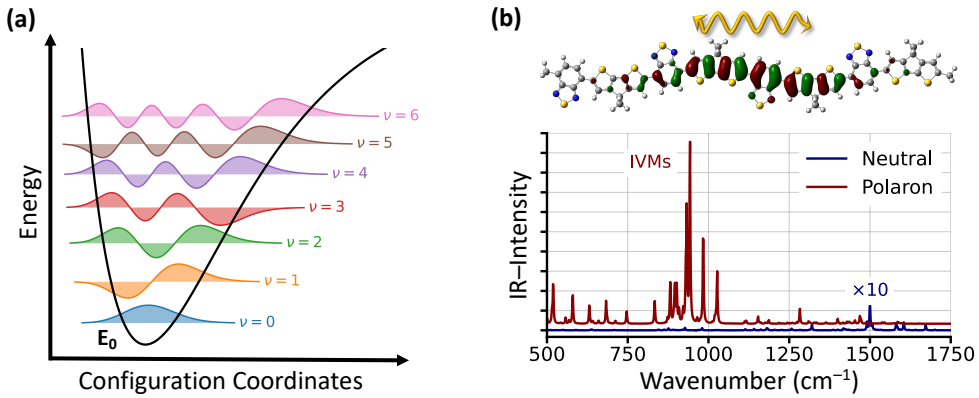

Figure 3.2: Vibrational wave function and intense vibrational modes. (a) Morse potential with corresponding vibrational wave functions. (b) Intense vibrational modes of a polaron (red) compared to the vibrational modes of the neutral system (blue). The example OSC is the positively charged or neutral PCPDT–BT. The spectrum of the neutral system is rescaled by a factor of 10; both spectra are shifted on the y-axis for better visualization and broadened by Lorentzian shapes with a half-width of 3 cm^{-1}. In addition, the unoccupied orbital reflecting the positive charge (missing electron) is displayed, and its oscillatory motion is indicated by a yellow wavy arrow. DFT @ cam-b3lyp/6-31g(d,p)/D3BJ.

At room temperature, the thermal energy ($k_BT \approx 25$ meV) is comparable to or larger than many low-frequency vibrational modes in OSCs, but remains much smaller than high-frequency vibrations. Consequently, low-frequency modes are often treated using a classical approximation, whereas high-frequency modes require a quantum-mechanical description. In the classical approach, Boltzmann distributions are used to describe thermal populations, and vibrational effects are incorporated phenomenologically via Gaussian or Lorentzian broadening functions. Such treatments effectively mimic the influence of finite temperature and environmental fluctuations and often permit analytical or semi-analytical solutions to otherwise intractable problems. The classical approximation is particularly suitable for low-frequency modes at higher temperatures, where thermal excitations are significant and quantum effects beyond zero-point motion are reduced. For high-frequency modes or at low temperatures, however, a fully quantum-mechanical treatment using phonon occupation numbers is required. This mixed quantum-classical framework is widely employed in simulations of charge transport in OSCs [77, 78].

In a realistic scenario, non-zero temperature and the environment (other OSC molecules and polymers, solution molecules, ...) induce transitions between vibrational wave functions, or in other words, the system evolves dynamically. The influence of these dynamics on the electronic structure is further discussed in Section 4.2.

3.4 Photoexcited States - The Exciton

High-energy radiation, such as visible light, can promote electrons to higher electronic energy levels, creating what is known as an excited state, analogous to the excitation of vibrational modes by low-energy absorption. These excited states are labeled with a subscript that indicates their order of increasing excitation energy within a given spin multiplicity. The ground state of a singlet system is accordingly labeled as S_0.

For neutral OSCs, the excited-state manifold includes not only singlet states (S_1, S_2, ...) but also triplet states (T_1, T_2, ...). Although these triplet states cannot be accessed directly by optical excitation because spin must be conserved, they can be populated indirectly through spin-flip processes enabled by spin-orbit coupling. These mechanisms will be examined in detail in Section 5.2.

Light absorption manifests as a decrease in the intensity of incoming light (photons in the quantum-mechanical description) and is governed by the frequency-dependent absorption cross section, $\sigma(\omega)$, which quantifies the probability per molecule that a photon of frequency ω will be absorbed [84]. Absorption occurs when the photon energy matches the energy difference between the initial and final electronic states, including their associated vibrational sublevels, provided sufficient vibrational wave function overlap exists. Because electronic motion occurs on a much faster timescale than nuclear motion (Born–Oppenheimer approximation), the transition is effectively vertical in nuclear coordinate space (*Franck–Condon principle*). This situation is illustrated in Figure 3.3(a). Following this vertical excitation, the system typically relaxes on the excited-state PES via vibrational relaxation until reaching the minimum-energy configuration, giving rise to a reorganization energy.

The oscillator strength f is introduced as a dimensionless measure of how strongly an electronic transition interacts with external light, effectively measuring that transition's contribution to the overall absorption spectrum. This parameter is directly related to the transition dipole moment between the involved states, as shown in Appendix A.2.3 [84]. Consequently, for triplet states f vanishes, since spin conservation renders the transition dipole moment formally zero.

The primary optical excitation in neutral OSCs is the lowest-energy singlet state, S_1. In the simplest single-particle picture, this excitation can be approximated as the promotion of an electron from the HOMO to the LUMO, as illustrated in Figure 3.3(b). The corresponding transition energy typically lies in the range of a few electronvolts.

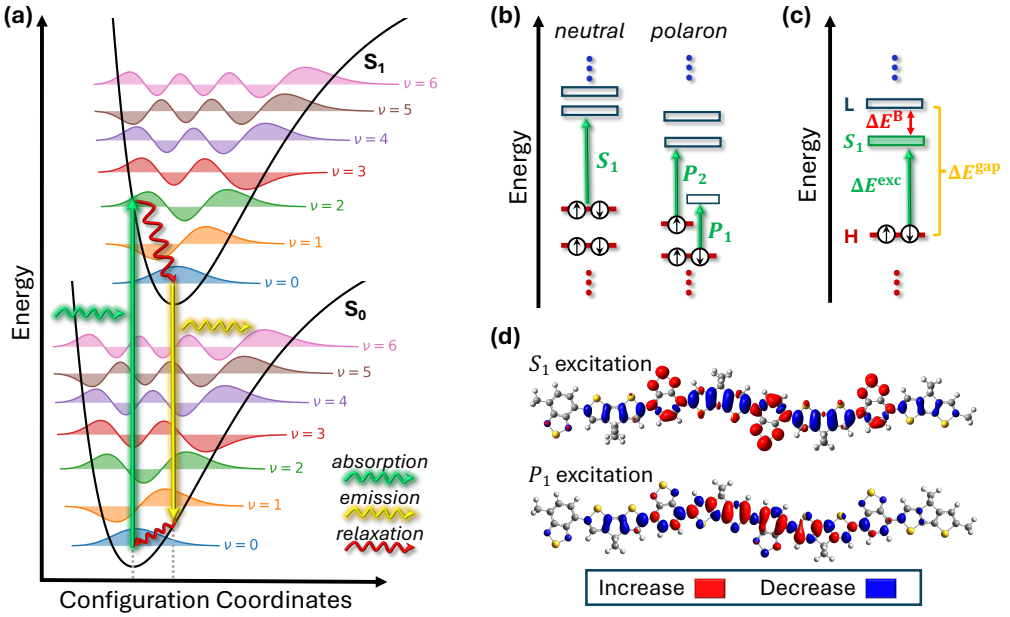

Figure 3.3: Electronic excitation schemes. (a) Franck–Condon diagramm for vertical excitation from the ground state (S_0) to the first singlet excited state (S_1). For illustration purpose, both potential energy surfaces are alike; the vibrational wave functions are included. The relaxation of the vertical excited state to its equilibrium position is illustrated as red waved arrow. (b) Orbital energy levels involved in the S_1 transition for neutral (singlet) OSC and polaronic absorption P_1 and P_2 for singly positive charged (doublet) OSC. (c) Schematic illustration of the difference between the single-particle band-gap (HOMO–LUMO separation, ΔE^{gap}) and the S_1 excitation energy (optical gap, ΔE^{exc}). The optical excitation corresponds to the formation of a bound electron-hole pair (exciton), whose energy lies below the band-gap due to Coulomb interaction. The exciton binding energy, ΔE^{B}, is indicated. (d) Charge density difference (CDD) for the S_1 and P_1 excitation of PCPDT–BT. TD-DFT @ cam-b3lyp/6-31g(d,p)/D3BJ.

Owing to electron-electron interactions, the S_1 excitation energy (ΔE^{exc}, optical gap) is lower than the single-particle band-gap (ΔE^{gap}, HOMO–LUMO gap), as shown in Figure 3.3(c). This reduction arises from the Coulomb attraction between the excited electron and the hole it leaves behind, which together form a bound electron-hole pair constituting a quasiparticle known as an exciton. The excitation simultaneously perturbs the electronic structure, inducing a redistribution of the remaining electrons and a corresponding modification of the orbital energies, particularly those associated with singly occupied states.

The difference between the single-particle band-gap ΔE^{gap} and the actual excitation energy ΔE^{exc} of the lowest exciton (after accounting for the accompanying redistribution of the

electronic structure) is referred to as the exciton binding energy ΔE^{B}. It is thus defined as

$$\Delta E^{\mathrm{B}} = \Delta E^{\mathrm{gap}} - \Delta E^{\mathrm{exc}} \,. \tag{3.12}$$

In OSCs, typical exciton binding energies lie on the order of several hundred meV, indicating that the electron and hole remain strongly bound [85]. Importantly, ΔE^{B} is not identical to the bare Coulomb interaction between an isolated electron and hole, which can be written as

$$E_{\mathrm{C}} = -\iint \frac{\rho^{\mathrm{hole}}(\mathbf{r}_1)\rho^{\mathrm{electron}}(\mathbf{r}_2)}{|\mathbf{r}_1 - \mathbf{r}_2|}\, \mathrm{d}^3 r_1\, \mathrm{d}^3 r_2 \,, \tag{3.13}$$

where ρ^{electron} and ρ^{hole} denote the electron and hole densities of the excited-state wave function, respectively.

Beyond the lowest-energy S_1 excitation, absorption of photons with energies well above the optical gap can populate higher-lying excited states, forming so-called *hot* excitons. In contrast to S_1, these higher excited states are generally not well described by a single HOMO-to-LUMO-type electron promotion within a simplified single-particle picture. Instead, their composition is more complex, typically involving a linear combination of several single-electron excitations between different occupied and unoccupied orbitals, leading to a stronger many-body character. Consequently, the concept of a well-defined exciton binding energy becomes less meaningful for such excited states, as their structure cannot be reduced to a simple electron-hole pair associated with a specific orbital transition.

In ionized OSCs, where a polaron is present, additional low-energy excitations appear in the ultraviolet region. These polaronic absorption features, denoted P_1 and P_2, arise from transitions involving singly (un)occupied molecular orbitals [86], as shown in Figure 3.3(b). As a result, absorption in the visible and ultraviolet spectral ranges provides a simple and powerful method for identifying different charged species in both experiments and theoretical calculations.

After excitation, the exciton may undergo several possible transitions within the excited-state manifold: it can transition to other excited states, dissociate into separated charges, or recombine to the (vibrationally excited) ground state. This recombination may be accompanied by photon emission, either spontaneously or through stimulated processes. The various pathways between (vibrationally) excited states will be detailed in Section 5.2, and their significance for practical applications, particularly their crucial role in the functioning of organic photovoltaic devices, will be explored in Section 8.

When analyzing these transitions between excited states (and the ground state), the molecular orbital representation (as in Figure 3.3(b,c)) is typically set aside in favor of a state-based description involving singlet and triplet manifolds, as illustrated in Figure 3.3(a). This state picture provides a more intuitive framework for describing and visualizing excited-state processes.

Analogous to the electrical dipole moment of the ground state, an excited-state dipole moment can be defined by replacing the ground-state electron density in Equation 3.1 with the electron density of the excited state. The corresponding polarizability can be interpreted in an analogous manner. The influence of this excited-state dipole moment on the operation of organic photovoltaic devices is discussed in detail in Section 8.

To characterize the nature of an excited state from a theoretical perspective, one often examines the difference between the electron densities of the excited and ground states, yielding the charge density difference (CDD). Similar to molecular orbital visualizations, the CDD offers an intuitive representation of electron and hole distributions. An alternative approach involves analyzing the natural transition orbitals (NTOs) [87], which describe the excitation in terms of a compact set of molecular orbitals rather than a full electron-density difference.

The computational methods employed in this thesis to model the electronic structure of ground and excited states are density functional theory (DFT) and time-dependent density functional theory (TD-DFT), respectively. A brief introduction to these methods is provided in Appendix A.4, together with the relevant concepts employed. As these tools are well established and widely used in the field, an extensive discussion in the main text is not included.

In the following section, the influence of the environment and the interactions between OSCs are examined. This discussion is essential because the functionality of organic electronic devices depends not only on the properties of individual molecules but also on the complex interplay among multiple OSCs.

Environmental Influences 4

As the morphology of the OSCs strongly affects the efficiency of the target application, understanding and controlling molecular interactions and structural organization is essential [30, 38–40]. Morphology describes the spatial arrangement and orientation of molecular systems across multiple length scales, ranging from local intermolecular packing at the molecular scale to extended structural organization at the nanoscale and (semi-)microscale.

In multi-component OSC systems (for example, donor:acceptor blends), aggregation of chemically identical species on larger length scales can give rise to compositionally enriched regions, potentially leading to phase separation and the formation of distinct domains. The boundary between such donor- and acceptor-rich domains is referred to as an interface. An example of such an interfacial morphology is shown in Figure 4.1 for a donor:acceptor blend investigated in this thesis, where nanoscale donor- and acceptor-rich regions form an interpenetrating network.

Depending on the intended application, specific packing motifs may be advantageous. These motifs are governed by molecular architecture, side-chain-induced solubility and steric effects, as well as processing conditions such as deposition method and temperature. While some OSCs adopt predominantly amorphous morphologies, others form clustered or (semi-)crystalline structures, which can significantly impact device performance [40].

Accurately modeling morphology remains a major challenge. Because such simulations require the dynamic evolution of systems comprising thousands of atoms, a fully quantum-mechanical treatment of the electronic structure, for example via DFT, is computationally prohibitive. Consequently, interatomic interactions are commonly approximated using parametrized empirical potentials, known as force fields. These describe bonded interactions (bond stretching, angle bending, and dihedral rotations) as well as non-bonded interactions, including Coulomb and van der Waals forces, and are employed within classical molecular dynamics simulations. The underlying force-field parameters, such as atomic partial charges and bond characteristics, are typically derived from DFT calculations, thereby retaining a link to an accurate quantum-mechanical description. Among the most widely used force

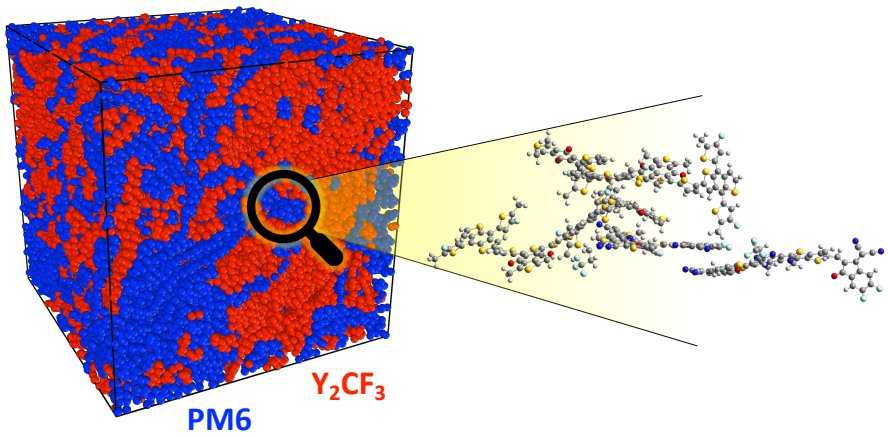

Figure 4.1: Morphology of PM6:Y_2CF_3 blends. Example of a unit cell from force-field molecular dynamics simulations of PM6:Y_2CF_3. Donor (PM6) atoms are shown in blue, while acceptor (Y_2CF_3) atoms are shown in red. Adapted from F. Bauch et al., *ACS Applied Materials & Interfaces* **18**, 2200-2211 (2026). Copyright © 2025 American Chemical Society.

fields for modeling OSC morphologies is OPLS–AA (Optimized Potentials for Liquid Simulations – All Atom) [88, 89]. On the basis of such force-field molecular dynamics simulations, representative molecular complexes can subsequently be extracted for quantum-chemical calculations, enabling detailed analysis of the electronic structure of relevant molecular complexes.

In this section the physical interaction between OSCs will be elaborated, starting with a brief summary of the different types of electronic interaction, followed by a discussion of the electronic-structure disorder in amorphous systems. Finally, the influence of surrounding solvent molecules on the OSCs will be discussed.

4.1 Different Types of Electronic Interaction

Molecular systems such as OSCs posses various interactions from different physical origins. These interactions govern not only the mutual electronic interaction itself, but also the underlying organization of the morphology. As such, a deep understanding of the interaction does not only provide a description of the electronic interaction itself but also provides significant insight into controlling the morphology. The electronic interaction can be substantiated into four significant contributions (although different, comparably weak interactions are also present), which are outlined thereafter.

Electrostatic.
This term captures the attractive or repulsive classical Coulomb interaction between static charge distributions, i.e., between negatively charged electrons and positively charged nuclei. For instance, any given electron in the OSC experiences the electric field generated by all other electrons and nuclei.

Exchange.
According to the Pauli exclusion principle, electrons with the same spin cannot occupy the same quantum state, which reduces their spatial overlap. This requirement gives rise to an effective short-range repulsive interaction known as Pauli repulsion.

Induction.
Induction, which corresponds to the polarization of a molecule, arises from electrostatic forces: the electric field of one charge distribution distorts the electron density of another. This polarization slightly separates positive and negative charges, creating an induced dipole.

Dispersion.
Dispersion interactions, or more commonly known as van der Waals forces, originate from quantum-mechanical fluctuations in electron density within OSCs. These fluctuations generate rapidly varying instantaneous dipoles and the associated electric fields. These fields, in turn, polarize neighboring molecules, inducing similarly fluctuating dipoles. The mutual, correlated polarization between molecules leads to interacting induced dipoles.

Dispersion is regarded as the key interaction governing the packing motifs of OSCs, together with electrostatic forces and the inherent molecular geometry. Consequently, in mixed OSC systems, the permanent electric dipole moment serves as an important indicator for predicting and controlling phase separation.

4.2 Interaction and Disorder in Organic Semiconductors

In real applications a manifold of OSC molecules is present, each with interacting electronic structures which in turn depend on the OSC's spatial arrangement, packing orientation, clustering, and which dynamically evolve in time due to electron-phonon coupling at finite temperatures. As such, modeling and interpreting such kind of time-dependent morphology is of great interest, as it controls, e.g., transfer integrals and orbital energy levels for charge transport or for the exciton dissociation dynamics which will be discussed

in detail in Sections 7.2 and 8, respectively. Such morphology is illustrated in Figure 4.1 for a donor:acceptor blend composed of donor polymer PM6 and acceptor molecule Y_2CF_3, depicting the complex interplay between both systems.

The electronic structure of the individual OSCs is screened due to the electrostatic interaction and polarization effects with the surrounding OSC matrix depending on the spatial position and orientation within this matrix. As a consequence of the local structural environment, the orbital energy levels are shifted and differ within this matrix, which is referred to as static disorder (or positional or site disorder), which is illustrated in Figure 4.2(a). In addition to the static disorder, electron-phonon coupling causes temporal fluctuations of the molecular geometry and electronic structure, which is referred to as the dynamic disorder. Note that both types of disorder are mutually dependent on each other, as the spatial position affect the electron-phonon coupling and *vice versa*. However, electron-dynamics are comparably much faster than large spatial rearrangements.

As a result, the electronic properties, such as orbital energies and the excitation energies, cover a broader energetic range within the matrix instead of a single value. This broader distribution of orbital energies is referred to as the density of states (DOS), describing the distribution (or probability) of the orbital energies, as illustrated in Figure 4.2(a). In OSC it is observed and commonly accepted that the disorder in the orbitals (especially the HOMO and LUMO) and excitation energies follow a Gaussian distribution, with the standard deviation of the distribution describing the total disorder (static and dynamic), typically in the range of 50-200 meV. However, also exponential edges have been observed and described [25, 45, 46, 90, 91]. Therefore, it is common practice to artificially broaden the orbital and excitation energies obtained from electronic structure calculations of isolated OSC molecules in order to approximate the energetic distribution present in a larger OSC matrix.

When a charge or exciton resides on an OSC, it significantly modifies the local electronic structure. Such effects manifest as on-site interactions, such as nuclear reorganization and intramolecular polarization, as well as inter-site interactions that extend to neighboring OSC molecules and modify their immediate molecular surroundings. Both exist in static and dynamic forms. Consequently, even though a charge or exciton is primarily localized on a single OSC, it induces shifts in the orbital energies of nearby neutral OSCs, as illustrated in Figure 4.2(b) for the case of a positive charge.

Beyond disorder in orbital and excitation energies, new physical processes emerge from intermolecular interactions. In mixed or heterogeneous OSC systems, these processes include

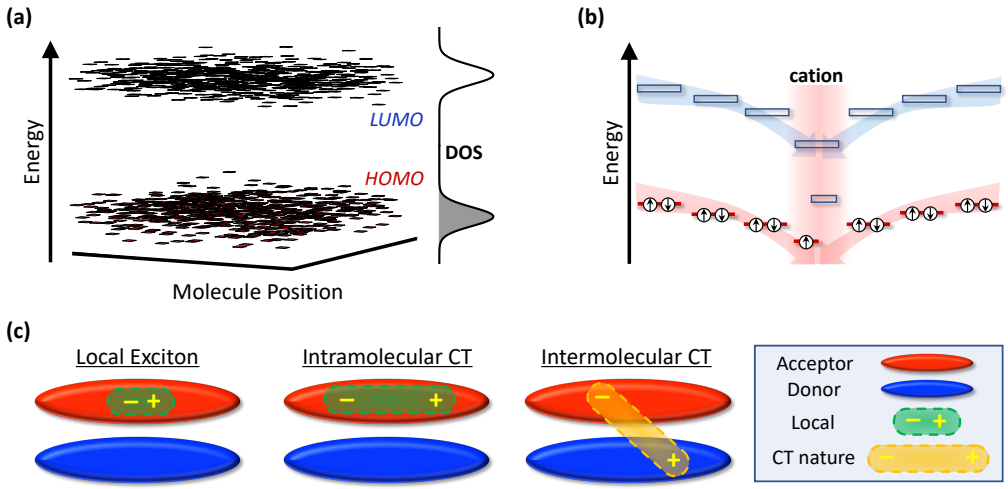

Figure 4.2: Disorder, intersite interactions, and exciton nature in organic semiconductors. (a) Illustration of static energetic disorder in HOMO and LUMO levels, modeled as Gaussian-distributed energy probability with a standard deviation of 0.1 eV. The density of states (DOS) is illustrated. (b) Effect of intersite Coulomb interactions on the orbital energies of neutral molecules in the vicinity of a positively charged molecule (cation). (c) Schematic representation of different exciton types in OSCs: strongly bound local (Frenkel-type) excitons, less tightly bound intramolecular charge-transfer (i-CT) excitons, and weakly bound intermolecular charge-transfer (CT) excitons.

charge transfer between OSCs, energy transfer following exciton formation (such as Förster and Dexter energy transfer) [28, 92, 93], hybridization of molecular orbitals from neighboring OSCs resulting in more delocalized orbitals (which is particularly prominent in highly symmetric molecular packings), and the formation of new excited states. Charge-transfer interactions are characterized by transfer integrals, whereas excited-state interactions are described by electronic or spin-orbit couplings.

In complex OSC systems, excitons can arise in several distinct forms. The most prevalent are Frenkel-type excitons, in which the electron and hole are tightly bound and remain localized on the same molecular unit; these are often simply referred to as excitons. However, interactions between different OSCs can also give rise to charge-transfer (CT) excitons, in which the electron and hole reside on separate molecular entities, resulting in a reduced Coulomb binding energy [45]. This type of excitation is especially relevant in donor:acceptor complexes, where differences in HOMO and LUMO energy levels localize the hole and electron on the different molecules.

In donor-acceptor polymers and small molecules, the exciton may similarly display CT

character with the HOMO and LUMO located on different segments of the same molecule. This intramolecular electron-hole separation leads to an intramolecular charge-transfer (i-CT) exciton, typically exhibiting a lower binding energy than the strongly localized exciton. In order to distinguish these from intermolecular CT excitons, excitations confined to a single OSC are generally termed local excitons or locally excited states. The distinctions among these three excited-state types are illustrated in Figure 4.2(c).

Consequently, the electronic disorder and OSC:OSC interaction plays a major role in both charge transport and charge generation, as it not only leads to broader distributions, but also affects transfer integrals and electronic couplings for charge transport and excited-state transitions, respectively. As such, its role and influences will be elaborated in more detail in the respective sections targeting the specific applications.

The polarizability and dipole moment partially govern the overall dielectric constant ε (or relative permittivity) of the microscopic and macroscopic systems, which is the general quantity describing the reaction of the electronic structure to external electric fields (quantified relative to vacuum). Due to the disordered nature, the morphology affects the dielectric constant by (mis-)aligning the individual molecular properties. While the alignment of the permanent dipole moment with the electric field is rather slow, the polarization contribution is very fast.[1] Typically, the dielectric constant for OSC lies somewhere between 2 and 5, much lower than for inorganic materials in the range of 10 or more. As a consequence, charges are rather localized and strongly interact with each other, a common issue of OSC in applications.

4.3 Interaction of Organic Semiconductors with Solvent Molecules

To optimize the performance of various applications, processing solvents are employed that influence both the morphology of the system, through steric interactions with the OSCs, as well as their electronic properties via dielectric screening. Commonly used solvents include chlorobenzene, chloroform, *p*-xylene, and toluene, among others. The differences between these solvents are not limited to their molecular geometry but extend to their polarity, which ultimately determines their dielectric constant ε and their response to

[1] The dielectric constant is a frequency-dependent quantity, as the electric field induced by dipoles changes more rapid than the complete system can react to these changes. Thus, for low frequencies, the system can react appropriately, whereas it cannot react appropriately to high frequency electric fields.

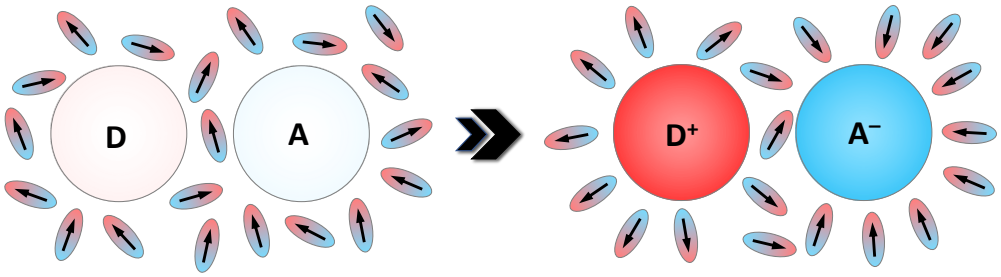

Figure 4.3: Illustration of outer shell reorganization of solvent molecules induced by formation of an intermolecular charge-transfer state. The electron-transfer from the donor (D) to the acceptor (A) molecule leads to a reorientation of the (non-)polar solvent molecules. Both the electronic properties of the OSC and the solvent influence each other via electrostatic and inductive interactions.

external electric fields. Owing to similarities in intermolecular interactions with the OSC itself, both polar and non-polar solvents can therefore be effectively utilized to tune the morphology and the electronic structure. It is important to note, however, that not all OSCs are compatible with every solvent, as miscibility can be limited.

From an electronic perspective, the charge distribution within an OSC interacts with that of the surrounding solvent molecules. In non-polar solvents, the local electric fields of the OSC induce polarization within the solvent, which in turn feeds back onto the OSC. In polar solvents, in addition to this induction effect, the permanent dipole moments of the solvent molecules can reorient and interact with the OSC charge distribution (see illustration in Figure 4.3). In both cases, the solvent interaction stabilizes the electronic states of the OSC, which in turn influences both the geometry of the OSC and the structural reorganization of the solvent environment. Noteworthy, the electronic response is rapid in comparison to geometrical reorientation. As a result, occupied molecular orbitals are typically shifted upward in energy, while unoccupied molecular orbitals are shifted downward. Within the scope of this work, solvation is treated implicitly by representing the OSC inside a polarizable cavity, since the explicit inclusion of solvent molecules is computationally impractical.

The geometric reorientation of surrounding molecules becomes especially important in the presence of charged OSCs, such as during electron-transfer events or the formation of CT excitons. In these scenarios, the strong electric fields generated by positive and negative charges induce electrostatic and inductive interactions not only with nearby solvent molecules but also with neighboring OSCs. This phenomenon is commonly captured by the concept of outer shell reorganization, which represents the reorganization energy

associated with the structural response of the environment. In contrast, the reorganization energy of the OSC undergoing the electronic transition itself is termed inner shell reorganization. This concept is now extended to the description of charge-transfer processes and excited-state transitions investigated in this work, which will be elaborated in the following section.

Interim Summary

Organic semiconductors can be described by different electronic states at a given nuclear configuration, where a typical single-particle picture is involved describing the electronic configuration. The nuclear configuration evolves dynamically due to vibrations, which is instantaneously followed by the electronic structure, giving rise to strong electron-phonon coupling. The electronic properties, such as molecular orbital energies, electronic distributions, and responses to external stimuli strongly depend on the environment as well as specific nuclear configuration of the OSC, giving rise to large electronic disorder.

Static Approaches of Charge Transfer and State Transitions 5

Transitions between states are dynamical processes by definition. However, a full quantum-mechanical treatment of electron-nuclear dynamics is conceptually intricate and computationally prohibitive. This section discusses the transfer rate constants (average transfer events per time) between electronic states. Transfer rates provide statistical predictions of average events, no explicit dynamic tracking of states is achieved. Within the course of this thesis, charge transfer processes AD $\rightarrow A^- D^+$ will be explored, which can be described within a chemical electron-transfer reaction, as well as transitions between excited states and excited to ground state transitions. These processes occur between identical molecular systems (a dimer in the case of two molecules) or different molecular systems forming complexes. Although these processes differ fundamentally in their physical nature, important similarities can still be drawn. Here, an analytical derivation is out of the scope of this thesis. Rather, a descriptive approach is chosen to provide necessary quantities for the understanding of this thesis.

5.1 Electron Transfer

Starting in a quantum-mechanical framework via Fermi's golden rule, the transfer rate k_{ij} from initial state i to the final state j is given by:

$$k_{ij} = \frac{2\pi}{\hbar} \left| \langle \Psi_i | \hat{\mathcal{H}}' | \Psi_j \rangle \right|^2 \rho(E_j) \ . \tag{5.1}$$

Here, $\Psi_{i(j)} = \Psi^{\text{el}}_{i(j)} \Psi^{\text{vib}}_{i(j)} \Psi^{\text{spin}}_{i(j)}$ is the wave function of the respective states, consisting of an electronic ($\Psi^{\text{el}}_{i(j)}$), vibrational ($\Psi^{\text{vib}}_{i(j)}$), and spin component ($\Psi^{\text{spin}}_{i(j)}$); $\rho(E_j)$ is the density of final states with matching energy E_j; $\hat{\mathcal{H}}'$ is the perturbation Hamiltonian driving the transition; and $\hbar$ is the reduced Planck constant. Decoupling the electronic (and spin) component(s) and the vibrational component of the wave function (*Franck–Condon approximation*), the instantaneous perturbation Hamiltonian for electron transfer affects only the electron (and

spin) component(s). Thus, Equation 5.1 reads:

$$k_{ij} = \frac{2\pi}{\hbar} \underbrace{\left| \langle \Psi_i^{\mathrm{el}} \Psi_i^{\mathrm{spin}} | \hat{\mathcal{H}}' | \Psi_j^{\mathrm{el}} \Psi_j^{\mathrm{spin}} \rangle \right|^2}_{\left|V_{ij}^{\mathrm{el}}\right|^2} \underbrace{\left| \langle \Psi_i^{\mathrm{vib}} | \Psi_j^{\mathrm{vib}} \rangle \right|^2 \rho(E_j)}_{\mathrm{FCWD}} \,. \tag{5.2}$$

The electronic and spin component together govern the overall electronic contribution that is described by the electronic coupling V_{ij}^{el}. The *Franck–Condon* (FC) factor $\left| \langle \Psi_i^{\mathrm{vib}} | \Psi_j^{\mathrm{vib}} \rangle \right|^2$ and $\rho(E_j)$ describe the vibrational component, it is termed as *Franck–Condon-weighted density of states* (FCWD).

Vibrational component.
In practice, it is not an easy task to describe the FCWD, as it requires knowledge of the quantized vibrational states of the initial and final states. Starting from an easy and intuitive picture of electron transfer in a chemical reaction, a *two-state model* of diabatic states is commonly employed, as schemed in Figure 5.1. Furthermore, a classical-approach of thermal fluctuations of the nuclear coordinates is applied, i.e., a non-quantized, smooth distribution of the vibrational energies under thermally distributed Boltzmann statistics is assumed. This leads to an Arrhenius-type proportionality of the FCWD for thermally activated transport [77]:

$$\mathrm{FCWD} \propto e^{-E_a/k_B T} \,. \tag{5.3}$$

Here, E_a is the activation energy, i.e., the height of the energy barrier (Figure 5.1). It can be viewed as the energy necessary to reach the crossing point of the diabatic PESs of the involved states from the initial equilibrium. Note, that this proportionality arises from the idea that thermal fluctuations lead to reaching of the crossing point, and thus facilitate the electron transfer.

Fundamental work on the electron transfer mechanism in chemical reactions has been done by R. A. Marcus, who related the activation energy under classical *harmonic approximation* of the (identical but shifted) diabatic parabolic PESs to the reorganization energy and the Gibbs free energy difference [94, 95]:

$$\mathrm{FCWD} = \sqrt{\frac{1}{4\pi k_B T \lambda}} \exp\left[\frac{-(\Delta G + \lambda)^2}{4 k_B T \lambda}\right] \,, \tag{5.4}$$

where ΔG is the Gibbs free energy difference between the equilibrium of the involved states (termed as driving force), and λ is the classical reorganization energy associated

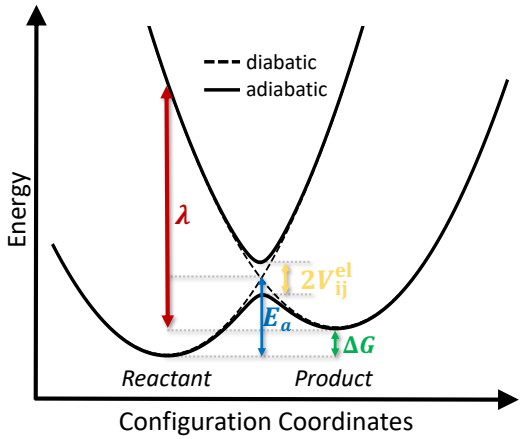

Figure 5.1: Potential energy surfaces for an electron transfer reaction. The diabatic and adiabatic PESs of the reactant and product states are shown. The shape of the PESs is for illustrative purposes only; the curvature of the diabatic PESs is identical. The activation energy E_a corresponding to the crossing point of the diabatic states is illustrated. In the framework of Marcus theory, the reorganization energy λ, the driving force ΔG, and the electronic coupling V_{ij}^{el} are shown.

with the transition (both illustrated in Figure 5.1). Combining the FCWD by Marcus with the quantum-mechanical framework as done by Levich and Dogonadze [96–99] ultimately leads to the famous semiclassical transfer rate constant in the Marcus theory [95], granting Marcus the Nobel Prize in Chemistry in 1992 [100]:

Equation 5.5

$$k_{ij} = \frac{2\pi}{\hbar}\left|V_{ij}^{\mathrm{el}}\right|^2 \sqrt{\frac{1}{4\pi k_B T \lambda}} \exp\left[\frac{-(\Delta G + \lambda)^2}{4 k_B T \lambda}\right] .$$

In the electron transfer mechanism described by Marcus, the reorganization energy consists of the sum of an internal vibrational contribution (inner shell, λ_{i}) and a surrounding environmental contribution (outer shell, λ_{s}), $\lambda = \lambda_{\mathrm{i}} + \lambda_{\mathrm{s}}$. The transfer rate constant evaluated via Equation 5.5 is illustrated in Figure 5.2 as a function of driving force at different temperatures and reorganization energies. Some key observation are:

1. The driving force ΔG should be in resonance with the energy-penalty of reorganizing the nuclear coordinates to maximize the rate constant.

2. Thermal population of high energy vibrational coordinates (increasing temperatures)

can promote the process by broadening the Gaussian distribution, thus facilitating higher rate constants for mismatching driving forces.

3. If the driving force increases beyond the reorganization energy ($-\Delta G > \lambda$) the transfer rate constant is reduced (*Marcus' inverted region*).

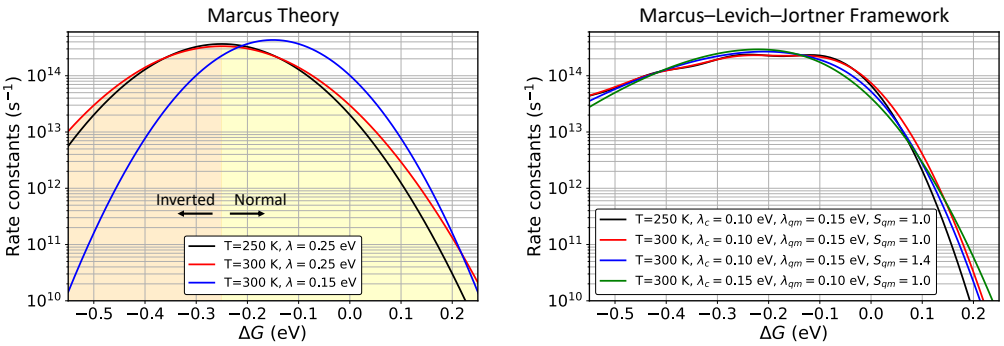

Figure 5.2: Evaluation of transfer rate constants for various parameters. The transfer rate constant evaluated within Marcus theory (Equation 5.5) is shown on the left, while the result obtained using the Marcus–Levich–Jortner framework (Equation 5.9) is shown on the right. The Marcus normal ($-\Delta G < \lambda$) and inverted ($-\Delta G > \lambda$) regions are illustrated as shaded areas below the red curve. The electronic coupling is set to 0.1 eV.

In most relevant physical processes OSC comprise high-frequency vibrational modes, that have to be embedded in the evaluation of the FCWD. Thus, a different approach comprising the quantized high-frequency modes while treating the low-frequency bath classically was developed, later known as the Marcus–Levich–Jortner (MLJ) framework. The general thoughts behind the MLJ framework will be briefly outlined; for a more detailed description the reader is referred to References [25, 78, 101–104].

Employing a harmonic oscillator approximation for the quantized vibrational modes, the reorganization energy λ_m induced by mode m with frequency ω_m for the relevant transition between the states can be related to its Huang–Rhys factor S_m [105] via [101]:

$$\lambda = \sum_m \lambda_m = \sum_m \hbar\omega_m S_m \ . \tag{5.6}$$

As such, the Huang–Rhys factor is a measure of the electron-phonon coupling.

The reorganization energy can be expressed in terms of the displacement along the normal coordinates, ΔQ_m, or more precisely, the change in these coordinates on the respective PESs for vibrational mode m. Within this framework, the Huang–Rhys factor S_m reflects the shift

in the equilibrium geometries of the states, projected onto the displacements associated with normal mode m under the harmonic approximation [78]:

$$S_m = \frac{1}{2}\omega_m \frac{\Delta Q_m^2}{\hbar} \,. \tag{5.7}$$

Here, ΔQ_m denotes the corresponding mass-weighted displacement in equilibrium geometry projected onto that normal mode.

Generally, describing the full dimension of the FC factor involves all transitions from the initial n-th vibrational state to the final m-th vibrational state. However, it can be assumed that initially only the 0-th ground state vibrational mode is active (this approximation is appropriate in the low temperature limit [103]), then the vibrational FC factor describes the probability of the 0-th vibrational level of the initial state to the m-th vibrational level of the final state. Moreover, in practice, instead of describing all individual vibrational levels, a single effective quantum-mechanical vibrational mode will be evaluated to describe all modes with corresponding S_{qm}, λ_{qm}, and ω_{qm}. Under these circumstances, the FC factor takes the form of a Poisson distribution [78, 101, 103, 104]:

$$\mathrm{FC} = \frac{S_{\mathrm{qm}}^m}{m!} e^{-S_{\mathrm{qm}}} \,. \tag{5.8}$$

Finally, the product of $\rho(E_j)$ and FC defines the FCWD.

Following this Ansatz, the transition rate evolves in the MLJ framework to:

Equation 5.9

$$k_{ij} = \frac{2\pi}{\hbar}\left|V_{ij}^{\mathrm{el}}\right|^2 \sqrt{\frac{1}{4\pi k_B T \lambda_{\mathrm{c}}}} \sum_{m=0}^{\infty} e^{-S_{\mathrm{qm}}} \frac{S_{\mathrm{qm}}^m}{m!} \exp\left[\frac{-(\Delta G + \lambda_{\mathrm{c}} + m\hbar\omega_{\mathrm{qm}})^2}{4 k_B T \lambda_{\mathrm{c}}}\right] \,.$$

Here, S_{qm} is the Huang–Rhys factor associated with the single effective high-frequency mode ω_{qm}, with $S_{\mathrm{qm}} = \frac{\lambda_{\mathrm{qm}}}{\hbar\omega_{\mathrm{qm}}}$, a measure for the electron-phonon interaction.

The transfer rate constant within the MLJ framework is illustrated in Figure 5.2(b) for different parameter sets. It is apparent that treating vibrational modes quantum-mechanically is especially important in Marcus' inverted region, where the driving force exceeds the classical reorganization energy in Marcus theory.

Typically, the reorganization energy used in Marcus theory or within the MLJ framework is obtained from electronic structure calculations of the OSC. In this thesis, the four-

point method is applied to compute the reorganization energy in Marcus theory [106], whereas the Huang–Rhys factors and corresponding reorganization energies in the MLJ approach are derived from vibrational mode analysis; both procedures are briefly described in Appendix A.3. Within the four-point method, the total reorganization energy is evaluated from the PESs of the two involved states as the sum of the relaxation energies after vertical excitation and de-excitation. The reorganization energy appearing in Marcus theory is then obtained as the arithmetic average of these two contributions, thereby recovering the single-reaction-coordinate definition of the Marcus reorganization energy. To incorporate environmental contributions, it is standard practice to add an estimated value to the classical component of the reorganization energy, commonly taken to be 0.1 eV, which is a reasonable value for extended π-conjugated systems [107–109].

Finally, it is noted that the electron-phonon coupling and reorganization energies depend on the specific reaction pathway, thus, they might be asymmetric in both the forward and backward process of the reaction, in contrast to the symmetry assumed in standard Marcus theory.

Electronic component.
Having discussed the vibrational component, the electronic coupling for electron transfer will be elucidated now, an important parameter governing the overall magnitude of the transfer rate constant for electron (or hole) transport. In the weakly-coupling *two-state model*, the electronic coupling is equal to half the energy splitting of the adiabtatic PESs of the dimer at the crossing point of the diabatic PESs of the relevant states (depicted in Figure 5.1). Determining the electronic coupling in this sense requires the knowledge of both the diabatic states and the adiabatic states, which is not feasible due to the multi-configurational size of the reaction coordinates and electronic system.

In a *one-electron approximation*, additional electrons (holes) can be considered to lie within a localized molecular orbital, that is the LUMO (HOMO) of the mononomer molecular system. Thus, it was commonly accepted to use half the energy splitting of the HOMO (LUMO) and HOMO−1 (LUMO+1) energies of the dimer to approximate the electronic coupling, which is approximately valid for orbitals without spatial overlap $\mathcal{S}_{ij}$ [110–113], i.e., strong local character. To compensate for this spatial overlap, the coupling and site energies for electron (and hole) transfer in a dimer, the *fragment orbital approach* emerged [114].

In this approach, within a *tight-binding two-state model*, the one-electron dimer states are expressed in terms of localized molecular orbitals Ψ_i and Ψ_j of the two monomer

components, with respective site energies e_i and e_j. In this representation, the electronic coupling (or termed transfer integral J_{ij} in the context of tight-binding) is then given by:

$$J_{ij} = \langle \Psi_i | \hat{\mathcal{H}} | \Psi_j \rangle \ , \tag{5.10}$$

where $\hat{\mathcal{H}}$ is the Hamiltonian of the interacting system. Importantly, in this representation one might mistake J_{ij} for the electronic coupling of the interacting dimer system, but this does not correctly reflect the interaction between the monomers in the dimer system, as J_{ij} is constructed from non-orthogonal monomer orbitals, whereas in the tight-binding approximation orthogonal orbitals are necessary. Employing Löwdin's symmetric transformation [115] to generate an orthonormal basis set while maintaining as much local character of the monomer orbitals as possible, effective orbital energies e_i^{eff} (effective site energies) and an effective electronic coupling J_{ij}^{eff} (which are now identical to the electronic coupling and site energies of the interacting dimer) can be constructed from the monomer quantities:

$$\begin{aligned} e_{i(j)}^{\text{eff}} &= \frac{1}{2} \frac{(e_i + e_j) - 2J_{ij}\mathcal{S}_{ij} \pm (e_i - e_j)\sqrt{1 - \mathcal{S}_{ij}^2}}{1 - \mathcal{S}_{ij}^2} \ , \\ J_{ij}^{\text{eff}} &= \frac{J_{ij} - \frac{1}{2}(e_i + e_j)\mathcal{S}_{ij}}{1 - \mathcal{S}_{ij}^2} \ , \end{aligned} \tag{5.11}$$

where $\mathcal{S}_{ij}$ is the overlap matrix element between the two orbitals. Plugging J_{ij}^{eff} into Marcus theory or the MLJ framework (Equations 5.5 and 5.9) with driving force $\Delta G = e_i^{\text{eff}} - e_j^{\text{eff}}$, one can evaluate the transfer rate constants.

Key notes for electron (or hole) transfer rate constants are:

1. The effective transfer integral (electronic coupling) should be as large as possible to maximize the transfer rate constant.

2. The effective transfer integral is sensitive to small changes in the dimer conformation (twists, lateral and horizontal displacement deviating from perfect equivalent two molecules), where the phase of the orbitals strongly impacts the overlap matrix $\mathcal{S}$ [112–114].

3. The effective site energies e^{eff} in the dimer strongly depend on environmental polarization effects, whereas the effective transfer integral J^{eff} in the dimer is largely robust to environmental polarization effects [114].

Although the motivation of Marcus theory and the MLJ framework lies in describing electron (or hole) transfer mechanisms in chemical reactions, they are widely used to describe transitions between excited states if the excited-state transition is characterized by a charge transfer process.

5.2 Excited-State Transitions

As illustrated in Figure 5.3, after excitation of a singlet state, the system can undergoe several transitions between excited states and can decay to the ground state. Generally, it can be distinguished between radiative transitions (photon absorption/emission) and non-radiative transitions (phonon absorption/emission). Moreover, these can then further be divided into transitions between excited-states with the same spin (internal conversion, IC) or opposite spin (intersystem crossing, ISC). To differentiate IC/ISC processes between excited-states and IC/ISC processes to the ground state, the latter will be termed (non-)radiative decay. In addition, IC and ISC processes are often differentiated according to whether they involve charge transfer or preserve the local excitonic character of the state.

Later in this thesis, these transfer processes will be elaborated on device functionalities in the relevant Section 8. In this current section, the underlying theoretical models to describe these transitions with particular focus on investigated processes within this thesis will be elaborated. Similar to the previous section, a descriptive approach is provided here; a more detailed analytic description of the approaches are provided in Appendix A.2.

Non-radiative internal conversion involving electron transfer.
Within the context of this thesis, of particular interest are transitions between localized excitons and charge-transfer states within the same spin, i.e., charge transfer processes. In this scenario, it is commonly accepted to employ Marcus theory (Equation 5.5) or the MLJ framework (Equation 5.9). The electron-phonon parameters as well as the driving forces are directly accessible from the adiabatic states, which in turn are directly accessible from excited-state electronic-structure calculations. In the framework of this thesis, the electronic coupling V^{el} between the relevant states is evaluated via the generalized Mulliken-Hush (GMH) method [116, 117], which will be briefly elaborated here; a more detailed description is provided in Appendix A.2.1.

By definition, the electronic coupling is the off-diagonal term of the Hamiltonian in the two-state diabatic basis, however, the off-diagonal Hamiltonian of the adiabatic states is zero by

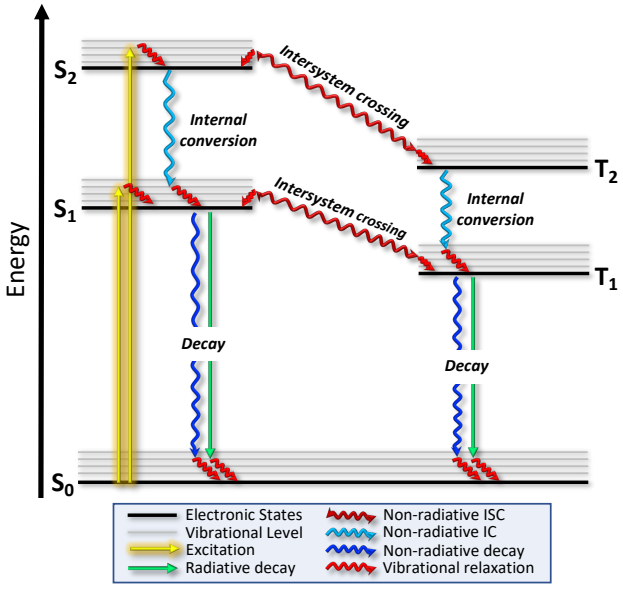

Figure 5.3: Relevant photophysical transitions illustrated in a Jablonksi diagram. After excitation of a singlet state, the system can undergoe different pathways: (i) Non-radiative transitions to lower excited states of the same spin (internal conversion, IC); (ii) non-radiative transition to excited states of other spin (intersystem crossing, ISC); (iii) Non-radiative or (iv) radiative decay to the ground state (only illustrated for the lowest excited states). Vibrational relaxation is illustrated. Some transitions are omitted for clarity.

definition of the adiabatic states. The GMH method relates the adiabatic state quantities to the electronic coupling. The idea is to form the diabatic states by linear combinations of the adiabatic states, while enforcing the linear combination coefficients to satisfy the transition dipole moment of the resulting diabatic states to vanish. This is achieved by constructing an orthogonal rotation matrix that is applied to the Hamiltonian and dipole matrices in the adiabatic basis. Following this Ansatz (as elucidated in more detailed in Appendix A.2.1), the electronic coupling within the GMH method relates to adiabatic quantities via:

$$V_{ab}^{\mathrm{el}} = \frac{\mu_{ab}\Delta E_{ab}}{\sqrt{(\Delta\mu_{ab})^2 + 4(\mu_{ab})^2}} \,. \tag{5.12}$$

Here, μ_{ab} is the transition dipole moment between adiabatic states a and b; ΔE_{ab} is the vertical energy difference (computed from the ground state) between these two states; and $\Delta\mu_{ab} = \mu_a - \mu_b$ is the difference in adiabatic dipole moments of the two states. Within this method, the dipole operator is projected onto the direction defined by the adiabatic dipole difference.

Non-radiative intersystem crossing involving electron transfer.
Strictly speaking, the spin-component in Fermi's golden rule (Equation 5.2) is either 0 (for singlet – triplet transitions, spin-forbidden) or 1 (same spin, spin-allowed). Thus, formally, transitions from singlet to triplet excited states and *vice versa* do not occur. However, the concept of Phosphorescence (photon emission from triplet states to ground state) shows that even spin-forbidden transitions may occur. These transitions arise form spin-orbit interactions, allowing (non-)radiative transition rate constants to exceed 0. If the transition involves electron transfer, Marcus theory or the MLJ framework can be employed. As evaluating the electronic coupling via the GMH method requires adiabatic PESs of same multiplicity, this approach cannot be used.

To evaluate the spin-orbit coupling in such a scenario, the perturbation Hamiltonian in Fermi's golden rule (Equation 5.2) takes the form of the relativistic *one-electron spin-orbit* Breit-Pauli Hamiltonian [118, 119]:[1]

$$\hat{\mathcal{H}}^{\mathrm{SO}} = \frac{\alpha_0^2}{2} \sum_{i}^{N_{\mathrm{el}}} \sum_{A}^{N_A} \frac{Z_A}{r_{\mathrm{iA}}^3} (\mathbf{r}_{iA} \times \hat{\mathbf{p}}_i) \cdot \hat{\mathbf{s}}_i \ . \tag{5.13}$$

Here, $\hat{\mathbf{l}}_i = \mathbf{r}_{iA} \times \hat{\mathbf{p}}_i$ is the orbital angular momentum operator and $\hat{\mathbf{s}}_i$ is the spin angular momentum operator of electron i; Z_A is the bare positive charge on nucleus A; α_0 is the fine-structure constant. The sum extends over all electrons i and nuclei A.

Inserting $\hat{\mathcal{H}}^{\mathrm{SO}}$ into Equation 5.2 one can compute the spin-orbit coupling from the singlet and triplet excited-state wave functions. Representing the Hamiltonian and wave functions within the second quantization [120], one can evaluate the spin-orbit coupling for specific singlet to triplet-state-manifolds from the excitation coefficients for the respective states that can be directly assessed from the excited-state electronic-structure calculations following Casida's Ansatz for the excited-state wave functions [121, 122] as implemented in Q-Chem 5.4 package [123]. The reader is referred to Appendix A.2.2 for a more detailed description and presentation of the equations.

[1] In the full Breit-Pauli Hamiltonian there are other contributions from, e.g., spin-other-orbit interactions. However, due to simplicity and strength of the interaction, the one-electron spin-orbit contribution is commonly employed.

Radiative decay from excited states.
Radiative recombination rates are determined using the Einstein coefficient relation for spontaneous emission [84], leading to the radiative decay rate constant:

Equation 5.14

$$k_\mathrm{r} \approx \frac{2}{3} f^\mathrm{osc} \times E^2 \times f(n) \ .$$

Here, f^osc is the oscillator strength for the vertical excitation from the ground state to the excited state; E the adiabatic emission energy from the excited state to the ground state ($E^\mathrm{ad}_\mathrm{em}$, in cm^{-1}); and $f(n) = \frac{n(n^2+2)^2}{9}$ is the *virtual cavity* model to describe the influence of the polarizable surrounding medium with refractive index n on the emission process [124–126]. In this work, a refractive index of $n = 1.4$ is chosen, which is appropriate for organic systems. This equation is derived in more detail in Appendix A.2.3.

Non-radiative decay from excited states.
Non-radiative transitions from localized excited states to the ground state are driven by nuclear motion along vibrational normal modes, which modulate the electronic wave functions. One framework to describe such transitions is the non-adiabatic coupling model [127, 128] combined with the thermal vibrational correlation function (TVCF) [129–131]. The essential aspects of this model are very briefly summarized here; a more detailed description is provided in Appendix A.2.4.

Within this framework, the electronic coupling is evaluated as non-adiabatic coupling between the initial and final states, evaluated with respect to the vibrational normal modes. The transition probability is governed by the correlation between the vibrational wave functions of the two electronic states and by vibrational energy conservation. The temperature influences the process by determining the thermal population of the initial vibrational states, thereby restricting which energy-conserving transitions are accessible.

If the non-radiative decay involves electron transfer and is primarily driven by electronic state energy differences, Marcus theory and the MLJ framework can be applied, alongside with the GMH electronic coupling or SOC.

Interim Summary

Charge transfer and excited-state non-radiative transition rates are commonly modeled using Marcus theory or the Marcus–Levich–Jortner framework. The treatment of electronic interactions – whether electronic or spin-orbit coupling – depends on the transition type. Energetic disorder substantially influences both the driving force and coupling strength. Electron-phonon coupling critically shapes the rate profiles; a quantum-mechanical description is essential for large driving forces within Marcus' inverted region. Radiative transitions can be modeled via the Einstein coefficient relation for spontaneous emission.

Dynamical Approaches for Electron-Nuclear Coupling 6

In the previous section, approaches for evaluating charge-transfer and excited-state transition rate constants were introduced, relying on a *static* description of nuclear configurations. In the following, attention shifts beyond this approximation to methods that *dynamically* propagate the nuclear degrees of freedom on adiabatic potential energy surfaces. For ground state dynamics (or more general, the dynamics of a single adiabatic state), *ab initio* molecular dynamics (AIMD) is employed, whereas non-adiabatic *ab initio* molecular dynamics (NA–AIMD) is used to describe excited-state processes involving electronic transitions. Because a fully quantum-mechanical treatment of nuclear motion is both conceptually intricate and computationally expensive, in this work, these methods adopt semi-classical approximations, in which classical nuclei evolve along classical trajectories governed by Newton's equations of motion.

6.1 Ab Initio Molecular Dynamics

When introducing the classical limit, it implicates that the nuclear wave function's character vanishes and the nuclei correspond to point particles with discrete positions, where the classical nuclear trajectory will be denoted as $\mathbf{R}^c = \{\mathbf{R}_1, \ldots, \mathbf{R}_{N_A}\}$. After separating the total wave function into a nuclear and electronic part under Born–Oppenheimer approximation, inserting this Ansatz into the corresponding time-dependent Schrödinger equation, and applying the classical limit, one can show that the nucleus A propagates according to Newton's law as [132]:

$$\mathbf{a}_A^c(t) = \frac{\mathrm{d}^2\mathbf{R}_A^c(t)}{\mathrm{d}t^2} = \frac{\mathbf{F}_A(t)}{M_A} = \frac{-\nabla_{\mathbf{R}_A^c} E_n(\mathbf{R}^c(t))}{M_A} \,. \tag{6.1}$$

Here, M_A is the mass of the nucleus A, and the force acting on nucleus A is given by the gradient of a single Born–Oppenheimer PES, E_n, with respect to the Cartesian coordinates $\mathbf{R}_A^c$. In conventional implementations of AIMD, the nuclei evolve on the electronic ground-

state PES, E_0. Essentially, coupled to electronic-structure methods like DFT one can compute the forces on the fly when propagating the classical trajectory.

The classical propagation of the positions and velocities can be computed via numerical algorithms; in this thesis, the Velocity Verlet algorithm [133] is used for time propagation Δt:

$$\mathbf{R}_A^c(t+\Delta t) = \mathbf{R}_A^c(t) + \mathbf{v}_\mathbf{A}^\mathbf{c}(t)\Delta t + \frac{\mathbf{a}_A^c(t)}{2}\Delta t^2 \,, \tag{6.2}$$

$$\mathbf{v}_A^c(t+\Delta t) = \mathbf{v}_A^c(t) + \frac{\mathbf{a}_A^c(t) + \mathbf{a}_A^c(t+\Delta t)}{2}\Delta t \,. \tag{6.3}$$

Initial velocities are generated randomly from a scalar Maxwell-Boltzmann velocity distribution, they are expressed via

$$\mathbf{v}_A^c(t=0) = \sqrt{\frac{k_B T_{\text{initial}}}{M_A}}\mathcal{N}(0,1) \,, \tag{6.4}$$

where T_{initial} is the initial temperature and $\mathcal{N}(0,1)$ is a random number generated from a gaussian distribution with variance 1 and mean value 0.

The temperature of the electron-nuclear system can be computed from the nuclear kinetic energy as

$$T = \frac{\sum_{A=1}^{N_A} M_A \left(\mathbf{v}_A^c\right)^2}{3N_A k_B} \,. \tag{6.5}$$

As the molecular system is coupled to an environmental heat bath with temperature T_0, it constantly exchanges heat and thus is kept at a stable thermal equilibrium. Initially, the temperature is governed solely by the velocities of the nuclei, which is quickly transformed into movement patterns that affect the potential energy of the electron-nuclear system, such as bond bendings. This transformation leads to a rapid loss in temperature. To compensate such effects and to maintain the thermal equilibrium, the molecular system is coupled to the heat bath by using a thermostat controlling the temperature. In this work, the Berendsen thermostat is used [134], where the time derivative of the temperature is given by

$$\frac{\mathrm{d}T}{\mathrm{d}t} = \frac{T_0 - T}{\tau} \,, \tag{6.6}$$

where the time constant τ is a measure of the coupling strength to the heat bath. In this

framework, the nuclear velocities are corrected to

$$\mathbf{v}_A^{c,\text{corrected}} = \sqrt{1 + \frac{\Delta t(T_0 - T)}{T\tau}}\mathbf{v}_A^c \,. \tag{6.7}$$

Moreover, the thermostat corrects for numerical errors that might arise in the propagation. The AIMD are implemented in the ORCA 6.0 software package [135].

6.2 Non-Adiabatic Ab Initio Molecular Dynamics

In situations where a single electronic state does not capture the relevant electron-nuclear coupling, such as transitions among excited states after photon absorption, the applicability of conventional AIMD is limited, necessitating approaches that explicitly account for multiple electronic states. A widely used method is the non-adiabatic *ab initio* molecular dynamics (NA–AIMD) employing a trajectory surface hopping, capturing this non-adiabatic interaction between excited states by allowing transitions between them. In this thesis, Tullys fewest switching surface hopping (FSSH) [136] is applied, based on Tullys original surface hopping [137]. In this scheme, the nuclei move along classical trajectories determined by a given active electronic state, while stochastically-allowed transitions between the electronic states occur, so-called hops. As in AIMD, the nuclear dynamics follow the classical equation of motion (Equation 6.1) and are numerically propagated from $t \longrightarrow t + \Delta t$ using the Velocity Verlet algorithm [133] for the currently active electronic state.

The quantum uncertainty of the nuclear degrees of freedom in the initial state is mimicked by propagating an ensemble of independent classical trajectories with different initial conditions sampled from a Wigner distribution. Furthermore, the nuclear wave package may split into several branches that evolve independently on different electronic PESs, leading to rapid decoherence between them. This decoherence, however, is lost in standard FSSH as all electronic states are evolved along a single classical trajectory associated with one active electronic state at a time. To address this, a decoherence correction is applied, damping the electronic amplitudes of unoccupied states appropriately, making the FSSH dynamics more internally consistent with quantum-mechanical behavior.

A time-dependent electronic wave function Ψ_e can be expanded from the Born–Oppenheimer

electronic states ϕ_j as [136, 138, 139]:

$$\Psi_e(\mathbf{r}, t) = \sum_j c_j(t)\phi_j(\mathbf{r}, \mathbf{R}) \,, \tag{6.8}$$

where $c_j(t)$ describes the contribution of electronic state j to the total electronic wave function at time t including the phase of the electron-nuclear wave function in this state. Inserting this Ansatz into the electronic time-dependent Schrödinger equation, the time-evolution of coefficients c_k reads:

$$i\hbar\frac{\partial c_k}{\partial t} = \sum_j c_j(t)\Big(\underbrace{\langle\phi_k|\,\hat{\mathcal{H}}_e\,|\phi_j\rangle}_{V_{kj}} - i\hbar\,\underbrace{\langle\phi_k|\dot{\phi}_j\rangle}_{\mathbf{v}^c\cdot\mathbf{d}_{kj}}\Big) \,. \tag{6.9}$$

Here, $\mathbf{v}^c$ is the velocity of the nuclei and $\mathbf{d}_{kj}$ is the non-adiabatic coupling vector introduced earlier; its product is commonly referred to as time-derivative non-adiabatic coupling. Note that the first term is diagonal due to the adiabatic representation. A reduced density matrix is introduced as

$$\rho_{kj} := c_k(t)c_j^*(t) \,, \tag{6.10}$$

where ρ_{kk} describes the probability of electronic state k to be observed in the dynamics.

The time-derivative non-adiabatic coupling is numerically estimated via the finite differences method in the Hammes-Schiffer and Tully approach [140, 141]:

$$\left[\mathbf{v}^c\cdot\mathbf{d}_{kj}\right](t) \approx \frac{1}{4\Delta t}\left[3S_{kj}(t) - 3S_{jk}(t) - S_{kj}(t-\Delta t) + S_{jk}(t-\Delta t)\right] \,, \tag{6.11}$$

where $S_{kj}(t) = \langle\phi_k(t)|\phi_j(t+\Delta t)\rangle$ are orbital overlaps at different times, evaluated by the *orbital derivative* approach [142, 143].

To describe a hopping probability $g_{k\to j}$ from state k to j, the fewest switching criterion introduced by Tully reads [136]:

$$g_{k\to j} = \max\left\{0, \frac{\Delta t\left(2\hbar^{-1}\mathcal{I}m(\rho_{kj}^*)V_{kj} - \mathcal{R}e(\rho_{kj}^*)\mathbf{v}^c\cdot\mathbf{d}_{kj}\right)}{\rho_{kk}}\right\} \,. \tag{6.12}$$

This is accompanied by two criteria that must be fulfilled for the hop to occur:

1. To provide a stochastic nature of hops, a random number $r_t \in \{0, 1\}$ is sampled, and

the following condition must be fulfilled:

$$\sum_{n=1}^{j-1} g_{k\to n} < r_t \leq \sum_{n=1}^{j} g_{k\to n} \,. \tag{6.13}$$

2. The total energy of the system before the hop has to be lower than after the hop to conserve the energy:

$$V_j - V_k \leq \frac{\sum_A^{N_A} \mathbf{v}_A^c \cdot \mathbf{d}_{jk}^A}{2\sum_A^{N_A} M_A^{-1} \left(\mathbf{d}_{jk}^A\right)^2} \,, \tag{6.14}$$

which includes a correction of the velocities based on the non-adiabatic coupling vector [140].

In a true quantum-mechanical description of the nuclear wave package, the electron-nuclear system quickly loses its coherent description and evolves on specific decoherent branches of the nuclear wave package. But, in the FSSH formalism, the off-diagonal terms of the density matrix are typically non-zero, induced by the fact that the coefficients of all states are propagated on the classical trajectory induced by a single electronic state, leading to non-physical electronic coherence. In this work, this coherence-problem is addressed by the decoherence correction proposed by Granucci and Persico [144], correcting the current active state c_m and all other states c_k to:

$$c_m^{\text{new}} = c_m \left[\frac{1 - \sum_{k\neq m} |c_k^{\text{new}}|^2}{|c_m|^2}\right]^{\frac{1}{2}} \,, \tag{6.15}$$

$$c_k^{\text{new}} = c_k \mathrm{e}^{-\Delta t/\tau_{km}} \,, \quad \text{with} \quad \tau_{km} = \frac{\hbar}{E_k - E_m}\left(1 + \frac{\alpha}{E_{\text{kin}}}\right) \,, \forall\, k \neq m \,, \tag{6.16}$$

where the empirical parameter α is set to 0.1 Hartree and E_{kin} is the nuclear kinetic energy.

The different initial conditions are based on the vibrational modes of the ground state, which follow a Wigner distribution in phase space, known as the nuclear ensemble approach, which is outlined in Appendix A.2.5. During the temporal dynamics, thermal equilibrium is controlled via the Anderson thermostat [145]. The formalisms are implemented in the Newton–X package [146], which, in this thesis, is coupled with Gaussian 16 [147] for electronic-structure calculations.

Interim Summary

Computationally feasible modeling of the dynamical evolution of electron-nuclear interactions relies on treating nuclei classically while describing electrons quantum-mechanically. *Ab initio* molecular dynamics comprise only a single adiabatic potential energy surface, whereas transitions between adiabatic states necessitate a non-adiabatic treatment. To approximate a quantum-mechanical nuclear phase-space distribution, an ensemble of trajectories must be propagated and statistically analyzed.

Part II

Organic Semiconductors in Applications

Single Charge Carriers in Organic Semiconductor Devices

7

Having discussed the foundations of the opto-electronic properties of OSCs, this second part of the thesis relates these properties to the mechanisms governing the operation of real-world devices. These mechanisms and their relevance will be elucidated and placed in the context of the scientific contributions presented in this work. This part starts with a discussion of single charge carriers in OSC devices, including their generation and transport. Afterwards, photoexcited charge carriers as primary result in organic photovoltaics will be discussed. This includes a comprehensive description of the device principle as well as excited-state cascades and dynamics of the exciton.

Understanding single-charge-carrier properties and increasing the charge-carrier density play a major role in enhancing and controlling the conductivity and charge-carrier mobility of OSCs, which are highly demanded in OLEDs, OFETs, and charge-carrier transport layers in OPVs, among other [2–5, 7–20, 25–27]. Two different type of charge carriers exists, negatively charged electrons (n-type) and positively charged holes (p-type). Typically, the charge-carrier density is increased by insertion of molecular guests that lead to the formation of charges on the OSC with balancing counter-charges on the molecular guest attracting each other via Coulomb forces. After inserting the charge carriers, they can overcome the Coulomb attraction leading to mobile charges within the OSC matrix with remaining counterions in the OSC matrix. These general mechanisms are illustrated in Figure 7.1 for p-type charge carriers. Hole transport in OSCs can be described as the transfer of a hole from one molecule to another, which is formally equivalent to an electron transferring in the opposite direction: from the neighboring OSC to the hole-hosting OSC.

As charges in the OSC matrix, including the counterions, modify the energetic landscape through Coulomb intersite interactions and strong Coulomb attraction, accurately describing the resulting electronic structure and the underlying mechanisms of charge insertion and transport is challenging and requires modeling the full environment. Moreover, besides

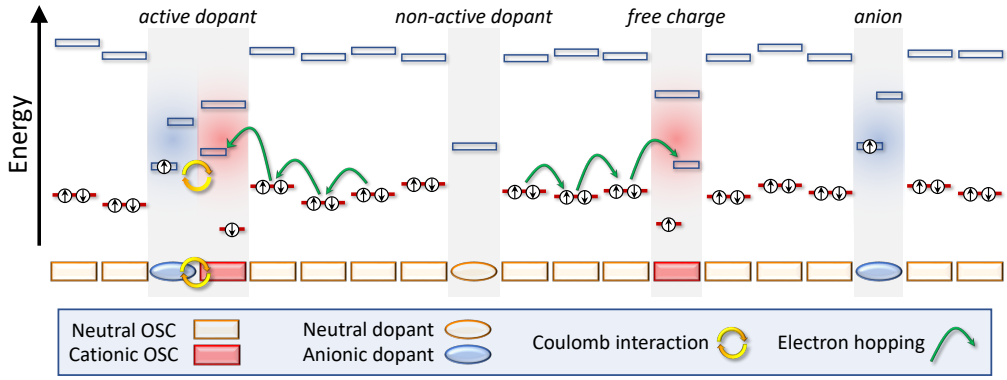

Figure 7.1: Active dopants, non-active dopants and free charges in OSC matrix. This scheme is shown for p-type doping of the OSC, a similar scheme can be drawn for n-type doping. The occupied and unoccupied orbital energies are shown and orbital energy splitting is indicated. For simplicity, intersite Coulomb interaction effects are not indicated. Electron hopping and Coulomb interaction is depicted. Anionic and cationic sites are represented by blue and red shadows, respectively.

energetic interactions, the OSC architecture also plays a role, as the OSC:molecular-guest morphology can influence the efficiency of the insertion and transport. In the next sections, different methods for the charge carrier insertion will be elaborated followed by a general description of the charge transport and its modeling.

7.1 Insertion of Charge Carriers by Molecular Guests

The most common approach to insert charge carriers is to use so-called molecular dopants that possess a higher electron affinity (EA) than the ionization potential (IP) of the OSC for p-type doping, and *vice versa* for n-type doping [148–153][1], so-called integer charge transfer (ICT) or ion-pair formation. As the EA and IP are considered equal to the LUMO and HOMO energies for single molecules, respectively, they are typically regarded as the orbitals responsible for charge transfer. By this, it is energetically advantageous to directly transfer a charge, and as such, making it a purely electronic mechanism. This mechanism is illustrated in Figure 7.2(a) alongside with the mechanism of charge transfer complex (CTC) formation. In the latter, instead of transferring a charge, the frontier molecular orbitals

[1] The intuitive comparison of IP and EA values (typically referenced to the vacuum level) is a simplified picture, as it neglects intermolecular interactions between the OSC and the dopant, which can significantly modify the effective energy levels in the solid state. Nevertheless, it is widely used for its intuitive physical interpretation.

hybridize to form inter-molecular orbitals with a correlated partial charge transfer [148–150, 152–154], ultimately leading to non-active dopants and prohibiting the formation of a free charge. These mechanisms are well-investigated and understood on their fundamental level.

To enhance the charge-insertion efficiency, molecular dopants with higher electron affinity can be employed, for example progressing from F_4TCNQto F_6TCNNQand further to CN6–CP [155, 156] for p-type doping. For n-type doping, dopants with a high ionization potential, such as N–DMBI [157], can be used. Notably, n-type doping is inherently harder to realize, since it demands dopant species whose occupied orbitals lie high enough in energy to donate an electron to the relatively high-lying LUMOs of the OSCs. It has been shown that Coulomb interaction between multiple ICT events can effectively reduce the Coulomb barrier [158], thereby promoting more efficient free charge-carrier generation. Most interestingly, the Coulomb barrier can be reduced by exchanging the remaining counterions after p- or n-type doping (ion-exchange doping) [149, 159, 160], ultimately leading to more efficient free charge-carrier generation consequently improves conductivity. Moreover, for very strong molecular dopants, transferring more than one charge is possible, leading to molecular double doping [161, 162].

The solubility of the compounds is a decisive factor for their mutual miscibility. Structural modification of F_4TCNQ to incorporate ester groups was shown to strongly increase its solubility compared to F_4TCNQ, which resulted in improved doping efficiency despite a simultaneous decrease in EA [163]. This highlights the critical importance of molecular design in achieving highly soluble dopants, which in turn promotes more effective OSC:dopant interactions. Furthermore, OSC side-chain engineering [164] has been demonstrated to mitigate dopant aggregation, facilitating improved dopant diffusion within the OSC matrix and thereby enhancing overall charge-carrier injection.

Besides the conventional and intuitive approach of molecular dopants, the use of Lewis acids, such as BCF, for p-type doping has been shown to outperform the typical molecular dopants by enhanced hole mobility, while the mechanism itself remained elusive [165, 166]. However, it has been proposed that the doping mechanism extends beyond a purely electronic picture; instead, it involves a reaction pathway that includes changes in the participating complexes. Yurash and coworkers [167] in *Nature Materials* reported on a higher doping efficiency as well as higher mobility of the charges for the Lewis acid BCF among other, and proposed a two step mechanism as shown in Figure 7.2(b): step 1) the Lewis acid forms a complex with H_2O (Brønsted-type acid formation) and protonation

of the OSCs backbone occurs, followed by step 2) electron transfer from another neutral OSC side to the protonated radical OSC, leaving a mobile hole on the former OSC.

Theoretical investigation of the reaction pathway emphasized on a more complex dimer-BCF with H_2O formation leading to exergonic protonation pathways [168], thus, confirming the initial step of the proposed mechanism. For organic salts, such as TrTPFB, an extended electrophilic attack reaction was proposed, where the cationic dopant forms an intermediate complex with the OSC, followed by electron transfer [169, 170].

The electron transfer mechanism was further investigated by Bauch et al. [171] using density functional theory (DFT) calculations, providing deeper insights into the underlying electronic structure. Their results showed that a single proton forms a localized charge around the proton position, while two protons (double protonation) induce an intramolecular charge transfer leading to the formation of a polaron state. The species were characterized by their distinctive vibrational and optical signatures, which exhibited intense vibrational modes and polaron absorption for the double-protonated species. In addition, electron transfer between a disturbed, double-protonated OSC and a former neutral OSC was identified, illustrating the second step of the proposed mechanism.

In harmony to the marvelous p-type doping mechanism via Lewis acids, a somewhat relatable mechanism was proposed for n-type doping via superbases, however, featuring a deprotonation of the OSC. Due to the strong proton affinity of superbases such as P2–t–Bu or P4–t–Bu, a proton is abstracted from the OSC and transferred to the superbase. This was experimentally shown by Wei et al. to significantly enhance charge generation efficiency and thus conductivity for $PC_{61}BM$ and N2200, outperforming conventional molecular dopant N–DMBI [172]. The deprotonation is proposed to be followed by a nucleophilic attack reaction [172–175], as illustrated in Figure 7.2(c), and by electron transfer to a neutral, unperturbed OSC species, resulting in a free negative charge on the latter [172].

Superbases are superior to the conventional molecular dopants such as N–DMBI, as they provide good miscibility within the OSC matrix [173] and good thermal device stability [174], positioning them as strong candidates for organic transistor and thermoelectric applications.

In this thesis, the electronic structure of the deprotonated, nucleophilic-attack reaction intermediate is analyzed, and electron transport in $PC_{61}BM$ is directly examined. To this end, the PES of the nucleophilic-attack pathway is explored. The calculations identify a metastable state in which no new bond is formed; in this configuration, the excess electron

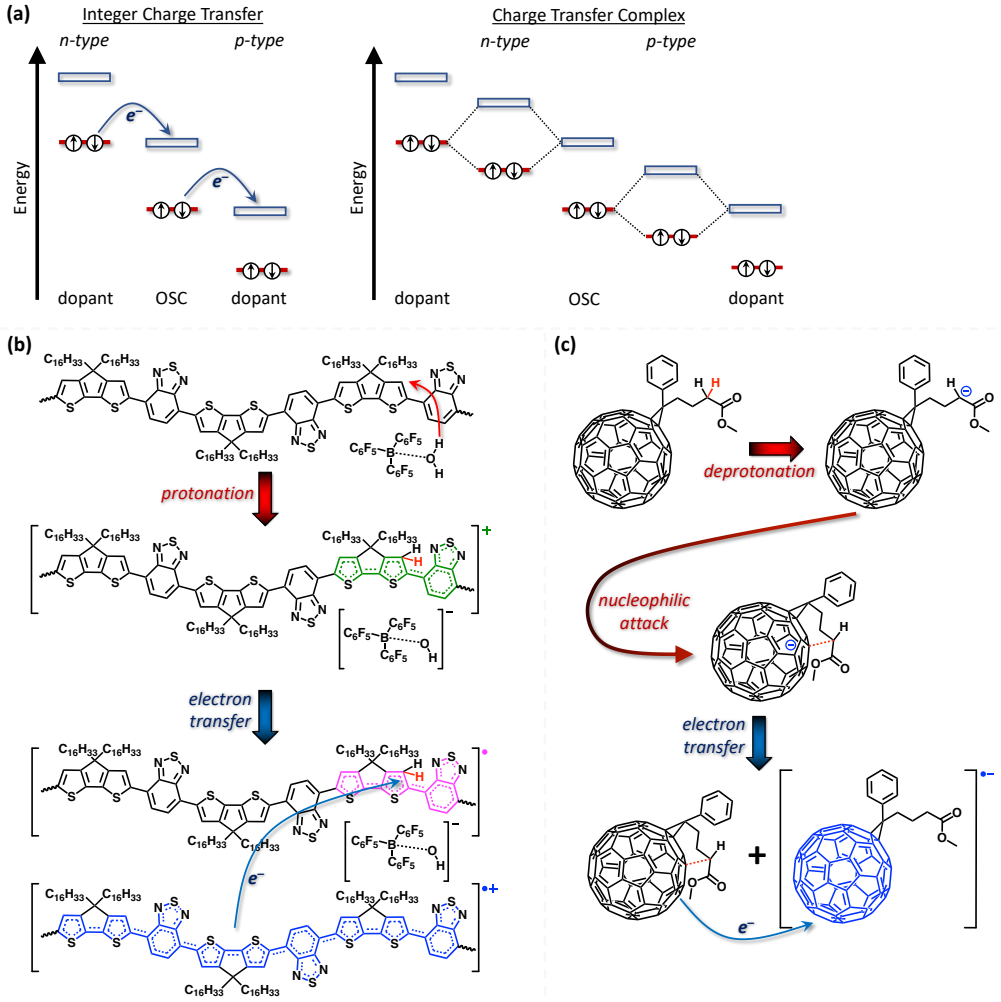

Figure 7.2: Different doping mechanisms for OSC via molecular guests. (a) Doping via molecular dopants. (b) P-type doping mechanism of PCPDT–BT with Lewis acid BCF. Illustration inspired by Reference [167]. The complex formation of dimer-BCF as proposed by Reference [168] is not included for simplicity. (c) N-type doping mechanism of $PC_{61}BM$ via superbases. The schemes of the superbases are not included for simplicity. Illustration inspired by Reference [172]. The electron transfers from or to the perturbed OSC originate from a neutral, unperturbed OSC species for the Lewis acid and superbase doping, respectively.

resides in an unpaired conjugated orbital on the fullerene. In contrast, formation of a new bond results in paired, localized orbitals.

Additionally, the electronic structure of the perturbed-$PC_{61}BM$:unperturbed-$PC_{61}BM$ complex is studied across several bi-molecular configurations. The simulations show that bond

formation, whether intra- or intermolecular, consistently leads to paired, localized electrons. However, in the absence of bond formation, the excess electron remains in an unpaired conjugated orbital on either the perturbed or unperturbed $PC_{61}BM$, depending on the geometric arrangement. In cases where it localizes on the unperturbed $PC_{61}BM$, electron transfer between the two molecules has occurred. The unpaired conjugated orbital is ultimately identified as a key factor enabling efficient doping, regardless of the molecular site on which it resides.

The results presented in this chapter were previously published and are reproduced below.

PCCP

ROYAL SOCIETY OF CHEMISTRY

PAPER

View Article Online
View Journal | View Issue

Cite this: *Phys. Chem. Chem. Phys.*, 2024, **26**, 4194

Charge transfer in superbase n-type doping of PCBM induced by deprotonation†

Chuan-Ding Dong, *[a] Fabian Bauch,[a] Yuanyuan Hu[b] and Stefan Schumacher[ac]

N-type electronic doping of organic semiconductors (OSCs) by using superbase compounds shows high doping efficiency (H. Wei, Z. Cheng, T. Wu, Y. Liu, J. Guo, P.-A. Chen, J. Xia, H. Xie, X. Qiu, T. Liu, B. Zhang, J. Hui, Z. Zeng, Y. Bai and Y. Hu, *Adv. Mater.* 2023, **35**, 2300084). While a deprotonation reaction is believed to trigger the doping process, the detailed mechanism therein is not yet fully understood. In the present work we theoretically study the electronic structure of the deprotonated Phenyl-C61-butyric acid methyl ester (PCBM) molecule, as well as the charge transfer (CT) between PCBM and its deprotonated species. We find that deprotonated PCBM without formation of a new bond between the deprotonated side chain and fullerene induces electronic structure with broken spin symmetry, where an in-gap state is singly occupied by an unpaired electron. A second scenario that we find to be possible is the formation of a new bond between the deprotonated side chain and a fullerene. This leads to a spin symmetric electronic structure with partially localized in-gap state, which is expected to contribute less to the effective doping. These results show that the deprotonated PCBM species without new bond formation predominantly accounts for the effective n-type doping of PCBM, an insight that will be useful for optimization of this recently discovered doping method.

Received 20th October 2023,
Accepted 11th January 2024

DOI: 10.1039/d3cp05105f

rsc.li/pccp

1 Introduction

Electronic doping can enhance the conductivity of organic semiconductors (OSCs) by orders of magnitude,[1,2] and is of fundamental importance for applications based on OSCs, such as in organic photovoltaics and organic electronics.[3–8] Molecular doping, where p-type or n-type molecular dopants are mixed with OSCs to induce charge carriers, is widely used and receives tremendous research interest.[9–12] Besides these more established approaches, efforts to explore alternative doping strategies with higher doping efficiency and improved electronic or structural properties are on the rise, leading to recent studies on Lewis acid doping,[13–15] ion exchange doping,[16] electrophilic p-type doping,[17] and doping with the aid of noble metal clusters.[18]

Different from the direct charge transfer (CT) between molecular dopants and OSC material, which in the simplest picture is driven by the energetic difference between HOMO and LUMO levels of the two entities, the mechanisms behind the more recently developed doping methods are more complex. In Lewis acid doping, it is proposed that an OSC polymer is first protonated by the Lewis acid and then attains an electron from a second polymer chain, leaving the latter in a p-doped state.[13] Microscopic details including inter- and intra-chain processes were ilucudated by use of atomistic quantum chemical approaches,[19] and detailed studies of the chemical complexes involved in this process.[20] A similar process is believed to account for electrophilic attack p-type doping by use of TrTPFB molecules. There the polymer is attacked by the trityl cation instead of a proton, followed by subsequent CT with a neighbouring polymer chain.[17] Both Lewis-acid doping and electrophilic attack show remarkable efficiencies of p-type doping, and avoid typical issues caused by molecular dopants such as deterioration of film morphology.

Very recently, a new n-type doping method using superbase compounds was reported and shown to significantly enhance efficiency in doping the molecular OSCs PCBM and N2200 copolymer, compared to molecular n-type doping with N-DMBI.[21] In analogy to the protonation in Lewis acid doping, a deprotonation of PCBM brought about by the superbase compound is believed to occur, with subsequent CT between deprotonated PCBM and 'intact' PCBM entities. However, as the species involved in the proposed process are difficult to experimentally identify, the exact mechanism remains to be verified. A more detailed understanding of the underlying

[a] *Department of Physics and Center for Optoelectronics and Photonics Paderborn (CeOPP), Paderborn University, Warburger Strasse 100, Paderborn 33098, Germany. E-mail: cddong@mail.uni-paderborn.de*
[b] *International Science and Technology Innovation Cooperation Base for Advanced Display Technologies of Hunan Province, School of Physics and Electronics, Hunan University, Changsha 410082, China*
[c] *Wyant College of Optical Sciences, University of Arizona, Tucson, AZ 85721, USA*

† Electronic supplementary information (ESI) available. See DOI: https://doi.org/10.1039/d3cp05105f

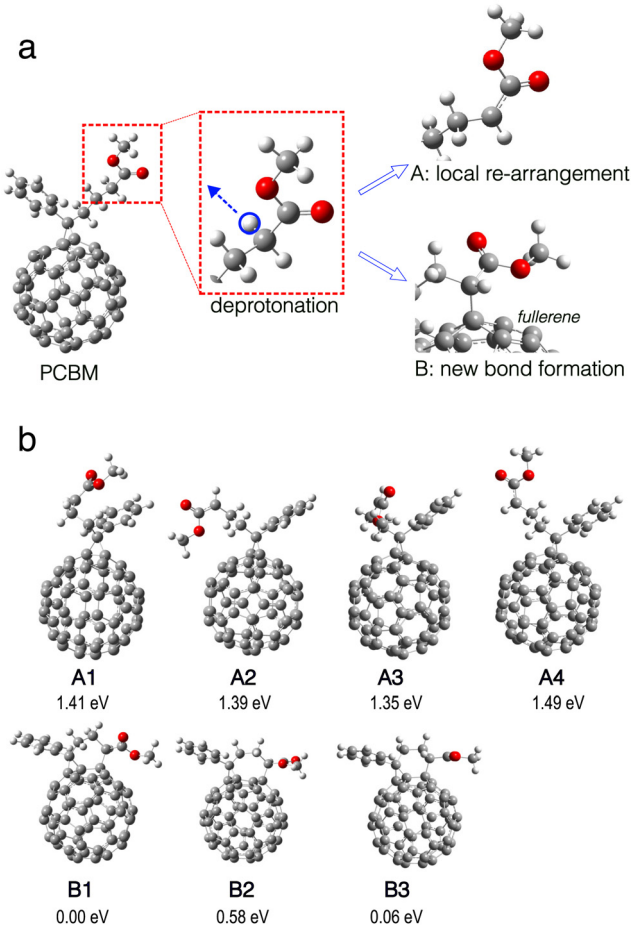

Fig. 1 (a) Illustration of deprotonation on the side chain of PCBM. After deprivation of the proton marked by the blue circle (left), either the local structure of the side chain re-arranges (upper right) or a new bond forms between the side chain and the fullerene part (lower right), leading to different structures, examples of which are shown in panel (b). (b) Different local minima structures resulting from deprotonation as shown in (a) including total energies relative to structure **B1**. **A1–A4** have local structural re-arrangement in the side chain. **B1–B3** result from new bond formation. Color code: grey for carbon, white for hydrogen, and red for oxygen.

microscopic mechanisms may allow further optimization of this new doping method and may also play a role in further optimization of electrophilic attack and Lewis-acid doping.

Here we present an in-depth investigation of the electronic structure of the deprotonated PCBM and its formation of CT complexes with PCBM molecules. We find that the electronic behavior of deprotonated PCBM crucially depends on the possible formation of a new C–C bond between the deprotonated side chain and the fullerene as illustrated in Fig. 1. The structures with new bond formation exhibit an electronic structure and an in-gap state, which is partially localized around this new bond and is therefore expected to contribute less to electronic transport. On the other hand, in the structures without formation of a new bond, the unpaired electron on the deprotonated PCBM migrates from the local C–H bond on the side chain to the conjugated electronic system on the fullerene. In that case, we further show that CT to a neighbouring PCBM, important for effective n-type doping, is generally possible.

2 Computational details

Following our and other researchers' previous works,[11,22–25] we performed the broken-symmetry DFT calculations. The B3LYP hybrid functional with dispersion correction in Grimme's D3 form[26] was used for single molecules (Fig. 1–3). The range separated hybrid functional ωB97XD with default ω was used for bi-molecular complexes (Fig. 4 and 5) for more reliable coverage of CT behavior.[23] In the DFT calculations, the initialization of charge density was realized by mixing spin-up (α) and spin-down (β) orbitals, to allow the separation of α and β states energetically and spatially, but without enforcing it. We note that this methodology generally gives good result for charge density distributions but is less accurate for the spin density due to possible spin contamination.[27] We note that ω B97XD generally gives a lower HOMO level and a higher LUMO level with respect to B3LYP, thus also overestimating the HOMO–LUMO gap. However, for the molecules and complexes studied in the present work we find that electronic structure and in particular ordering and character of relevant electronic states turns out to be very similar comparing results obtained with the two functionals (not shown). The 6-31g(d,p) basis set was used for all calculations except for the bond length scanning calculations in 3, where a smaller basis set 6-31g(d) was used. The geometries of single molecules and bi-molecular complexes were all optimized.

The DFT calculations were performed using the Gaussian16[28] package. The Hirshfeld charge decomposition presented in Fig. 4 and 5, which was previuosly shown to agree well with other charge decomposition schemes,[23,29] as well as the calculation of density of states (DOS) were performed by using the Multiwfn software.[30]

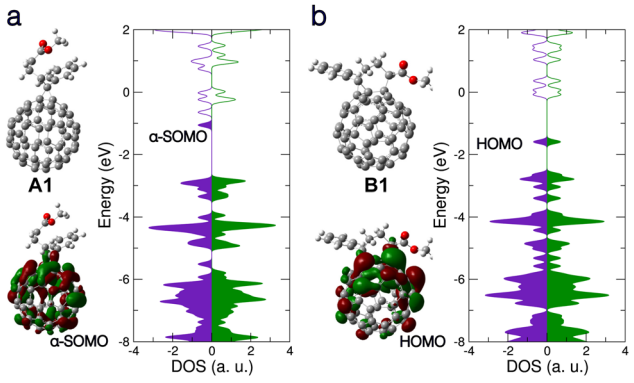

Fig. 2 Electronic structures of two different local minima structures of deprotonated PCBM as introduced in Fig. 1. (a) Upper left: **A1** structure without formation of new intramolecular bond. Lower left: spin-up α SOMO molecular orbital. Right: Calculated density of states (DOS) in spin-up α (left, indigo) and spin-down β (right, green) channels, showing broken spin symmetry. DOS of occupied states is filled with color. (b) Same as panel (a) but for **B1** structure with new bond formation. Lower left: HOMO molecular orbital. Right: DOS, showing spin symmetry.

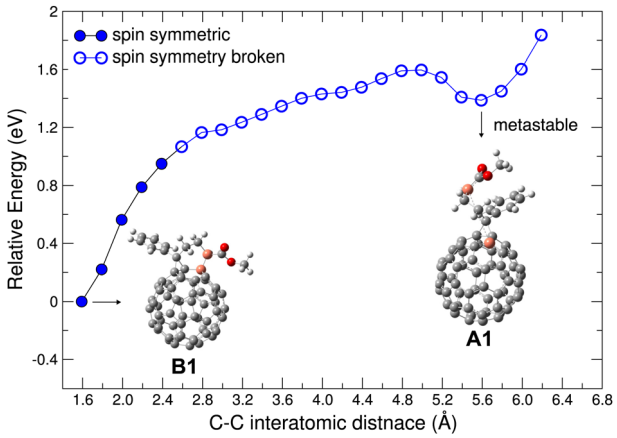

Fig. 3 Energy variation in scanning the C–C interatomic distance between the C atoms marked in orange. Local minima structures, **B1** (with new bond formation) and **A1** (without new bond formation) as discussed in Fig. 1 and 2 and in the text are shown. Spin symmetric electronic structure is denoted by filled circles, broken spin symmetry by open circles.

3 Results and discussion

The deprotonation reaction caused by the superbase is well known and considered crucial for the highly effective n-type doping observed for PCBM.[21] It is generally accepted that the deprotonation takes place at the methyl ester side chain, as shown in Fig. 1. The deprotonated PCBM molecule still possesses the same number of electrons as an 'intact' PCBM and therefore carries a negative net charge. We find that the molecular structure of this anion either stays similar to PCBM with just modest local structural re-arrangement, or the structure changes significantly with a new C–C bond forming between the deprotonated side chain and the fullerene. In the structural optimization, we identify several local minima structures, examples of which are shown in Fig. 1(b). Representative structures from each class found, namely **A1** without and **B1** with new bond formation, are shown in Fig. 2 together with the calculated HOMO orbitals and electronic DOS.

Interestingly, the two structures show dramatically different electronic structures: the DOS of **A1** shows broken spin symmetry with a singly occupied in-gap state around −1.05 eV, namely the α-SOMO (singly occupied molecular orbital). As shown in Fig. 2(a), this in-gap state is an electronically well conjugated orbital on the fullerene. The Hirshfeld net charge on the fullerene part of the deprotonated PCBM is −0.84 e, in comparison with −0.05 e in the case of neutral PCBM. This indicates that the residual electron migrates to the fullerene after deprotonation of the side chain. In contrast, the structure **B1** shows a spin-symmetric electronic structure. The formation of the new bond induces re-organization of the conjugated electronic system on the fullerene and gives rise to a doubly occupied in-gap state. This in-gap state is less delocalized and partially localized around the new bond compared to the singly occupied in-gap state in **A1**, indicating a significant effect of the new bond formation on the electronic system of the deprotonated PCBM. In addition, the energy separation between the in-gap state and the LUMO is significantly smaller in **A1** than in **B1**, implying a more active electronic behavior for the former.

Given the distinctly different electronic behavior without and with new bond formation (*cf.* results for **A1** and **B1**), it is interesting to examine in more detail the evolution of the molecular structure associated with the new bond. To this end, starting from **B1**, we scanned the relevant C–C interatomic distance from 1.59 Å up to 6.2 Å and investigated the electronic states and energies of each optimized structures (with the scanned C–C distance fixed). As shown in Fig. 3, the total energy rises with increasing C–C distance (as expected). The energy minimum structure at C–C distance of 5.6 Å is the **A1** structure. Along the scanning path this energy minimum has a depth of about 0.2 eV. We note that a rigorous investigation of energy minimum depth require a full potential surface sampling, which is computationally challenging and out of the interest of the present work. For the purposes of the present work, we believe it is sufficient to note that this meta-stable state we identify is already associated with other important structural parameters of PCBM such as the rotation of the methyl ester around the side chain. Compared with **B1**, the structure **A1** is energetically less favorable, which may indicate lower stability and in turn a reduced doping efficiency. Nevertheless, we believe that this aspect might be mitigated by

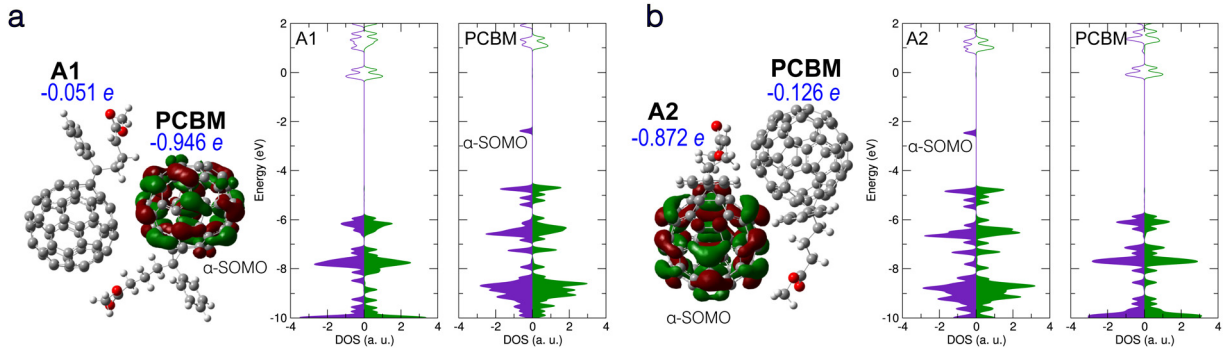

Fig. 4 Electronic structure of bi-molecular complexes consisting of one PCBM and one deprotonated PCBM without new bond formation. (a) Left: **A1/PCBM** complex, with the calculated α-SOMO and Hirshfeld net charge on each molecule given. Right: Partial DOS of each molecule. (b) **A2/PCBM** complex with α-SOMO and Hirshfeld net charges and partial DOS as in panel (a). Notation and colors same as in Fig. 2 above.

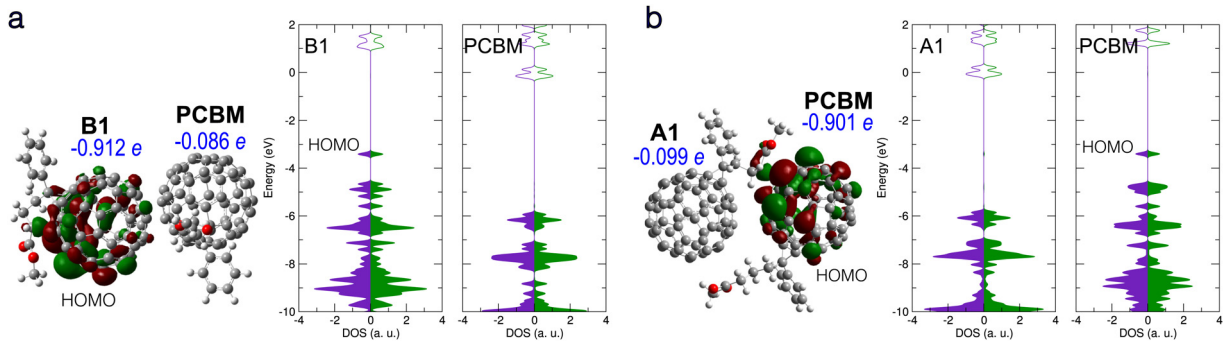

Fig. 5 (a) Electronic structure of **B1/PCBM** complex. Left: **B1/PCBM** structure, with HOMO, Hirshfeld net charges, and partial DOS given. (b) Electronic structure of **A1/PCBM** complex with an intermolecular bond forming between the molecules. HOMO, Hirshfeld net charges, and partial DOS are given. Notation and colors same as in Fig. 2 above.

several factors: (i) Besides **A1** the deprotonated PCBM appears in multiple other configurations with similar electronic behavior, such as structures **A2–A4** shown in Fig. 1b, which can also contribute to the doping. Our calculations showed that structure **A2–A4** can all induce CT to neighboring PCBM as well as **A1**. (ii) The scanning results shown in Fig. 3 did not take into account the effect of the molecular surroundings, where the solvent molecules and their dynamics will also have an effect on potential energy landscapes and influence occurrence and lifetimes of **A1–A4** and other related structure.

Interestingly, when the C–C distance is stretched to about 2.6 Å, we find that the electronic structure turns from spin symmetric to spin symmetry-broken and keeps this property in each structure for the remainder of the scanning path, including the energy minimum around 5.6 Å. These results strongly suggest that the broken spin symmetry will be an important feature of the deprotonated PCBM as long as the new C–C bond is not formed and the system remains in a meta-stable state, which is likely to occur and play a role in a realistic setting with partially hindered relaxation pathways and environmental influences.

The CT between PCBM and deprotonated PCBM is believed to contribute directly to the superbase-induced n-type doping of PCBM.[21] To examine the possibility of the CT, we analyze the electronic structure of bi-molecular complexes containing one PCBM and one deprotonated PCBM. To this end, different local minima structures of the latter were investigated. Fig. 4 shows two molecular complexes containing deprotonated PCBM without new bond formation. The **A1/PCBM** complex contains the local minimum structure **A1**, while in Fig. 4(b) the complex consists of PCBM and another local minimum of deprotonated PCBM, **A2**. (see Fig. 1).

The DOS and Hirshfeld charge decomposition show that **A1/PCBM** does undergo integer CT, while **A2/PCBM** does not. These results show that CT is possible without the formation of a new bond, but depends on the structure of the deprotonated PCBM as well as the relative position of the two molecules. Both complexes in Fig. 4(a) and (b) show electronic structures of broken spin symmetry with a singly occupied in-gap state. In complex **A2/PCBM** (Fig. 4(b)) the in-gap state (α-SOMO) is a conjugated state based on the deprotonated PCBM. The Hirshfeld net charge on the deprotonated PCBM reads −0.87 e, showing a behavior similar to the individual deprotonated PCBM (**A1**) without significant CT. On the other hand, in complex **A1/PCBM** the in-gap state, also α-SOMO, is based on the PCBM and the net negative charge is mostly on PCBM (−0.94 e), indicating a clear integer CT. In the DOS in Fig. 4(a), it is interesting to notice that the state β-SOMO is lying energetically close to α-(SOMO-1) and forms the energy gap bottom, so that it may contribute less to the effective doping.

It is intriguing that the frontier orbitals in these two cases without and with CT, namely the energy levels and the nature of the in-gap states and the overall DOS profile around the HOMO and the LUMO, are actually very similar to each other and barely distinguishable from an energetic point of view. Indeed, in both cases the in-gap state is located on the fullerene and therefore less impacted by the proton missing from the side chain, while the other molecule, either the PCBM in **A2/PCBM** or the deprotonated PCBM in **A1/PCBM**, stays virtually neutral in charge and has less electrostatic effect. Furthermore, in both **A1/PCBM** and **A2/PCBM**, the same orbital character of the in-gap states implies similar behavior of the induced electron as a charge carrier. For completeness, the possible effect of chlorobenzene solvent, which was used in ref. 21 was also addressed by using the PCM model with $\varepsilon = 5.69$. The CT results read −0.075 e (A1)/−0.925 e (PCBM) for **A1/PCBM** and −0.930 e (A2)/−0.068 e (PCBM) for **A2/PCBM**, which deviate only slightly from the results without dielectric environment.

The CT between the PCBM and the deprotonated PCBM with new bond formation was also studied by using different local minimum structures of the latter. However, no CT with the neighbouring PCBM was found in our calculations. Fig. 5(a) shows a typical case of a bi-molecular complex containing PCBM and the **B1** structure. As in the case of the individual **B1** structure, a doubly occupied in-gap state forms, which turns out to be a partially localized orbital located on **B1**, while the PCBM stays nearly neutral. We also considered the possibility of the structure **A1** forming a bond with the neighbouring PCBM, as presented in Fig. 5(b). In this case the new bond induces an in-gap state, as well as a net charge of −0.90 e, on the side of PCBM. Similar to the complex **B1/PCBM**, the in-gap state of **A1/PCBM** (with new intermolecular bond) shows also

partial localization around the new bond. Therefore we propose that in both complexes the in-gap state contributes only little to the effective doping.

4 Conclusion

In the present work we theoretically studied the molecular structure and electronic behavior of deprotonated PCBM, as well as the possibility of CT between deprotonated PCBM and an 'intact' PCBM, by using broken-symmetry DFT. We find that deprotonated PCBM can form different local minima structures, largely depending on the arrangement of the deprotonated side chain. Structures with the side chain bending towards the fullerene and forming a new C–C bond are favorable in energy, while the structures without formation of a new intramolecular bond are found to be meta stable. The structures with new intramolecular bond have spin symmetric electronic structure with a doubly occupied in-gap state. In that case, the in-gap states are partially localized around the new bond and CT to a neighbouring PCBM turns out to be difficult, effectively hindering electronic doping. On the other hand, the deprotonated PCBMs without new intramolecular bond formation show broken spin symmetry with a singly occupied in-gap state that is electronically well conjugated and delocalized on the fullerene. In that case, CT to a neighbouring PCBM is shown to be possible, with details depending on geometrical arrangement. Also with occurrence of CT, the conjugated character and energy of the in-gap state are preserved, such that efficient contribution to doping is expected. With these results, our work reveals that electronic behavior of deprotonated PCBM strongly depends on intramolecular bonding. Those structures without intramolecular bonding appear to play the most important role in the investigated doping with superbases. In turn, inhibition of intramolecular and intermolecular bonding of PCBM after superbase deprotonation may be an effective approach to further optimize efficiency of superbase n-type doping.

Conflicts of interest

There are no conflicts to declare.

Acknowledgements

A grant for computing time at the Paderborn Center for Parallel Computing (PC^2) is gratefully acknowledged. C. D. thanks Dr Yugang Bai for enlightening discussions.

Notes and references

1 J.-L. Brédas, D. Beljonne, V. Coropceanu and J. Cornil, *Chem. Rev.*, 2004, **104**, 4971–5004.
2 V. Coropceanu, J. Cornil, D. A. da Silva Filho, Y. Olivier, R. Silbey and J.-L. Brédas, *Chem. Rev.*, 2007, **107**, 926–952.
3 G. Zhang, F. R. Lin, F. Qi, T. Heumüller, A. Distler, H.-J. Egelhaaf, N. Li, P. C. Y. Chow, C. J. Brabec, A. K. Y. Jen and H.-L. Yip, *Chem. Rev.*, 2022, **122**, 14180–14274.
4 L. Sun, K. Fukuda and T. Someya, *npj Flexible Electron.*, 2022, **6**, 89.
5 S. Reineke, F. Lindner, G. Schwartz, N. Seidler, K. Walzer, B. Lüssem and K. Leo, *Nature*, 2009, **459**, 234–238.
6 T.-H. Han, Y. Lee, M.-R. Choi, S.-H. Woo, S.-H. Bae, B. H. Hong, J.-H. Ahn and T.-W. Lee, *Nat. Photonics*, 2012, **6**, 105–110.
7 H. Kleemann, K. Krechan, A. Fischer and K. Leo, *Adv. Funct. Mater.*, 2020, **30**, 1907113.
8 G. Horowitz, *Adv. Mater.*, 1998, **10**, 365–377.
9 I. Salzmann, G. Heimel, M. Oehzelt, S. Winkler and N. Koch, *Acc. Chem. Res.*, 2016, **49**, 370–378.
10 I. E. Jacobs and A. J. Moulé, *Adv. Mater.*, 2017, **29**, 1703063.
11 D. Di Nuzzo, C. Fontanesi, R. Jones, S. Allard, I. Dumsch, U. Scherf, E. von Hauff, S. Schumacher and E. Da Como, *Nat. Commun.*, 2015, **6**, 6460.
12 M. Schwarze, C. Gaul, R. Scholz, F. Bussolotti, A. Hofacker, K. S. Schellhammer, B. Nell, B. D. Naab, Z. Bao, D. Spoltore, K. Vandewal, J. Widmer, S. Kera, N. Ueno, F. Ortmann and K. Leo, *Nat. Mater.*, 2019, **18**, 242–248.
13 B. Yurash, D. X. Cao, V. Brus, D. Leifert, M. Wang, A. Dixon, M. Seifrid, A. E. Mansour, D. Lungwitz, T. Liu, P. J. Santiago, N. Graham, K. R. abd Koch, G. C. Bazan and T.-Q. Nguyen, *Nat. Mater.*, 2019, **18**, 1327–1334.
14 P. Pingel, M. Arvind, L. Kölln, R. Steyrleuthner, F. Kraffert, J. Behrends, S. Janietz and D. Neher, *Adv. Electron. Mater.*, 2016, **2**, 1600204.
15 E. H. Suh, J. G. Oh, J. Jung, S. H. Noh, T. S. Lee and J. Jang, *Adv. Energy Mater.*, 2020, **10**, 2002521.
16 Y. Yamashita, J. Tsurumi, M. Ohno, R. Fujimoto, S. Kumagai, T. Kurosawa, T. Okamoto, J. Takeya and S. Watanabe, *Nature*, 2019, **572**, 634–638.
17 J. Guo, Y. Liu, P.-A. Chen, X. Wang, Y. Wang, J. Guo, X. Qiu, Z. Zeng, L. Jiang, Y. Yi, S. Watanabe, L. Liao, Y. Bai, T.-Q. Nguyen and Y. Hu, *Adv. Sci.*, 2022, **9**, 2203111.
18 H. Guo, C.-Y. Yang, X. Zhang, A. Motta, K. Feng, Y. Xia, Y. Shi, Z. Wu, K. Yang, J. Chen, Q. Liao, Y. Tang, H. Sun, H. Y. Woo, S. Fabiano, A. Facchetti and X. Guo, *Nature*, 2021, **599**, 67–73.
19 F. Bauch, C.-D. Dong and S. Schumacher, *RSC Adv.*, 2022, **12**, 13999–14006.
20 P. S. Marqués, G. Londi, B. Yurash, T.-Q. Nguyen, S. Barlow, S. R. Marder and D. Beljonne, *Chem. Sci.*, 2021, **12**, 7012–7022.
21 H. Wei, Z. Cheng, T. Wu, Y. Liu, J. Guo, P.-A. Chen, J. Xia, H. Xie, X. Qiu, T. Liu, B. Zhang, J. Hui, Z. Zeng, Y. Bai and Y. Hu, *Adv. Mater.*, 2023, **35**, 2300084.
22 T. Bathe, C.-D. Dong and S. Schumacher, *J. Phys. Chem. A*, 2022, **126**, 2075–2081.
23 C.-D. Dong and S. Schumacher, *J. Phys. Chem. C*, 2019, **123**, 30863–30870.
24 C.-D. Dong and S. Schumacher, *J. Mater. Chem. C*, 2020, **8**, 11929–11935.

25 D. Fazzi, S. Fabiano, T.-P. Ruoko, K. Meerholza and F. Negri, *J. Mater. Chem. C*, 2019, **7**, 12876–12885.
26 S. Grimme, J. Antony, S. Ehrlich and H. Krieg, *J. Chem. Phys.*, 2010, **132**, 154104.
27 F. Neese, *Coord. Chem. Rev.*, 2009, **253**, 526–563.
28 M. J. Frisch, G. W. Trucks, H. B. Schlegel, G. E. Scuseria, M. A. Robb, J. R. Cheeseman, G. Scalmani, V. Barone, G. A. Petersson, H. Nakatsuji, X. Li, M. Caricato, A. V. Marenich, J. Bloino, B. G. Janesko, R. Gomperts, B. Mennucci, H. P. Hratchian, J. V. Ortiz, A. F. Izmaylov, J. L. Sonnenberg, D. Williams-Young, F. Ding, F. Lipparini, F. Egidi, J. Goings, B. Peng, A. Petrone, T. Henderson, D. Ranasinghe, V. G. Zakrzewski, J. Gao, N. Rega, G. Zheng, W. Liang, M. Hada, M. Ehara, K. Toyota, R. Fukuda, J. Hasegawa, M. Ishida, T. Nakajima, Y. Honda, O. Kitao, H. Nakai, T. Vreven, K. Throssell, J. A. Montgomery Jr, J. E. Peralta, F. Ogliaro, M. J. Bearpark, J. J. Heyd, E. N. Brothers, K. N. Kudin, V. N. Staroverov, T. A. Keith, R. Kobayashi, J. Normand, K. Raghavachari, A. P. Rendell, J. C. Burant, S. S. Iyengar, J. Tomasi, M. Cossi, J. M. Millam, M. Klene, C. Adamo, R. Cammi, J. W. Ochterski, R. L. Martin, K. Morokuma, O. Farkas, J. B. Foresman and D. J. Fox, *Gaussian~16 Revision C.01*, Gaussian Inc., Wallingford CT, 2016.
29 C.-D. Dong and S. Schumacher, *J. Phys. Chem. C*, 2021, **125**, 21824–21830.
30 T. Lu and F. Chen, *J. Comput. Chem.*, 2012, **33**, 580–592.

7.2 Charge Carrier Transport

Understanding charge-carrier transport in OSCs is essential because it offers critical insight into how these materials operate across a wide range of applications. This process spans multiple length scales: it begins at the molecular level, where charge transfer occurs between individual OSC molecules, and extends to the nano- and microscale [34], which involve interactions within the OSC matrix and the formation of large-scale transport pathways. Although modeling charge-carrier transport at the microscopic level is a central goal, the comparatively large molecular dimensions at this scale make a fully quantum-mechanical treatment of every molecular complex across the entire simulation domain computationally unfeasible. Even so, quantum-mechanical descriptions remain necessary for accurately capturing the fundamental transport mechanisms.

In the following section, charge transport will be examined from both the molecular to the microscopic perspectives, with particular emphasis on the molecular scale. The specific contribution of this thesis to the field will then be outlined.

Essential descriptor of charge-transport is the mobility (μ) of charges, describing the efficiency of which the charges move within the material. One can distinguish the mobility to be induced by diffusion and drift, the former describing the local movement of charges around their average position, while the latter describes the displacement of the average position of the charges [25]. The diffusion is key in the absence of any external potential and it can be described via a diffusion equation:

$$\langle x^2 \rangle = nDt, \tag{7.1}$$

where $\langle x^2 \rangle$ describes the mean-square displacement of the charges, D is the diffusion coefficient, n is the dimension ($n = 2, 4, 6$ for 1D, 2D, 3D), and t is the time. From the diffusion coefficient, the charge mobility can be described via the Einstein-Smoluchowski equation [25, 176]:

$$\mu = \frac{eD}{k_B T}\,, \tag{7.2}$$

where e and k_B are the electron charge and Boltzmann constant, respectively, and T is the temperature. In addition, since external applied electric fields (F) affect the drift-velocity of the charges (v) and thus displaces the average position of the charges, it can be defined as the ratio between the former amplitude and the latter. For weak fields it reads:

$$\mu = \frac{v}{F}\,. \tag{7.3}$$

One can distinguish between electron and hole charge mobility (n- or p-type), which stems from the ability to inject the different types of charges into the OSCs. Experimentally, several different methods have been employed to measure charge mobility in OSCs, such as Time-of-Flight experiments, Field-Effect Transistor Configuration, Diode Configuration, and Pulse-Radiolysis Time-Resolved Microwave Conductivity. The former three probing the drift, while the latter one probing the diffusion [25].

From a quantum-mechanical point of view, charge-transport in OSCs can be described by two different physical mechanisms: hopping transport and tunneling transport. As such, in good approximation, the total mobility can be described as the sum of both respective mechanisms. For low electron-phonon coupling and in highly crystalline structures, the charges are strongly delocalized, reflecting a band-like transport similarly observed in inorganic systems [176, 177]. However, due to the amorphous nature of most OSCs and their strong electron-phonon coupling, the hopping mechanism is dominant, leading to dominant incoherent transport. While the hopping transport in principle can be described dynamically by the FSSH method, this approach is computationally not feasible due to the relative large size of the systems that need to be modeled.

Charge transport can further be partitioned into intermolecular and intramolecular transport [177]. The latter is relevant for long (distorted) polymeric structures. Despite the fact that intramolecular transport is fast compared to intermolecular transport, the intermolecular hopping limits the charge mobility.

In early approaches, in 1959 Holstein developed an analytic Hamiltonian model of the small polaron formation for a 1D-crystal lattice, where localized charge carriers are coupled to local (on-site) phonons [178, 179]. Although not originally formulated for OSCs, this concept laid the foundation for the microscopic understanding of phonon-assisted charge transport in molecular crystals.

To explain the conductivity of polyacetylene, Su, Schrieffer, and Heeger introduced in 1979 the SSH model [180], describing charge transport in a 1D dimerized lattice with alternating nearest-neighbor hopping amplitudes induced by bond (non-local) electron-phonon coupling, where lattice distortions modulate the electronic hopping integrals.

Building upon these concepts, Holstein–Peierls-type Hamiltonians were later introduced to incorporate both local phonon coupling and non-local, bond-modulating phonons [25, 181], providing a more realistic description of charge transport in molecular and organic crystalline systems.

However, charge transport in amorphous OSCs is dominated by structural and energetic disorder [25], which gives rise to inherently stochastic transport dynamics rather than periodic-lattice behavior. Although the above theoretical frameworks offer essential microscopic insight into electron-phonon interactions and transport mechanisms, their straightforward application to arbitrary, fully disordered, non-periodic systems is highly challenging. This limitation motivates the development of alternative, computationally tractable approaches specifically suited to modeling charge transport in amorphous OSCs.

At the heart of all models lies the transition probability for a charge carrier to switch the sites it is localized on from the initial state (i) to the final state (f), that can be accounted for as the transfer rate (k_{if}) of the charge carrier, evaluated from molecular descriptors. From this transfer rate, for instance, the diffusion coefficient can be accounted for and thus the mobility can be computed [25, 177, 182]. When computing the transfer rate within Marcus theory or the MLJ framework, the key descriptors are the driving force, electron-phonon coupling (Huang–Rhys factor and reorganization energy), as well as the electronic coupling (transfer integral).

In large amorphous systems, due to the strong electronic disorder, charges can be trapped in deep-lying, localized trap states [32]. In doped OSCs, counterions can lead to traps due to their attractive Coulomb potential [183]. Moreover, the strong electron-phonon coupling lead to self-trapping of the charges on specific OSC sites, hindering the charges to hop and thus may impede transport [184]. The local morphology can strongly impact the hopping rate [25, 112] and nanoscale morphology as well as grain boundaries can impact the overall connectivity between molecular sites and thus the transport pathway and mobility [176]. Based on evaluation of quantum-mechanical properties and transfer rates, (kinetic) Monte Carlo simulations can be performed to estimate the macroscopic quantities [185–188].

In this thesis, a contribution is made with a particular focus on identifying charge-transport descriptors at the molecular scale. Two polymers (PCPDT–BT and P3HT) are investigated in a positively-charged dimer configuration. Specific vibrational modes within each dimer are found to facilitate charge transfer through strong intermolecular electron-phonon coupling. AIMD simulations further reveal changes in the electron distribution that can be linked to charge-transfer processes. Building on these observations, the dimers are conceptually decomposed into their constituent monomers, allowing the adiabatic dimer representation to be interpreted loosely in terms of diabatic monomer states. This approach highlights that the polaron energy levels of isolated monomers serve as an excellent descriptor for predicting charge-transfer events.

The results presented in this chapter were previously published and are reproduced below. Reprinted from F. Bauch et al., Dynamics-induced charge transfer in semiconducting conjugated polymers, *Journal of Materials Chemistry C* **11**, 12992-12998 (2023), https://-doi.org/10.1039/d3tc02263c. The supplementary information can be found on the journal's website.

Journal of Materials Chemistry C

ROYAL SOCIETY OF CHEMISTRY

PAPER

View Article Online
View Journal | View Issue

Cite this: J. Mater. Chem. C, 2023, 11, 12992

Dynamics-induced charge transfer in semiconducting conjugated polymers†

Fabian Bauch,[a] Chuan-Ding Dong *[a] and Stefan Schumacher[ab]

Received 28th June 2023,
Accepted 5th September 2023

DOI: 10.1039/d3tc02263c

rsc.li/materials-c

The mechanism of charge transport in semiconducting conjugated polymers is of fundamental importance. The role of polymer dynamics therein is considered crucial but is not yet fully explored. In the present work, we combine density functional theory (DFT) and *ab intio* molecular dynamics (AIMD) simulations to study the dynamics-induced charge transfer (CT) in ordered bi-molecular systems of the widely investigated polymers PCPDTBT and P3HT, respectively. By using static DFT calculations, we show that interchain CT in the bi-molecular systems is induced by the vibrational dynamics and significant coupling of electrons to specific vibrational modes. Furthermore, our AIMD simulations capture interchain and intrachain CT providing valuable insights into polaron energetics during the CT processes. We find that the polaron shared by the two neighboring molecules is energetically stabilized with respect to the single oligomer polaron; in a film environment this stabilization could make the polaron transfer to the surrounding polymer matrix less favourable. This could be an important parameter in designing efficient organic semiconductor materials. Our results provide detailed insights into charge transport mechanisms at the molecular level and illustrate the role of polaron energetics in dynamical charge transfer.

1 Introduction

Organic semiconductors (OSCs) are finding numerous applications in electronic devices such as light-emitting diodes,[1–3] transistors,[4,5] and photovoltaic heterojunctions,[6,7] where excellent electronic transport properties are highly desirable.[8] As with inorganic semiconductors, there has been considerable interest in increasing and optimizing carrier concentration in OSCs, and various doping methods have been developed with increasing understanding at the molecular level.[9–13] On the other hand, the intrinsic charge mobility in OSCs is of fundamental importance.[14–16]

However, the theoretical description of charge mobility of OSC at the molecular level remains a challenging task.[16–20] By comparison, the methodologies for the conductivity of crystalline solids are comparably well developed. Boltzmann transport equation (BTE) in the relaxation time approximation, based on the electronic band structures and perturbation treatment of phonon-electronic scattering, has been widely used to describe the conductivity of inorganic semiconductors at the first-principles level.[21] Nevertheless, the application of BTE in OSC materials is difficult due to the significant electron–phonon coupling (EPC), as well as the less dispersive bands and the mostly amorphous molecular order in the OSC films.[19,22]

In the strong EPC limit, carrier hopping is considered the primary mechanism of transport in OSCs.[23–25] The hopping picture is often combined with numerical methods such as kinetic Monte Carlo to statistically investigate details of OSC transport, such as structural order or disorder and doping efficiency.[26,27] Nevertheless, in the regime of comparable strengths between EPC and electron transfer integral, neither the band-structure transport nor the hopping picture is well applicable.[19,28] In that case, the combination of the Kubo formula, which presents a general formalism for the carrier mobility, with model Hamiltonians is finding increasing research interests in recent years, with different designs of Hamiltonians and theoretical approaches that have been proposed.[29–32] For example, the transient localization (TL) theory uses a Hamiltonian which couples charge carriers linearly to the intermolecular motion, and efficiently reconciles the contradiction between the band-like extended charge carriers and localization phenomena.[33] Recently, Shuai *et al.* proposed a density matrix renormalization group method to treat the non-local EPC, and identified different physical pictures in different regimes as a function of transfer integral and non-local EPC.[34,35]

[a] Department of Physics and Center for Optoelectronics and Photonics Paderborn (CeOPP), Paderborn University, Warburger Strasse 100, 33098 Paderborn, Germany. E-mail: cddong@mail.uni-paderborn.de
[b] Wyant College of Optical Sciences, University of Arizona, Tucson, AZ 85721, USA

† Electronic supplementary information (ESI) available. See DOI: https://doi.org/10.1039/d3tc02263c

The theories and methods described above often allow for deep physical insights into electronic transport and EPC. However, being based on simplified model Hamiltonians they do typically not capture all the details and dynamical features of charge transfer in OSC aggregates, where van der Waals interaction dominates the intermolecular or interchain interaction, which results in significant anharmonic features in the dynamics.[19] Furthermore they are mostly applied to transport problems in molecular OSCs, mostly with good structural order, but less for the transport in semiconducting conjugated polymers (CP).[15,36,37] For the latter systems *ab initio* molecular dynamics (AIMD) are capable of a fully microscopic and detailed description of the charge transfer dynamics in CP aggregates of finite size.

Conjugated polymers constitute a major class of OSC materials and in doped CPs the charge carriers are mostly polarons. The transport properties of CPs are directly involved with the intrachain and interchain transfer of polarons.[38] The electronic band structure of CPs typically has modest dispersion and can contribute to the intrachain carrier conducting. The interchain transport, and its interplay with the intrachain process, are considered to play an important role as well, but the mechanistic understanding of the latter are still limited. Bearing the significant EPC in CP systems in mind, a comprehensive description of charge transfer (CT) processes and polymer dynamics at the molecular level is highly desirable for a distinct picture of EPC and carrier hopping in CPs. In this work, we investigate the dynamics-induced CT process by using quantum chemical calculations, with the emphasis on the interchain CT. To this end, we consider a bi-molecular aggregate in stack configuration of two p-type conjugated polymers with $+1e$ total net charge. The dynamics of the polymer aggregates are addressed in two ways. First we address the vibrational normal modes of the aggregates and investigate how the displacement along vertain vibrational modes induces interchain CT. Then we perform full AIMD simulations of the polymer aggregates and observe the dynamics-induced interchain CT process, including the intrinsic anharmonicities. In the dynamical data we find that the energetics of a single oligomer's polaron is closely related to the interchain CT. Moreover, we find that the structural order of the polymer aggregates studied leads to polaron stabilization. We propose that an over-stabilization of the polaron due to the well-stacked aggregates could confine the polaron within the ordered domain and may be difficult to transfer to the neighboring less ordered polymer, and therefore a slightly less structural order of polymer aggregates could be favorable to induce interchain CT. On the other hand the same polaron stabilization may also increase the energy cost for the polaron to hop into the surrounding matrix of the CP film.

2 Systems and computational details

In this work we investigate the donor–acceptor alternating polymer poly[2,6-(4,4-bis-(2-ethylhexyl)-4*H*-cyclopenta [2,1-*b*;3,4-*b*′]dithiophene)-*alt*-4,7(2,1,3-benzothiadiazole)] (PCPDTBT) and the polymer poly(3-hexylthiophen-2,5-diyl) (P3HT) as shown in Fig. 1a and b. The lengths of the oligomers are chosen to be 4 donor units and 3 acceptor units for PCPDTBT, following our previours works,[39,40] and 9 repeat units for P3HT. For simplicity the alkyl side chains of the polymers chains are replaced by H atoms. The geometries of the polymer aggregates with $+1e$ net charge are optimized and the vibrational normal modes are calculated. Based on the optimized geometries, the deformed geometries of the polymer aggregates according to certain normal modes are prepared by using manual displacement functionality provided in GaussView6[41] software with the same shift increment ratio. The amplitudes of the shifts, or the actual displacement of each atom, are around 0.01 Angstrom by 10% shift, but can be different between the modes, since the normal coordinates of the modes, as well as the reduced masses, are different from each other, while the energy costs caused by the shifts are presented in Fig. 1.

In the present work we use the range-separated cam-B3LYP functional together with the 6-31g(d) basis set for a sufficient description of the CT transfer character as in our previous work on doping OSCs.[39,40,42,43] van der Waals interaction correction is included by using the Grimme D3 method with Becke–Johnson damping function.[44,45] The DFT calculations are performed by using Gaussian16[46] package. The Hirshfeld charge decomposition presented in Fig. 1, which was shown to agree well with other charge decomposition schemes,[39,47] was performed by using Multiwfn software.[48] The charge decomposition results for the AIMD simulations shown in Fig. 2 use Mulliken decompsition scheme, which is implemented in ORCA.[49] The AIMD simulations of the polymer aggregates with $+1e$ net charge are performed for the temperature 293 K, controlled by using the Berendsen thermostat with a time constant of 10.0 fs. This value is suitable to reduce the temperature fluctuations during the simulation without strongly coupling the system to the thermostat and thus strongly affecting the dynamics of the system.

Since the occupation of virtual orbitals at this temperature is low, and no optical electronic excitation is involved, in the present work we considered only electronic ground state and did not include non-adiabatic effects.[50,51]

The time step for the molecular dynamics (MD) simulation is 1.0 fs. At each MD step, the DFT calculation also uses cam-B3LYP functional and 6-31g(d) basis set. The simulations started with the optimized geometries with different initial velocities from a random initial velocity distribution of 293 K for all atoms. The AIMD simulations are performed by using ORCA software package.[49] We would like to note that energy differences between occupied and unoccupied molecular orbitals are known to be largely overestimated with the use of the cam-B3LYP functional for the materials studied here,[39,40] so that only relative alignment and changes of energy levels for different systems should be interpreted as being physically relevant. More background information of AIMD and Berendsen thermostat is presented in a Computational Methods section in the ESI.†

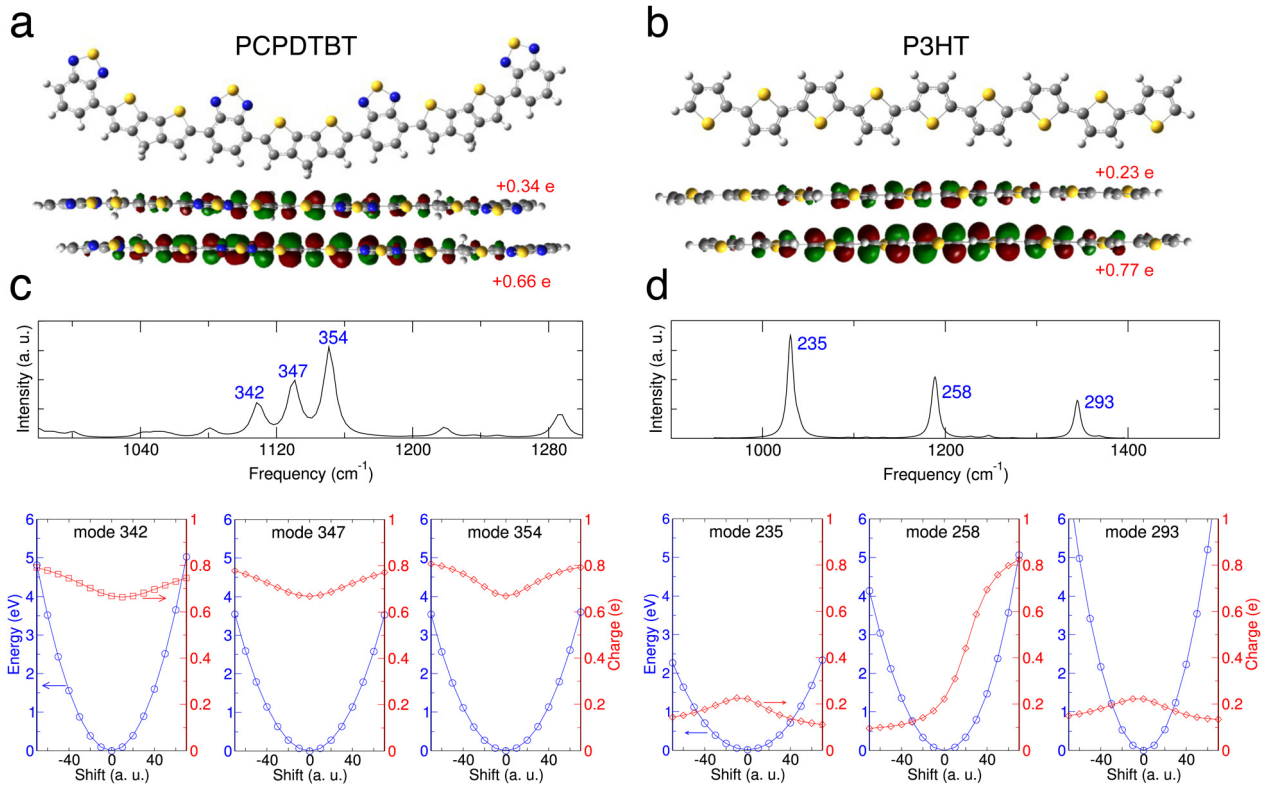

Fig. 1 Chemical structures of PCPDTBT (a) and P3HT (b). Color code: black for N, yellow for S, grey for C and white for H, as well as the optimized aggregates with 1 +*e* net charge. Also shown are the calculated LUMO orbitals as a representation of the polaron, and the Hirshfeld charge of each polymer chain. (c) and (d) Vibration induced charge transfer in cationic PCPDTBT (c) and P3HT (d). Upper: Calculated vibrational IR spectrum of the aggregates, labelled with the mode numbers of the three strongest normal modes. Lower: Variation of Hirshfeld net charge on the lower chain as well as the energy change of the aggregate for displacement along each of the three strongest normal modes as examples.

3 Results and discussion

3.1 Charge transfer modes

The oligomers in the optimized aggregates of both PCPDTBT and P3HT show almost planar configurations, which is typical for positively charged CP. The calculated Hirshfeld charge values show that the +1*e* net charge is actually shared between the two oligomers (Fig. 1a and b), indicating significant hybridization of the electronic orbitals of the two oligomers. In such open-shell electronic structure, the positive +1*e* net charge on the polymers, or polaron, can be well represented by the calculated β-LUMO (lower in energy than the α-LUMO), which verifies the electronic hybridization in the aggregates.

To probe the possible dynamics-induced interchain charge transfer, we start by examining the vibrations of the aggregates. Given the large number of the normal modes, we restrict ourselves to the three strongest modes as marked in Fig. 1c and d, and investigate the variations of energy and charge distribution caused by each of these modes. We note that these modes are only shown as examples and other modes could also show qualitatively similar behavior. Selecting the most intense modes seems to be a natural approach, even if there is no clear correlation between IR mode intensity and contribution to charge transfer. For the PCPDTBT aggregate, the vibrations in these three modes (Fig. 1c) lead to only modest charge transfers around 0.1*e* with energy costs of around 5 eV. For the P3HT aggregate (Fig. 1d), whereas the mode 235 and mode 293 see insignificant interchain CT, a significant interchain CT of around 0.7*e* is observed in mode 258 accompanied by an energy cost as high as more than 4 eV, demonstrating that vibration-induced interchain CT in this aggregate is in principle possible but could be energetically highly demanding.

Taking the mode 235 (without interchain CT) and mode 258 (with interchain CT) of P3HT aggregate as the examples, the polaron orbitals of the aggregate at different geometric positions of the normal modes are also observed by single point calculations, as presented in Fig. S1 (ESI†). In the vibration process of mode 258, the polaron transfer from one oligomer to the other is clearly seen, as expected. Interestingly, the polarons show also back-and-forth movement along the backbones of the oligomers in both mode 235 and mode 258. This back-and-forth motion of polaron driven by normal modes is well known for conjugated polymers,[52] which does not depend on our system and is more universal than interchain CT. Moreover, the possible vibration-induced interchain CT in the polymer aggregates of shorter lengths are also examined. Fig. S2 (ESI†) demonstrates the results for the PCPDTBT aggregate with oligomers of 2 donor units and 2 acceptor units, and for P3HT aggregate with oligomers of 5 repeating units. Interestingly, multiple modes of both PCPDTBT and P3HT aggregates

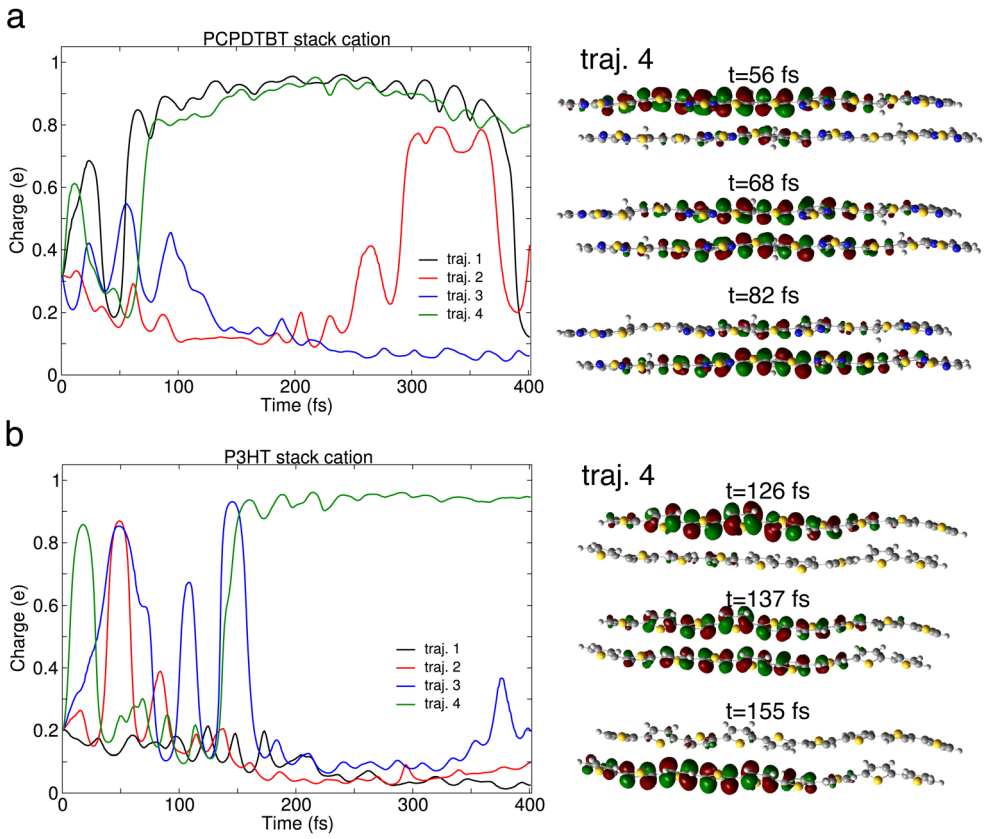

Fig. 2 Charge transfer dynamics for cationic polymer aggregates in MD simulations. Four different MD simulations with the same optimized initial geometry but different initial velocities for PCPDTBT (a) and P3HT (b) are presented. Left panel: The evolution of net charge of the same polymer chain (the bottom chain) along different MD trajectories. Right panel: The distribution of the polaron, represented by the calculated β-LUMO orbital, at three different time points of a charge transfer process in MD trajectory 4.

are found leading to significant interchain CT with typical energy costs less than 1 eV, implying that the aggregate length, or the finite length confinement, could play a role in the vibration-induced interchain CT. The significant motion of charge distribution driven by harmonic normal modes, both the polaron oscillation in the oligomer backbone and the interchain CT in the aggregates, can be taken as the equivalence of the frozen phonon approximation in solid materials and evidence the pronounced electron-vibration coupling in the CP systems as mentioned before.

An interesting observation from the vibrations modes in Fig. 1 as well as those in Fig. S2 (ESI†) is that the modes leading to interchain CT are characterized by anti-symmetric stretching patterns of the same corresponding C–C bonds of both polymers, while the modes without interchain CT exhibit symmetric bond stretching patterns. It should be noted that the normal modes addressed in Fig. 1 could be populated by less than 1% under room temperature, and have virbation periods around just 30 fs, and therefore can hardly represent the actual dynamic process, which will be addressed in next section by AIMD simulations.

3.2 Dynamic charge transfer

Compared with investigating the selected harmonic normal modes, MD simulations provide a more realistic pictures of the dynamics and incorporate both harmonic and anharmonic contributions. For both PCPDTBT and P3HT, we perform AIMD simulations to capture the interchain CT behavior. Fig. 2 shows the charge distribution of both aggregates along the MD trajectories from different initial conditions. Quite a few interchain CT occurrences can be identified by the change of around 0.7*e* in the net positive charge on a single polymer chain in the early phase below 150 fs and also in the later phase at times past 300 fs for PCPDTBT. We note that the system before around 150 fs is in an equilibrating process, from the total energy evolution shown in Fig. S3 (ESI†). For several trajectories the interchain CT occurs more than once before a relatively long time of stabilization. Fig. 2 shows also the calculated polaron orbitals at different time points of the interchain CT processes of two representative trajectories. At the middle time point of the CT process, the polaron is nearly equally shared between the two oligomers, which reflects the variation of electronic coupling between the oligomers resulting from the geometric change of the aggregates in the dynamic process. The distribution of the shared polaron clearly shows a continuous CT process, with a nearly equal weight between the two polymers at the middle time point. It is interesting to view the CT process as the preference of the polaron at different polymers and analyze the role the polaron energetics therein.

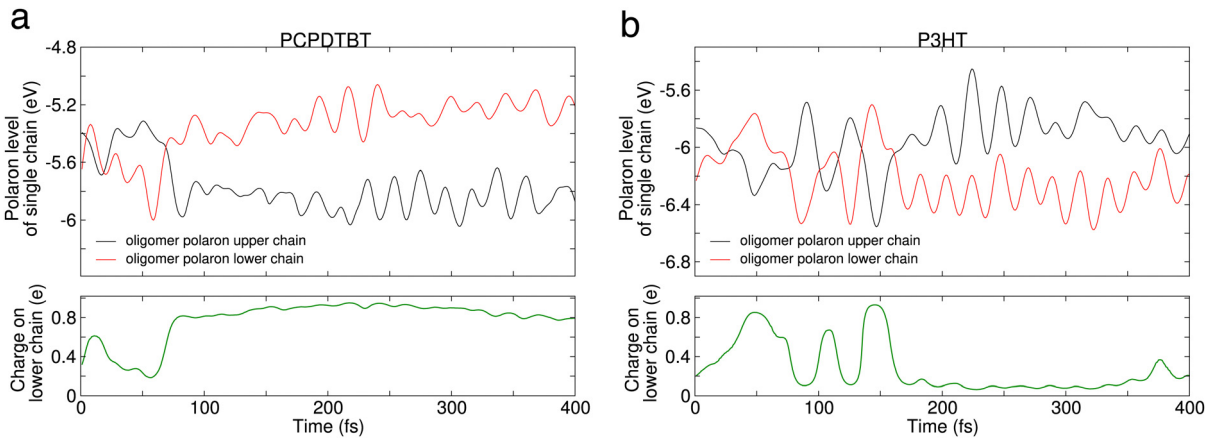

Fig. 3 Correlation between oligomer polaron energy (see text) and interchain charge transfer in respective trajectory 4 of PCPDTBT (a) and in P3HT (b). The variation of the two polymer chains' oligomer polaron energies along the MD simulation trajectory are shown in the upper part, accompanied by the charge transfer in the same trajectory shown in the lower part.

An intuitive mechanistic understanding of the interchain CT, or polaron preference, could be acquired by considering the single oligomer polaron energies, namely the polaron energies on the two separated oligomer geometries, respectively. In detail, for a certain MD simulation, the polaron energy is calculated for each oligomer with fixed geometry at each time point in the dynamics to gain an estimation which oligomer is energetically favored by the polaron. Note that since a polaron is a positive net charge and represented by an unoccupied orbital, the higher energy level indicates the energetic preference. Fig. 3 shows the results for the respective trajectories 4 of PCPDTBT and P3HT, respectively. A clear correspondence is found between the preference indicated by the two oligomer polaron energies, and the calculated charge distribution in the aggregate. For PCPDTBT (Fig. 3a), in the time interval between t = 20 fs and t = 68 fs, the oligomer polaron energy of the lower chain (red curve) is lower-lying than that of the upper chain (black curve). Correspondingly, in this time interval the lower chain hosts less than +0.4e charge, indicating less energetic preference of polaron. After t = 68 fs the polaron energy level of the lower chain turns higher than that of the upper chain, which is accompanied by the increased weight of the polaron (around +0.8e). Similarly, along the trajectory of P3HT (Fig. 3b), the relative positions of the two oligomer polaron energies switches several times, the time points also agree well with the interchain CT events. The results show that the single oligomer polaron energy can be an indicator of the energetic preference of the polaron on a single chain to reflect the trend of the interchain CT events. In this sense, the trend of polaron transfer could be estimated based on its energetics as a single particle. In addition, since the oscillation of single polaron energies, as the result of intrachain vibration, is apparently faster than the interchain CT, as can be seen from Fig. 3, our results support the separated treatment of intrachain EPC and interchain EPC in model Hamiltonian studies.[30,31,34]

In the dynamic process shown in the trajectories, from around t = 100 fs the temperatures and the total energies of the systems tend to stabilized and show no apparent changes corresponding to the interchain CT events, as shown in Fig. S3 (ESI†). This indicates that the interchain CT is an energetically continuous process driven by the dynamics of the aggregates, and in this sense, of the same nature as the intrachain polaron motion along the polymer backbone. In both cases, the polaron is actually shared by the two oligomers of the aggregates, and the interchain CT shown in Fig. 2 could then be taken as the motion of the shared polaron within the aggregate but across the polymer backbones.

It is interesting to compare the energetic position of the shared polaron with that of the polaron on a single oligomer. As shown in Fig. 4, for both PCPDTBT and P3HT, the energy levels of the shared polaron in the dynamical process oscillates in the vicinity of the shared polaron's energy of the optimized aggregates, indicating that the latter can roughly represent the spectral position of the shared polaron in the dynamics. The shared polaron in the optimized aggregate is energetically higher than the polaron in the optimized single oligomer which indicates a stabilization of the polaron (since the polaron is of positive charge nature). This stabilization effect is significantly larger for PCPDTBT (0.72 eV) than for P3HT (0.30 eV). Adding a third oligomer to the aggregates leads to further stabilization of the polarons, but less so for PCPDTBT (0.19 eV) than for P3HT (0.28 eV).

Based on the insight that the polaron energy on an oligomer could be an indicator of CT, as discussed with Fig. 3, we presume that the stabilization of a polaron in the aggregate could make the polaron transfer from the aggregate to a neighbouring oligomer energetically less favorable. In that context, it is interesting to note that for P3HT the oscillating energy of the shared polaron in the dynamics can compensate for the stabilization energy and dynamically reach the level of the optimized single oligomer polaron. This may indicate a possbility for dynamical polaron transfer away from the aggregate to a neighbouring oligomer. By comparison, in PCPDTBT the over-stabilization of the shared polaron in the aggregate

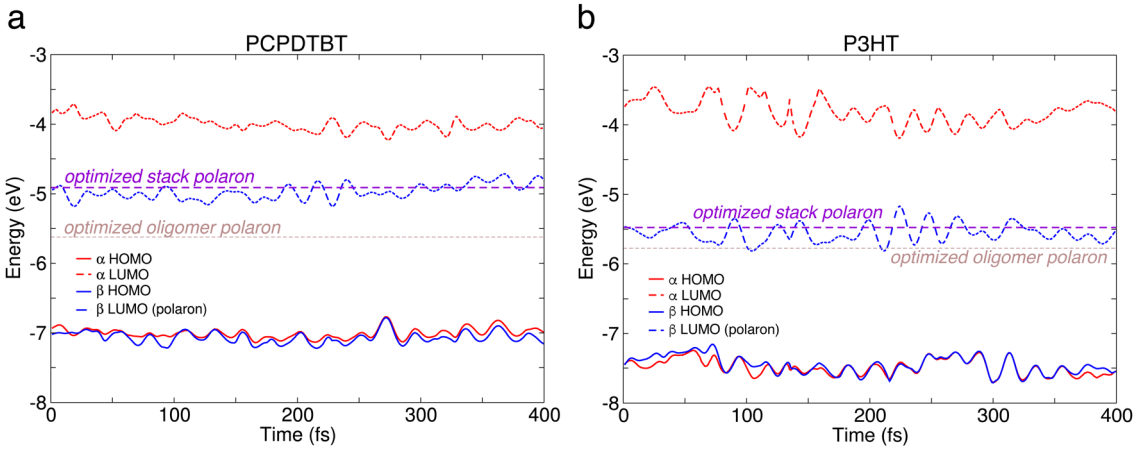

Fig. 4 Variation of calculated HOMO and LUMO levels in MD simulation trajectories 4 of the cationic PCPDTBT (a) and P3HT (b). The MD simulation trajectories are the same as those shown in Fig. 3. α and β spin states are shown separately since the cationic systems are open-shell. The β-LUMO levels are taken as the polaron energies of the aggregates. The polaron energies of the optimized aggregates as well as those of the optimized oligomers are included for both materials.

could lead to reduced odds of transfer to an oligomer even under dynamic conditions. These findings indicate that the strength of the stabilization of the shared polaron is material specific and could play a different role for polaron hopping in different OSC materials.

In summary, given the stabilization of the polaron, the highly ordered and closely packed polymer backbones may have two opposing effects. On the one hand, such structural feature can in principle facilitate the delocalization of the shared polaron and in turn lead to band-like transport, as suggested in earlier studies. On the other hand, the stacking-induced stabilization of the delocalized polaron tends to trap the polaron in the ordered domain and may reduce the dynamics-induced transfer outwards.

4 Conclusion

In the present work we examine the charge carrier transfer in the electronic transport mechanism in CP. A particular focus lies on the primary step, namely the interchain CT, which we investigate based on AIMD simulations of a small CP aggregate. This approach includes full microscopic details including the anharmonic nature of the (van der Waals) interaction between the polymer chains. The vibrational dynamics of the polymer aggregate drives both the intrachain CT and the interchain CT. We find that the polaron energetics associated with the geometries of the oligomers in the dynamics is a good descriptor of the interchain CT events. On the other hand, the interchain CT is associated with a polaron dynamically shared between chains in the aggregate, which by electronic coupling is energetically stabilized with respect to the single oligomer polaron. As a consequence the polaron transfer away from the aggregate onto neighboring oligomers of a polymer film may be hindered by this stabilization effect. This effect is found to be of different strength in the two materials studied here, PCPDTBT and P3HT. Our work provides important insights into the processes underlying interchain charge transfer in CPs, and suggests valuable indicators related to charge mobility in OSC films. With these first insights into the effects of dynamics, future work will be devoted to ensemble systems for a more profound mechanistic understanding of charge transport in OSCs.

Conflicts of interest

There are no conflicts to declare.

Acknowledgements

A grant for computing time at the Paderborn Center for Parallel Computing (PC^2) is gratefully acknowledged. C. D. thanks Dr Zi-Di Yu and Dr Yang Lu for enlightening discussions.

Notes and references

1 G. Gustafsson, Y. Cao, G. M. Treacy, F. Klavetter, N. Colaneri and A. J. Heeger, *Nature*, 1992, **357**, 477–479.
2 S. Reineke, F. Lindner, G. Schwartz, N. Seidler, K. Walzer, B. Lüssem and K. Leo, *Nature*, 2009, **459**, 234–238.
3 T.-H. Han, Y. Lee, M.-R. Choi, S.-H. Woo, S.-H. Bae, B. H. Hong, J.-H. Ahn and T.-W. Lee, *Nat. Photonics*, 2012, **6**, 105–110.
4 B. Lüssem, A. Günther, A. Fischer, D. Kasemann and K. Leo, *J. Phys.: Condens. Matter*, 2015, **27**, 443003.
5 H. Kleemann, K. Krechan, A. Fischer and K. Leo, *Adv. Funct. Mater.*, 2020, **30**, 1907113.
6 G. Zhang, F. R. Lin, F. Qi, T. Heumüller, A. Distler, H.-J. Egelhaaf, N. Li, P. C. Y. Chow, C. J. Brabec, A. K. Y. Jen and H.-L. Yip, *Chem. Rev.*, 2022, **122**, 14180–14274.
7 L. Sun, K. Fukuda and T. Someya, *npj Flexible Electron.*, 2022, **6**, 89.
8 L. Ding, Z.-D. Yu, X.-Y. Wang, Z.-F. Yao, Y. Lu, C.-Y. Yang, J.-Y. Wang and J. Pei, *Chem. Rev.*, 2023, **123**, 7421–7497.

9 D. Di Nuzzo, C. Fontanesi, R. Jones, S. Allard, I. Dumsch, U. Scherf, E. von Hauff, S. Schumacher and E. Da Como, *Nat. Commun.*, 2015, **6**, 6460.
10 I. E. Jacobs and A. J. Moulé, *Adv. Mater.*, 2017, **29**, 1703063.
11 B. Yurash, D. X. Cao, V. Brus, D. Leifert, M. Wang, A. Dixon, M. Seifrid, A. E. Mansour, D. Lungwitz, T. Liu, P. J. Santiago, N. Graham, K. R. Abd Koch, G. C. Bazan and T.-Q. Nguyen, *Nat. Mater.*, 2019, **18**, 1327–1334.
12 Y. Yamashita, J. Tsurumi, M. Ohno, R. Fujimoto, S. Kumagai, T. Kurosawa, T. Okamoto, J. Takeya and S. Watanabe, *Nature*, 2019, **572**, 634–638.
13 Y. Lu, Z.-D. Yu, Y. Liu, Y.-F. Ding, C.-Y. Yang, Z.-F. Yao, Z.-Y. Wang, H.-Y. You, X.-F. Cheng, B. Tang, J.-Y. Wang and J. Pei, *J. Am. Chem. Soc.*, 2020, **142**, 15340–15348.
14 N. Karl, *Synth. Methods*, 2019, **7**, 12876–12885.
15 J.-L. Brédas, D. Beljonne, V. Coropceanu and J. Cornil, *Chem. Rev.*, 2004, **104**, 4971–5004.
16 V. Coropceanu, J. Cornil, D. A. da Silva Filho, Y. Olivier, R. Silbey and J.-L. Brédas, *Chem. Rev.*, 2007, **107**, 926–952.
17 J. L. Brédas, J. P. Calbert, D. A. da Silva Filho and J. Cornil, *Proc. Natl. Acad. Sci. U. S. A.*, 2002, **99**, 5804–5809.
18 Z. Shuai, H. Geng, W. Xu, Y. Liaoc and J.-M. André, *Chem. Soc. Rev.*, 2014, **43**, 2662–2679.
19 H. Oberhofer, K. Reuter and J. Blumberger, *Chem. Rev.*, 2017, **117**, 10319–10357.
20 C. Wiebeler, R. Tautz, J. Feldmann, E. von Hauff, E. Da Como and S. Schumacher, *J. Phys. Chem. B*, 2013, **117**, 4454–4460.
21 S. Poncé, W. Li, S. Reichardt and F. Giustino, *Rep. Prog. Phys.*, 2020, **83**, 036501.
22 F. Knoop, T. A. R. Purcell, M. Scheffler and C. Carbogno, *Phys. Rev. Mater.*, 2020, **4**, 083809.
23 N. Tessler, Y. Preezant, N. Rappaport and Y. Roichman, *Adv. Mater.*, 2009, **21**, 2741–2761.
24 N. Lu, L. Li and M. Liu, *Phys. Rev. B: Condens. Matter Mater. Phys.*, 2015, **91**, 195205.
25 S. Ihnatsenka, X. Crispin and I. V. Zozoulenko, *Phys. Rev. B: Condens. Matter Mater. Phys.*, 2015, **92**, 035201.
26 H. Yang, F. Gajdos and J. Blumberger, *J. Phys. Chem. C*, 2017, **121**, 7689–7696.
27 A. Fediai, F. Symalla, P. Friederich and W. Wenzel, *Nat. Commun.*, 2019, **10**, 4547.
28 X. Crispin and S. V. Kalinin, *Nat. Mater.*, 2017, **16**, 704–705.
29 J. H. Fetherolf, D. Golež and T. C. Berkelbach, *Phys. Rev. X*, 2020, **10**, 021062.
30 S. Hutsch, M. Panhans and F. Ortmann, *Phys. Rev. B*, 2021, **104**, 054306.
31 S. Hutsch, M. Panhans and F. Ortmann, *npj Comput. Mater.*, 2022, **8**, 228.
32 M. Panhans and F. Ortmann, *Phys. Rev. Lett.*, 2021, **127**, 016601.
33 S. Fratini, D. Mayou and S. Ciuchi, *Adv. Funct. Mater.*, 2016, **26**, 2292–2315.
34 Y. Ge, W. Li, J. Ren and Z. Shuai, *J. Chem. Theory Comput.*, 2022, **18**, 6437–6446.
35 W. Li, J. Ren and Z. Shuai, *Nat. Commun.*, 2021, **12**, 4260.
36 S. D. Kang and G. J. Snyder, *Nat. Mater.*, 2017, **16**, 252–257.
37 S. Fratini, M. Nikolka, A. Salleo, G. Schweicher and H. Sirringhaus, *Nat. Mater.*, 2020, **19**, 491–502.
38 D. Beljonne, G. Pourtois, C. Silva, E. Hennebicq, L. M. Herz, R. H. Friend, G. D. Scholes, S. Setayesh, K. Müllen and J. L. Brédas, *Proc. Natl. Acad. Sci. U. S. A.*, 2002, **99**, 10982–10987.
39 C.-D. Dong and S. Schumacher, *J. Phys. Chem. C*, 2019, **123**, 30863–30870.
40 C.-D. Dong and S. Schumacher, *J. Mater. Chem. C*, 2020, **8**, 11929–11935.
41 R. Dennington, T. A. Keith and J. M. Millam, 2019.
42 T. Bathe, C.-D. Dong and S. Schumacher, *J. Phys. Chem. A*, 2022, **126**, 2075–2081.
43 F. Bauch, C.-D. Dong and S. Schumacher, *RSC Adv.*, 2022, **12**, 13999–14006.
44 S. Grimme, J. Antony, S. Ehrlich and H. Krieg, *J. Chem. Phys.*, 2010, **132**, 154104.
45 S. Grimme, S. Ehrlich and L. Goerigk, *J. Comput. Chem.*, 2011, **32**, 1456–1465.
46 M. J. Frisch, G. W. Trucks, H. B. Schlegel, G. E. Scuseria, M. A. Robb, J. R. Cheeseman, G. Scalmani, V. Barone, G. A. Petersson, H. Nakatsuji, X. Li, M. Caricato, A. V. Marenich, J. Bloino, B. G. Janesko, R. Gomperts, B. Mennucci, H. P. Hratchian, J. V. Ortiz, A. F. Izmaylov, J. L. Sonnenberg, D. Williams-Young, F. Ding, F. Lipparini, F. Egidi, J. Goings, B. Peng, A. Petrone, T. Henderson, D. Ranasinghe, V. G. Zakrzewski, J. Gao, N. Rega, G. Zheng, W. Liang, M. Hada, M. Ehara, K. Toyota, R. Fukuda, J. Hasegawa, M. Ishida, T. Nakajima, Y. Honda, O. Kitao, H. Nakai, T. Vreven, K. Throssell, J. A. Montgomery, Jr., J. E. Peralta, F. Ogliaro, M. J. Bearpark, J. J. Heyd, E. N. Brothers, K. N. Kudin, V. N. Staroverov, T. A. Keith, R. Kobayashi, J. Normand, K. Raghavachari, A. P. Rendell, J. C. Burant, S. S. Iyengar, J. Tomasi, M. Cossi, J. M. Millam, M. Klene, C. Adamo, R. Cammi, J. W. Ochterski, R. L. Martin, K. Morokuma, O. Farkas, J. B. Foresman and D. J. Fox, *Gaussian'16 Revision C.01*, Gaussian Inc., Wallingford CT, 2016.
47 C.-D. Dong and S. Schumacher, *J. Phys. Chem. C*, 2021, **125**, 21824–21830.
48 T. Lu and F. Chen, *J. Comput. Chem.*, 2012, **33**, 580–592.
49 F. Neese, F. Wennmohs, U. Becker and C. Riplinger, *J. Chem. Phys.*, 2020, **152**, 224108.
50 C. Wiebeler, F. Plasser, G. J. Hedley, A. Ruseckas, I. D. W. Samuel and S. Schumacher, *J. Phys. Chem. Lett.*, 2017, **8**, 1086–1092.
51 M. Mondelo-Martell, D. Brey and I. Burghardt, *J. Chem. Phys.*, 2022, **157**, 094108.
52 M. Anderson, C. Ramanan, C. Fontanesi, A. Frick, S. Surana, D. Cheyns, M. Furno, T. Keller, S. Allard, U. Scherf, D. Beljonne, G. D'Avino, E. von Hauff and E. Da Como, *Phys. Rev. Mater.*, 2017, **1**, 055604.

Photoexcited Charge Carriers in Organic Photovoltaic Devices

8

As renewable energy has become one of the fastest-growing sectors worldwide, understanding the mechanisms of photoinduced charge generation has become increasingly important. Organic photovoltaic cells (OPVs), which convert light into electrical energy, are a promising class of low-cost and versatile solar energy devices [6–9, 189–191]. OPVs, in their simplest form, consist of an active layer, an anode, and a cathode. The active layer is responsible for exciton dissociation and charge-carrier generation. Typically, the active layer is arranged in a bulk heterojunction (BHJ) composed of a donor and acceptor component, pioneered by the group of Alan Heeger [4, 5, 192, 193], or ternary composition (three components). In the BHJ, the components finely interprenate each other, leading subtle donor:acceptor interfaces at the nanoscale between the donor and acceptor phases, as illustrated in Figure 8.1.

Upon illumination, photons are absorbed in the active layer, generating excitons in the respective phases. However, due to the comparably high exciton binding energy, they are inefficiently split into free charges (although charge generation in single-components are reported [194, 195] as discussed below). Thus, these excitons then have to diffuse to the donor:acceptor interface via various energy transfer processes [28]. At the interface, charge transfer occurs: the hole moves to the donor and the electron remains in the acceptor (exciton dissociation), forming so-called interfacial charge-transfer (CT) states [45], as shown in Figure 8.1.

This separation process is driven by the energy difference between the CT state and the locally excited (LE) state ($\Delta E = E^{\mathrm{CT}} - E^{\mathrm{LE}}$), or more general, due to the energy offset between the orbital energy levels, which explains the use of at least one donor and one acceptor component in the active layer. The separated charges are transported through their respective materials and collected at the anode and cathode, generating photoinduced current. Moreover, other layers, such as electron and hole transfer layers, can be incorporated to

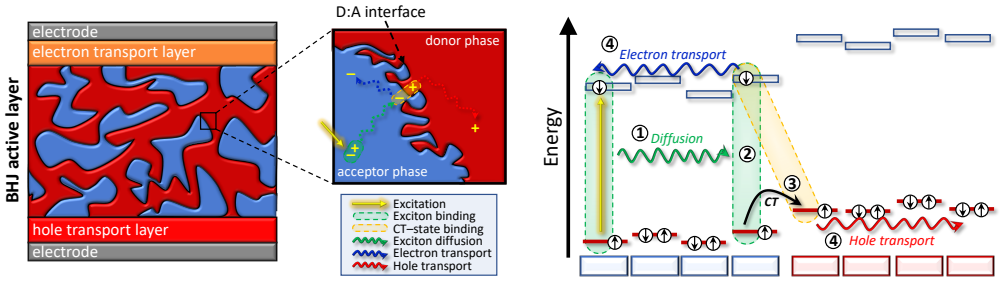

Figure 8.1: Active layer in OPVs. Structure diagram of a typical bulk heterojunction OPV. In the active layer, photoinduced excitons in the donor or acceptor phase diffuse to the donor:acceptor interface. At the interface, they dissociate into charge-transfer states which subsequently separate into free charges that will be transported in the respective phases towards the electrodes. The mechanism is illustrated in a single-particle picture on the right; local polarization effects are not illustrated. (1) The exciton diffuses towards the interface; (2) the exciton at the interface undergoes charge transfer (CT) to form a charge-transfer state (3); and (4) the charges separate further leading to the generation of free charges.

optimized the device functionality.

The primary metric used to evaluate OPV performance is the power conversion efficiency (PCE), which quantifies the ratio of the electrical power produced by the device to the incident optical power [196]:

$$\mathrm{PCE} = \frac{P_{\mathrm{output}}}{P_{\mathrm{incident}}} = \frac{J_{\mathrm{SC}} \times V_{\mathrm{OC}} \times \mathrm{FF}}{P_{\mathrm{incident}}}, \tag{8.1}$$

where P_{incident} denotes the incident light power, FF the fill factor, V_{OC} the open-circuit voltage, and J_{SC} the short-circuit current density. The quantity J_{SC} represents the maximum current density under illumination at zero external bias and is governed by light absorption, exciton diffusion, charge separation, and charge extraction. The open-circuit voltage V_{OC} corresponds to the maximum attainable voltage in the absence of current flow and is approximately determined by the energy difference between the donor HOMO and the acceptor LUMO, minus energetic losses. These losses arise from the offset ΔE as well as additional radiative and non-radiative recombination processes. The fill factor FF reflects how effectively the device converts voltage and current into usable power.

Achieving a high PCE therefore requires strong light absorption, well-aligned energy levels that minimize losses while providing adequate driving force, high exciton diffusion efficiency (i.e., limited recombination prior to charge-transfer state formation), and efficient

charge separation at the interface and further transport.

The emergence of non-fullerene acceptors (NFAs), in particular Y6 and its derivatives [197–200], has boosted the PCE in combination with donor polymers in the last years. While fullerene acceptors show low PCE values around a few percent, today, state-of-the-art OPV devices reach typical values of V_{OC} of 0.7-1.0 V, J_{SC} of 10-25 mAcm^{-2}, and FF of 60-80% [41, 201, 202], reaching remarkable PCE values reaching up to 21% [42, 203, 204] for highly optimized systems. The reason for this drastic increase in recent years has been the optimization of opto-electronic properties through chemical modification, as well as the improvement of beneficial morphology, for example via side-chain engineering [205–208], optimized OSC:solvent interactions [209], and the use of solid additives to promote favorable molecular packing and phase separation [210].

In this section, a brief description of the charge generation process governed by the electronic state manifold in OPVs is provided. Moreover, relevant photo-physical properties (such as driving force, reorganization energy, . . .) are related to the device performance. Afterwards, the intrinsic dynamics of the exciton and corresponding properties that govern the exciton lifetime and exciton splitting are discussed.

8.1 Device Principle on Excited State Manifold

To describe the exciton dissociation process, the excited states are labeled according to their character, i.e., as locally excited (LE) or charge-transfer (CT) states. The spin multiplicity is indicated as a superscript preceding the state label, while the energetic ordering is denoted by a subscript. For example, the lowest-energy singlet LE and CT states are written as $^1LE_1$ and $^1CT_1$, respectively.

Turning to a specific description of the processes at the interface, multiple different pathways are available, as shown in Figure 8.2: the charge generation process is initiated by a transition of the singlet ^{1}LE state to a singlet ^{1}CT state (1), followed by charge separation into CS states and ultimately free charges (FC) (2) that contribute to the photocurrent. Spin-orbit coupling enables intersystem crossing between singlet and triplet states (^{1}LE/^{1}CT $\leftrightarrow$ ^{3}LE/^{3}CT) (3), while transitions between ^{3}LE and ^{3}CT states may also occur (4). Moreover, energy transfer processes can convert ^{1,3}LE states from the higher-gap material to ^{1,3}LE states at the lower-gap material (not illustrated). Owing to the central role of the CT state, transitions involving electron transfer are explicitly identified and labeled to distinguish them from the broader classes of internal conversion and intersystem crossing.

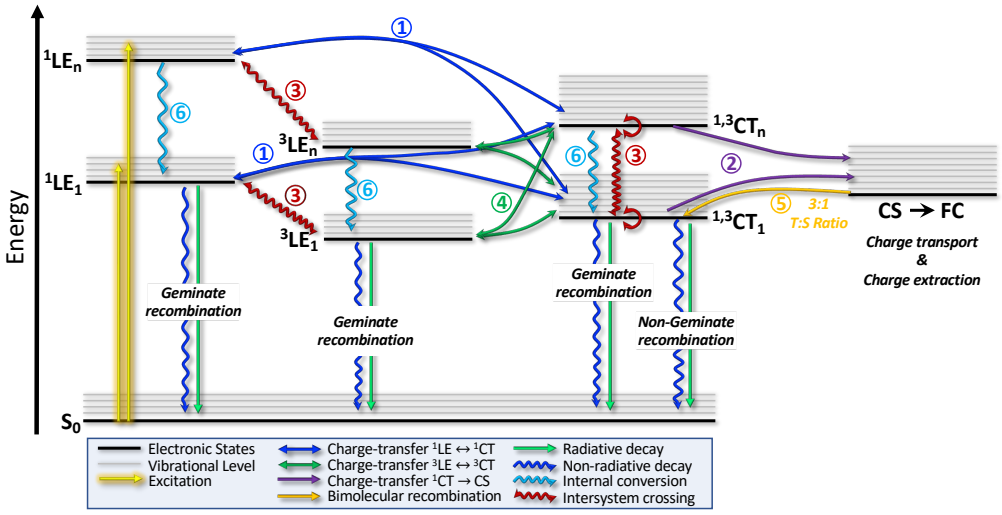

Figure 8.2: Excited-state manifold for charge generation and recombination in OPVs illustrated as a Jablonski diagram. After absorption of low- or high-energy photons, the resulting singlet exciton can (1) form a singlet charge-transfer (CT) state at the interface, which (2) separates into a charge-separated (CS) state, leading to free charge-carriers (FC) and charge transport. General loss processes include (3) intersystem crossing leading to triplet excitons or triplet CT states, (4) formation of triplet excitons from triplet CT states, and geminate recombination of CT states and excitons. (5) Free charges may reform CT states or undergo non-geminate recombination. (6) Internal conversion to lower excited states can occur, modifying relaxation pathways. Some transitions are omitted for clarity. Energy levels are shown schematically and do not necessarily reflect the actual energetic alignment. Vibrational relaxation, energy transfer processes, and exciton-exciton annihilation are not shown.

General loss processes include intersystem crossing to triplet ^{3}LE or triplet ^{3}CT states (3), as well as charge transfer from triplet ^{3}CT to triplet ^{3}LE states (4). Furthermore, free charges as well as ^{1,3}CT and ^{1,3}LE states may undergo geminate recombination (recombination of charge carriers generated in the same event) either radiatively or non-radiatively. In addition, internal conversion to lower-lying excited states may occur (6), thereby modifying relaxation pathways and promoting non-radiative decay.

Due to (non-)radiative recombination, losses in both the J_{SC} and V_{OC} arise. For the latter, the non-radiative voltage loss ($\Delta V_{OC}^{non\text{-}rad}$) stemming from the ^{1}CT states can be estimated from the electroluminescent external quantum efficiency (EQE_{el}) as [196]:

$$\Delta V_{OC,CT}^{non\text{-}rad} \approx -\frac{k_b T}{q} \ln(EQE_{el}) \text{ , with } EQE_{el} \propto \frac{p_e k_{rad}}{p_e k_{rad} + k_{non\text{-}rad}} \text{ .} \tag{8.2}$$

Here, q denotes the elementary charge, k_B the Boltzmann constant, T the temperature, and p_e the emission probability.

A highly emissive material (in particular, the lower-gap material) thus can lead to reduced non-radiative voltage loss [30, 211] by possible re-absorption of the photons. The non-radiative decay rates $k_{\text{non-rad}}$ from CT states can be computed via Marcus theory or the MLJ framework and the radiative decay k_{rad} via Einstein coefficient relation for spontaneous emission. Likewise, the conversion from ^{1,3}LE states to ^{1,3}CT states can be modeled via Marcus theory or the MLJ framework.

After formation of the free charges, these diffuse through their respective phases to the electrodes, thus, a high, uniform and balanced p- and n-mobility of the materials is required to optimize J_{SC}. Free charges, however, can non-geminately (originating from different events) recombine towards a singlet or triplet CT state and then follow the different cascades again (transition (5) in Figure 8.2), leading to additional losses in both the J_{SC} and V_{OC}. Due to spin-statistics, the singlet:triplet ratio of non-geminated recombination of uncorrelated charges is 1:3, again highlighting the relevance of triplet states in the system. Moreover, also non-geminate singlet (and triplet) exciton annihilation processes can occur, leading to additional losses in the J_{SC}.

It has been readily shown, that the local morphology at the D:A interface can strongly impact the device performance. Due to energetic disorder in the electronic state manifold (singlet and triplet excited-state energies, driving forces, and electronic couplings), the exciton dissociation, charge-separation efficiency as well as charge transport is strongly affected [45, 90, 212–214]. Minimized electronic disorder was shown to increase the overall device performance [31]. Thus, optimizing the interfacial morphology with detailed understanding of the photo-physical processes on the molecular scale, and minimizing disorder are most relevant in optimizing local charge-generation efficiency and reduce losses.

A large change in the electric dipole moment of the ^{1}LE state relative to the ground state ($\Delta\boldsymbol{\mu}$) was shown to generally increase the charge-separation yield [215–218], which can be attributed to a more separated electron and hole wave function lowering the Coulomb binding in an intramolecular charge-transfer (i-CT) state.

Besides CT states at the D:A interface and the i-CT state, intra-moiety excimer-like states (i-EX, i.e., CT states within the same moiety) in NFA Y6 aggregates were observed and correlated to strongly increase charge dissociation efficiency [219–222]. Moreover, small aggregation of the donor molecule or polymer was also shown to be beneficial due to

delocalization effects of the hole and electron in the CT state as well as environmental polarization effects [223].

It has been shown that increasing the ^{1}CT energy relative to the ^{1}LE energy reduces voltage loss [211, 224], which is accompanied by a reduced driving force. However, it has been shown that NFAs with low driving force can still achieve high PCEs [30, 225]. This can be partially supported by promoting hybridization between LE and CT states, which is induced by strong electronic coupling between LE and CT states due to small energy differences and reduced non-radiative losses due to emitting CT states [226].

In general, it is advantageous to reduce the singlet-triplet energy gap of the components ($\Delta E^{\mathrm{ST}} = E^{\mathrm{T1}} - \Delta E^{S1}$), thereby increasing the probability of thermalization of the ^{3}LE state to the ^{3}CT state and thus reducing losses via triplet excitons [227]. In addition to optimizing the energy levels of the OSCs, it has been shown that reducing the reorganization energy (electron-phonon coupling) of the LE states, CT states, and charge transport levels overall leads to a reduction in energy losses and recombination [228].

The initial exciton can be excited to its lowest excited state (^{1}LE$_1$) or to higher-lying excited states (^{1}LE$_n$), which are referred to as *cold* and *hot* states, respectively, with the latter being attributed an excess of energy compared to the lowest state (see Figure 8.2). *Hot* states can also be populated by energy transfer processes from a LE state of the higher-gap-material. Owing to internal conversion, such *hot* states typically relax rapidly to *cold* states, as shown in Figure 8.2 as transition (6). In some contexts, *hot* states are alternatively classified as vibrationally excited ^{1}LE$_1$ states that arise from above-gap excitation, leading to the population of higher vibrational levels within ^{1}LE$_1$.

Analogously, the population of interfacial CT state can be inherently *cold* or *hot*. The role of *hot* LE and CT states remains a subject of ongoing debate [229]. While some studies report that the CT dissociation efficiency is largely insensitive to whether CT states are formed *hot* and *cold* [230, 231], other studies suggest that excess energy associated with *hot* CT state formation enhances charge dissociation [232, 233]. Furthermore, the relaxation of *hot* CT states to *cold* CT states is proposed to set an upper time limit for competing processes at the interface, thereby influencing the efficiency of charge separation [234].

The next section explains the dynamics of the ^{1}LE states, which exhibit i-CT character for molecular systems comprising donor and acceptor architectures, and its significance for the charge-separation process.

8.2 Dynamics of the Exciton

A detailed investigation of the dynamics of *hot* and *cold* excitons provides valuable insight into the processes governing OPVs. In particular, such studies deepen the understanding of molecular properties that control exciton lifetimes, which ultimately constrain exciton diffusion lengths [28], and clarify how the intrinsic nature of excitons can enhance charge-separation efficiency. The diffusion length of the exciton is reciprocal to its lifetime, thus, a high exciton lifetime is generally beneficial for device performance.[1] This is particularly important because even for single molecular systems without donor:acceptor interfaces, free charge-carrier generation has been reported after photoexcitation [194, 195]. This can be attributed to the i-EX states [219–222], but the i-CT nature of the exciton on the donor polymer has also been highlighted to explicitly yield polaron pairs [235–238].

In this context, it has been reported, particularly for donor-acceptor copolymers, that the *hot* excitons promote the conversion of the original exciton state into i-CT states, which convert into charge-separating species on the same polymer chain and are precursors for free charge carriers within the first 200 fs after excitation [239–241]. Rapid planarization of a π-bridge ($<$ 400 fs) in donor-π-acceptor copolymers has been reported to increase the i-CT lifetime [242], resulting in lower recombination. The free charge-carrier generation from the i-CT state can be understood from a molecular picture: the i-CT state, which is more polarized than a pure exciton due to a better separated electron and hole wave function, can be separated more easily due to the weaker Coulomb attraction of the particles [236].

Experimentally, the dynamics of excited states can be observed and analyzed through transient absorption experiments (pump-probe experiments); from a theoretical perspective, NA–AIMD simulations can be used to investigate the nature and corresponding dynamics of excited states. For example, NA–AIMDs have been used to track *hot* and *cold* excited-state transitions in thiophene monomers and dimers [243, 244], providing insights into non-radiative decay mechanisms and the energy alignment of ^{1}LE and ^{1}CT states during the processes.

[1] A high exciton lifetime or a low (non-)radiative decay rate of the exciton itself. In the active layer, a high exciton lifetime can also indicate a poor donor:acceptor mixing, which hinders the population of charge-transfer states and leads to a reduction of device performance.

This thesis includes the following three contributions with focus on the donor:acceptor interfaces as well as exciton dynamics:

1. The donor:acceptor interface of a novel NFA with a trifluoromethyl-substituted side chain, namely Y_2CF_3, in combination with the polymer PM6 was modeled. Subsequently, the opto-electronic properties were investigated and a comprehensive evaluation of the exciton dissociation and geminate recombination at the interface was performed. Moreover, the electron transport in Y_2CF_3 and the hole transport in PM6 were investigated, illustrating highly efficient electron transport pathways. The influence of local molecular packing motifs on exciton dissociation and on charge-transport behavior was systematically analyzed.
   This work was carried out during a research stay with the research group of Prof. Jean-Luc Brédas in 2024. The results presented in this chapter were previously published and are reproduced below. Reprinted from F. Bauch et al., Electronic Properties of Organic Solar Cells based on CF_3-Functionalized Non-Fullerene Acceptors, *ACS Applied Materials & Interfaces* **18**, 2200-2211 (2026), https://doi.org/10.1021/acsami.5c18819. Copyright © 2025 American Chemical Society. The supplementary information can be found on the journal's website.

2. Donor molecules with A-π-Core-π-A architecture were systematically modified to investigate the influence of different electron-withdrawing terminal units and extended π-delocalized bridges in the molecule on the opto-electronic properties and on the transition rate constants for the formation of CT states in complexes with NFA Y6.
   The results presented in this chapter were previously published and are reproduced below. Reprinted from F. Bauch et al., Designing High Performance Organic Donor Molecules for Photovoltaics, *Advanced Theory and Simulations*, e01560 (2025), https://-doi.org/10.1002/adts.202501560. Copyright ©2025 The Author(s). *Advanced Theory and Simulations* published by Wiley-VCH GmbH. This article is licensed under a Creative Commons Attribution 4.0 International (CC BY 4.0) licence: https://creativecommons.org/licenses/by/4.0/. No changes were made. The supplementary information can be found on the journal's website.

3. The influence of the excited-state dipole moment and the Coulomb attractive energy of *hot* excitons on polaron-pair formation was investigated across four distinct donor-acceptor polymer architectures. NA–AIMD simulations combined with statistical ensemble analyses were performed to evaluate both the dynamical evolution

and the static values of these parameters, which were subsequently correlated with polaron-pair formation. The results reinforce the critical role of excited-state dipole moments and Coulomb attraction in promoting this process.

The results presented in this chapter were previously published and are reproduced below. Reprinted from F. Bauch et al., Dynamics of Electron–Hole Coulomb Attractive Energy and Dipole Moment of Hot Excitons in Donor–Acceptor Polymers, *The Journal of Physical Chemistry C* **128**, 3525-3532 (2024), https://doi.org/10.1021/acs.jpcc.3c07513.
 The supplementary information can be found on the journal's website.

ACS APPLIED MATERIALS & INTERFACES

www.acsami.org

Research Article

Electronic Properties of Organic Solar Cells Based on CF_3–Functionalized Non-Fullerene Acceptors ⊥

Published as part of ACS Applied Materials & Interfaces special issue "The Celebration of the 90th Birthday of Dr. Alan Heeger".

Fabian Bauch, Xiaojuan Ni, Saied Md Pratik, Sadisha Nanayakkara, Tonghui Wang, Jean-Luc Brédas,* Stefan Schumacher,* and Veaceslav Coropceanu*

Cite This: *ACS Appl. Mater. Interfaces* 2026, 18, 2200–2211

Read Online

ACCESS | Metrics & More | Article Recommendations | Supporting Information

ABSTRACT: Efficient exciton dissociation and charge separation at donor/acceptor interfaces as well as balanced charge transport within each phase are critical for advancing next-generation organic photovoltaics. In this work, we study a trifluoromethyl-substituted nonfullerene acceptor (NFA), Y_2CF_3, whose central-core fluorinated side chain modification induces favorable crystal packing and markedly improves device performance (Cho et al., *J. Am. Chem. Soc.*, **147**, 758 (2025)). Combining molecular dynamics simulations and density functional theory calculations, we comprehensively describe the electronic processes and charge transport in PM6:Y_2CF_3 blends and compare them to the benchmark PM6:Y6 blends. Y_2CF_3 shows a red-shifted singlet local exciton (^{1}LE) energy but nearly unchanged charge transfer (^{1}CT) energies, narrowing the ^{1}LE–^{1}CT gap and enabling rapid conversion as precursor of charge separated states. Enhanced electron transfer rates among Y_2CF_3 molecules arise from strong terminal–terminal interactions as dominantly found in the Y_2CF_3 crystal structure. Thermal fluctuations are found to substantially enhance the hole transport rates in PM6, narrowing the disparity between electron and hole transport. These findings clarify how targeted side chain fluorination at the NFA core can optimize packing, charge separation, transport, and OPV efficiency.

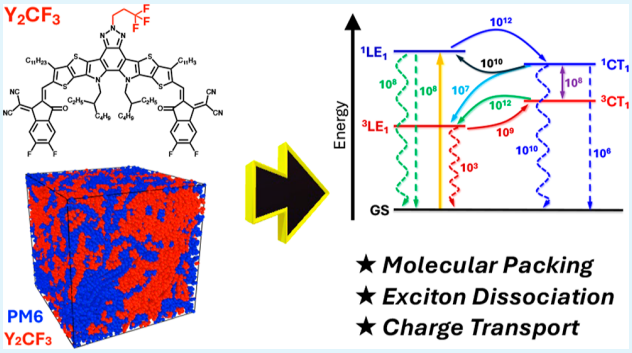

KEYWORDS: *exciton dissociation, charge transfer, organic solar cell, fluorine functionalization, molecular packing*

1. INTRODUCTION

At the heart of organic solar cells lies the photoactive layer, typically composed of a blend of organic semiconductors arranged in a bulk heterojunction (BHJ) architecture pioneered namely by the Heeger group 30 years ago.[1−4] In a BHJ, finely interpenetrating electron-donating (donor) and electron-accepting (acceptor) phases facilitate efficient exciton dissociation and charge transport. These organic photovoltaic (OPV) devices represent a promising class of solar energy technologies due to their potential for low-cost fabrication, mechanical flexibility, lightweight construction, and compatibility with large-area, roll-to-roll processing.[5−9]

The power conversion efficiency (PCE) of OPVs surged in recent years, now reaching values up to 21.0%.[10−12] In addition to the optimization of the BHJ architecture, this remarkable progress is largely attributed to the development of nonfullerene acceptors (NFAs), particularly the Y6 family of materials.[13−16] These NFAs, based on a benzotriazole core unit, exhibit finely tuned optoelectronic properties and favorable molecular interactions with donor polymers, resulting in optimized device morphology and improved charge dynamics.

Despite these advancements, a critical challenge remains: achieving a balanced interplay between donor and acceptor materials. This includes not only aligning their energy levels while maintaining complementary absorption characteristics but also controlling the nanoscale donor/acceptor interface of the BHJ, which plays a decisive role in exciton dissociation, charge separation, and transport.[17−23] Tailoring molecular structures, particularly the design and placement of side chains, has proven highly effective in influencing phase behavior, intermolecular packing, and domain purity, all of which are key to optimizing device performance.[24−27]

Received: September 23, 2025
Revised: December 19, 2025
Accepted: December 24, 2025
Published: December 30, 2025

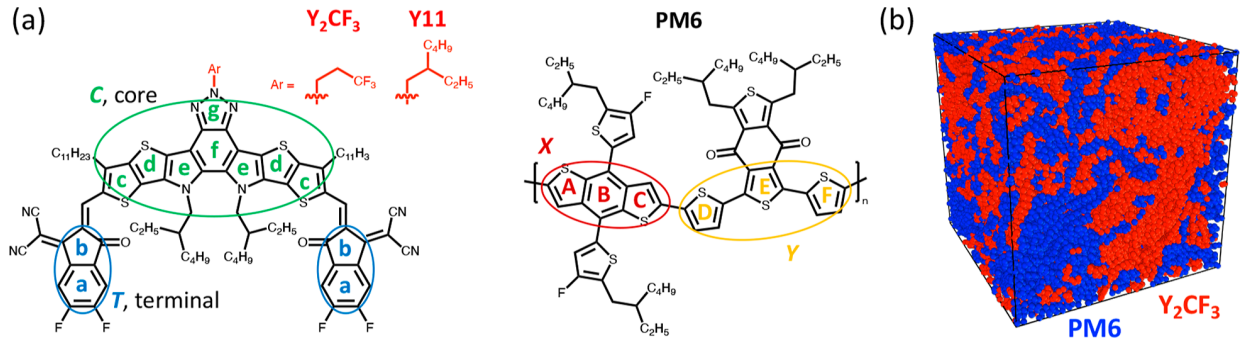

Figure 1. (a) Molecular structure of nonfullerene acceptors (NFAs) Y_2CF_3 and Y11 investigated in this work alongside donor polymer PM6. Terminal and core fragments of the NFA are highlighted in blue and green, respectively. The X and Y fragments of PM6 are labeled in red and orange, respectively. Labels of a to g in the NFA and A to F in PM6 are used in the molecular packing analyses. (b) Illustration of the simulation box for the MD-simulated PM6:Y_2CF_3 blend.

However, even with side chain engineering, a persistent issue in Y6-based and other systems is their strong sensitivity on processing conditions and used solvents, which can hinder reproducibility and limit large-scale fabrication. To address this matter, recent strategies have focused on the incorporation of functional side chains that mediate their interactions with solvent and promote favorable morphology independently of processing conditions. For instance, Zhang et al. reported that attachment of polar oligo(ethylene glycol) (OEG) chains to the central nitrogen of the Y11 benzotriazole core enables stable and high-efficiency blends with the donor polymer PM6 that are insensitive to the processing solvents.[28]

Similarly, Cho et al. showed that the introduction of trifluoromethyl terminated $-(CH_2)_n-CF_3$ side chains to the Y11 central core unit to yield Y_nCF_3 acceptors, has a strong effect on charge generation and charge recombination.[29,30] CF_3-functionalization thus offers another avenue for improving device photovoltaic efficiency and structural stability. In order to shed more light on the effect of CF_3-functionalization, we investigate here the electronic properties of the Y_2CF_3 acceptor film and PM6:Y_2CF_3 BHJ (Figure 1).[30] We analyze the energy landscape, including energetic disorder, optical responses, and electronic couplings for both electron and hole transport. Finally, the results are compared to those derived for the well-studied Y6 and PM6:Y6 systems.

2. METHODS AND COMPUTATIONAL APPROACHES

2.1. Molecular Dynamics Simulations. All-atom molecular dynamics (MD) simulations were conducted for both the Y_2CF_3 neat film and the PM6:Y_2CF_3 blend with the LAMMPS (Large-scale Atomic/Molecular Massively Parallel Simulator) package using the OPLS-AA (Optimized Potentials for Liquid Simulations-All Atom) force field.[31−34] To accurately describe the intramolecular and intermolecular interactions, the generalized OPLS-AA parameters were tuned using long-range-corrected DFT calculations for atomic charges, bond lengths, bond angles, and dihedral angles of PM6 and Y_2CF_3.[28,35,36] Atomic charges were obtained by fitting the electrostatic potential obtained at the ωB97X-D/cc-PVTZ level of theory.[37−39] Bond lengths and angles were taken from the PM6 and Y_2CF_3 molecules optimized at the ωB97X-D/6−31G** level, while keeping the original harmonic force constants. The dihedral potentials between the core and the terminal group were also updated based on the DFT (ωB97X-D/6−31G**) scan of potential energy surfaces. All DFT calculations were performed using the Gaussian 16 package.[40]

The Y_2CF_3 neat films were generated through a multistage isothermal−isobaric ensemble (*NPT*) MD. 200 Y_2CF_3 molecules were randomly packed into a cubic simulation box (172 Å per side, ~0.1 g/cm^3 density) with periodic boundary conditions using the Polymatic code.[41] The system was equilibrated at 650 K and 1 atm for 15 ns. Subsequently, it was cooled from 650 to 300 K at a rate of 20 K/ns, followed by an additional 15 ns of equilibration at 300 K and 1 atm to obtain amorphous films. The final 5 ns of the NPT trajectory were used for analysis. All MD simulations employed the velocity-Verlet integrator with a 2 fs time step, with temperature and pressure controlled via the Nosé-Hoover thermostat and barostat. The van der Waals interactions were considered using a cutoff of 12 Å and long-range electrostatics were computed with the particle-particle-particle-mesh (pppm) method. To minimize bias from initial configurations, three independent simulations were performed. For the PM6:Y_2CF_3 blends, ten PM6 polymer chains (each consisting of 20 repeat units) and 180 Y_2CF_3 molecules were randomly packed in a cubic simulation box (500 Å per side, ~0.007 g/cm^3) with periodic boundary conditions also using the Polymatic code.[41] The same MD simulation protocol as employed for the Y_2CF_3 neat films was applied to the blend system. The densities for the acceptor thin films and PM6:Y_2CF_3 blends were calculated to be 1.17 and 1.16 g/cm^3, respectively, which lies well within the experimentally measured range of 1.128−1.256 g/cm^3 for Y_2CF_3 thin films.[30] For subsequent DFT calculations, monomers and dimers/complexes were extracted from snapshots of the MD simulations using the Pysimm toolkit.[42] Dimer/complex selection was based on the number of "close contacts" between adjacent molecules, defined as interatomic distance less than 4 Å.[35,36]

2.2. Electronic-Structure Calculations. The electronic structures of the monomers and dimer pairs were calculated using long-range corrected DFT and its time-dependent variant under Tamm-Dancoff approximation (TDA-DFT). The DFT calculations were based on the ωB97X-D functional and the 6−31G** basis set. Ground-state DFT calculations were performed using the Gaussian 16 package[40] and the TDA calculations were carried out with the Q-Chem 5.4.0 package.[43] The screening parameter ω was set to 0.01 Bohr^{-1} as determined by a gap-tuning approach applied for the Y_2CF_3 acceptor.[44,45] All calculations included a dielectric environment modeled via the polarizable continuum model (PCM) with a dielectric constant ε = 3.0, which is a reasonable value for organic semiconductors and was extensively used in our previous studies on Y-family of acceptors.[17,35,36,46]

2.3. Transfer Rate Evaluations. To evaluate electron and hole transport rate constants, a large number of Y_2CF_3/Y_2CF_3 and of PM6/PM6 dimers were extracted from MD results. The related electronic couplings (transfer integrals) were computed using a fragment orbital approach, based on the lowest unoccupied molecular orbital (LUMO) and the highest occupied molecular orbital (HOMO) levels of the isolated molecules for electron and hole transport, respectively.[44,47] The transfer rate constants are then obtained within the semiclassical Marcus-Levich-Jortner (MLJ) formalism[17,48,49]

https://doi.org/10.1021/acsami.5c18819
ACS Appl. Mater. Interfaces 2026, 18, 2200−2211

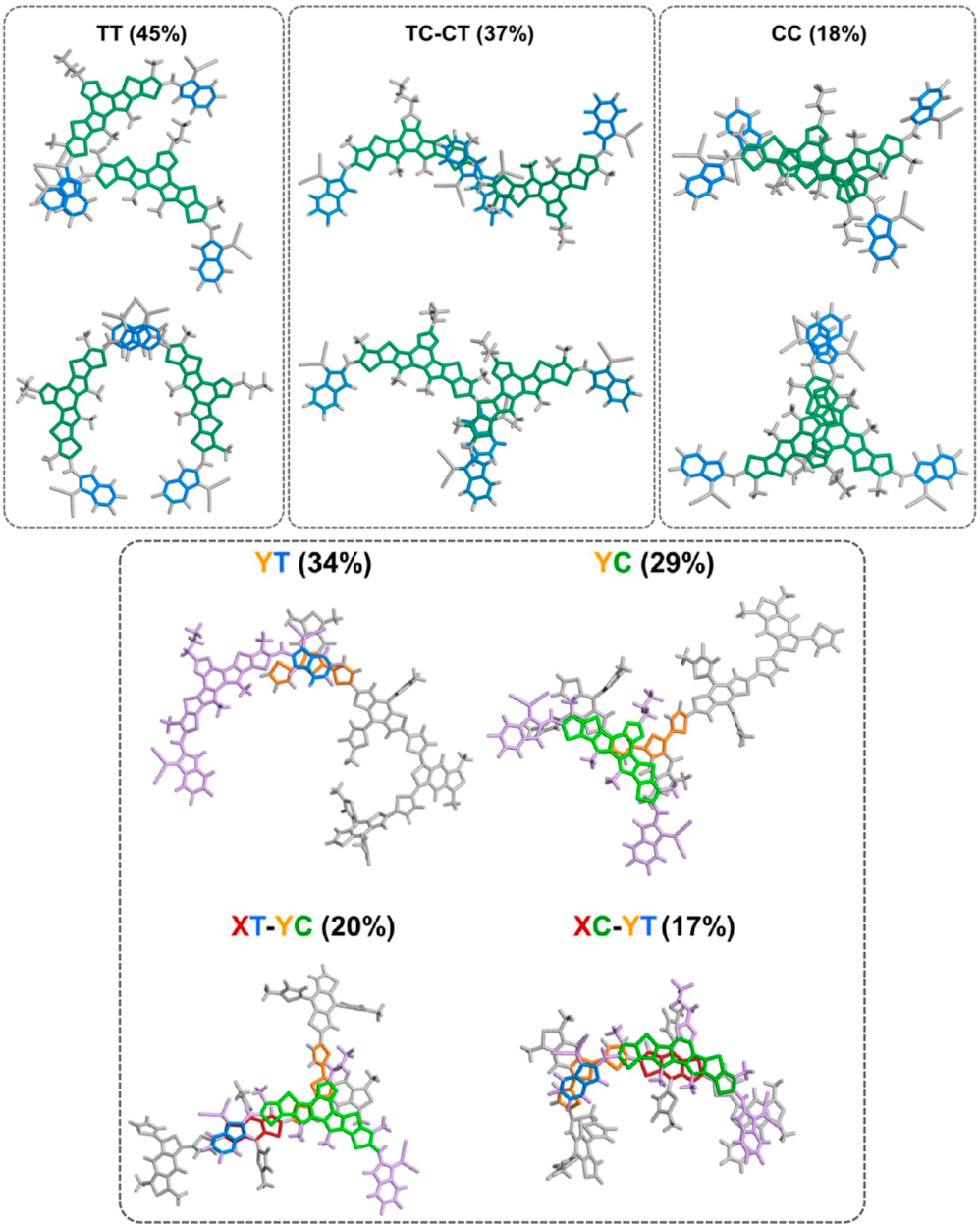

Figure 2. Representative packing configurations commonly observed in the simulated thin-film and blend, extracted from MD simulations. Top: Y_2CF_3 dimer configurations. Bottom: PM6:Y_2CF_3 complex configurations. The Y_2CF_3 and PM6 backbones are shown in purple and gray, respectively. Side chains are omitted for clarity.

$$k = \frac{2\pi}{\hbar} V^2(\mathrm{FCWD}) = \frac{2\pi}{\hbar} V^2 \frac{1}{\sqrt{4\pi\lambda_c k_b T}} \sum_{n=0}^{\infty} \frac{e^{-S_{qm}} S_{qm}^n}{n!} e^{-(\Delta E + \lambda_c + n\hbar\omega_{qm})^2/4\lambda_c k_b T} \quad (1)$$

Here, (FCWD) denotes the Franck−Condon-weighted density of states; V, the electronic coupling; λ_c, the classical reorganization energy from low-frequency modes; S_{qm}, the Huang−Rhys factor; and ω_{qm}, the reorganization energy associated with high-frequency modes, with $\lambda_{qm} = \hbar\omega_{qm}S_{qm}$. T is the temperature set to 300 K (room temperature); k_b and $\hbar$ denote the Boltzmann and reduced Planck constants, respectively. The nonradiative charge transfer rates in PM6:Y_2CF_3 complexes are also computed via eq 1, where V is evaluated using the generalized Mulliken-Hush (GMH) scheme.[50] For intersystem crossing (singlet−triplet transitions), V corresponds to the spin−orbit coupling. The λ and S_{qm} parameters are provided in Supporting Information Section SC. The nonradiative decay rates from the singlet LE exciton states to the ground state were evaluated withing the nonadiabatic coupling (NAC) model,[51,52] in combination with the thermal vibrational correlation function approach,[53−55] as implemented in the MOMAP package.[56] Radiative recombination rates are determined using the Einstein coefficient relation[36,57]

$$k_r = \frac{f \times E^2 \times f(n)}{1.5} \quad (2)$$

with f the oscillator strength, E the adiabatic emission energy (E_{em}^{ad}, in cm^{-1}), and $f(n) = \frac{n(n^2+2)^2}{9}$, assuming a refractive index of n = 1.4, which is appropriate for organic systems. The nonradiative voltage loss is computed as[58,59]

https://doi.org/10.1021/acsami.5c18819
ACS Appl. Mater. Interfaces 2026, 18, 2200−2211

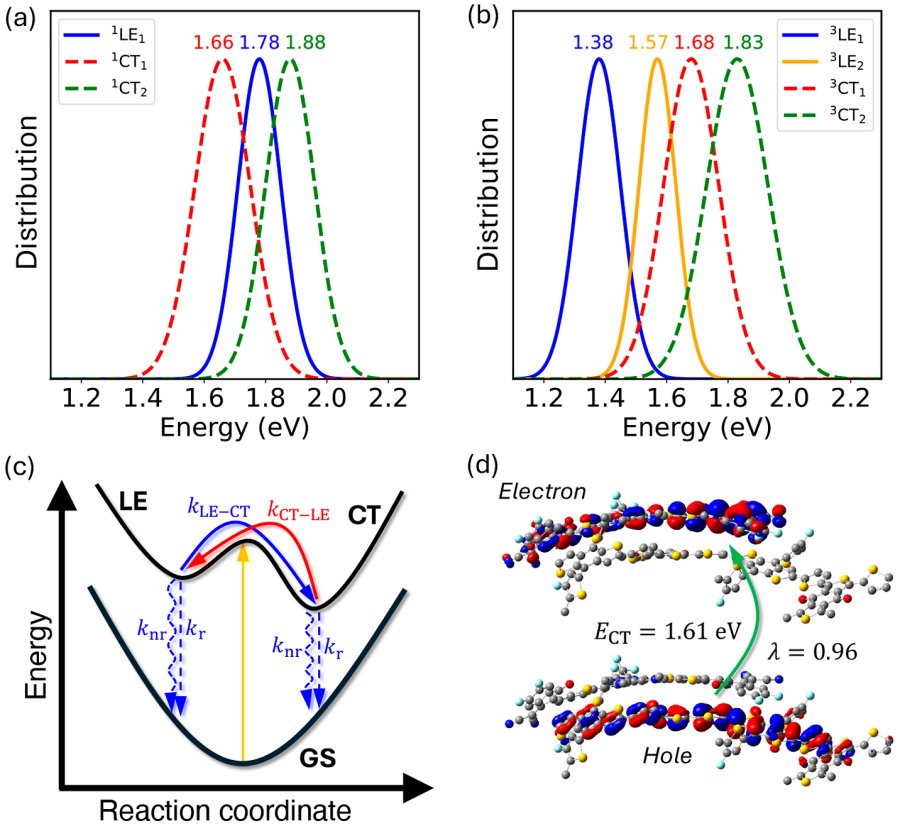

Figure 3. Normalized Gaussian distribution of the lowest (a) singlet and (b) triplet states in the simulated blends. The Gaussian functions are centered on the average excitation energy and broadened by the standard deviation. The average values (eV) are given; see also Table S3. (c) Potential energy surfaces of the ground state (GS) and the excited state, which branches into the local exciton (LE) and charge transfer (CT) states. The relevant transitions analyzed in this work are indicated. (d) Natural transition orbital (NTO) corresponding to the $^1CT_1$ state of a representative PM6-Y_2CF_3 pair extracted from the simulated blend. The vertical excitation energy is given, with λ corresponding to the contribution of the given NTO to the description of the excited state.

$$\Delta V_{OC}^{non\text{-}rad} = \frac{k_B T}{q} \ln\left(\frac{1}{EQE_{EL}}\right) \quad (3)$$

where q is the elementary charge and EQE_{EL}, the external electroluminescence quantum efficiency defined as $EQE_{EL} = \frac{k_r p_e}{k_r p_e + k_{nr}}$, with p_e the photon emission probability. Further computational details are provided in Supporting Information Section SC.

3. RESULTS AND DISCUSSION

3.1. Molecular Packing. Figure 1b illustrates the simulation box of the PM6:Y_2CF_3 blend. The donor and acceptor components are seen to penetrate each other, leading to a subtle nanoscale interface. To assess the impact of molecular packing on excited-state properties, we employed the k-means clustering algorithm[60] to identify distinct packing configurations present in the MD-simulated acceptor films and donor−acceptor blends. The procedure is elucidated in more detail in Supporting Information Section SA. The terminal (T) and core (C) fragments of Y_2CF_3 molecules as well as the electron-rich group (X) and the electron-poor group (Y) of PM6 are illustrated in Figure 1a.

Based on the dimers selected by the close-contact criteria, three primary Y_2CF_3 dimer configurations were identified in the simulated thin film following the fragment definitions (representative packing motifs are shown in Figure 2). The most prevalent configuration involves terminal−terminal (TT) interactions, accounting for approximately 45% of all dimers extracted from the MD trajectories. This TT packing configuration has also been observed in the Y_2CF_3 crystal structure.[30] The remaining dimers exhibit core-terminal (CT-TC) and core-core (CC) interactions, comprising ca. 37% and 18% of the population, respectively. In the PM6/Y_2CF_3 blends, the three Y_2CF_3 dimer packing configurations (TT, CT-TC, and CC) are found to occur with similar proportions of 43%, 37%, and 20%, respectively. These packing configurations are consistent with the results of related structures on Y6-based systems with[61] and without[35] consideration of the steric influence of solvent molecules.

In the simulated blend, four distinct PM6:Y_2CF_3 complex configurations were identified and are illustrated in Figure 2. The dominant interactions are the YT and YC packing patterns, which together account for over 50% of all extracted complexes. The XT-YC and XC-YT configurations contribute 20% and 17%, respectively. The PM6 electron-poor moiety (Y) has unidirectional branched side chains, making it more accessible for interactions than the sterically hindered bidirectional side chains of the PM6 electron-rich unit (X).

To examine the effect of CF_3 fluorinated side chains on packing motifs, we compared the morphology of the Y_2CF_3 film with that of its parent Y11 system (see Supporting Information Section SA, experimentally investigated in, e.g., ref 28). As shown in Tables S2 and S3, Y_2CF_3 and Y11 thin films

https://doi.org/10.1021/acsami.5c18819
ACS Appl. Mater. Interfaces 2026, 18, 2200−2211

exhibit similar packing motifs. In simulated blends, the Y_2CF_3 dimer packing remains essentially unchanged between film and blend, as discussed above. The implication of the geometric configurations formed within the donor/acceptor blend on the electronic states is discussed in the following Section.

3.2. Singlet and Triplet Electronic States. Excited-state calculations were carried out on a subset of 300 randomly selected donor/acceptor (PM6:Y_2CF_3) or acceptor/acceptor (Y_2CF_3:Y_2CF_3) pairs (100 pairs from each of the three simulation boxes) for both blends and thin films. The character (local vs charge-transfer) of an excited state was determined by analyzing the amount of charge transfer upon excitation, as illustrated in Supporting Information Section SB. We note that the set of 300 randomly selected structures reliably captures the structural diversity and yields well-converged statistical analysis of the excited-state properties, as detailed in Supporting Information Section SB. In the PM6:Y_2CF_3 complexes extracted from the simulated blend, the second singlet excited state (S_2) corresponds to a local exciton (LE) state on Y_2CF_3, while the first and third singlet excited states (S_1 and S_3) are identified as charge-transfer (CT) states between PM6 and Y_2CF_3. The lowest two triplet states (T_1 and T_2) are also localized on Y_2CF_3, whereas T_3 and T_4 exhibit CT character.

The average excitation energies of the lowest singlet and triplet states in the blend are shown in Figure 3. The singlet LE state ($^1LE_1$, S_2) has an average excitation energy of 1.78 eV (696 nm); this corresponds to a red-shift of 0.06 eV compared to Y6, previously reported at 1.84 eV (673 nm) using a comparable methodology,[36] as illustrated in Figure S7. This computed red-shift is consistent with experimental observations, which reported 36 and 25 meV red-shifts for Y_2CF_3 compared to Y6 in solution and thin film, respectively.[30] The lowest two singlet CT states ($^1CT_1$ and $^1CT_2$, corresponding to S_1 and S_3) lie 0.12 eV below and 0.10 eV above the $^1LE_1$ state, respectively. Notably, the ^1CT excitation energies remain largely unchanged relative to those in PM6:Y6 blends.[36]

The average energies of the localized triplet states ($^3LE_1$ and $^3LE_2$) are calculated to be 1.38 and 1.57 eV, respectively, exhibiting shifts relative to $^1LE_1$ state similar to those computed for Y6.[36] The $^3CT_1$ state at 1.68 eV lies in close proximity to the $^1CT_1$ state, whereas the $^3CT_2$ state is shifted to lower energies compared to the $^1CT_2$ state.

In the case of the acceptor dimers extracted from the MD-generated thin films, the average excitation energy of the lowest singlet state (S_1) is red-shifted by approximately 110 meV in comparison with the $^1LE_1$ energy and closely matches the $^1CT_1$ state energy in PM6:Y_2CF_3 complexes. The intermolecular excimer-like (EX) character of this state (Supporting Information Section SB) is similar to that observed both theoretically and experimentally in Y6-based systems,[36,62] which is considered to be beneficial for charge separation. In contrast, the lowest triplet states in Y_2CF_3 dimers remain localized on individual molecules.

The energetic distribution of the LE and CT states is governed by dynamic and static disorder. The standard deviations (σ) of the distributions of the ^1CT and $^1LE_1$ states in the PM6:Y_2CF_3 blend are estimated to be around 80−90 and 70 meV, respectively, while the σ values of the ^3CT and ^3LE states are about 90−100 meV and 60−70 meV, respectively. These values are in a similar range or even slightly lower than those estimated for Y6 systems within the same computational framework.[35,36] The disorder of the localized excitation in Y_2CF_3 dimers (extracted from the thin-film structure) is reduced to 50−60 meV, a trend similarly observed for Y6 excimers.[36]

3.3. Exciton Dissociation and Geminate Recombination. To estimate the rate constants for transitions between excited states in PM6:Y_2CF_3 pairs, only pairs in which the lowest excited states could be unambiguously classified as either charge-transfer (CT) or local exciton (LE) states were included in this analysis, as detailed in Supporting Information Section SC. The distributions of electronic couplings for exciton dissociation and geminate recombination processes are shown in Figures S13 and S14, while those of spin−orbit couplings for various processes are given in Figure S15. Rate constants for these processes were then computed using the average coupling values and average excitation energies (Table S4). The computed rate constants are presented in Figure 4; see also Tables S6 and S7.

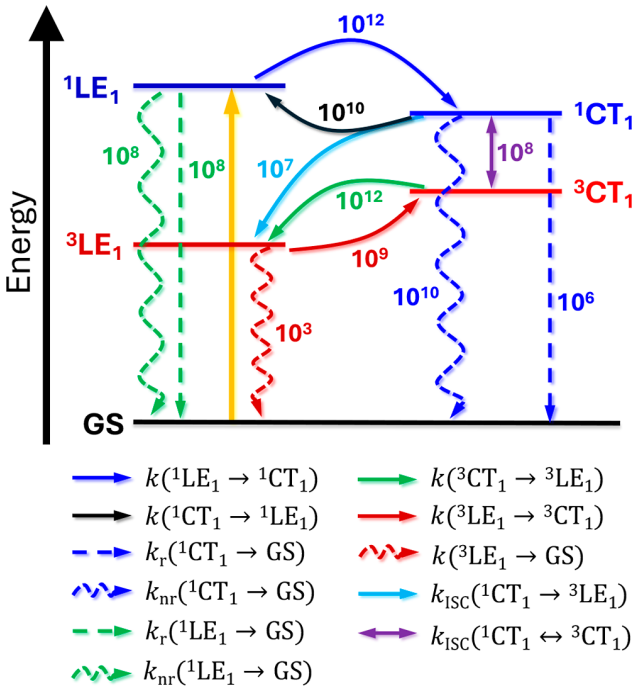

Figure 4. Schematic of key transitions occurring at the donor/acceptor interface. Transitions calculated in this work are shown in color with rates given in s^{-1}.

Upon photon absorption, local excitons can migrate to the PM6:Y_2CF_3 interface; as illustrated in Figure 3c, several pathways are then available: (a) they can recombine to the ground state (GS), either nonradiatively or radiatively; (b) alternatively, they can dissociate into singlet charge-transfer (^1CT) states. These ^1CT states can themselves then either dissociate into charge-separated (CS) states or recombine to the GS or form back singlet local exciton states (^1LE). Another possible pathway is intersystem crossing (ISC), through which the exciton converts into a triplet charge transfer (^3CT) or triplet local excited (^3LE) state. Both $^1CT_1$ and $^1CT_2$ states located below ^1LE were included in the analysis.

Focusing on the dissociation process at the PM6:Y_2CF_3 interface, the rate for forming $^1CT_1$ from $^1LE_1$ is estimated to be ~3.1×10^{12} s^{-1}. The radiative decay rate from the $^1LE_1$ state to the GS is estimated to be $k_r = 3.9 \times 10^8$ s^{-1} when using

https://doi.org/10.1021/acsami.5c18819
ACS Appl. Mater. Interfaces 2026, 18, 2200−2211

the DFT-calculated average excitation energy, and $k_r = 1.8 \times 10^8$ s^{-1} when adopting the experimental optical gap of 1.35 eV.[30] It can be expected that the nonradiative decay rate to the GS is similar to that in Y6, that is on the order of 10^8 s^{-1}.[36] Because this radiative decay is significantly slower than the transition rate leading to population of the $^1CT_1$ state, the dominant processes can be expected to follow the $^1CT_1$ pathway.

As mentioned above, once the $^1CT_1$ state is formed, a possible decay path is for it to recombine to the GS. We evaluate nonradiative rates of about $k_{nr} = 1.1 \times 10^{10}$ s^{-1} and radiative rates of about $k_r = 4.4 \times 10^6$ s^{-1}, both computed with the averaged DFT-calculated $^1CT_1$ energy extracted from the blend. Based on these values and assuming that the nonradiative decay originates predominately in the $^1CT_1$ state, the nonradiative voltage loss $\Delta V_{OC}^{non\text{-}rad}$ is computed to be 202 mV, which is in good agreement with the experimentally reported nonradiative voltage loss of 217 mV.[30]

Another pathway is for the $^1CT_1$ state to undergo back electron transfer to repopulate the $^1LE_1$ state ($^1CT_1 \rightarrow {}^1LE_1$). We evaluate here a high rate of $\sim 2.6 \times 10^{10}$ s^{-1}, which is attributed to the small energy offset of 0.12 eV between the $^1LE_1$ and $^1CT_1$ states. As discussed in the previous Section, the $^1CT_1$ excitation energies of Y_2CF_3 and Y6 are nearly identical, whereas the $^1LE_1$ excitation energy of Y_2CF_3 is reduced relative to that of Y6. This reduction leads to a small energetic offset, thereby facilitating efficient back electron transfer. High back transfer rates are advantageous in mitigating voltage losses. We also evaluated the first step in CT → CS dissociation by computing the rate constant for electron hopping from an interfacial Y_2CF_3 to its neighboring Y_2CF_3 moiety. The calculated rate constants are 2.62×10^{10} s^{-1} and 5.63×10^{11} s^{-1} when electrostatic interactions are included or neglected, respectively. These rates are comparable to or faster than the CT → LE back-transfer rate and exceed the CT recombination rate, as detailed in Figure 4.

Nonradiative decay pathways from the $^1CT_1$ state via intersystem crossing (ISC) to one of the ^3LE and the $^3CT_1$ states were also evaluated. The ISC rate populating the ^3LE states is estimated to be $\sim 1-2 \times 10^7$ s^{-1}. The ISC rate to $^3CT_1$ is higher, around $\sim 2.71 \times 10^8$ s^{-1}, with the reverse process estimated to be of a similar magnitude of around $\sim 1.25 \times 10^8$ s^{-1}. While the $^1CT_1 \rightarrow {}^3LE$ transition involves reorganization energy comparable to its singlet counterpart, the transition to $^3CT_1$ does not involve any significant nuclear reorganization. For this reason, the (FCWD) factor used in computing the $^1CT_1 \rightarrow {}^3CT_1$ rate via eq 1 was estimated as (FCWD) = Γ^{-1}, where Γ, as in our previous work,[36] was estimated by the averaged difference between the energies of the singlet and triplet CT states; this value for PM6:Y_2CF_3 was computed to be about 2×10^{-3} eV.

After the formation of either one of the ^3LE or $^3CT_1$ state, transitions can occur between them, or they can recombine to the GS. The conversion from the $^3CT_1$ state to a ^3LE state occurs at a rate of approximately $10^{11}-10^{12}$ s^{-1}, whereas the reverse process from $^3LE_1$ and $^3LE_2$ to $^3CT_1$ is much slower, around $\sim 10^6$ s^{-1} and $\sim 10^9$ s^{-1}, respectively. We note that in the case of PM6:Y6 the experimental energy difference between $^3CT_1$ and $^3LE_1$ is about 0.1 eV smaller than computed. If a similar correction is made in the present case then the $^3LE_1$ to $^3CT_1$ rate constant is estimated as 5.9×10^9 s^{-1}. The nonradiative decay rate from the $^3LE_1$ state to the GS is estimated to be 2.8×10^3 s^{-1}. These results indicate rapid conversion from ^3CT states to ^3LE states, while the small $^3LE \rightarrow$ GS rate points to minimal geminate recombination from this state. Note that the overall population and lifetime of the ^3LE states are also influenced by nongeminate recombination pathways, which lie beyond the scope of the present methodology. The slow repopulation of the $^3CT_1$ state arises from the fact that the ^3LE states lie significantly lower in energy, as is the case for the $^1LE_1$ state, when compared to Y6.

In summary, the main message is that the exciton dissociation efficiency of the Y_2CF_3-based system closely mirrors that of Y6,[36] exhibiting similarly rapid dynamics. With dissociation rates reaching up to 10^{12} s^{-1}, the system positions itself for highly efficient charge separation at the donor/acceptor interface.

3.4. The Effect of Morphology on the Rate Constants. The morphology at the PM6:Y_2CF_3 interface plays a critical role in the exciton dissociation process. To investigate how different packing arrangements influence this process, the PM6:Y_2CF_3 molecular pairs analyzed in the previous Section were categorized into the observed four packing patterns: YC, YT, XC-YT, and XT-YC. Subsequently, rate constants relevant to exciton dissociation were calculated for each type of pairs and analyzed.

For packing patterns with extensive donor/acceptor contacts, specifically XT-YC and XC-YT, the excitation energies of both singlet and triplet CT states are reduced by approximately 50 meV compared to those with limited interfacial contact (see Figure S18). In the XC-YT configuration, the LE states exhibit a comparable excitation energy reduction, while in the other three configurations the LE state energies show less variation. Generally, a higher CT state energy is beneficial in reducing the nonradiative recombination rate.

To shed further light on the packing effects, the distances between the donor X and Y components and the acceptor C and T components were evaluated and correlated with the dissociation rates (the $^1LE_1 \rightarrow {}^1CT_1$ transition serving as the precursor to charge separation), as described in Supporting Information Section SD. While the rate constants are broadly distributed, their overall distributions remain similar across the relevant distance motifs (XT, XC, YT, and YC). Notably, closer X-T contacts (<10 Å) tend to more consistently yield transition rates exceeding 10^{12} s^{-1}, whereas increasing the X-T separation reduces the proportion of such high rates. No clear trend is observed for the other three configurations. It is also worth noting that most configurations exhibit X-T distances below 10 Å.

Despite these energetic differences, the calculated dissociation rates do not exhibit any consistent or significant trend across the various packing patterns (see Table S8). This suggests that, at least in the present systems, no single packing motif predominantly governs exciton dissociation efficiency. Instead, the presence of well-mixed donor/acceptor interfaces that facilitate sufficient intermolecular contact appears to be the key factor enabling efficient exciton dissociation.

3.5. Electron Transport. Efficient charge transport is critical for solar cell performance, with neat Y_2CF_3 films and polymer/Y_2CF_3 blends showing experimentally higher electron mobility than their Y6 counterparts.[30] Specifically, electron mobility for Y_2CF_3 [Y6] was measured to be 3.49×10^{-4} [3.08×10^{-4}] cm^2 V^{-1} s^{-1} in the polymer/NFA blend and 6.26×10^{-4} [4.46×10^{-4}] cm^2 V^{-1} s^{-1} in the NFA film. To probe the

https://doi.org/10.1021/acsami.5c18819
ACS Appl. Mater. Interfaces 2026, 18, 2200−2211

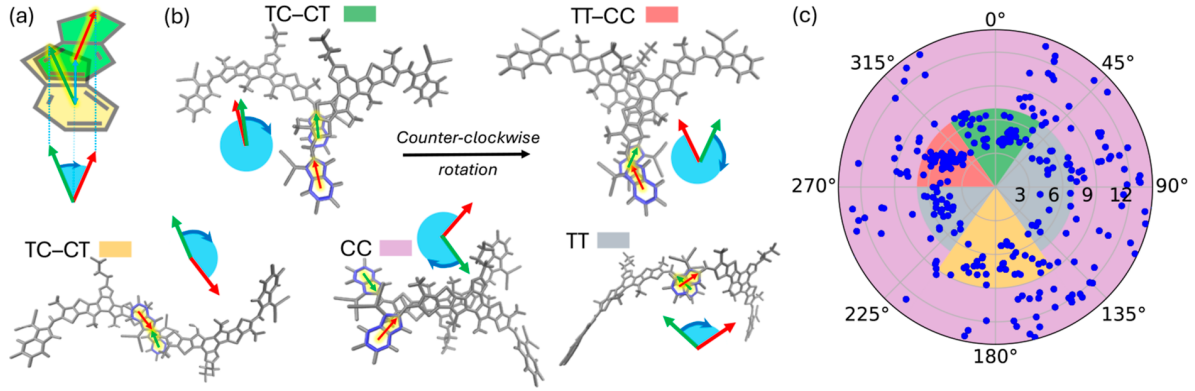

Figure 5. Y_2CF_3 dimer configurations as a function of the orientation of the acceptor terminal units in the simulated thin films. (a) Schematic illustration of the orientation angle (blue angle) and distance (blue arrow) between two acceptor end units. (b) Representative Y_2CF_3 dimer structures corresponding to different configurations, with the projected orientation angles spanned by green and red arrows and illustrated by the blue arc. The relevant terminal groups are highlighted in blue. (c) Distribution of Y_2CF_3 dimers as a function of orientation angle and distance (radial spacing, with concentric rings spaced by 3 Å). The colored sectors correspond to the representative configurations shown in (b).

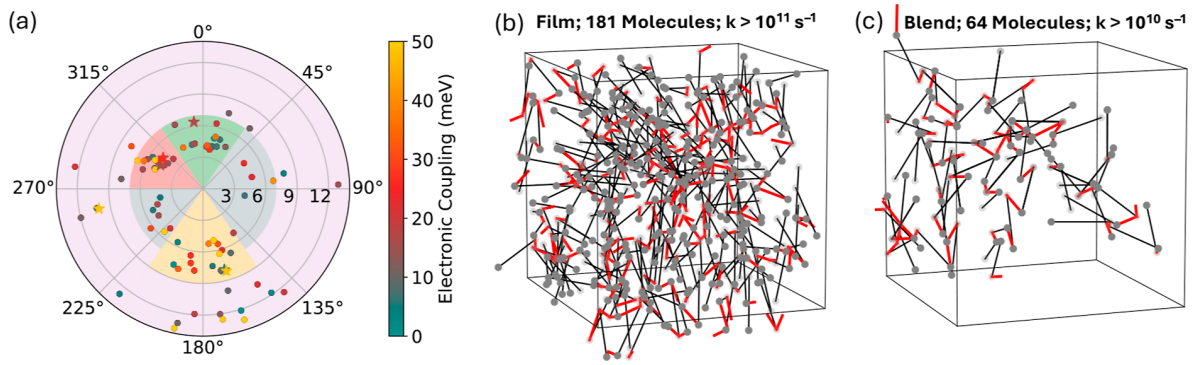

Figure 6. Electron transfer in the simulated films and blend. (a) Electronic coupling values for representative dimers extracted from the Y_2CF_3 films. The stars indicate the representative structures shown in Figure 5. Note that some coupling values exceed 50 meV; however, this upper limit was chosen for illustrative clarity. The sectoral coloring (TC-CT (green and yellow), TT (gray), TT-CC (red), and CC (purple)) is only weakly emphasized to aid visual interpretation. (b) Illustration of Y_2CF_3 connecting networks exhibiting electron transfer rates $>10^{11}$ s^{-1} in the film and (c) $> 10^{10}$ s^{-1} in the blend. Gray dots denote the center of mass of the Y_2CF_3 terminal groups, gray lines represent the Y_2CF_3 backbone, and red lines mark the TT connections between the two molecules. The corresponding cluster sizes are provided.

role of morphology in electron transport, we estimated the intermolecular electronic couplings using a dimer approach and analyzed 300 randomly selected molecular pairs from simulated Y_2CF_3 films, focusing on the distance between benzene rings and the orientation of terminal units. The configurations were evaluated and classified, with representative examples shown in Figure 5b and the full statistical summary presented in Figure 5c, with further details provided in Supporting Information Section SE.

For close terminal contacts (~5 Å), two orientations are favored. A near-parallel one (green sector in Figure 5c) gives a TT configuration that shifts into TC-CT with increasing distance. Another, at ~300° (red sector), produces a CC-TT arrangement that strengthens core−core interactions. The TC-CT state can rotate into TT-CC, enhancing core overlap, while a smaller rotation to ~270° (gray sector) yields TT with weaker core interactions. At antiparallel orientations (yellow sector), terminal distances grow. Here, TC-CT dominates, though antiparallel TT also appears. Between 0°-135°, only a few short contacts (TT) occur, whereas larger separations favor core−core interactions (purple sector).

To assess how dimer configurations affect electron transport, the electronic couplings were calculated for ~75 representative pairs (~25 per simulated box), focusing on the yellow, green, and red sectors. As shown in Figure 6a, the average coupling is 21.7 meV (see Figure S23), consistent with reported values for Y6 dimers.[35,61] While quantitative mobility estimates require large-scale transport-pathways simulations beyond the scope of this study, the high and uniformly distributed electronic couplings suggest efficient transport.

Parallel terminal configurations (green sector) yield relatively lower couplings. For instance, the representative TC-CT pair shows a coupling of ~17 meV. In contrast, the representative antiparallel TC-CT configuration reaches a ~47 meV coupling, reflecting the generally stronger couplings in this sector. As terminals shift toward core-terminal interactions, more cases with couplings exceeding 40 meV appear. Rotated terminals in the red sector, enabling core−core overlap, also give high couplings; for example, a CC configuration reaches couplings of ~26 meV, with some exceeding 40 meV. These findings indicate that both core−core and terminal−core interactions enhance the electronic couplings, which promotes electron transfer, especially in antiparallel or slightly rotated geometries.

Due to the minimal overlap between the energy distributions of the LUMO and LUMO+1 levels and their substantial

https://doi.org/10.1021/acsami.5c18819
ACS Appl. Mater. Interfaces 2026, 18, 2200−2211

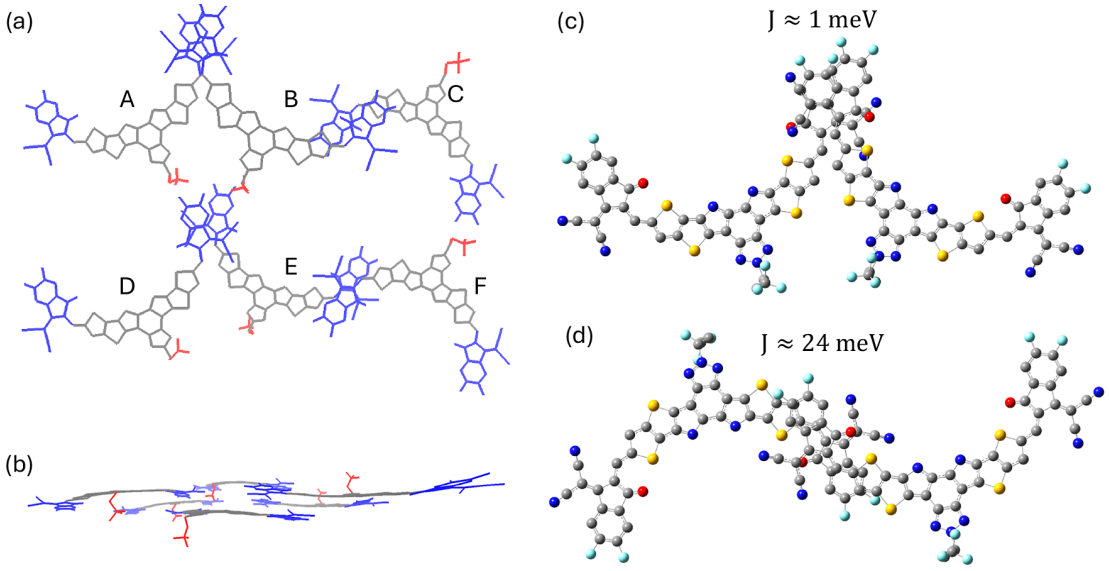

Figure 7. Illustrations of representative pairs from the Y_2CF_3 crystal structure, shown in top view (a) and side view (b), to compare the electronic couplings for electron transfer with the simulated thin films. The crystal structure is reproduced from ref 30 Copyright 2025 American Chemical Society. The terminal group is colored in blue, the backbone gray, and the central core's CF_3 side chain red. The molecule labels are used to identify the pairs. The electronic couplings (transfer integrals *J*) for electron transfer between the interacting pairs are provided in Table S9. Pairs A-B (c) and B-C (d) from the crystal structure are illustrated, along with their respective *J* values for electron transfer. Alkyl side chains and hydrogen atoms are omitted for clarity.

average energy gap of ∼220 meV, the thermal population of the higher-lying LUMO+1 state is unlikely to be significant (see Figure S22). Therefore, electron transport can be expected to proceed essentially via the LUMO levels. Rate constants were calculated for each individual pair, resulting in an average electron transfer rate of approximately $\sim 1.8 \times 10^{13}$ s^{-1}, under the assumption that the individual electron transfer steps are exergonic, which is consistent with previously reported values for Y6 and related NFAs.[63]

To highlight the efficient charge transport in Y_2CF_3, the networks formed among connected Y_2CF_3 molecules are depicted in Figure 6b,c for the simulated film and blend, respectively, as well as in Figure S25. A detailed description of the procedure is provided in Supporting Information Section SE. In the simulated film, the largest cluster of connected molecules comprises 199 out of 200 Y_2CF_3 molecules, with 181 of them forming the largest cluster that shows electron transfer rates exceeding 10^{11} s^{-1} for each linked pair. In the simulated blend, the largest connected Y_2CF_3 cluster contains 69 out of 180 molecules, while the largest cluster exhibiting electron transfer rates greater than 10^{10} s^{-1} for each linked pair consists of 64 molecules. These findings demonstrate the presence of highly efficient charge-transport pathways within the acceptor domains. However, the cluster size may be influenced by the donor material, potentially reducing the extent of the connecting network.

We also investigated the electron transport characteristics using the reported crystal structure of Y_2CF_3,[30] depicted in Figure 7a,b. The CF_3 side chains of the core interact with the terminal fluorine atoms of adjacent molecules, leading to dominant intermolecular terminal−terminal overlap and largely excluding interactions among conjugated cores.

The key molecular pair configurations relevant for electron transport are A-B (equivalent to D-E) and B-C (equivalent to E-F), which are both expected to dominate the charge transport pathways.[30] However, as shown in Figure 7c,d, the electronic couplings (transfer integrals) for the A-B configuration are relatively low (∼1 meV), whereas the B-C configurations exhibit much higher couplings of ∼24 meV. Other configurations involving CF_3 side chain-terminal interactions exhibit negligible electronic couplings (∼0 meV), as detailed in Supporting Information Section SF.

As elucidated for the electronic couplings in the simulated films, these findings suggest that although terminal−terminal interactions are structurally prominent in the A-B configuration of the crystal structure, their spatial arrangement deviates from optimal orbital overlap with the conjugated cores, resulting in poor electronic couplings.

3.6. Hole Transport. Achieving balanced electron and hole transport is critical for optimizing the performance of OPV devices. Experimentally, blends incorporating Y_2CF_3 exhibit enhanced hole mobilities compared to those using Y6 (2.72×10^{-4} vs 2.03×10^{-4} cm^2 V^{-1} s^{-1}), resulting in slightly more favorable electron-to-hole mobility ratios.[30] To investigate the microscopic origin of this improvement, we computed the electronic couplings (*J*) for hole transport across 150 randomly selected PM6 dimers extracted from the simulated blend morphology.

Assuming that hole transport occurs predominantly through the HOMO, we find that the average coupling between PM6 dimers is relatively weak, with a mean value of approximately 10.5 meV. The coupling distribution follows an exponential decay, with ∼60% of dimers exhibiting values below 10 meV. Using these couplings, the hole transfer rates for each dimer were calculated individually and averaged, yielding a mean rate of $\sim 3.2 \times 10^{12}$ s^{-1}, which is approximately 1 order of magnitude lower than the corresponding electron transfer rate for Y_2CF_3.

To gain deeper insight into hole transport within PM6 in the blend, we evaluated the planarity of the polymer backbone by analyzing its torsion angles, as described in Supporting Information Section SG. As shown in Figure S33, the hole

https://doi.org/10.1021/acsami.5c18819
ACS Appl. Mater. Interfaces 2026, 18, 2200−2211

transfer rate increases with backbone planarity, especially with planarity of the acceptor moieties. This seemingly counterintuitive behavior can be rationalized by noticing that electronic coupling for holes along polymer chains has a superexchanger character, i.e., the effective transfer integral is due to the hybridization of the donor orbitals with the bridge acceptor orbitals; this hybridization becomes weaker in cases of strongly twisted acceptor conformations.

4. CONCLUSION

In the present study, we employed all-atom molecular dynamics (MD) simulations in conjunction with density functional theory (DFT) calculations to explore the packing structure, electronic characteristics, exciton dissociation, and charge transport properties of a CF_3-substituted nonfullerene acceptor, Y_2CF_3, blended with the donor polymer PM6.

Our results indicate that while the local exciton (LE) of Y_2CF_3 is red-shifted relative to Y6, the excitation energy of the charge transfer (CT) states at the interface remains largely unchanged. This results in a more favorable energy separation between the LE and CT states, promoting efficient back electron transfer into the ^{1}LE state. Apart from this difference, exciton dissociation pathways are largely comparable to those observed with Y6.

In the Y_2CF_3 domain, electron transport benefits from increased electronic couplings due to both terminal−terminal interactions and overlap with the core, leading to transfer rates around 1×10^{13} s^{-1}. These interactions are similarly observed in the crystal structure, which is significantly influenced by the CF_3-terminated side chains.[30] Hole transport within the PM6 domain is somewhat slower, with an estimated rate of approximately 3×10^{12} s^{-1}.

As we mentioned above, Zhang et al. have shown that attaching polar OEG chains to the central nitrogen of the benzotriazole core of Y11 significantly increases the side chain-solvent interactions, which leads to high-efficiency PM6:acceptor blends insensitive to the processing solvent.[28] CF_3-based acceptors also show good solubility in many common solvents, which motivates us to investigate as a next step the interactions between $-(CH_2)_n-CF_3$ side chains and solvents; these studies will be reported elsewhere.

Overall, this work provides a comprehensive analysis of the optoelectronic properties of Y_2CF_3, a promising NFA currently under active experimental investigation for its potential to surpass the performance of Y6.

■ ASSOCIATED CONTENT

Supporting Information

The Supporting Information is available free of charge at https://pubs.acs.org/doi/10.1021/acsami.5c18819.

JOURNAL-LINK. Computational details for the packing configuration analysis along with corresponding results; characterization of electronic states in the simulated blends and films; computational details and results for evaluating (non)radiative transfer rate constants and intersystem crossing rates; computational details and results for evaluating excited-state electronic couplings, spin−orbit couplings, and oscillator strengths; parameters for reorganization energies and Huang−Rhys factors; computational details and results for electron transport in Y_2CF_3 dimers; electronic coupling results for electron transport within the Y_2CF_3 crystal structure; and computational details and results for hole transport between PM6 dimers (PDF)

■ AUTHOR INFORMATION

Corresponding Authors

Jean-Luc Brédas − *Department of Chemistry and Biochemistry, The University of Arizona, Tucson, Arizona 85721-0041, United States;* orcid.org/0000-0001-7278-4471; Email: jlbredas@arizona.edu

Stefan Schumacher − *Department of Physics and Center for Optoelectronics and Photonics Paderborn (CeOPP), Paderborn University, Paderborn 33098, Germany; Wyant College of Optical Sciences, The University of Arizona, Tucson, Arizona 85721, United States;* Email: stefan.schumacher@upb.de

Veaceslav Coropceanu − *Department of Chemistry and Biochemistry, The University of Arizona, Tucson, Arizona 85721-0041, United States;* orcid.org/0000-0003-1693-2315; Email: coropceanu@arizona.edu

Authors

Fabian Bauch − *Department of Physics and Center for Optoelectronics and Photonics Paderborn (CeOPP), Paderborn University, Paderborn 33098, Germany; Department of Chemistry and Biochemistry, The University of Arizona, Tucson, Arizona 85721-0041, United States*

Xiaojuan Ni − *Department of Chemistry and Biochemistry, The University of Arizona, Tucson, Arizona 85721-0041, United States;* orcid.org/0000-0002-5845-7404

Saied Md Pratik − *Department of Chemistry and Biochemistry, The University of Arizona, Tucson, Arizona 85721-0041, United States;* orcid.org/0000-0002-4900-4323

Sadisha Nanayakkara − *Department of Chemistry and Biochemistry, The University of Arizona, Tucson, Arizona 85721-0041, United States;* orcid.org/0000-0002-1316-1888

Tonghui Wang − *Key Laboratory of Automobile Materials, Ministry of Education, and School of Materials Science and Engineering, Jilin University, Changchun 130022, China*

Complete contact information is available at: https://pubs.acs.org/10.1021/acsami.5c18819

Notes

The authors declare no competing financial interest.

■ ACKNOWLEDGMENTS

The Paderborn team gratefully acknowledge the computing time provided to them on the high-performance computers Noctua 2[64] at the NHR Center PC2. These are funded by the Federal Ministry of Education and Research and the state governments participating on the basis of the resolutions of the GWK for the national highperformance computing at universities (www.nhr-verein.de/unsere-partner). Part of the computations for this research were performed using computing resources under project hpc-prf-hdpadi. The Arizona team thank the Office of Naval Research, Awards No. N00014-20-1−2110 and N00014-24-1−2114, and the College of Science of the University of Arizona for funding of this work; they acknowledge the Research Data Center at The University of Arizona for providing high-performance computing resources. The computational work was also supported in

part by a grant of computer time from the DOD High Performance Computing Modernization Program.

DEDICATION

⊥This article is dedicated to Professor Alan Heeger at the occasion of his 90th Birthday. We wish Alan the very best and thank him for his pioneering work that opened the field of organic electronics, his mentorship that inspired generations of scientists on all continents, and his friendship.

REFERENCES

(1) Yu, G.; Heeger, A. J. Charge separation and photovoltaic conversion in polymer composites with internal donor/acceptor heterojunctions. *J. Appl. Phys.* **1995**, *78*, 4510−4515.
(2) Yu, G.; Gao, J.; Hummelen, J. C.; Wudl, F.; Heeger, A. J. Polymer photovoltaic cells: Enhanced efficiencies via a network of internal donor-acceptor heterojunctions. *Science* **1995**, *270*, 1789−1791.
(3) Halls, J. J. M.; Walsh, C. A.; Greenham, N. C.; Marseglia, E. A.; Friend, R. H.; Moratti, S. C.; Holmes, A. B. Efficient photodiodes from interpenetrating polymer networks. *Nature* **1995**, *376*, 498−500.
(4) Wei, X.; Vardeny, Z. V.; Sariciftci, N. S.; Heeger, A. J. Absorption-detected magnetic-resonance studies of photoexcitations in conjugated-polymer/C_{60} composites. *Phys. Rev. B* **1996**, *53*, 2187−2190.
(5) Brabec, C. J.; Sariciftci, N. S.; Hummelen, J. C. Plastic solar cells. *Adv. Funct. Mater.* **2001**, *11*, 15−26.
(6) Brédas, J.-L.; Norton, J. E.; Cornil, J.; Coropceanu, V. Molecular understanding of organic solar cells: The challenges. *Acc. Chem. Res.* **2009**, *42*, 1691−1699.
(7) Clarke, T. M.; Durrant, J. R. Charge photogeneration in organic solar cells. *Chem. Rev.* **2010**, *110*, 6736−6767.
(8) Hou, J.; Inganäs, O.; Friend, R. H.; Gao, F. Organic solar cells based on non-fullerene acceptors. *Nat. Mater.* **2018**, *17*, 119−128.
(9) Yi, J.; Zhang, G.; Yu, H.; Yan, H. Advantages, challenges and molecular design of different material types used in organic solar cells. *Nat. Rev. Mater.* **2024**, *9*, 46−62.
(10) Zhu, L.; Zhang, M.; Zhou, G.; Wang, Z.; Zhong, W.; Zhuang, J.; Zhou, Z.; Gao, X.; Kan, L.; Hao, B.; Han, F.; Zeng, R.; Xue, X.; Xu, S.; Jing, H.; Xiao, B.; Zhu, H.; Zhang, Y.; Liu, F. Achieving 20.8% organic solar cells via additive-assisted layer-by-layer fabrication with bulk p-i-n structure and improved optical management. *Joule* **2024**, *8*, 3153−3168.
(11) Jiang, Y.; Liu, K.; Liu, F.; Ran, G.; Wang, M.; Zhang, T.; Xu, R.; Liu, H.; Zhang, W.; Wei, Z.; Cui, Y.; Lu, X.; Hou, J.; Zhu, X. 20.6% efficiency organic solar cells enabled by incorporating a lower bandgap guest nonfullerene acceptor without open-circuit voltage loss. *Adv. Mater.* **2025**, *37*, 2500282.
(12) Fu, J.; Li, H.; Liu, H.; Huang, P.; Chen, H.; Fong, P. W. K.; Dela Peña, T. A.; Li, M.; Lu, X.; Cheng, P.; Xiao, Z.; Lu, S.; Li, G. Two-step crystallization modulated through acenaphthene enabling 21% binary organic solar cells and 83.2% fill factor. *Nat. Energy* **2025**, *10*, 1251−1261.
(13) Yuan, J.; Zhang, Y.; Zhou, L.; Zhang, G.; Yip, H.-L.; Lau, T.-K.; Lu, X.; Zhu, C.; Peng, H.; Johnson, P. A.; Leclerc, M.; Cao, Y.; Ulanski, J.; Li, Y.; Zou, Y. Single-junction organic solar cell with over 15% efficiency using fused-ring Acceptor with electron-deficient core. *Joule* **2019**, *3*, 1140−1151.
(14) Yuan, J.; Huang, T.; Cheng, P.; Zou, Y.; Zhang, H.; Yang, J. L.; Chang, S.-Y.; Zhang, Z.; Huang, W.; Wang, R.; Meng, D.; Gao, F.; Yang, Y. Enabling low voltage losses and high photocurrent in fullerene-free organic photovoltaics. *Nat. Commun.* **2019**, *10*, 570.
(15) Shoaee, S.; Luong, H. M.; Song, J.; Zou, Y.; Nguyen, T.-Q.; Neher, D. What we have learnt from PM6:Y6. *Adv. Mater.* **2024**, *36*, 2302005.
(16) Chen, C.; Wang, L.; Xia, W.; Qiu, K.; Guo, C.; Gan, Z.; Zhou, J.; Sun, Y.; Liu, D.; Li, W.; Wang, T. Molecular interaction induced dual fibrils towards organic solar cells with certified efficiency over 20%. *Nat. Commun.* **2024**, *15*, 6865.
(17) Coropceanu, V.; Chen, X.-K.; Wang, T.; Zheng, Z.; Brédas, J.-L. Charge-transfer electronic states in organic solar cells. *Nat. Rev. Mater.* **2019**, *4*, 689−707.
(18) Zhu, L.; Zhang, M.; Xu, J.; Li, C.; Yan, J.; Zhou, G.; Zhong, W.; Hao, T.; Song, J.; Xue, X.; Zhou, Z.; Zeng, R.; Zhu, H.; Chen, C.-C.; MacKenzie, R. C. I.; Zou, Y.; Nelson, J.; Zhang, Y.; Sun, Y.; Liu, F. Single-junction organic solar cells with over 19% efficiency enabled by a refined double-fibril network morphology. *Nat. Mater.* **2022**, *21*, 656−663.
(19) Liu, W.; Liu, Q.; Xiang, C.; Zhou, H.; Jiang, L.; Zou, Y. Theoretical exploration of optoelectronic performance of PM6:Y6 series-based organic solar cells. *Surf. Interfac* **2021**, *26*, 101385.
(20) Xiang, C.; Zhao, Q.; Liu, W.; Cao, J.; Zou, Y.; Zhou, H. Theoretical exploration of molecular packing and the charge transfer mechanism of organic solar cells based on PM6:Y6. *J. Mater. Chem. A* **2022**, *10*, 25611−25619.
(21) Zhang, G.; Wu, Q.; Duan, Y.; Liu, W.; Jeong, S. Y.; Woo, H. Y.; Zhao, Q.; Zhou, H. Achieving 19.4% Efficiency Polymer Solar Cells by Reducing Backbone Disorder in Donor Terpolymers. *Adv. Funct. Mater.* **2024**, *34*, 2408678.
(22) Liu, Q.; Xiang, C.; Wu, Q.; Zhou, Z.; Zou, Y.; Liu, W. Theoretical exploration of the molecular stacking and charge transfer mechanism of PBQx:Y6 OSCs. *Surf. Interfac* **2024**, *44*, 103767.
(23) Wu, Q.; Xiang, C.; Zhang, G.; Zou, Y.; Liu, W. Multiscale computational analysis of the effect of end group modification on PM6:BTP-x OSCs performance. *J. Mater. Chem. C* **2024**, *12*, 13311−13324.
(24) Zhou, Y.; Kurosawa, T.; Ma, W.; Guo, Y.; Fang, L.; Vandewal, K.; Diao, Y.; Wang, C.; Yan, Q.; Reinspach, J.; Mei, J.; Appleton, A. L.; Koleilat, G. I.; Gao, Y.; Mannsfeld, S. C. B.; Salleo, A.; Ade, H.; Zhao, D.; Bao, Z. High performance all-polymer solar cell via polymer side-chain engineering. *Adv. Mater.* **2014**, *26*, 3767−3772.
(25) Lu, L.; Zheng, T.; Wu, Q.; Schneider, A. M.; Zhao, D.; Yu, L. Recent advances in bulk heterojunction polymer solar cells. *Chem. Rev.* **2015**, *115*, 12666−12731.
(26) Zhang, G.; Lin, F. R.; Qi, F.; Heumüller, T.; Distler, A.; Egelhaaf, H.-J.; Li, N.; Chow, P. C. Y.; Brabec, C. J.; Jen, A. K.-Y.; Yip, H.-L. Renewed prospects for organic photovoltaics. *Chem. Rev.* **2022**, *122*, 14180−14274.
(27) Luo, Z.; Xu, T.; Zhang, C.; Yang, C. Side-chain engineering of nonfullerene small-molecule acceptors for organic solar cells. *Energy Environ. Sci.* **2023**, *16*, 2732−2758.
(28) Zhang, R.; Chen, H.; Wang, T.; Kobera, L.; He, L.; Huang, Y.; Ding, J.; Zhang, B.; Khasbaatar, A.; Nanayakkara, S.; Zheng, J.; Chen, W.; Diao, Y.; Abbrent, S.; Brus, J.; Coffey, A. H.; Zhu, C.; Liu, H.; Lu, X.; Jiang, Q.; Coropceanu, V.; Brédas, J.-L.; Li, Y.; Li, Y.; Gao, F. Equally high efficiencies of organic solar cells processed from different solvents reveal key factors for morphology control. *Nat. Energy* **2025**, *10*, 124−134.
(29) Cho, Y.; Sun, Z.; Lee, K. M.; Zeng, G.; Jeong, S.; Yang, S.; Lee, J. E.; Lee, B.; Kang, S.-H.; Li, Y.; Li, Y.; Kwak, S. K.; Yang, C. CF_3-terminated side chain enables efficiencies surpassing 18.2% and 16.1% in small- and large-scale manufacturing of organic solar cells. *ACS Energy Lett.* **2023**, *8*, 96−106.
(30) Cho, Y.; Sun, Z.; Li, G.; Zhang, D.; Yang, S.; Marks, T. J.; Yang, C.; Facchetti, A. CF_3-functionalized side chains in nonfullerene acceptors promote electrostatic interactions for highly efficient organic solar cells. *J. Am. Chem. Soc.* **2025**, *147*, 758−769.
(31) Jorgensen, W. L.; Tirado-Rives, J. The OPLS [optimized potentials for liquid simulations] potential functions for proteins, energy minimizations for crystals of cyclic peptides and crambin. *J. Am. Chem. Soc.* **1988**, *110*, 1657−1666.
(32) Plimpton, S. Fast parallel algorithms for short-range molecular dynamics. *J. Comput. Phys.* **1995**, *117*, 1−19.
(33) Dahlgren, M. K.; Schyman, P.; Tirado-Rives, J.; Jorgensen, W. L. Characterization of biaryl torsional energetics and its treatment in OPLS all-atom force fields. *J. Chem. Inf. Model.* **2013**, *53*, 1191−1199.

https://doi.org/10.1021/acsami.5c18819
ACS Appl. Mater. Interfaces 2026, 18, 2200−2211

(34) Thompson, A. P.; Aktulga, H. M.; Berger, R.; Bolintineanu, D. S.; Brown, W. M.; Crozier, P. S.; in 't Veld, P. J.; Kohlmeyer, A.; Moore, S. G.; Nguyen, T. D.; Shan, R.; Stevens, M. J.; Tranchida, J.; Trott, C.; Plimpton, S. J. LAMMPS − a flexible simulation tool for particle-based materials modeling at the atomic, meso, and continuum scales. *Comput. Phys. Commun.* **2022**, *271*, 108171.
(35) Kupgan, G.; Chen, X.; Brédas, J. Molecular packing of non-fullerene acceptors for organic solar cells: Distinctive local morphology in Y6 vs. ITIC derivatives. *Mater. Today Adv* **2021**, *11*, 100154.
(36) Pratik, S. M.; Kupgan, G.; Brédas, J.-L.; Coropceanu, V. Analysis of the charge generation and recombination processes in the PM6:Y6 organic solar cell. *Energy Environ. Sci.* **2025**, *18*, 841−852.
(37) Weigend, F.; Ahlrichs, R. Balanced basis sets of split valence, triple zeta valence and quadruple zeta valence quality for H to Rn: Design and assessment of accuracy. *Phys. Chem. Chem. Phys.* **2005**, *7*, 3297−3305.
(38) Chai, J.-D.; Head-Gordon, M. Systematic optimization of long-range corrected hybrid density functionals. *J. Chem. Phys.* **2008**, *128*, 084106.
(39) Chai, J.-D.; Head-Gordon, M. Long-range corrected hybrid density functionals with damped atom−atom dispersion corrections. *Phys. Chem. Chem. Phys.* **2008**, *10*, 6615−6620.
(40) Frisch, M. J.; Trucks, G. W.; Schlegel, H. B.; Scuseria, G. E.; Robb, M. A.; Cheeseman, J. R.; Scalmani, G.; Barone, V.; Petersson, G. A.; Nakatsuji, H.; Li, X.; Caricato, M.; Marenich, A. V.; Bloino, J.; Janesko, B. G.; Gomperts, R.; Mennucci, B.; Hratchian, H. P.; Ortiz, J. V.; Izmaylov, A. F.; Sonnenberg, J. L.; Williams-Young, D.; Ding, F.; Lipparini, F.; Egidi, F.; Goings, J.; Peng, B.; Petrone, A.; Henderson, T.; Ranasinghe, D.; Zakrzewski, V. G.; Gao, J.; Rega, N.; Zheng, G.; Liang, W.; Hada, M.; Ehara, M.; Toyota, K.; Fukuda, R.; Hasegawa, J.; Ishida, M.; Nakajima, T.; Honda, Y.; Kitao, O.; Nakai, H.; Vreven, T.; Throssell, K.; Montgomery, J. A., Jr.; Peralta, J. E.; Ogliaro, F.; Bearpark, M. J.; Heyd, J. J., et al. *Gaussian 16*; Revision C.01; Gaussian Inc.: Wallingford CT., 2016.
(41) Abbott, L. J.; Hart, K. E.; Colina, C. M. Polymatic: a generalized simulated polymerization algorithm for amorphous polymers. *Theor. Chem. Acc.* **2013**, *132*, 1334.
(42) Fortunato, M. E.; Colina, C. M. pysimm: A python package for simulation of molecular systems. *SoftwareX* **2017**, *6*, 7−12.
(43) Epifanovsky, E.; Gilbert, A. T. B.; Feng, X.; Lee, J.; Mao, Y.; Mardirossian, N.; Pokhilko, P.; White, A. F.; Coons, M. P.; Dempwolff, A. L.; Gan, Z.; Hait, D.; Horn, P. R.; Jacobson, L. D.; Kaliman, I.; Kussmann, J.; Lange, A. W.; Lao, K. U.; Levine, D. S.; Liu, J.; McKenzie, S. C.; Morrison, A. F.; Nanda, K. D.; Plasser, F.; Rehn, D. R.; Vidal, M. L.; You, Z.-Q.; Zhu, Y.; Alam, B.; Albrecht, B. J.; Aldossary, A.; Alguire, E.; Andersen, J. H.; Athavale, V.; Barton, D.; Begam, K.; Behn, A.; Bellonzi, N.; Bernard, Y. A.; Berquist, E. J.; Burton, H. G. A.; Carreras, A.; Carter-Fenk, K.; Chakraborty, R.; Chien, A. D.; Closser, K. D.; Cofer-Shabica, V.; Dasgupta, S.; de Wergifosse, M.; Deng, J.; Diedenhofen, M.; Do, H.; Ehlert, S.; Fang, P.-T.; Fatehi, S.; Feng, Q.; Friedhoff, T.; Gayvert, J.; Ge, Q.; Gidofalvi, G.; Goldey, M.; Gomes, J.; González-Espinoza, C. E.; Gulania, S.; Gunina, A. O.; Hanson-Heine, M. W. D.; Harbach, P. H. P.; Hauser, A.; Herbst, M. F.; Hernández Vera, M.; Hodecker, M.; Holden, Z. C.; Houck, S.; Huang, X.; Hui, K.; Huynh, B. C.; Ivanov, M.; JászJi, Á.H.; Jiang, H.; Kaduk, B.; Kähler, S.; Khistyaev, K.; Kim, J.; Kis, G.; Klunzinger, P.; Koczor-Benda, Z.; Koh, J. H.; Kosenkov, D.; Koulias, L.; Kowalczyk, T.; Krauter, C. M.; Kue, K.; Kunitsa, A.; Kus, T.; Ladjánszki, I.; Landau, A.; Lawler, K. V.; Lefrancois, D.; Lehtola, S.; Li, R. R.; Li, Y. P.; Liang, J.; Liebenthal, M.; Lin, H. H.; Lin, Y. S.; Liu, F.; Liu, K. Y.; Loipersberger, M.; Luenser, A.; Manjanath, A.; Manohar, P.; Mansoor, E.; Manzer, S. F.; Mao, S. P.; Marenich, A. V.; Markovich, T.; Mason, S.; Maurer, S. A.; McLaughlin, P. F.; Menger, M. F. S. J.; Mewes, J. M.; Mewes, S. A.; Morgante, P.; Mullinax, J. W.; Oosterbaan, K. J.; Paran, G.; Paul, A. Ç.; Paul, S. K.; Pavošević, F.; Pei, Z.; Prager, S.; Proynov, E. I.; Rák, Á.; Ramos-Cordoba, E.; Rana, B.; Rask, A. E.; Rettig, A.; Richard, R. M.; Rob, F.; Rossomme, E.; Scheele, T.; Scheurer, M.; Schneider, M.; Sergueev, N.; Sharada, S. M.; Skomorowski, W.; Small, D. W.; Stein, C. J.; Su, Y. C.; Sundstrom, E. J.; Tao, Z.; Thirman, J.; Tornai, G. J.; Tsuchimochi, T.; Tubman, N. M.; Veccham, S. P.; Vydrov, O.; Wenzel, J.; Witte, J.; Yamada, A.; Yao, K.; Yeganeh, S.; Yost, S. R.; Zech, A.; Zhang, I. Y.; Zhang, X.; Zhang, Y.; Zuev, D.; Aspuru-Guzik, A.; Bell, A. T.; Besley, N. A.; Bravaya, K. B.; Brooks, B. R.; Casanova, D.; Chai, J. D.; Coriani, S.; Cramer, C. J.; Cserey, G.; et al. Software for the frontiers of quantum chemistry: An overview of developments in the Q-Chem 5 package. *J. Chem. Phys.* **2021**, *155*, 084801.
(44) Valeev, E. F.; Coropceanu, V.; da Silva Filho, D. A.; Salman, S.; Brédas, J.-L. Effect of electronic polarization on charge-transport parameters in molecular organic semiconductors. *J. Am. Chem. Soc.* **2006**, *128*, 9882−9886.
(45) Hu, Z.; Zhou, B.; Sun, Z.; Sun, H. Prediction of excited-state properties of oligoacene crystals using polarizable continuum model-tuned range-separated hybrid functional approach. *J. Comput. Chem.* **2017**, *38*, 569−575.
(46) Westbrook, R. J. E.; Levin, A. J.; Gao, W.; Bothra, U.; Pratik, S. M.; Fan, B.; Lin, F. R.; Zhang, Q.-Q.; Ngo, K.; Kaminsky, W.; Brédas, J.-L.; Coropceanu, V.; Jen, A. K.-Y.; Toney, M. F.; Ginger, D. S. Solid-State Packing Controls Exciton Delocalization and Photophysics in Nonfullerene Acceptors. *J. Am. Chem. Soc.* **2025**, *147*, 30199−30209.
(47) Coropceanu, V.; Cornil, J.; da Silva Filho, D. A.; Olivier, Y.; Silbey, R.; Brédas, J.-L. Charge transport in organic semiconductors. *Chem. Rev.* **2007**, *107*, 926−952.
(48) Bixon, M., Jortner, J. *Electron Transfer: From Isolated Molecules to Biomolecules; Advances in Chemical Physics*; Wiley: New York, 1999; Vol*106*, pp 35−202.
(49) Brédas, J.-L.; Beljonne, D.; Coropceanu, V.; Cornil, J. Charge-transfer and energy-transfer processes in π-conjugated oligomers and polymers: A molecular picture. *Chem. Rev.* **2004**, *104*, 4971−5004.
(50) Cave, R. J.; Newton, M. D. Generalization of the Mulliken-Hush treatment for the calculation of electron transfer matrix elements. *Chem. Phys. Lett.* **1996**, *249*, 15−19.
(51) Send, R.; Furche, F. First-order nonadiabatic couplings from time-dependent hybrid density functional response theory: Consistent formalism, implementation, and performance. *J. Chem. Phys.* **2010**, *132*, 044107.
(52) Lingerfelt, D. B.; Williams-Young, D. B.; Petrone, A.; Li, X. Direct ab initio (meta-)surface-hopping dynamics. *J. Chem. Theory Comput.* **2016**, *12*, 935−945.
(53) Niu, Y.; Peng, Q.; Deng, C.; Gao, X.; Shuai, Z. Theory of excited state decays and optical spectra: Application to polyatomic molecules. *J. Phys. Chem. A* **2010**, *114*, 7817−7831.
(54) Peng, Q.; Niu, Y.; Shi, Q.; Gao, X.; Shuai, Z. Correlation function formalism for triplet excited state decay: Combined spin−orbit and nonadiabatic couplings. *J. Chem. Theory Comput.* **2013**, *9*, 1132−1143.
(55) Shuai, Z.; Peng, Q. Excited states structure and processes: Understanding organic light-emitting diodes at the molecular level. *Phys. Rep.* **2014**, *537*, 123−156.
(56) Shuai, Z. Thermal vibration correlation function formalism for molecular excited state decay rates. *Chin. J. Chem.* **2020**, *38*, 1223−1232.
(57) Hilborn, R. C. Einstein coefficients, cross sections, f values, dipole moments, and all that. *Am. J. Phys* **1982**, *50*, 982−986.
(58) Rau, U. Reciprocity relation between photovoltaic quantum efficiency and electroluminescent emission of solar cells. *Phys. Rev. B* **2007**, *76*, 085303.
(59) Blank, B.; Kirchartz, T.; Lany, S.; Rau, U. Selection metric for photovoltaic materials screening based on detailed-balance analysis. *Phys. Rev. Appl.* **2017**, *8*, 024032.
(60) Pedregosa, F.; Varoquaux, G.; Gramfort, A.; Michel, V.; Thirion, B.; Grisel, O.; Blondel, M.; Prettenhofer, P.; Weiss, R.; Dubourg, V.; Vanderplas, J.; Passos, A.; Cournapeau, D.; Brucher, M.; Perrot, M.; Duchesnay, E. Scikit-learn: Machine learning in python. *J. Mach. Learn. Res* **2011**, *12*, 2825−2830.
(61) Wen, Z.; Zhou, R.; Peng, S.; Shi, Y.; Zhang, R.; Zheng, Z.; Gao, F.; Zhao, Y. Impact of solvent processing on the PM6/Y6 morphology

https://doi.org/10.1021/acsami.5c18819
ACS Appl. Mater. Interfaces 2026, 18, 2200−2211

and charge transfer in organic solar cells. *J. Mater. Chem. C* **2024**, *12*, 17215−17222.
(62) Wang, R.; Zhang, C.; Li, Q.; Zhang, Z.; Wang, X.; Xiao, M. Charge separation from an intra-moiety intermediate state in the high-performance PM6:Y6 organic photovoltaic blend. *J. Am. Chem. Soc.* **2020**, *142*, 12751−12759.
(63) Padula, D.; Landi, A.; Prampolini, G. Assessing alkyl side chain effects on electron transport properties of Y6-derived non-fullerene acceptors. *Energy Adv* **2023**, *2*, 1215−1224.
(64) Bauer, C.; Kenter, T.; Lass, M.; Mazur, L.; Meyer, M.; Nitsche, H.; Riebler, H.; Schade, R.; Schwarz, M.; Winnwa, N.; Wiens, A.; Wu, X.; Plessl, C.; Simon, J. Noctua 2 supercomputer. *Journal of large-scale research facilities JLSRF* **2024**, *9*..

https://doi.org/10.1021/acsami.5c18819
ACS Appl. Mater. Interfaces 2026, 18, 2200−2211

Advanced Theory and Simulations

ADVANCED THEORY AND SIMULATIONS
www.advtheorysimul.com

RESEARCH ARTICLE OPEN ACCESS

Designing High Performance Organic Donor Molecules for Photovoltaics

Fabian Bauch[1] | Chuan-Ding Dong[1] | Stefan Schumacher[1,2]

[1]Department of Physics and Center for Optoelectronics and Photonics Paderborn (CeOPP), Paderborn University, Paderborn, Germany | [2]Wyant College of Optical Sciences, University of Arizona, Tucson, AZ, USA

Correspondence: Stefan Schumacher (stefan.schumacher@uni-paderborn.de)

Received: 14 August 2025 | **Revised:** 4 November 2025 | **Accepted:** 25 November 2025

Keywords: all-small-molecule OPVs | density functional theory (DFT) | exciton dissociation | Marcus theory | opto-electronic properties | organic photovoltaics (OPVs) | small-molecule donors

ABSTRACT

The advancement of non-fullerene acceptors has rocketed the power conversion efficiency (PCE) of organic photovoltaic (OPV) devices to values reaching close to 21%. However, the development of complementary donor materials has not kept pace, posing a key challenge for further improving device performance. In this theoretical study, we combine density functional theory (DFT) with Marcus theory to systematically design and evaluate donor molecules with A-π-Core-π-A architectures. Our focus lies in tuning electronic and optical properties – such as frontier molecular orbital energies, and singlet and triplet excitation characteristics – toward more efficient charge generation when coupled to non-fullerene acceptor Y6. In small donor systems featuring fused thiophene π-bridges, we find two-dimensional delocalization of the highest occupied molecular orbital (HOMO) across the backbone and the core's side chain, which enhances the transition dipole moment. Furthermore, while fused π-bridges lead to relatively stable transition rate constants across various interfacial configurations, they exhibit a limited CT state manifold, which may impede efficient charge separation following excitation of the acceptor. These findings provide molecular design insights critical for next-generation high-performance all-molecule OPV devices.

1 | Introduction

The growing demand for sustainable energy solutions has driven intensive research into next-generation photovoltaics, with organic photovoltaics (OPVs) emerging as a promising candidate due to their potential for lightweight, flexible, and low-cost solar energy conversion [1, 2]. While significant progress has been made in enhancing power conversion efficiencies (PCEs), further improvements in performance and stability are needed to meet commercial viability. A key breakthrough in the field was the development of non-fullerene acceptors (NFAs) [3–5], which have largely superseded fullerene-based acceptors by offering superior optical absorption, tunable energy levels, and better morphological control. Among these, the Y6 family has set a new benchmark, enabling single-junction OPV devices to reach efficiencies of up to ≈21% [6–10]. Y6's broad absorption spectrum, optimized electronic structure, and favorable charge transport characteristics have shifted the focus of material innovation toward the design of compatible and efficient donor materials [11, 12]. In parallel, theoretical screening of diverse NFA structures has emerged as a powerful tool to identify and understand promising candidates, accelerating the rational design of high-performance OPV systems [13–15].

Within this context, all-small-molecule (ASM) OPVs – featuring small molecules as both donors and acceptors – have emerged as a compelling alternative to polymer-based systems. Although polymer donors have historically dominated the OPV landscape,

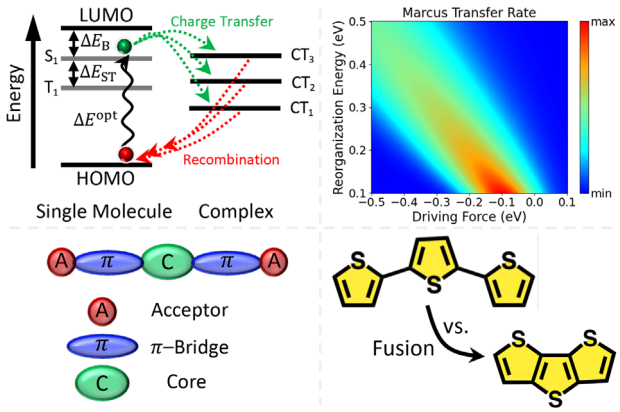

FIGURE 1 | Top left: Schematic overview of the key properties investigated in this work. Top right: Illustration of the charge transfer rate as a function of driving force, based on Marcus theory, assuming a constant electronic coupling of $V_{EC} = 0.1$ eV. Bottom left: Structural representations of the donor molecules studied. Bottom right: Illustration of thiophene-ring fusion within the π-bridge.

[16–18] small-molecule donors offer well-defined structures, precise electronic tunability, and excellent reproducibility, making them highly suitable for systematic investigation and rational material design. Recent advances have demonstrated that ASM OPVs can now achieve PCEs approaching those of their polymer-based counterparts [19–23], underscoring their potential to contribute to the next wave of high-efficiency, stable, and scalable OPV technologies.

A key limitation in organic photovoltaics (OPVs) is the strong Coulombic attraction between photo-generated electrons and holes, which leads to tightly bound excitons. The energy difference between the fundamental and optical gaps – known as the exciton binding energy ($\Delta E_B = E_{gap}^{fund} - E_{gap}^{opt}$, Figure 1) – is typically much larger in organic materials (0.1–0.5 eV) than in inorganic semiconductors, where thermal energy is often sufficient for exciton dissociation. Efficient charge generation in OPVs thus depends on the formation of interfacial charge transfer (CT) states [24], from which free charges can be more easily separated and collected [25]. A lower exciton binding energy reduces the barrier for exciton dissociation, thereby improving photocurrent and overall device efficiency [26, 27].

The singlet–triplet energy gap (ΔE_{ST}), the difference between the S_1 and T_1 states, is another important factor. Large ΔE_{ST} values often lead to energy losses via non-radiative triplet decay [28], whereas small gaps can reduce recombination and enable beneficial processes like reverse inter system crossing, enhancing charge generation and reducing energy loss [29, 30].

To model charge separation, the rate of electron or hole transfer from local excitons to CT states is central. Marcus theory describes this rate as dependent on electronic coupling, reorganization energy, and the driving force determined by excited-state energetics [31, 32]. As illustrated in Figure 1, optimal tuning of these factors ensures that charge transfer out competes recombination pathways [33]. The molecular design of donor materials – especially the backbone and electron-withdrawing terminal groups – critically affects these parameters by modulating frontier molecular orbital alignment and donor:acceptor coupling.

In this work, we present a theoretical investigation aimed at enhancing the charge separation efficiency in all-molecule organic solar cells by engineering the donor molecule structure. The donor molecules under study adopt an A-π-Core-π-A architecture, paired with the benchmark Y6 acceptor. Specifically, we modulate the chemical structure of the π-bridge by fusing tiophene rings (illustrated in Figure 1) and increasing the π-bridge length and by modifying the electron-withdrawing terminal groups to systematically study their influence on the exciton binding energy, singlet–triplet gap, and rate constants from localized excitons to charge transfer states in a donor:acceptor complex. By combining density functional theory (DFT) with a tuned-range-separated functional with Marcus theory, this study aims to elucidate structure–property relationships that govern charge generation processes in ASM OPV systems, providing design guidelines for next-generation donor molecules compatible with high-performance NFAs like Y6.

2 | Computational Details

To calculate the exciton characteristic and the transition rate constants from a localized state to a charge transfer state, we use density functional theory (DFT) and its time dependent (TD) variants in combination with Marcus theory. All DFT calculations were performed employing the Gaussian 16 package [34]. Isolated molecules are optimized with the b3lyp functional and the Pople type 6-311g(d,p) basis set. The complexes consisting of one donor molecule and one non-fullerene acceptor Y6 molecule were optimized at the b3lyp/6-31g(d) level of theory in combination with van-der-Waals interaction via Grimmes' D3 method with Becke-Johnson damping.

To adequately describe the opto-electronic properties of the engineered donor molecules a gap tuning approach has been employed based on the optimized structures of the isolated donor molecules to tune the description of the orbital energies toward the fundamental gap (energy difference between the ionization potential and electron affinity), providing a more accurate and reasonable description of the opto-electronic properties [35]. This is performed using the range-separated ωb97xd functional and the 6-311g(d,p) basis set. Since the dielectric environment is relevant for the frontier molecular orbital (FMO) energies it is included via the polarizable continuum model (pcm) with $\varepsilon = 3.0$, which is a reasonable value for organic semiconductors [36]. The range-separation parameter ω is tuned so that the energy of the highest occupied molecular orbital (HOMO) of the neutral system is equal to its ionization potential and the HOMO of the anionic system is equal to the electron affinity, thus, they satisfy Koopmans' theorem. The minimizing function reads

$$J(\omega) = |E_+(\omega) - E_0(\omega) + \varepsilon_0^H| + |E_0(\omega) - E_-(\omega) + \varepsilon_-^H|, \quad (1)$$

where E_+, E_0, and E_- denote the energy of the cationic, neutral, and anionic system, respectively. ε_0^H and ε_-^H are the HOMO energies of the neutral and anionic system, respectively. A more detailed description and a verification that the method pro-

duces realistic and trustworthy results is provided in Section SA (Supporting Information).

To adequately describe the singlet–triplet energy gap (ΔE_{ST}) and the exciton binding energy ($\Delta E_B = E_{gap}^{fund} - E_{gap}^{opt}$) of the single molecules the Tamm-Dancoff approximation (TDA) is used, where E_{gap}^{opt} is the optical gap, i.e., the singlet S_1 excitation energy and E_{gap}^{fund} is the fundamental gap, i.e., in the employed method, the energy difference between the HOMO and LUMO. We note that TDA provides improved stability to describe triplet state energies compared to TD-DFT while simultaneously negligibly affecting singlet excited state energies [37]. The TD-DFT variant is used for singlet states of the donor:acceptor complexes involved in the charge transfer.

The transition rate constants from localized to charge transfer states within the donor:acceptor complexes are calculate via the semiclassical Marcus formula [31, 32] as

$$k = \frac{2\pi}{\hbar}|V_{EC}|^2 \frac{1}{\sqrt{4\pi\lambda k_b T}} \exp\left[-\frac{(\lambda + \Delta G)^2}{4\lambda k_b T}\right], \quad (2)$$

where V_{EC} is the electronic coupling between the relevant excited states calculated using the Generalized Mulliken-Hush (GMH) method [32, 38], λ is the inner reorganization energy for this transition calculated via the four-point method [39], ΔG is the difference in Gibbs free energy of the involved excited states, T is the temperature set to 293.15 K (20°C), and $\hbar$ and k_b are Planck's reduced constant and Boltzmann constant, respectively. A detailed description how the values are calculated is provided in Section SB (Supporting Information).

The multiwfn software package [40] is used to analyze the charge distribution of the singlet excited states to identify local excited states and CT states. Moreover, it is used to calculate the dipole moments of the exited states as well as the transition dipole moments between excited states, necessary to calculate V_{EC}.

3 | Results and Discussion

Modification of the π-bridge of the A-π-Core-π-A molecular donor by extending the number of tiophene rings and fusion of the tiophene rings has been systematically performed and the influence of the electron-withdrawing (EW) terminal group of the donor molecule was investigated. With a focus on the π-bridge, we discuss the findings on the selected molecules shown in Figure 2, which we enlight to be representative of the systematic modifications for a total of ten different π-bridges (presented in Section SC, Supporting Information). Since the electron-withdrawing BBT core unit (experimentally used in, e.g., the BBTSM family [21, 22]) and the terminal group are the same for this part, to clarify the nomenclature, we label the molecular systems according to the number of fused tiophenes and the number of repetitions of this sub-unit (via single bonds) as $(\#\text{fused-rings})_{\#\text{repetitions}}$. For instance, $(1T)_4$ indicates the donor molecule with four single-bonded tiophene rings as π-bridge. Note, that the terminal used for engineering the influence of the π-bridge is thought to be the least EW group investigated to ensure a clear view on the effects of the π-bridges.

When modifying the terminal groups, we focused on assessing how variations in EW strength influence molecular properties. To this end, we selected commonly used terminal groups from experimental studies, for which the relative EW effects – such as those from nitrile, carbonyl, and fluorine substituents – can be reasonably estimated and compared. The terminal groups under investigation are shown in Figure 2, the complete molecular schemes are presented in Section SC (Supporting Information). A1 (*cyanoacetate* terminal group, used in, e.g., refs. [21, 41]) is thought to show strong EW effects due to nitrile and carbonyl, however, it lacks of conjugation with the backbone due to absence of ring conjugation. A2 (*rhodanine* terminal group, used in e.g., refs. [20, 42, 43]) is believed to show the weakest EW effects among the terminal groups studied, but its present ring conjugation could lead to similar EW capabilities as A1 or beyond. The terminal group A2CN (*2-(1,1-dicyanomethylene)rhodanine*), a derivative of A2, exhibits strong EW properties and is commonly employed in NFA materials, e.g., refs. [44, 45]. In the present study, it is utilized to represent the transition from donor to acceptor materials. A3 (*1,3-Indandione* terminal group) is thought to possess moderate EW capability induced by carbonyl, whereas A3F as fluorinated companion of A3 (both used in, e.g., ref. [19]) is believed to show stronger EW effects compared with A2.

To explore the impact of geometric distortion in donor molecules and to gain insight into the dissociation process, donor:acceptor interactions were modeled using π—π stacked complexes with the non-fullerene acceptor Y6. In addition to these stacked configurations, five alternative interfacial geometries were constructed for both $(1T)_4$ and $(4T)_1$ π-bridges focusing on the orientation of Y6's terminal group relative to either the donor's terminal group or the π-bridge to further assess the influence of local structural variation on the electronic and excitonic properties (the complex configurations are presented in Section SC).

3.1 | Frontier Molecular Orbitals

The discussion begins with an analysis of the electronic properties of the optimized donor molecules and non-fullerene acceptor Y6, focusing initially on representative structures. The complete set of results is provided and discussed in Section SD (Supporting Information). For Y6, the HOMO energy is calculated to −5.59 eV and the LUMO energy to −3.26 eV, resulting in a FMO gap of 2.33 eV. We note that the FMO gap is systematically overestimated compared to an experimentally measured value of ≈1.55 eV [6].

3.1.1 | The Molecular Backbone

For the modeled donor molecules with engineered π-bridges, the energies of the HOMO and LUMO for the representative structures are shown in Figure 3a. We find the energy as well as the orbital distribution to be influenced by three competing factors:

i) *π-bridge length*: As the length of the π-bridge increases, both the HOMO and LUMO energies rise. For instance, the HOMO level shifts from –5.44 eV to –5.39 eV to –5.28 eV for $(3T)_1$, $(4T)_1$, and $(6T)_1$, respectively. This trend is attributed to enhanced delocalization of the HOMO

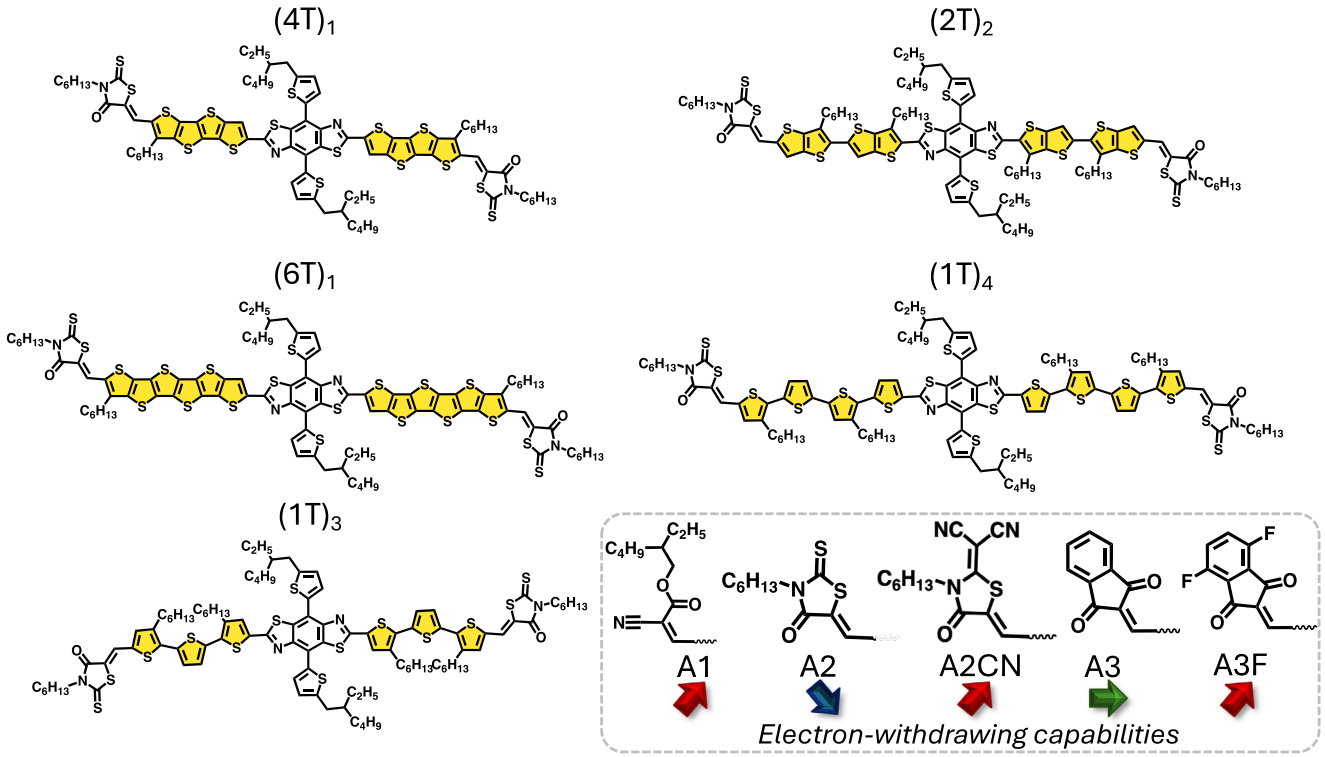

FIGURE 2 | Representative molecular structures illustrating the effects of engineering the π-bridge and modifying the terminal group. Thiophene units within the π-bridge are highlighted in yellow for clarity, with corresponding labels provided. Terminal group A2 is used for these models. The various terminal groups investigated in this work are displayed in the grey-outlined box, with their electron-withdrawing strengths indicated by arrows: upward for stronger and downward for weaker withdrawing ability.

along the molecular backbone, whereas the LUMO becomes more extended over the π-bridge and terminal groups, with reduced distribution on the core.

ii) *Fusion pattern*: Non-fused π-bridges exhibit twists between the thiophene rings, which enhances HOMO delocalization and raises its energy. However, this structural feature also causes the LUMO to localize at the terminal ends of the molecule, leading to an increase in its energy as well.

iii) *The core's side chain*: For small, fused π-bridges (up to four thiophene units), the side chains on the donor molecule's core contribute significantly to the HOMO delocalization. An example corresponding orbital is illustrated in Figure 3c. In contrast, their influence is diminished in both longer π-bridges (six or more thiophene units) and in non-fused π-bridges. For instance, in $(3T)_1$, the inclusion of the core's side chain increases the HOMO energy by 70 meV, whereas in $(1T)_4$ it has a negligible effect (Figure 3a, semitransparent lines). This difference may be due to the more twisted geometry of non-fused π-bridges, which disfavors delocalization onto the side chains, and the preference of long π-bridges for linear delocalization along the backbone. The resulting 2D HOMO distribution across the backbone and side chains in short, fused π-bridges may have implications for charge separation and transfer as elucidated later.

As a result of these competing factors, for short π-bridges, introducing single bonds leads to a noticeable increase in LUMO energy due to localization on the terminal group, while the HOMO also rises but to a lesser extent. This results in a slightly larger FMO gap for non-fused π-bridges compared to fused ones. For longer π-bridges, the HOMO energy continues to increase with π-bridge length, whereas the LUMO energy tends to converge to a finite value due to localization, leading to a consistent decrease in the FMO gap with increasing π-bridge length.

3.1.2 | Geometrical Distortion

Interestingly, when donor molecules adopt the geometrically distorted conformations found in π–π-stacked complexes with Y6 the previously observed trends are reversed, as evidenced by calculations on the isolated, distorted donor structures. The corresponding HOMO and LUMO energies of the distorted donor molecules is shown in Figure 3a as dotted lines. In particular, for non-fused π-bridges, the FMO gap is reduced by approximately 0.25 eV, while it remains almost unchanged for fused π-bridges. This reduction can be attributed to a partial planarization of the twisted non-fused π-bridges upon complex formation, which enhances delocalization. The result is an increase in the HOMO energy by roughly 150 meV and a smaller decrease in LUMO energy (≈100 meV). This effect appears to be systematic: across multiple different stacking configurations, the HOMO of $(1T)_4$ increases by ≈150 meV and the LUMO decreases by ≈100 meV, while both energies remain largely unchanged for $(4T)_1$ (see Section SD, Supporting Information). Such energetic stability of the FMOs is advantageous for charge separation and transport in organic photovoltaics, as it helps reduce energy disorder and suppresses charge trapping [46].

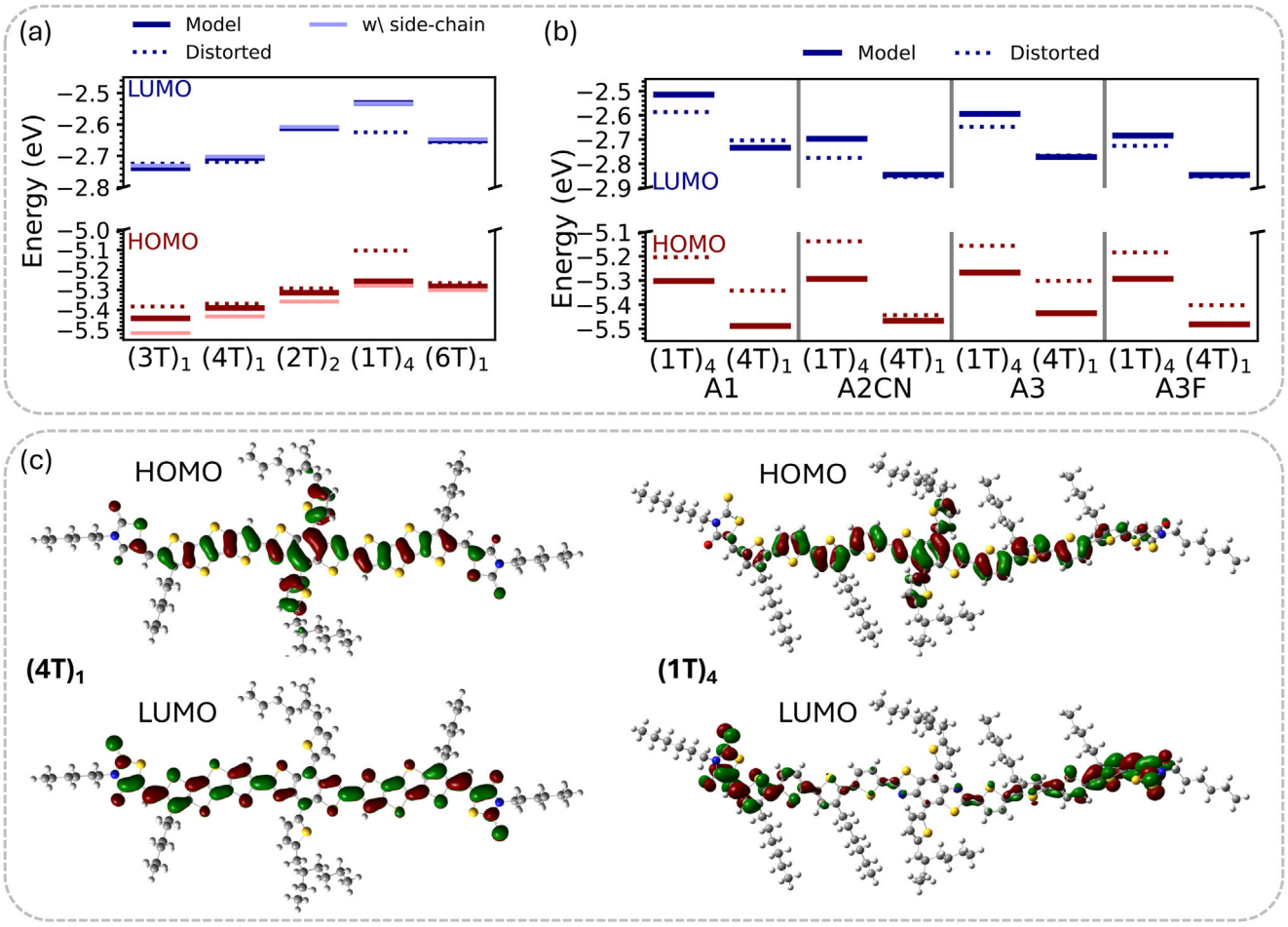

FIGURE 3 | Frontier molecular orbitals of the engineered donor molecules. HOMO and LUMO energy levels of the donor molecules featuring (a) different engineered π-bridges coupled to terminal group A2 and (b) various terminal groups coupled to the $(1T)_4$ and $(4T)_1$ π-bridges. Solid lines represent values for the optimized geometries (*Model*), while dotted lines correspond to the isolated donor molecules in their distorted geometries as extracted from the π—π-stacked complexes with Y6 (*Distorted*). Semi-transparent lines indicate energy levels calculated for structures without the core's side chain (replaced by methyl groups). Grey lines are shown for visualization purpose to separate the terminal groups. (c) Visualizations of the HOMO and LUMO orbitals for representative donor molecules $(1T)_4$ and $(4T)_1$.

3.1.3 | The Terminal Groups EW Effects

The FMO energies of the donor molecules with varying terminal groups coupled with the $(1T)_4$ and $(4T)_1$ π-bridge is shown in Figure 3b. As the A2 group is expected to show the least EW effects among the investigated groups in this study, the donor molecules with the A2 group serves as baselines for the investigation of the EW effects.

The HOMO energies show modest but consistent shifts in response to the EW strength of the terminal groups. Specifically, all terminal groups lower the HOMO energies compared to the reference A2, with the difference between the $(1T)_4$ and $(4T)_1$ π-bridges increasing to approximately 0.2 eV, i.e., the influences induced by the fusing pattern of the π-bridges will be amplified. The strongest HOMO shifts are observed for A1 and A3F, which contain strong EW substituents such as nitrile, carbonyl, and fluorine. To understand this unbalanced shift in energy in more detail, the contribution of the different fragments of the donor molecules on the HOMO and LUMO are examined via a partial density of states, analyzed by the Hirshfeld method (Section SD, Supporting Information). When coupled to the $(1T)_4$ π-bridge, the stronger EW capabilities of A1, A2CN, and A3F lead to more localization of the HOMO on the core and the inner two tiophene rings (≈80%) than on the outer two tiophene rings and the terminal group itself (≈20%), whereas this relation is about ≈72% and ≈28% for the A2 donor molecule, respectively. This localization on the core is even more pronounced in the fused $(4T)_1$ π-bridge. Thus, these substituents effectively stabilize the HOMO by electrostatic repulsion effects, where the EW character resides in lower energy electronic states rather than the HOMO. In contrast, A3 – with its moderately EW substituents – induces a relatively smaller downshift in the HOMO energy compared to A1 and A3F.

Interestingly, the response of the LUMO energy to different terminal groups is more nuanced. A3, A3F, and A2CN lead to a noticeable lowering of the LUMO energy, which is consistent with stronger stabilization of the molecule's LUMO due to their pronounced EW effects, pulling the LUMO distribution to about ≈87% on the periphery of the donor molecule strongly incorporating the terminal group, whereas it is little less for A2.

A2CN and A3F exhibit comparable EW effects, resulting in a similar reduction of the LUMO energy level. A1 induces only a minimal shift relative to A2, which is the consequence of the limited conjugation of A1, restricting the delocalization of the LUMO onto the terminal group itself. Instead, the LUMO remains more delocalized on the central backbone and core, which diminishes the overall impact of A1's EW groups on the FMO energy. As a result of these orbital shifts, the FMO energy gap follows a general trend of A1 > A2 > A3 > A3F > A2CN across both types of π-bridges.

Focusing on the molecules with varying terminal groups in the π—π-stacked configurations with Y6, the geometrical distortion leads to very similar effects as for terminal group A2, i.e., for the non-fused π-bridges the HOMO is shifted upwards and the LUMO is shifted downwards. Noteworthy, for the stronger EW groups, also the fused π-bridges show similar spectral shifts, that were not present for A2, indicating that the more balanced HOMO delocalization for the donor molecule with terminal group A2 is more robust through geometrical distortion (compared to its optimized structure).

In summary, both the fusing pattern and the π-bridge length can effectively tune the FMO energies by systematically influencing the delocalization characteristics of the HOMO and LUMO. Notably, the side chain of the core plays a significant role in HOMO delocalization for short and fused π-bridges, whereas this contribution diminishes in longer and non-fused architectures. The EW strength of the terminal can amplify the effects of the fusing pattern, thus shielding the HOMO more towards the core while pulling the LUMO towards the donor periphery. To minimize voltage losses in blended OPV systems, the energy offset between the FMOs of the donor and acceptor should be minimized [47]. A small to medium-sized π-bridge is therefore expected to be most effective in achieving this alignment with Y6. However, a reduced energy offset may also implicate a lower driving force for charge transfer, potentially impairing the efficiency of charge separation, which will be discussed later.

3.2 | Excited States and Exciton Characteristics

Having analysed the electronic properties and it's engineering through the π-bridge and terminal group, we now turn toward the optical response of the donor molecules. The full set of results is provided in Section SD (Supporting Information).

3.2.1 | Excitation Energies

Upon fusing the thiophene rings in the π-bridge, the singlet (S_1) and triplet (T_1) excitation energies of the optimized isolated donor molecules decrease by approximately 50 meV and 50–100 meV, respectively, while variations in π-bridge length have little effects. For example, the S_1 excitation energies for $(1T)_4$ and $(4T)_1$ are calculated to be 2.19 and 2.14 eV, respectively, as shown in Figure 4a (solid lines), with corresponding charge density differences depicted in Figure 4e, f. As with the FMO energies, the core's side chain influence the S_1 excitation nature. As it raises the HOMO energy through delocalization, it consequently lowers the S_1 excitation energy; in contrast, the T_1 energy remains largely unaffected (see Section SD, Supporting Information).

When geometric distortion is introduced via π–π-stacked complex formation with Y6 this fusion-pattern trend reverses. In such distorted geometries, the S_1 excitation energy of non-fused π-bridges red-shifts by roughly 200 meV – placing it ≈100 meV below that of fused-ring analogues – while the S_1 energy of fused π-bridges remains nearly unchanged (Figure 4a, dotted lines). Notably, similar to the FMO energies, the S_1 and T_1 excitation energies shifts are robust in various differently complex configurations implicating low energetic disorder. This red-shift effectively brings the absorption capabilities of the donor closer to the absorption peak of Y6 (absorption maximum at 1.51 eV measured in solution in ref. [6], S_1 excitation energy calculated to 1.83 eV in this work), narrowing the spectral gap and potentially enhancing the overall absorption profile of the active layer in OPV devices by covering a broader portion of the solar spectrum.

The EW terminal groups affects the S_1 excitation energy similar to the FMO gap, which results in the excitation energy order A1 > A2 > A3 > A3F ≈ A2CN, however, the changes are not as prominent as for the FMO gap. Notably, the ordering A1 > A2 aligns with experimental findings reporting a reduction in the optical bandgap within the BBTSM family when replacing the terminal group A1 [21] with A2 [22], although the BBTSM molecules incorporate the $(1T)_3$ π-bridge. The T_1 excitation energy follows the order A1 > A3 > A3F > A2 > A2CN.

3.2.2 | Exciton Binding Energy

When increasing the number of tiophene rings in the engineered π-bridge, the exciton binding energy for the optimized modeled donor molecules decreases, as shown in Figure 4b (red points). For instance, $(3T)_1$ has an ΔE_B of 0.58 eV decreasing by 30 meV to 0.55 eV for $(4T)_1$ and further decreasing to 0.53 eV for $(6T)_1$. While this decrease is induced by a more delocalized electron and hole distribution, a further decrease can be induced by introduction of single bonds separating tiophene rings. For instance, the four tiophene rings in $(1T)_4$ reduces ΔE_B by 10 meV compared to its fused counterpart. Forming repeated thienothiophene, for instance in $(2T)_3$, ΔE_B is reduced to 0.47 eV that can even be reduced to 0.40 eV for $(2T)_4$. Reason for the reduction is that the single-bonds lead to a twisted backbone, strongly delocalizing the hole (i.e., the HOMO) on the π-bridge while simultaneously slightly rendering the electron to be more localized on the terminal groups (i.e., the LUMO), separating the electron and hole. This separation is enhanced by introduction of stronger EW terminal groups showing conjugation (A3, A3F, and A2CN), reducing ΔE_B of the non-fused π-bridge by 50 meV relative to its fused counterpart and the non-fused A2 donor molecule, as illustrated in Figure 4c (red points). A reduced exciton binding energy (ΔE_B) likely lowers the energy losses associated with the dissociation process by decreasing the barrier for charge separation. It is worth noting that, beyond monomer-level electronic properties, ΔE_B can also be significantly affected by solid-state polarization effects [48] and dielectric screening effects induced by the dielectric environment [49], which in this study were only implicitly accounted for through the use of an implicit solvation model.

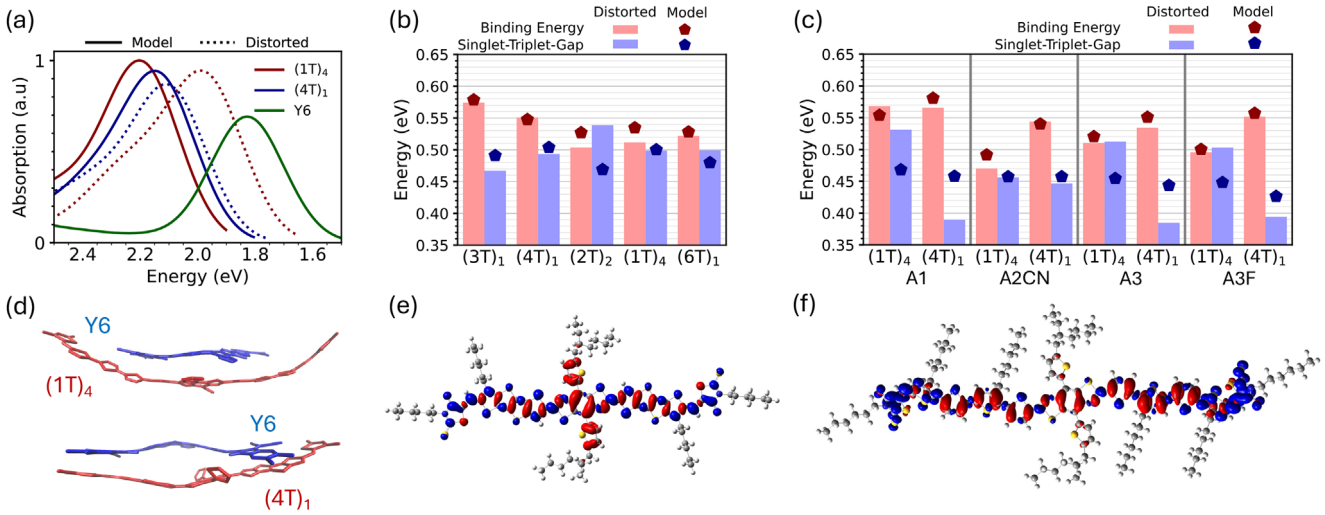

FIGURE 4 | Excited state and exciton properties. (a) Simulated UV–vis absorption spectra of $(1T)_4$ (red), $(4T)_1$ (blue), and Y6 (green) in their optimized geometries (solid lines, *Model*) and in the distorted geometries extracted from the π—π-stacked complexes (dotted lines, *Distorted*). (b) Exciton binding energies (red) and singlet–triplet energy gaps (blue) for representative donor molecules with engineered π-bridges coupled to terminal group A2. Points represent the values for the *Model* structures and bars the *Distorted* structures. (c) Corresponding values for donor molecules with different terminal groups. Grey lines are shown for visualization purpose to separate the terminal groups. (d) Representative π—π-stacked donor:acceptor complexes. (e, f) Charge density differences (relative to the ground state) of the first singlet (S_1) excitation for $(4T)_1$ and $(1T)_4$, respectively.

3.2.3 | Singlet-Triplet Energy Gap

The π-bridge length has only a modest effect on the singlet-triplet energy gap ΔE_{ST}; also the fusing pattern does not significantly influence ΔE_{ST}. The modest influence is induced by very similar shifts in the S_1 and T_1 excitation energies. This is some interesting phenomena, since the hole distribution of the T_1 excitation does not involve the core's side chain at all (in contrast to S_1 excitation) and mostly localizes on the outer part of the π-bridges and the terminal groups and, especially for larger and non-fused π-bridges, breaks symmetry and mainly distributes on one end of the donor molecule (Section SD, Supporting Information). Thus, the similar energy shift and relatively unaffected ΔE_{ST} appears surprisingly. We speculate that to maximize the governing exchange interaction in the triplet state configuration, the localization and the avoidance of the core's side chain is detrimental to facilitate a stable triplet state.

Modulating the terminal groups, ΔE_{ST} shows a general decreasing trend with stronger EW capabilities, which can be attributed to a relative increase in the T_1 excitation energy (Figure 4c, blue points). We attribute this to a more localized electron in the triplet state driven by stronger electron-withdrawal, which limits the spatial overlap between electron and hole densities. This reduced exchange interaction effectively narrows the singlet–triplet gap, despite the altered orbital characters between the singlet and triplet excitation (see Section SD, Supporting Information, for details).

3.2.4 | Geometrical Distortions

Due to the systematic decrease of the FMO gap and the S_1 excitation energy caused by geometric distortion of the donor molecules in complex configurations with Y6, both values tend to shift in a correlated manner. As a result, shown in Figure 4b as red and blue bars, ΔE_B and ΔE_{ST} become largely insensitive to such distortions in the case of rhodanine-based terminal groups (A2 and A2CN), likely due to strong interactions that lock the terminal–π-bridge conformation and restrict the rotational barrier. For the non-rhodanine-based terminal groups, ΔE_B remains relatively unaffected by geometric distortion as well (Figure 4c, red bars). In contrast, ΔE_{ST} shows a more nuanced dependence: it systematically increases for non-fused π-bridges and decreases for fused π-bridges as the EW strength of the terminal group increases (Figure 4c, blue bars). This behavior can be attributed to a greater reduction in the T_1 excitation energy relative to the S_1 energy in distorted non-fused systems, whereas in fused systems, the T_1 state remains nearly unchanged and only the S_1 state experiences a moderate lowering. This differential response highlights the influence of both molecular rigidity and terminal group EW capabilities on excited-state energetics.

3.2.5 | Light Absorption Capabilities

The oscillator strength of the S_1 transition is influenced by the spatial distribution of the HOMO: in small, fused π-bridges, delocalization across the two-dimensional structure including the core's side chain reduces HOMO–LUMO overlap, thereby lowering oscillator strength. In contrast, for longer π-bridges, the HOMO adopts a more linear distribution along the backbone, minimizing side chain contributions and improving spatial overlap with the LUMO. As a result, oscillator strength increases with π-bridge length – nearly doubling from 1.9 to 3.7 between $(3T)_1$ and $(4T)_1$, and rising to 5.0 for $(6T)_1$. Taken together, these results suggest that increasing π-bridge length and leveraging structural distortion through π–π-stacking both contribute to enhanced light absorption by closing the gap to Y6 and improved electronic properties, which are favorable for efficient organic photovoltaic performance.

TABLE 1 | Absolute values of the dipole moment of the ground state ($\boldsymbol{\mu}^{g}$), the singlet excited state ($\boldsymbol{\mu}^{e}$) and the difference between the dipole moments $\Delta\boldsymbol{\mu}^{ge} = \sqrt{(\mu_x^g - \mu_x^e)^2 + (\mu_y^g - \mu_y^e)^2 + (\mu_z^g - \mu_z^e)^2}$ of the donor molecules with varying terminal group (T) and π-bridge. All values in Debye.

	$(1T)_4$			$(4T)_1$		
T	$\boldsymbol{\mu}^{g}$	$\boldsymbol{\mu}^{e}$	$\Delta\boldsymbol{\mu}^{ge}$	$\boldsymbol{\mu}^{g}$	$\boldsymbol{\mu}^{e}$	$\Delta\boldsymbol{\mu}^{ge}$
A1	7.8	13.0	5.2	0.8	0.8	0.2
A2	10.2	17.6	7.8	1.2	1.3	0.1
A2CN	16.7	27.1	11.2	1.0	1.1	0.3
A3	3.7	12.4	9.1	0.6	0.6	0.1
A3F	5.2	15.4	10.8	0.7	0.7	0.1

In summary, the results demonstrate that the core's side chain plays a crucial role in shaping the opto-electronic properties, particularly for short to medium-sized π-bridges. Tailoring this structural element offers a promising strategy for optimizing electronic behavior. Additionally, the nature of the terminal group markedly alters the donor's electronic characteristics: stronger EW groups not only stabilize FMO energies but also affect exciton binding and triplet formation. These stronger EW effects intensify the influence of the π-bridges fusing pattern and the core on the donor backbone architecture. Notably, combining asymmetric core side chains with terminal group engineering proves to be an effective strategy for optimizing both opto-electronic properties and morphological packing [41, 50]. Importantly, we observe that geometric distortions in complex configurations lead to systematic shifts in the energy landscape relative to optimized geometries – an essential consideration when screening and evaluating potential donor systems. In addition to morphology induced disorder, dynamic fluctuations in FMO energies can influence and facilitate charge transport [51], which is beyond the scope of this work.

3.3 | (Excited-State) Dipole Moments

The permanent dipole moment in the ground state ($\boldsymbol{\mu}^{g}$) plays a critical role in the aggregation behavior of organic molecules, which in turn affects the morphology at the donor:acceptor interface – an essential factor in OPV performance. Additionally, the difference between the locally excited- and ground-state dipole moments ($|\Delta\boldsymbol{\mu}^{ge}| = |\boldsymbol{\mu}^{g} - \boldsymbol{\mu}^{e}|$) was reported to hold considerably inportance in the OPV performance, as a larger change in dipole moment can facilitate charge separation by promoting more weakly bound exciton states [52, 53], probably leading to lower energy losses [54].

For the non-fused $(1T)_4$ systems, the permanent dipole moments follow the trend A2CN (≈17 D) > A2 (≈10 D) > A1 (≈8 D) > A3F (≈5 D) > A3 (≈4 D), as shown in Table 1. Their fused $(4T)_1$ analogues exhibit the same order but much lower absolute values, typically around 0–1 D, likely due to the increased molecular symmetry and rigidity introduced by the fused-ring architecture, which limits molecular polarization. A large permanent dipole moment can disrupt donor-acceptor miscibility, promoting aggregation that impedes exciton diffusion and ultimately lowers PCEs [53, 55].

Upon photo-excitation, the change in dipole moment ($\Delta\boldsymbol{\mu}^{ge}$) for the non-fused π-bridges follows the order A2CN > A3F > A3 > A2 > A1 and falls within the range of ≈5–11 D, indicating a strong charge transfer character in their local excitons. In contrast, the fused π-bridges show negligible $\Delta\boldsymbol{\mu}^{ge}$, suggesting more localized excitons. This trend aligns with the calculated reduction in exciton binding energy (cf. Figure 4c), implying that non-fused π-bridges host more weakly bound excitons that are potentially easier to dissociate. This is further supported by our earlier work using non-adiabatic ab initio molecular dynamics (NA-AIMD) simulations [56], which discusses that a highly polarized excited-state can promote high initial polaron yields by enabling strong delocalization and separation of electron and hole.

3.4 | Dissociation Process

Having analyzed the opto-electronic properties of the isolated (and geometrically distorted) donor molecules, we now shift the focus to the exciton dissociation process in donor:acceptor complexes following local photo-excitation of either component. Exciton dissociation generally proceeds via the conversion of a localized exciton into a charge transfer (CT) state at the donor:acceptor interface, which may subsequently separate into free charges. This process competes with other pathways such as non-geminate recombination to the ground state and intersystem crossing (ISC) to triplet states, which can divert the excited-state population. Additionally, energy transfer between localized donor and acceptor excitons may occur, depending on their relative alignment in energy.

Central to the present study is the population of CT states within the complex, as these states are key to facilitating charge separation. Accordingly, the excited states were first classified as either locally excited (LE) or CT in character, followed by evaluation of the electronic coupling (EC) between the relevant pairs. Rate constants for CT state formation were then computed – specifically, hole transfer (HT) from an initially excited acceptor (LE_A) and electron transfer (ET) from an initially excited donor (LE_D). We note that the employed methodology does not consider triplet states, which may introduce additional relaxation channels via ISC. The complete set of results is provided in Section SE (Supporting Information).

3.4.1 | Hole Transfer

Starting with the dissociation of the acceptor excitons, Figure 5 presents the calculated transition rate constants, along with the EC, for selected representative donor molecules stacked with the non-fullerene acceptor Y6 in a π—π-stacked configuration. Focusing first on HT, a clear trend emerges for small π-bridges composed of three or four thiophene units: fully fusing all thiophenes leads to significantly lower total HT rates (sum of all transitions to any CT state) as well as reduced individual transition rates. For example, the non-fused $(1T)_4$ π-bridge exhibits a total HT rate of $1.38 \cdot 10^{14}$ s^{-1}, while the fully fused $(4T)_1$ π-bridge shows a markedly lower rate of $2.07 \cdot 10^{13}$ s^{-1}.

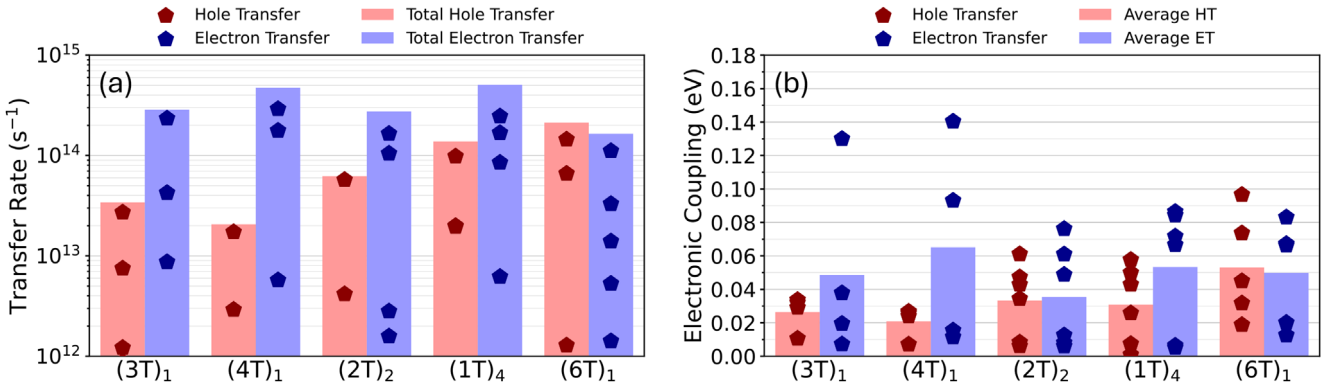

FIGURE 5 | Rate constants for engineering the π-bridges. Electron (blue) and hole (red) transitions associated with modulation of the π-bridge in the molecular donor, modeled within π—π-stacked donor–acceptor complexes. (a) The total charge transfer rates from the localized S_1 states of the donor and acceptor to charge transfer (CT) states are shown as bars; individual transition rates are shown as points. (b) Average electronic coupling per transition is shown as bars, while electronic coupling values for individual transitions are depicted as points.

This reduction is primarily attributed to weaker EC between the LE_A state and the CT states induced by the fused systems.

The electronic coupling is governed by the energy difference between states and a multiplicative factor dependent on the transition dipole moment strength ($\boldsymbol{\mu}_{LE_A \to CT}$) and the alignment between the dipole moments of the LE_A ($\boldsymbol{\mu}^{LE_A}$) and CT states ($\boldsymbol{\mu}^{CT}$) – here referred to as the dipole factor, given by the following expression:

$$\frac{|\boldsymbol{\mu}_{LE_A \to CT}|}{\sqrt{(\boldsymbol{\mu}^{CT} - \boldsymbol{\mu}^{LE_A})^2 + 4|\boldsymbol{\mu}_{LE_A \to CT}|^2}}. \tag{3}$$

Although fused π-bridges tend to have poorer dipole alignment compared to their non-fused counterparts, they compensate with higher transition dipole strengths, which ultimately enhances the dipole factor. This increased transition dipole strength may result from greater spatial overlap of the hole wavefunction by including the core's side chain, thereby improving the overlap with the hole on Y6. In contrast, non-fused π-bridges – such as $(1T)_4$ – have donor backbones that extend well beyond the size of Y6, reducing the effective hole overlap and thus the transition dipole moment.

However, despite the improved dipole factor in the fused systems, the number and spectral distribution of accessible CT states is more favorable in the non-fused π-bridges. For instance, $(1T)_4$ features three CT states lying below the LE_A state, compared to just one for $(4T)_1$. This renders the CT state energetics one of the limiting factors for overall large HT rate constants in fused π-bridges. A well-aligned driving force relative to the reorganization energy, enabled by a broader distribution of energetically favorable CT states, is essential for efficient charge separation. However, nonradiative losses can be mitigated by relatively high-lying CT states [57] while simultaneously loss in the open circuit voltage might be higher due to large energy difference between the local and CT state [58]. Therefore, the overall PCE of non-fused π-bridges may be limited by their intrinsically low-lying CT-state manifold.

Introducing partial fusion – i.e., fusing pairs of thiophenes into repeated thienothiophene units as in $(2T)_2$ – yields intermediate behavior. The HT rate is higher than for the fully fused $(4T)_1$ due to improved dipole alignment through modest geometric adjustment, though CT energetics remain less favorable than in the non-fused $(1T)_4$, thus, the HT rate is diminished compared to $(1T)_4$.

For medium-sized π-bridges consisting of six thiophene units, the trend reverses: fused π-bridges begin to outperform non-fused analogs. The total HT rate increases significantly across $(2T)_3$, $(3T)_2$, and $(6T)_1$, from $6.13 \cdot 10^{13}$ s^{-1} to $1.53 \cdot 10^{14}$ s^{-1} and $2.13 \cdot 10^{14}$ s^{-1}. This improvement is attributed to both a larger number of CT states below the LE_A state and enhanced EC via stronger transition dipole moments. In contrast, non-fused π-bridges at this size show highly delocalized hole distributions that exclude the core and its side chain, limiting transition dipole strength and thus EC.

Finally, in large π-bridges with eight thiophene rings, hole transfer rates again decrease relative to the fused six-ring systems. The underlying issue remains the same: delocalization of the hole primarily along the extended π-bridge backbone with minimal involvement of the core unit results in reduced dipole strength and, consequently, weaker EC for HT.

As shown in Figure 6, for HT, the terminal group does not alter the influence of the π-bridge, i.e., the HT rate constants for the $(1T)_4$ π-bridge outperforms the $(4T)_1$ π-bridge despite different strength of the EW capabilities of the terminal group. This was expected, since the hole distribution ($\approx$ HOMO) is mainly delocalized on the backbone and the core while only slightly incorporating the terminal group itself, thus, modification of the latter should not significantly alter the HT characteristics. However, noteworthy, the HT rate for the A3 system is significantly low due to overall very low EC.

3.4.2 | Electron Transfer

Turning to ET in π—π-stacked configurations with Y6, i.e., dissociation of the donor exciton, we want to note that some donor molecules exhibit LE_D states that show a partial hybridized character, i.e., the LE_D state is not fully localized but rather

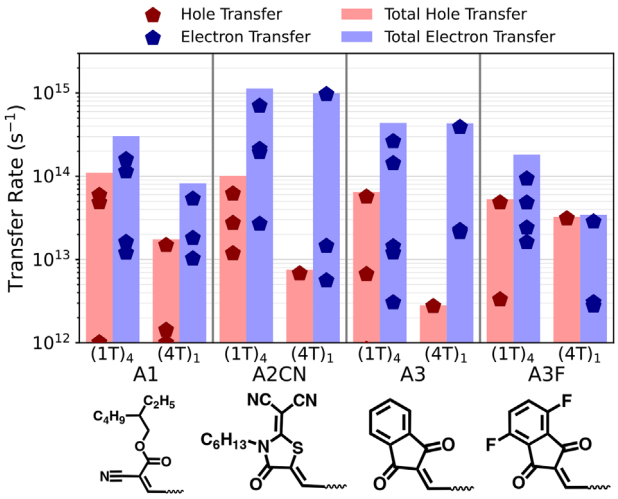

FIGURE 6 | Rate constants for varying terminal groups. Electron (blue) and hole (red) transitions for π—π-stacked donor:acceptor complexes with different terminal groups and donor bridges ((1T)$_4$ and (4T)$_1$). The total charge transfer rates from the localized S_1 states of the donor and acceptor to charge transfer (CT) states are shown as bars; individual transition rates are shown as pentagon-shaped points. Molecular structures of the different terminal groups used in the donor molecules are shown below.

shows a partial charge transfer of 0.25–0.3 e. This concerns the following π-bridges coupled to A2: (1T)$_4$, (3T)$_2$, (2T)$_4$, and (4T)$_2$, i.e., comparably large π-bridges, the (4T)$_1$ π-bridge coupled to A1 and A3, and also the A2CN architectures. This, in turn, can influence the calculated ET rate constants by increased transition dipole moments as well as artificially aligned dipole moments. This thought of artificially LE$_D$ state was consistent through different tested π—π-stacked configurations, though, we keep the discussion to the other, clearly characterized π-bridges but present the least hybridized character configuration for the named π-bridges for completeness. Nevertheless, we want to note that hybridized local and CT states were reported to effectively enhance the charge generation [59].

The ET rate constants for the small-sized π-bridges (three or four tiophene rings) is significantly larger than the HT rate constants exceeding $\approx 10^{14}$ s^{-1}. Reason for this is a generally larger EC between the LE$_D$ states and the CT states. Breaking the fusion of the rings, excitation of non-fused π-bridges exhibit a rather localized electron distribution on the terminal groups, in turn, decreasing the dipole alignment and decreasing the EC of the LE$_D$ and the CT states, therefore decreasing the rate constants for donor molecules largely exceeding the size of Y6. This is a reasonable and intuitively result, since an exceeded size of the donor molecule compared to Y6 increases the distance between both respective electron distributions on the donor molecule and Y6, ultimately decreasing the coupling and reducing the transfer capabilities. For larger π-bridges of six tiophene rings, the ET rate constant decreases and is roughly similar to the HT rate. This is, again, induced by reduced EC due to misaligned dipole moments.

The largest ET rate constants are achieved for CT states lying roughly 0.3–0.4 eV below the LE$_D$ states, i.e., energetically close to the LE$_A$ state. Thus, this hot CT state (relative to the lowest CT state) can undergoe internal conversion to lower-lying cold CT states and back electron transfer to the LE$_A$ state might occur before the charge separation takes place. We note again that energy transfer between localized donor and acceptor excitons may occur and potentially compete with the ET process due to the relatively high excitation energy of the LE$_D$ state compared to the LE$_A$ state; however, this mechanism lies outside the scope of the present study. The presence of excess energy is on the charge generation is still under debate; while some reports show increased charge yield induced by excess excitation energy, [60] thus hot CT state generation, other reports show no direct influence of excess energy on the dynamics and charge yield [61].

The ET characteristics of donor molecules with modified EW terminal groups are particularly noteworthy, as these groups predominantly influence the LUMO and thus the electron distribution in the excited state. Similar to the trend observed for HT, ET rates are generally lower for the fused π-bridge compared to the non-fused π-bridge in the presence of strong EW terminal groups such as A1 and A3F. Interestingly, this contrasts with the trend seen for the weaker EW group A2, where the non-fused π-bridge performs very similar to the fused π-bridge. Note, that (4T)$_1$ in combination with A1 or A3 exhibits slightly hybridized LE$_D$ states. Overall, donor systems incorporating strongly EW terminal groups (A1 and A3F) show reduced ET rate constants, which can be attributed to diminished EC. This effect seems to result from a reduced transition dipole moment, while the alignment of the local and CT state dipole moments shows only negligible improvement.

3.4.3 | Disordered Complexes

As the local geometric arrangement at the donor:acceptor interface plays a crucial role in determining the efficiency of exciton dissociation, the ET and HT rate constants for the five differently stacked configurations were calculated, offering a broader view of potential interfacial arrangements. The two donor molecules featuring the (1T)$_4$ and (4T)$_1$ π-bridges were selected as representative systems to capture the key differences introduced by fusion patterns – namely, the impact of a 2D hole distribution over the core's side chain in fused systems and the increased structural flexibility of non-fused π-bridges. A summary of the average ECs and total rate constants is presented in Table 2. The values are listed in Section SF (Supporting Information).

Interestingly, both donor systems – regardless of fusion pattern – exhibit similar average ECs for HT and ET, around 19 and 20 meV, respectively. However, the average total HT rate constants differ significantly between the two systems. The non-fused (1T)$_4$ π-bridge shows a higher average rate of $5.25 \cdot 10^{13}$ s^{-1}, compared to a lower rate of $1.6 \cdot 10^{13}$ s^{-1} for the fused (4T)$_1$ π-bridge. Despite this, the fused system demonstrates a more consistent performance across different configurations. Apart from one notably low value for the total HT ($9.34 \cdot 10^{11}$ s^{-1}), the total HT rates for (4T)$_1$ remain close to its π—π-stacked configuration with a highest total HT rate of $4.30 \cdot 10^{13}$ s^{-1}, suggesting that HT in fused systems is more robust and primarily constrained by the available CT state manifold rather than by EC itself.

TABLE 2 | Averaged calculated values for five complex configuration with varying stacking arrangements, for both $(1T)_4$ and $(4T)_1$ π-bridges. Shown are the average total transfer rates, with the minimum and maximum values indicated in parentheses. The average electronic coupling per transition is also included.

	Hole Transfer		Electron Transfer	
Bridge	**Total transfer rate (s^{-1})**	**EC (meV)**	**Total transfer rate (s^{-1})**	**EC (meV)**
$(1T)_4$	$5.25 \cdot 10^{13}$ ($7.90 \cdot 10^{12} - 1.65 \cdot 10^{14}$)	18.2	$5.32 \cdot 10^{13}$ ($5.04 \cdot 10^{12} - 1.69 \cdot 10^{14}$)	20.4
$(4T)_1$	$1.86 \cdot 10^{13}$ ($9.34 \cdot 10^{11} - 4.30 \cdot 10^{13}$)	19.4	$7.11 \cdot 10^{13}$ ($3.88 \cdot 10^{12} - 2.04 \cdot 10^{14}$)	20.5

In contrast, the total HT rate constant for $(1T)_4$ shows greater sensitivity to interfacial geometry. While one configuration ($1.65 \cdot 10^{14}$ s^{-1}) matches the π—π stacked HT rate constant, three of them drop to $\approx 1 \cdot 10^{13}$ s^{-1}, contributing to a wider distribution and a lower average compared to the π—π-stacked case. This indicates that although $(1T)_4$ can achieve higher HT rates, its performance is more interfacial-geometry-dependent.

Regarding ET, both systems exhibit comparable behavior. The average total ET rate constant is slightly lower for the $(1T)_4$ π-bridge ($5.32 \cdot 10^{13}$ s^{-1}) than for the $(4T)_1$ π-bridge ($7.11 \cdot 10^{13}$ s^{-1}), with both falling below their respective π–π-stacked values (note the presence of a hybridized LE_D state in the π–π-stacked configuration of $(1T)_4$). Given the similar EC values and CT state distributions, we conclude that the π-bridge fusion pattern does not significantly affect ET through electronic interactions alone. However, limitations may arise from morphological factors, such as increased donor molecule size in the non-fused configuration, it's flexibility, and enhanced permanent dipole moment can change the overall donor:acceptor interface configuration.

When comparing the calculated rate constants to those of the reference donor polymer PM6 paired with Y6, we find that PM6:Y6 in a representative π—π-stacked configuration exhibits total HT and ET rate constants of approximately $6 \cdot 10^{12}$ and $5 \cdot 10^{13}$ s^{-1}, respectively (see Section SG, Supporting Information). In contrast, the donor molecules investigated in this study show significantly higher rate constants for both HT and ET, primarily due to enhanced EC. This indicates that finite size donor molecules may offer a promising molecular architecture for achieving highly efficient OPV devices, owing to their more readily tunable FMO energy levels and exceptionally high transition rate constants, which is indicative of efficient charge generation. However, it is important to note that donor polymers and small-molecule donors differ markedly in their aggregation behavior, which plays a critical role in device performance. Although our study focuses on the intrinsic electronic interactions at the donor:acceptor interface, it does not address morphological effects. A comprehensive understanding of morphology-driven phenomena at the interface remains an essential avenue for future research.

In the context of the 2D electronic structure opened by the core's side chain, we highlight the recent integration of 'four-arm' donor molecules as an additional component in OPV devices, particularly in ternary blends such as PM6:Y6:four-arm-donor [62] and PM6:four-arm-donor:L8-BO [63]. These four-arm structures can be viewed as extensions of the core's side chain by incorporating π-bridges with terminal groups. The advanced donor architecture in ternary blends has been shown to reduce overall electronic disorder by promoting a more favorable morphology – driven by strong van der Waals interactions between the four-arm donor and the PM6 polymer. This morphological optimization results in improved PCEs in the ternary blend and enhanced hole mobility in the donor complex compared to systems using only isolated PM6 or the donor molecule alone. As discussed earlier, the 2D HOMO distribution in the engineered donor systems profoundly affects both their opto-electronic properties and HT rates, primarily through the (mis)-alignment of excited-state dipole moments. A more systematic investigation into the design of the core's side chain – particularly its role in shaping morphology and enabling extended HOMO delocalization in two- or even 3D architectures – could provide deeper insights into the mechanisms behind the observed improvements in hole transport in these advanced donor complex architectures.

4 | Conclusion

In this work, we systematically engineered donor molecules of the form A–π–Core–π–A by modulating the π-bridge and electron-withdrawing (EW) terminal group, with the goal of tuning their electronic structure, excitonic properties, and charge transfer (CT) characteristics in complexes with non-fullerene acceptor (NFA) Y6. Using a combined approach based on density functional theory and Marcus theory, we identified four key findings:

1. For small, fused π-bridges, the HOMO is significantly influenced by the core's side chain, resulting in more 2D delocalization. In contrast, for longer or non-fused π-bridges, the HOMO is primarily distributed linearly along the molecular backbone.
2. The exciton binding energy (ΔE_B) can be effectively tailored by adjusting the length and fusion pattern of the π-bridge, whereas the singlet–triplet energy gap (ΔE_{ST}) is predominantly controlled by the EW strength of the terminal group. Stronger EW groups confine the LUMO and HOMO distributions toward the terminal and central parts of the molecule, respectively.
3. The 2D HOMO delocalization in small, fused π-bridges enhances the transition dipole moment but slightly misaligns the dipole moments of the locally excited (LE) and CT states. Combined with a reduced CT-state manifold, this leads to slightly lower hole transfer (HT) rate constants compared to their non-fused analogs. Electron transfer (ET) rate constants, on the other hand, decrease with increasing

molecular length and are strongly influenced by the EW character of the terminal groups.

4. Geometric disorder has a more pronounced impact on the electronic and optical properties of non-fused systems than on fused ones, though in a systematic and predictable fashion that preserves energy disorder. ET and HT rate constants, however, are more sensitive to local interfacial configurations in non-fused systems, while remaining more stable in fused architectures.

Finally, we emphasize that this study does not consider the detailed aggregation or morphological behavior of donor molecules – factors that play a crucial role in real-world device performance. Nonetheless, our findings offer valuable insight into the intrinsic electronic structure and charge transfer dynamics of designed donor systems, providing a foundation for further exploration of efficient all-molecule organic photovoltaic architectures. The developed design rules and molecular systems can drive experimental efforts to synthesize materials with specifically tailored opto-electronic properties and targeted energy offsets, offering deeper insight into their impact on device efficiency. Additionally, large-scale molecular dynamics simulations can reveal packing patterns and interactions with NFAs, further clarifying specific structure–performance relationships.

Acknowledgements

The authors are grateful to Jean-Luc Brédas and Veaceslav Coropceanu for valuable discussions regarding morphology-induced changes in the exciton dissociation process. The authors gratefully acknowledge the computing time provided to them on the high-performance computers Noctua 2 [64] at the NHR Center PC2. These were funded by the Federal Ministry of Education and Research and the state governments participating on the basis of the resolutions of the GWK for the national high-performance computing at universities (www.nhr-verein.de/unsere-partner). The computations for this research were performed using computing resources under project hpc-prf-hdpadi.

Conflicts of Interest

The authors declare no conflicts of interest.

Data Availability Statement

The data that support the findings of this study are available in the supplementary material of this article.

References

1. G. Dennler, M. C. Scharber, and C. J. Brabec, "Polymer-fullerene bulk-heterojunction solar cells," *Advanced Materials* 21, no. 13 (2009): 1323–1338.

2. J. Yi, G. Zhang, H. Yu, and H. Yan, "Advantages, challenges and molecular design of different material types used in organic solar cells," *Nature Reviews Materials* 9, no. 1 (2024): 46–62.

3. Y. Lin, J. Wang, Z.-G. Zhang, et al., "An electron acceptor challenging fullerenes for efficient polymer solar cells," *Advanced Materials* 27, no. 7 (2015): 1170–1174.

4. W. Zhao, S. Li, H. Yao, et al., "Molecular optimization enables over 13% efficiency in organic solar cells," *Journal of the American Chemical Society* 139 (2017): 7148–7151.

5. J. Hou, O. Inganäs, R. H. Friend, and F. Gao, "Organic solar cells based on non-fullerene acceptors," *Nature Materials* 17, no. 2 (2018): 119–128.

6. J. Yuan, Y. Zhang, L. Zhou, et al., "Single-junction organic solar cell with over 15% efficiency using fused-ring acceptor with electron-deficient core," *Joule* 3, no. 4 (2019): 1140–1151.

7. A. Armin, W. Li, O. J. Sandberg, et al., "A history and perspective of non-fullerene electron acceptors for organic solar cell," *Advanced Energy Materials* 11 (2021): 20003570.

8. P. Murugan, T. Hu, X. Hu, and Y. Chen, "Fused ring A-D-A'-D-A (Y-series) non-fullerene acceptors: recent development and design strategies for organic photovoltaics," *Journal of Materials Chemistry A* 10 (2022): 17968–17987.

9. C. Chen, L. Wang, W. Xia, et al., "Molecular interaction induced dual fibrils towards organic solar cells with certified efficiency over 20%," *Nature Communications* 15, no. 1 (2024): 6865.

10. L. Zhu, M. Zhang, G. Zhou, et al., "Achieving 20.8% organic solar cells via additive-assisted layer-by-layer fabrication with bulk p-i-n structure and improved optical management," *Joule* 8, no. 11 (2024): 3153–3168.

11. S. Shoaee, H. M. Luong, J. Song, Y. Zou, T.-Q. Nguyen, and D. Neher, "What we have learnt from PM6:Y6," *Advanced Materials* 36 (2024): 2302005.

12. S. Mahadevan, T. Liu, S. M. Pratik, et al., "Assessing intra- and intermolecular charge transfer excitations in non-fullerene acceptors using electroabsorption spectroscopy," *Nature Communications* 15, no. 1 (2024): 2393.

13. W. Qiu and S. Zheng, "Designing and screening high-performance non-fullerene acceptors: A theroetical exploration of modified Y6," *Solar RRL* 5 (2021): 2100023.

14. M. Khalid, M. U. Khan, E.-T. Razia, et al., "Exploration of efficient electron acceptors for organic solar cells: rational design of indacenodithiophene based non-fullerene compounds," *Scientific Reports* 11, no. 1 (2021): 19931.

15. G. Bary, L. Ghani, M. I. Jamil, et al., "Designing small organic non-fullerene acceptor molecules with diflorobenzene or quinoline core and dithiophene donor moiety through density functional theory," *Scientific Reports* 11, no. 1 (2021): 19683.

16. G. Yu, J. Gao, J. C. Hummelen, F. Wudl, and A. J. Heeger, "Polymer photovoltaic cells: Enhanced efficiencies via a network of internal donor-acceptor heterojunctions," *Science* 270, no. 5243 (1995): 1789–1791.

17. H. Fu, Z. Wang, and Y. Sun, "Polymer donors for high-performance non-fullerene organic solar cells," *Angewandte Chemie International Edition* 58 (2019): 4442–4453.

18. Y. Li, W. Huang, D. Zhao, et al., "Recent progress in organic solar cells: A review on materials from acceptor to donor," *Molecules* 27, no. 6 (2022): 1800.

19. D. Deng, Y. Zhang, J. Zhang, et al., "Fluorination-enabled optimal morphology leads to over 11% efficiency for inverted small-molecule organic solar cells," *Nature Communications* 7 (2016): 13740.

20. K. Sun, Z. Xiao, S. Lu, et al., "A molecular nematic liquid crystalline material for high-performance organic photovoltiacs," *Nature Communications* 6 (2015): 6013.

21. D. Han, S. Wen, F. Bi, et al., "Small molecular donor materials based on electron withdrawing benzobisthiazole core unit enable an efficiency of 11.8% for organic solar cells," *Chemical Engineering Journal* 463 (2023): 142400.

22. D. Han, S. Wen, K. Song, et al., "Benzobisthiazole and rhodanine based low energy level small molecule donors for organic solar cells," *Dyes and Pigments* 234 (2025): 112564.

23. H. Gao, Y. Sun, L. Meng, C. Han, X. Wan, and Y. Chen, "Recent progress in all-small-molecule organic solar cells," *Small* 19, no. 3 (2023): 2205594.

24. S. M. Menke, A. Cheminal, P. Conaghan, et al., "Order enables efficient electron-hole separation at an organic heterojunction with a small energy loss," *Nature Communications* 9, no. 1 (2018): 277.

25. T. M. Clarke and J. R. Durrant, "Charge photogeneration in organic solar cells," *Chemical Reviews* 110, no. 11 (2010): 6736–6767.

26. L. Zhu, Y. Yi, and Z. Wei, "Exciton binding energies of nonfullerene small molecule acceptors: Implication for exciton dissociation driving forces in organic solar cells," *The Journal of Physical Chemistry C* 122 (2018): 22309–22316.

27. Y. Zhu, F. Zhao, W. Wang, Y. Li, S. Zhang, and Y. Lin, "Exciton binding energy of non-fullerene electron acceptors," *Advanced Energy and Sustainability Research* 3 (2022): 2100184.

28. A. Köhler and H. Bässler, "Triplet states in organic semiconductors," *Materials Science and Engineering: R: Reports* 66, no. 4 (2009): 71–109.

29. N. Aizawa, Y. Harabuchi, S. Maeda, and Y.-J. Pu, "Kinetic prediction of reverse intersystem crossing in organic donor–acceptor molecules," *Nature Communications* 11, no. 1 (2020): 3909.

30. G. Han, T. Hu, and Y. Yi, "Reducing the singlet-triplet energy gap by end-group π-π stacking toward high-efficiency organic photovoltaics," *Advanced Materials* 32 (2020): 2000975.

31. R. A. Marcus, "Electron transfer reactions in chemistry: Theory and experiment," *Reviews of Modern Physics* 65 (1993): 599–610.

32. V. Coropceanu, X.-K. Chen, T. Wang, Z. Zheng, and J.-L. Brédas, "Charge-transfer electronic states in organic solar cells," *Nature Reviews Materials* 4 (2019): 689–707.

33. T. Fukuhara, Y. Tamai, and H. Ohkita, "Nongeminate charge recombination in organic photovoltaics," *Sustainable Energy Fuels* 4, no. 9 (2020): 4321–4351.

34. M. J. Frisch, G. W. Trucks, H. B. Schlegel, et al., "Gaussian˜ 16 Revision C.01," (gaussian Inc., Wallingford CT, 2016).

35. Z. Hu, B. Zhou, Z. Sun, and H. Sun, "Prediction of excited-state properties of oligoacene crystals using polarizable continuum model-tuned range-separated hybrid functional approach," *Journal of Computational Chemistry* 38 (2017): 569–575.

36. L. Kronik and S. Kümmel, "Dielectric screening meets optimally tuned density functionals," *Advanced Materials* 30, no. 41 (2018): 1706560.

37. S. Hirata and M. Head-Gordon, "Time-dependent density functional theory within the tamm-dancoff approximation," *Chemical Physics Letters* 314 (1999): 291–299.

38. J. E. Subotnik, S. Yeganeh, R. J. Cave, and M. A. Ratner, "Constructing diabatic states from adiabatic states: Extending generalized mulliken–hush to multiple charge centers with boys localization," *The Journal of Chemical Physics* 129 (2008): 244101.

39. V. Lemaur, M. Steel, D. Beljonne, J.-L. Brédas, and J. Cornil, "Photoinduced charge generation and recombination dynamics in model donor/acceptor pairs for organic solar cell applications: A full quantum-chemical treatment," *Journal of the American Chemical Society* 127 (2005): 6077–6086.

40. T. Lu and F. Chen, "Multiwfn: a multifunctional wavefunction analyzer," *Journal of Computational Chemistry* 33 (2012): 580–592.

41. Q. Wang, X. Zhang, Y. Miao, et al., "Synergy effect of symmetry-breaking and end-group engineering enables 16.06% efficiency for all-small-molecule organic solar cells," *ACS Materials Letters* 6, no. 2 (2024): 713–719.

42. Z. Li, G. He, X. Wan, et al., "Solution processable rhodanine-based small molecule organic photovoltaic cells with a power conversion efficiency of 6.1%," *Advanced Energy Materials* 2, no. 1 (2012): 74–77.

43. R. Zhou, Z. Jiang, C. Yang, et al., "All-small-molecule organic solar cells with over 14% efficiency by optimizing hierarchical morphologies," *Nature Communications* 10 (2019): 5393.

44. G. Zhang, G. Yang, H. Yan, et al., "Efficient nonfullerene polymer solar cells enabled by a novel wide bandgap small molecular acceptor," *Advanced Materials* 29, no. 18 (2017): 1606054.

45. X. Xu, Z. Bi, W. Ma, et al., "Highly efficient ternary-blend polymer solar cells enabled by a nonfullerene acceptor and two polymer donors with a broad composition tolerance," *Advanced Materials* 29, no. 46 (2017): 1704271.

46. J. Wu, J. Lee, Y.-C. Chin, et al., "Exceptionally low charge trapping enables highly efficient organic bulk heterojunction solar cells," *Energy & Environmental Science* 13 (2020): 2422–2430.

47. D. Qian, Z. Zheng, H. Yao, et al., "Design rules for minimizing voltage losses in high-efficiency organic solar cells," *Nature Materials* 17, no. 8 (2018): 703–709.

48. L. Zhu, Z. Wei, and Y. Yi, "Exciton binding energies in organic photovoltaic materials: A theoretical perspective," *The Journal of Physical Chemistry C* 126, no. 1 (2022): 14–21.

49. S. Y. Leblebici, T. L. Chen, P. Olalde-Velasco, W. Yang, and B. Ma, "Reducing exciton binding energy by increasing thin film permittivity: An effective approach to enhance exciton separation efficiency in organic solar cells," *ACS Applied Materials & Interfaces* 5, no. 20 (2013): 10105–10110.

50. Z. Li, X. Wang, N. Zheng, et al., "Over 17% efficiency all-small-molecule organic solar cells based on an organic molecular donor employing a 2d side chain symmetry breaking strategy," *Energy & Environmental Science* 15, no. 10 (2022): 4338–4348.

51. F. Bauch, C.-D. Dong, and S. Schumacher, "Dynamics-induced charge transfer in semiconducting conjugated polymers," *Journal of Materials Chemistry C* 11 (2023): 12992–12998.

52. B. Carsten, J. M. Szarko, H. J. Son, et al., "Examining the effect of the dipole moment on charge separation in donor–acceptor polymers for organic photovoltaic applications," *Journal of the American Chemical Society* 133 (2011): 20468–20475.

53. B. Carsten, J. M. Szarko, L. Lu, et al., "Mediating solar cell performance by controlling the internal dipole change in organic photovoltaic polymers," *Macromolecules* 45, no. 16 (2012): 6390–6395.

54. M. Privado, P. de la Cruz, P. Malhotra, G. D. Sharma, and F. Langa, "Influence of the dipole moment on the photovoltaic performance of polymer solar cells employing non-fullerene small molecule acceptor," *Solar Energy* 221 (2021): 393–401.

55. C. J. Takacs, Y. Sun, G. C. Welch, et al., "Solar cell efficiency, self-assembly, and dipole–dipole interactions of isomorphic narrow-band-gap molecules," *Journal of the American Chemical Society* 134, no. 40 (2012): 16597–16606.

56. F. Bauch, C.-D. Dong, and S. Schumacher, "Dynamics of electron–hole coulomb attractive energy and dipole moment of hot excitons in donor–acceptor polymers," *The Journal of Physical Chemistry C* 128, no. 8 (2024): 3525–3532.

57. S. Xie, Y. Xia, Z. Zheng, et al., "Effects of nonradiative losses at charge transfer states and energetic disorder on the open-circuit voltage in nonfullerene organic solar cells," *Advanced Functional Materials* 28 (2018): 1705659.

58. X. Liu, B. P. Rand, and S. R. Forrest, "Engineeering charge-transfer states for efficient, low-energy-loss organic photovoltaics," *Trends in Chemistry* 1 (2019): 815–829.

59. G. Han and Y. Yi, "Local excitation/charge-transfer hybridization simultaneously promotes charge generation and reduces nonradiative voltage loss in nonfullerene organic solar cells," *Journal of Physical Chemistry Letters* 10 (2019): 2911–2918.

60. G. Grancini, M. Maiuri, D. Fazzi, et al., "Hot exciton dissociation in polymer solac cells," *Nature Materials* 12 (2013): 29–33.

61. B. R. Gautam, R. Younts, W. Li, et al., "Charge photogeneration in organic photovoltaics: Role of hot versus cold charge-transfer excitons," *Advanced Energy Materials* 6, no. 1 (2016): 1301032.

62. X. Li, A. Tang, H. Wang, et al., "Benzotriazole-based 3d four-arm small molecules enable 19.1% efficiency for PM6:Y6-based ternary organic solar cells," *Angewandte Chemie International Edition* 62 (2023): e202306847.

63. W. Miao, Y. Liu, Y. Wu, et al., "Energy disorder suppression, charge transport channel establishment by integrating four-arm donor molecule for high-performance organic solar cells," *Advanced Functional Materials* 35 (2025): 2501143.

64. C. Bauer, T. Kenter, M. Lass, et al., "Noctua 2 supercomputer," *Journal of large-scale research facilities JLSRF* 9 (2024): A187.

Supporting Information

Additional supporting information can be found online in the Supporting Information section.

Supporting File: adts70265-sup-0001-SuppMat.pdf.

THE JOURNAL OF PHYSICAL CHEMISTRY C
A JOURNAL OF THE AMERICAN CHEMICAL SOCIETY

pubs.acs.org/JPCC

Article

Dynamics of Electron−Hole Coulomb Attractive Energy and Dipole Moment of Hot Excitons in Donor−Acceptor Polymers

Fabian Bauch, Chuan-Ding Dong, and Stefan Schumacher*

Cite This: J. Phys. Chem. C 2024, 128, 3525−3532

Read Online

ACCESS | Metrics & More | Article Recommendations | Supporting Information

ABSTRACT: Understanding charge separation processes after photoexcitation in organic photovoltaics is of great importance for optimizing device performance. Many studies have associated a polaron-pair or intrachain charge transfer state in organic polymers with an increased charge separation efficiency. It is then natural to ask how the chemical structure influences charge separation, enabling a more targeted material design. Here, we report on nonadiabatic *ab initio* molecular dynamics simulations of the hot exciton dynamics following photoexcitation for a series of donor−acceptor polymers. We provide detailed insights into the Coulomb attractive energy and the dynamical evolution of dipole moments in the excited states. The former is correlated with polaron-pair recombination, thus preventing charge separation; the latter is a potential enabler of charge separation. We calculate the ultrafast dynamics of these relatively simple charge-separation-efficiency quantifiers, correlate them with the underlying chemical structure, and relate them to their static counterparts in statistical ensembles. Our work provides an ensemble description of the dynamic process of the photoexcited polaron formation and solidifies the role of Coulomb attractive energy and excited state dipole moment as the descriptors of this process on a microscopic level.

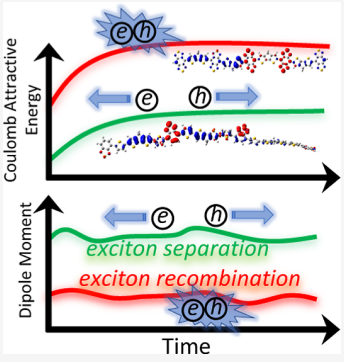

INTRODUCTION

Increasing energy consumption has led to a growing interest in organic semiconductors (OSCs), especially in the field of organic photovoltaics (OPV), converting light into an electric current. Due to many advantages over their inorganic counterparts, such as the flexibility of organic materials, high availability, and low-cost production, to name a few, organic systems hold great promise for future everyday applications.[1−5] Although the class of potential applications and advantages of OSCs is numerous, a complete understanding and optimization of the electronic properties of OSCs is challenging due to their complexity compared to inorganic solids.

The understanding of photoexcited excitons (Coulomb-bonded electron−hole pairs) in OPV is of major importance because their behavior dominates the materials' photophysics, including exciton migration and dissociation (charge separation of electron and hole).[6,7] The low dielectric constant of OSCs leads to a comparably strong Coulomb interaction between the electron and hole,[8] and as a result, a low power conversion efficiency with one of the highest reports of 18.66% for a nonfullerene acceptor in a ternary blend.[9] A critical limiting factor for the efficiency of photoexcited devices is the exciton lifetime, during which electrons and holes recombine and the excited state relaxes back to the system's ground state. It has been shown that photoexcitation with higher energy than band gap energy, generating so-called hot excitons, leads to higher efficiency of charge separation at the donor−acceptor interface via the occupation of hot charge transfer (CT) states (CT excitons).[8] Theoretical description via nonadiabatic dynamics simulation was employed[10,11] to gain further insights revealing the hot CT excitons to drive charge separation at the interface[12] and a large energy gap between CT states and lower excitonic states to increase the exciton lifetime in molecular aggregates.[13]

Even without a donor−acceptor interface, free charge generation was reported[14,15] and traced back to a spontaneous intramolecular splitting process in nonfullerene acceptor Y6[15] or to an intermoiety charge transfer exciton (i-EX) within the acceptor (or donor) aggregates.[9,16,17] Similar to the i-EX state within an aggregate, an intramolecular charge transfer (ICT) state, or polaron-pair state, within one OSC chain/molecule is believed to favor subsequent charge separation due to a delocalized electron and hole wave function and thus lower Coulomb interaction correlating the charges.[18,19] Such ICT states were found to be quickly occupied and to act as precursors for a charge-separated state within <200 fs. Such dynamics is favored by the excitation of higher-lying excited states,[20−23] rendering the ICT state more relevant in the early times of exciton generation. Moreover, the importance of a highly polarized state, i.e., a large electrical dipole moment,

Received: November 14, 2023
Revised: January 16, 2024
Accepted: February 2, 2024
Published: February 15, 2024

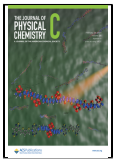

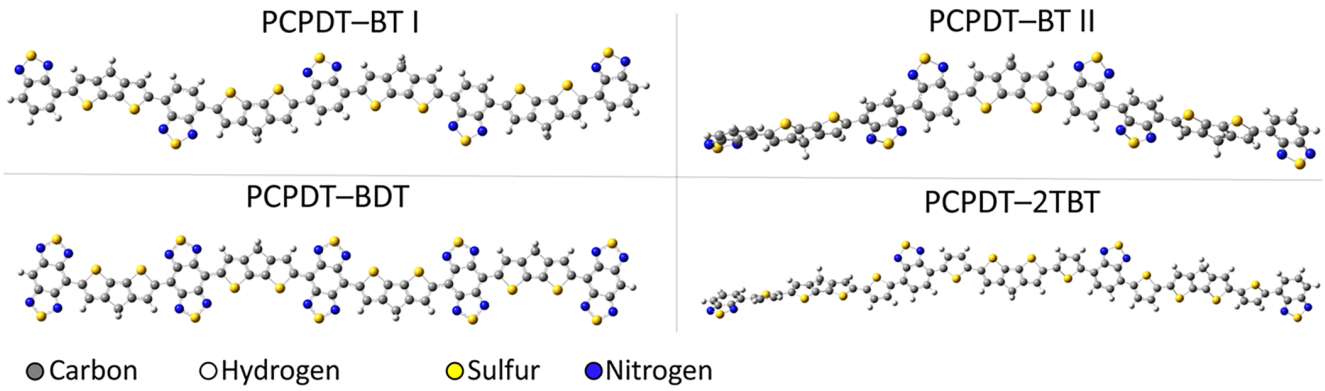

Figure 1. Optimized structures of the donor–acceptor polymers investigated in this work. The polymers PCPDT–BT I, PCPDT–BDT, and PCPDT–2TBT were investigated experimentally by Tautz et al.[29] PCPDT–BT II is a model polymer to investigate the effect of an enlarged acceptor unit.

created by the exciton was found to indicate an easier charge separation because of a better separated electron and hole wave function[24−26] and consequently weaker Coulomb interaction with the delocalization promoting charge separation.[20]

Recombination and charge separation processes are sensitive to the OSC structure. A promising route is to use donor–acceptor alternating polymers with their electron "push" and "pull" effects[27] to promote spatially separated electron and hole wave functions,[28] i.e., polarized ICT or polaron-pair states. Investigation of four similar donor–acceptor polymers based on the CPDT-donor component by Tautz et al.[29] revealed that acceptor units with higher electron affinity lead to higher initial polaron-pair state generation but also increased charge recombination (lower lifetime), whereas a π-spacer between both units leads to a decreased charge recombination probability (higher lifetime) while also lowering the initial polaron-pair generation probability,[19] possibly due to a π-bridge planarization mechanism reported within 400 fs.[13] The detailed understanding of general design rules to inhibit exciton recombination and thus enhance the efficiency of the charge separation process, however, is still somewhat limited.

In this work, we use nonadiabatic *ab initio* molecular dynamics (NA-AIMD) simulations to investigate the hot exciton behavior within the first 200 fs after photoexcitation on single chains of an extended series of CPDT-donor-based polymers experimentally investigated by Tautz et al.[29] (Figure 1) in order to understand the effects of different donor–acceptor structures on the electron–hole interaction.

By analyzing the photoexcitation dynamics in terms of the (time-resolved) Coulomb attractive energy between the electron and hole density on one polymer chain and the (time-resolved) dipole moment, we investigate the ultrafast charge separation. We obtain detailed microscopic insights that systematically substantiate the analysis of experimental observations and correlate the charge generation efficiency with the structures of the investigated donor–acceptor polymers. While the Coulomb attractive energy is used as a quantifier that can drive fast recombination, a polarized excited state with a large dipole moment correlates with enhanced charge separation. Increasing the latter and reducing the former are identified as a viable strategy in the search for new promising materials for OPV devices.

COMPUTATIONAL DETAILS

The calculations are based on density functional theory (DFT) and related time-dependent DFT (TD-DFT) by employing the Gaussian 16[30] package. For all calculations a range-separated functional is used, similar to our previous work,[31−34] namely, ωb97xd, where ω is kept at its default value. We note that this functional incorporates dispersion corrections, i.e., van der Waals interaction. The Pople-type 6-31G(d,p) basis set is used throughout the calculations. All calculations are done in gas phase.

The oligomers optimized in their ground states are shown in Figure 1. We replaced the side chains and saturated the polymer ends with hydrogen atoms to reduce the computational cost, which has only small effects on the electronic structure and optical excitations. We point out that the oligomer structures investigated in the present work contain 4 or 5 acceptor units and 3 or 4 donor units, which ensures sufficient length to describe the electronic behavior of the single polymers. Due to the high computational cost, in the present work, we restrict ourselves to individual polymers and did not address the CT behavior in typical morphologies in solution or film, such as aggregated polymers or polymers with self-folding,[35] which could be the goal of our future work. We checked that all optimized polymers exhibit positive frequencies only, verifying the ground state optimization. Single-point TD-DFT calculations of 30 singlet excited states are performed to calculate the excitation spectra for the optimized polymers. An ensemble of 1000 structures based on the nuclear ensemble approach[36] is used to calculate an ensemble absorption spectrum. For both the single-point TD-DFT and the ensemble approach, the transitions are convoluted by Lorentzian shapes with a phenomenological broadening of 0.2 eV.

The NA-AIMD simulations are performed using Gaussian 16[30] interfaced with Newton-X.[37] The 1000 structures for the ensemble absorption spectrum are used as initial conditions centered at the high energy absorption peaks, as indicated by the blue lines in Figure 2. The energy width of each excitation was chosen such that about 100 initial conditions were accepted, as explained in more detail in the Supporting Information. The exact numbers of initial conditions and the values of excitation conditions are shown in Table S1 in the Supporting Information. The NA-AIMD simulations employ trajectory surface hopping with the fewest switching criterion.[38−40] In the NA-AIMD calculations, the motion of

https://doi.org/10.1021/acs.jpcc.3c07513
J. Phys. Chem. C 2024, 128, 3525−3532

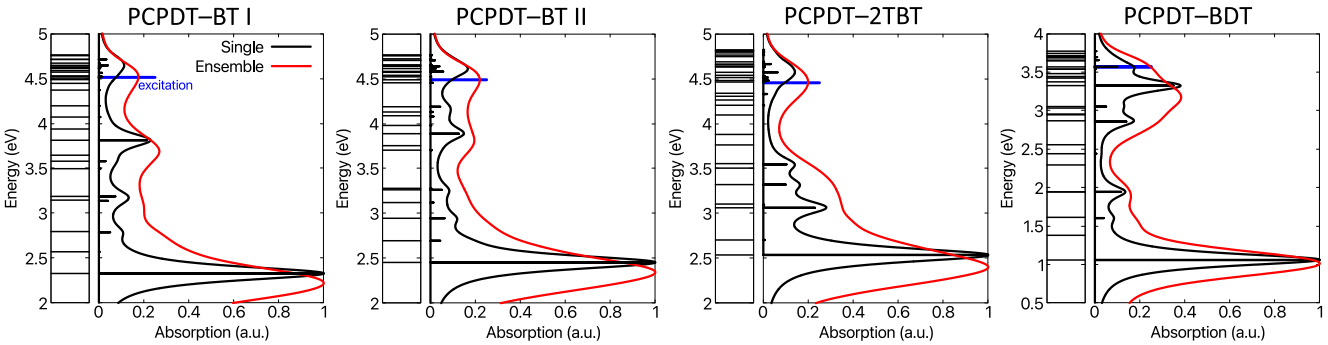

Figure 2. Normalized absorption spectra of the donor−acceptor polymers. The small left columns give a feeling for the density of the excited states for the optimized polymer structures. The big columns show the normalized absorption spectra of the optimized polymer structures (black) and the polymer ensembles (red), as discussed in the main text. The horizontal black lines show the normalized oscillator strength of the excited states for the optimized polymers. The blue line indicates the excitation energy for the NA-AIMD simulations. Note the different energy scales for PCPDT−BDT.

the nuclei is treated classically with a chosen time step of 0.5 fs, while the electrons are treated on a quantum level. The nonadiabatic couplings that determine the transitions between electronic states are evaluated based on overlaps between excitonic wave functions, which were already used for the NA-AIMD simulations of oligothiophenes.[10,13] Here, a screening threshold of 5×10^{-4} and the decoherence correction proposed by Granucci and Persico[41] with the default value were used. We deem this mixed quantum-classical approach suitable for the purposes of the present work, where quantization of the motion of nuclei is not the focus. The NA-AIMD trajectories were propagated by involving 30 excited singlet states. To calculate the properties of the ground and excited states, i.e., the charge density difference, Coulomb attractive energy, and the electrical dipole moment, we use the Multiwfn[42] package.

RESULTS AND DISCUSSION

Absorption Spectra. The calculated absorption spectra for the optimized polymers and for the ensembles consisting of 1000 sampled polymer structures are shown in Figure 2. The ensemble absorption spectra for PCPDT−BT I, PCPDT−2TBT, and PCPDT−BDT reproduce the experimental features qualitatively well.[29] PCPDT−BT I features one main peak at around 2.22 eV with a shoulder peak at around 3.06 eV, a second peak at around 3.69 eV, and a third peak at around 4.52 eV. We note that the absolute values of the excitation energies depend much on the method used and are not directly comparable to the experiment. We did not consider the interaction between the polymer chains such as in self-aggregated, folded polymer chains.[35] However, the relative ordering of the main absorption peaks for the investigated polymers is well described by the method used and agrees with the experimentally reported ordering. By increasing the spacing between the donor and acceptor units by a π-linker, i.e., polymer PCPDT−2TBT, the main absorption peak shifts by about 0.19 eV to a slightly higher energy (around 2.41 eV) and the second peak shifts by around 0.39 eV to a slightly lower energy around 3.30 eV, appearing as a shoulder of the main peak. Both shifts are qualitatively in good agreement with the experiment[29] and decrease the energy gap between the main peak and the second peak. The third peak is almost unaffected by the increased distance between the donor and acceptor units. Increasing the electron affinity of the acceptor unit, i.e., polymer PCPDT−BDT, the absorption spectrum changes fundamentally. A main peak appears at 1.02 eV and a second peak appears at 1.88 eV. Moreover, a broad absorption band at higher energies with a maximum at 3.17 eV is formed. Increasing the acceptor unit size, i.e., model polymer PCPDT−BT II, the main peak shifts slightly to a higher energy (2.34 eV). The second peak is reduced in amplitude and shifted to a slightly higher energy at around 3.82 eV. The third peak is almost unaffected, similar to the π-linker polymer.

Static Coulomb Attractive Energy. Let us now turn to the Coulomb attractive energy (CAE), which quantifies the attractive force between charges and thus serves as an indicator of the expected charge separation efficiency. The CAE is evaluated by the electrostatic expression

$$E_C = -\iint \frac{\rho^{hole}(\mathbf{r}_1)\rho^{ele}(\mathbf{r}_2)}{|\mathbf{r}_1 - \mathbf{r}_2|} d\mathbf{r}_1\, d\mathbf{r}_2 \quad (1)$$

where ρ^{hole} (ρ^{ele}) is the hole (electron) density of the excited state wave function,[42,43] including normalization. For a more detailed description, we refer the reader to the Multiwfn[42] manual. We note that this CAE is not identical with the exciton binding energy, which is the energy difference between an exciton and both isolated negative and positive free charges. We use a subensemble of 200 structures for each polymer based on the 1000 structure ensembles to calculate the mean value of the CAE for each polymer. We note that 200 structures are sufficient for convergence of the values, as shown in Figure S1 in the Supporting Information. This approach leads to a static CAE estimate based on a ground state ensemble. The mean values of the CAE are shown in Figure 3.

Different trends are apparent for the four different polymers. PCPDT−BT I features a high CAE for the lowest five excited states and then monotonically decreases to about excited state 15 and saturates to a low CAE for higher excited states. The model polymer PCPDT−BT II appears similar and the curves almost overlap; however, the lowest excited states feature lower CAE than the lowest excited states of PCPDT−BT I. The extended separation between the donor and acceptor unit, i.e., PCPDT−2TBT, leads to an overall lower CAE for the lowest 15 excited states. Higher states feature a saturation value similar to that for PCPDT−BT I and II. While these three systems show quite similar behavior, the strong acceptor polymer PCPDT−BDT features overall much higher CAE values. For higher excited states, the CAE for this polymer saturates to the CAE values approximately 0.3 eV higher than

https://doi.org/10.1021/acs.jpcc.3c07513
J. Phys. Chem. C 2024, 128, 3525−3532

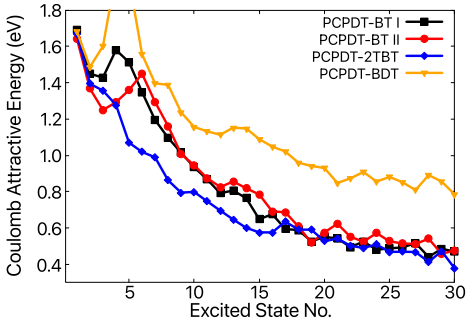

Figure 3. Mean values of the Coulomb attractive energy for each polymer. The mean values cover 200 structures for each polymer. The values of excited states four and five of PCPDT−BDT are 1.99 and 1.97 eV, respectively.

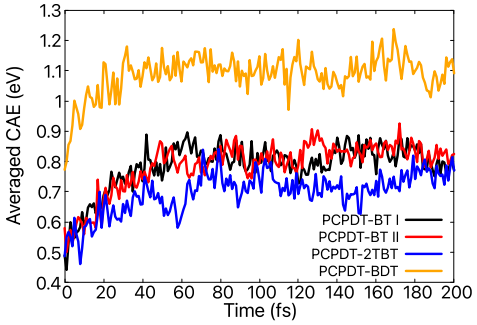

Figure 4. Time-dependent Coulomb attractive energy for each polymer averaged over all trajectories of the dynamics. The Coulomb attractive energy values are calculated at each 1 fs time step.

the other three polymers. Also, the lower excited states feature much higher CAE values.

Based on the CAE for the excited states of the optimized polymers and the charge density difference of the corresponding excited states (as discussed in more detail in the Supporting Information with Figure S2), we can assign three general design rules to modify the CAE: (i) by increasing the spacing between the donor and acceptor units, the overlap of the hole and electron wave functions decreases, thus decreasing the CAE; (ii) the π-character of the hole wave function in the high-lying excited states decreases, consequently decreasing the CAE. In contrast, a strong $\pi \rightarrow \pi^*$ character increases the CAE and is thus unfavorable for high-lying excited states; (iii) a larger acceptor unit leads to a larger distributed electron wave function and therefore lowers the overlap of the electron and hole wave functions and consequently lowers the CAE. We note that rule (iii) applies only to the lowest excited states, since at higher states the hole wave function involves the conjugated backbone of the acceptor units and consequently leads to a similar overlap between electron and hole for larger and smaller acceptor units.

Dynamic Coulomb Attractive Energy. Let us now turn to the dynamics of the systems. Starting from the photoexcitation with a certain excitation energy, the relaxation processes of the systems were described by a series of independent dynamic trajectories in the NA-AIMD simulations. For each polymer, the excitation energy is set to be higher than 3.5 eV, representing a hot exciton excitation in a high-lying excited state, as marked in Figure 2, acting as a precursor for polaron-pair states.[20−22] These trajectories are analyzed by computing the CAE via eq 1 for each trajectory at each 1 fs time step in the respective excited state and then averaging over all trajectories for each polymer. The dynamic evolution of the average CAE is shown in Figure 4.

For PCPDT−BT I, PCPDT−BT II, and PCPDT−2TBT, the dynamic CAE value starts from about 0.55 eV at 0 fs, increases about linearly, and then saturates. For the first two polymers PCPDT−BT I and II, the linear rise time is about 50 fs, and the saturation value of the CAE is about 0.8 eV, with no strong fluctuation. For the latter polymer PCPDT−2TBT, the linear rise time appears to be similar, but because of an apparent decrease at about 60 fs, the rise time cannot be fully estimated. This early time deviation from the rising trend may reflect the physical significance of a better-separated electron and hole wave function due to the distance between donor and acceptor moieties.

We note that the quick stabilization within about 60 fs of the dynamic CAE is consistent with the experimental reports on the generation of polaron-pair states. Rolczynski et al. have reported a pseudo-charge transfer state (polaron-pair state) and charge transfer state formation within 160 fs in a PTBF series,[20] and Cho et al. have reported on a new fast dissociation pathway (within 34 fs) in PTB7 after excitation with excess energy, which might have its origin in a pseudo-charge transfer state.[23]

The saturation value for PCPDT−2TBT is about 0.1 eV lower than those of the first two polymers. This is to be expected since the static CAE shows a similar trend for the lower half of the total excited states considered. For the polymer with the strong acceptor moiety, namely, PCPDT−BDT, the dynamic CAE is significantly higher than for the other three polymers but follows a similar trend. The linear initial rise time is about 35−40 fs, and the saturation value is about 1.1 eV, showing similar fluctuations to the other three polymers.

Dynamic Dipole Moment. Analogously to the calculation of the dynamic CAE, the electric dipole moment of the excited states is calculated for each trajectory at each 1 fs time step in the respective excited state by

$$\mu^{\mathrm{exc}} = \left| -e \int \rho^{\mathrm{exc}}(\mathbf{r})\mathbf{r}\, \mathrm{d}\mathbf{r} \right| \tag{2}$$

and then averaged over all trajectories for each polymer, where e is the elementary charge and ρ^{exc} is the density of the respective excited state. The results are shown in Figure 5. In

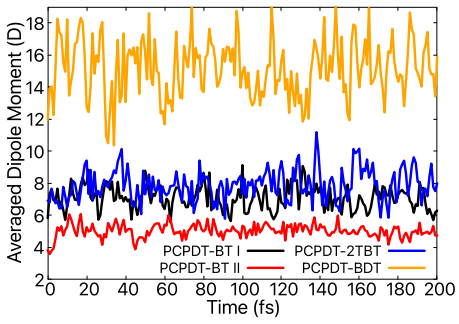

Figure 5. Time-dependent dipole moment for each polymer averaged over all trajectories of the dynamics. The dipole moment values are calculated for every 1 fs time step.

https://doi.org/10.1021/acs.jpcc.3c07513
J. Phys. Chem. C 2024, 128, 3525−3532

contrast to the dynamic CAE, the polymers PCPDT−BT I and PCPDT−BT II show a different behavior for the dynamic dipole moment. While for the former polymer the dipole moment shows fluctuations around a mean value of about 7 D, the latter polymer shows fluctuations around a lower value of about 5 D.

PCPDT−2TBT, on the other hand, appears similar to PCPDT−BT I, with the dipole moment fluctuating around a slightly higher mean value of about 7.5−8 D and exhibiting larger fluctuations. The polymer PCPDT−BDT with the highest CAE values also has the highest values for the dynamic dipole moment, fluctuating around a mean value of about 15 D. Interestingly, while the fluctuations for the polymer with the lowest dynamic dipole moments are very small, an increase in the mean value of the dipole moment leads to an increased fluctuation, e.g., the values for PCPDT−BDT fluctuate by about ±2 D. This feature is of electronic origin since the nuclei do not reorganize much on this very fast time scale. The high mobility and consequently time-dependent variation of electron and hole wave functions, possibly due to intersections of electronic states, could be responsible for this behavior.

Discussion. Analyzing experimental observations with detailed theoretical calculations and modeling is of great importance for a better understanding of the photophysical properties and mechanisms on a microscopic level. Based on our results, the experimental findings of Tautz et al.[29] can be substantiated, confirming the CAE as a driving force and good quantifier for the exciton recombination rate. The discussion is further extended by the effect that the electrical dipole moment has on charge separation and polaron-pair generation as proposed by Carsten et al.[24] We note that relatively high pump intensities were used in the experiments that might go beyond the regime simulated in the present work. Furthermore, we cannot rule out the self-aggregation of the polymers under experimental conditions. Experimentally, it was found that the polymer PCPDT−BDT features a high initial polaron-pair yield, followed by a high recombination rate (low lifetime). Moreover, PCPDT−BT I was found to have a lower generation of polaron pairs and also a lower recombination rate (higher lifetime), the latter being favorable for subsequent charge separation. The polymer with the π-spacer lowered both quantities even further and featured long-lived polaron-pair states.

The dynamic dipole moment and the dynamic CAE of PCPDT−BDT are both comparably high. The former can be seen as one of the indicators for the initial polaron-pair yield[24] and thus in line with the experimental results. The latter can be seen to be responsible for a charge recombination process. While the positive and negative charges of the exciton have to overcome the Coulomb barrier to be separated, the high CAE prevents charge separation and thus leads to recombination. The on-average relatively high dipole moment of PCPDT−BDT follows from contributions from trajectories that exhibit either an asymmetric or symmetric electron−hole distribution, as illustrated in Figure S3 in the Supporting Information. In some trajectories, the hole is mainly located in the backbone between two acceptor units that accommodate most of the delocalized electron. This symmetric distribution leads to a low dipole moment. On the other hand, an asymmetric electron−hole distribution, where the hole is located at the edge of the polymer backbone and the electron is more localized on the acceptor units in the center of the polymer, leads to a large dipole moment. Spatially separated electrons and holes are generally considered beneficial for subsequent charge separation; therefore, these results support the interpretation of the high dipole moment as an indicator for the efficient generation of polaron pairs.

To further explore the idea of the CAE being an indicator of recombination, we calculated the static CAE for PTB7 and PBB3 that were investigated by Carsten et al.[24] The lower static CAE of PBB3 in the lowest excited states (Figure S4 in the Supporting Information) is in line with the experimental finding of long-lived excitonic states for this polymer, thus demonstrating the CAE to correlate with the experimental findings for different polymers. In terms of relatively simple quantifiers, it is therefore possible to associate the charge recombination and charge separation with CAE and dipole moment, respectively.

Taking also geometrical considerations into account, the dynamic dipole moment as the indicator of charge separation appears to be influenced by the geometrical arrangement of the polymers. While the dynamic dipole moment and thus the degree of polarization of PCPDT−BT I and PCPDT−2TBT are quite similar, the experimental observations indicate a somewhat lower polaron-pair yield for the latter. This suggests that although the dipole moment correlates with the polarized ICT character of the state,[26] the spatial separation of the electron and hole wave function to form a polaron-pair state might be prevented by the rotational barriers between the π-spacer and the donor and acceptor units, which planarize on the sub-ps time scale to produce ICT states.[44] This shows that the complexity of the structure, especially the rotational barriers between the subunits of the polymers, influences the separation of the electron and hole wave function and must be considered in addition to physical quantities such as the dipole moment.

The overall lower dynamic CAE of the π-spaced polymer indicates a lower attractive potential and thus a lower recombination rate of the charges, possibly due to the spatial separation of the donor and acceptor units induced by the π-spacer, in line with the experimental findings.

These results indicate a competition between the charge separation process via a highly polarized ICT or polaron-pair state, which correlates to the dipole moment, and the CAE as an attractive interaction between the electron and hole to recombine. While the former needs to be comparably high to spatially separate the electron and hole, the latter should be reduced simultaneously. A possible route to achieve a polymer featuring these two properties is to increase the size of the acceptor unit instead of increasing the electron affinity of the acceptor unit (e.g., via the BDT acceptor unit). The idea is that, while a delocalized hole wave function reduces the recombination rate of the polaron-pair,[24] a delocalized electron wave function might have a similar effect. Our model polymer PCPDT−BT II features an acceptor unit consisting of two BT units rotated by 180°. While the dynamic CAE of the model polymer is similar to the CAE of PCPDT−BT I and indicates a similar recombination behavior, the dynamic dipole moment is lower than for PCPDT−BT I, indicating a less polarized excited state and consequently less initial polaron-pair generation. Both results combined lead to the expectation that the larger acceptor unit operates worse in OPV devices than PCPDT−BT I. The fundamentally different effect of the extended electron wave function due to a larger acceptor unit compared to the larger hole wave function initiated by a π-spacer for a hot exciton may originate from the fact that the

https://doi.org/10.1021/acs.jpcc.3c07513
J. Phys. Chem. C 2024, 128, 3525−3532

extension of the acceptor unit not only increases the backbone of the acceptor unit but also increases the interaction of the electron wave function with the enhanced "pulling" effect of the N-substitutions, thus trapping the electron wave function. We note that lower energy excitons, i.e., only the lowest excited states, may exhibit a different behavior for PCPDT−BT II. These insights indicate that there is a size limit for the acceptor unit similar to a size limit of the π-bridge[19] to optimize the device performance, thus providing new design rules to increase the polaron-pair separation. The optimized donor−acceptor polymer should have a donor and small acceptor unit well separated by a π-bridge with the acceptor unit's electron affinity being high enough to produce a strongly polarized excited state but not so high as to allow recombination due to strong Coulomb interaction of the excited electron and hole.

In a larger picture of charge separation processes in OPV, the initial polaron-pair formation on a single polymer/molecule would favor subsequent charge separation within polymer aggregates or at the donor/acceptor interface. The concept of interpreting the dipole moment and CAE as indicators for electron and hole wave function splitting or recombination, respectively, can also be applied to the aggregates and the interface itself, making this approach useful for the study and qualitative analysis of various polymer structures as well as complex morphology effects. The latter are known to have a strong influence on the dissociation of excitons through a disordered energy landscape,[45] close packing for extended delocalization of excitonic states[46] and thus an extended dipole moment, and relative orientation to influence the interfacial CT states.[47] However, the theoretical description and effects of large ensembles of different aggregates/interfaces are limited in the literature. Thus, modeling different aggregate ensembles of donor−acceptor interfaces, e.g., the widely used and promising polymer PM6 and the nonfullerene acceptor Y6, and analyzing their static or dynamic CAE as well as dipole moment can provide clues to the advantages of certain aggregates and possible charge separation pathways.

CONCLUSIONS

In conclusion, polaron-pair formation is believed to play an important role as a possible precursor for subsequent charge separation at donor−acceptor interfaces or within aggregates in OPV devices. In the present work, we performed detailed NA-AIMD calculations on a series of different polymer structures previously investigated experimentally to investigate the driving forces for the polaron-pair formation at high excitation energies. Our results and discussion provide further evidence that the dipole moment of the excited (excitonic) state can be interpreted as an indicator of efficient initial polaron-pair formation. In contrast, the Coulombic attractive energy appears to drive recombination. Thus, the former promotes subsequent charge separation, while the latter inhibits efficient charge generation. Our work provides an ensemble description of the dynamic process of photoexcited polaron formation and solidifies the role of Coulomb attractive energy and excited state dipole moment as the descriptors of this process on a microscopic level. The calculation of these two physical quantities, in a dynamic or static manner, can be used to explain the experimentally observed photovoltaic efficiencies for different interfaces.

ASSOCIATED CONTENT

Supporting Information

The Supporting Information is available free of charge at https://pubs.acs.org/doi/10.1021/acs.jpcc.3c07513.

Coulomb attractive energy convergence depending on ensemble size; charge density difference for the first 30 excited states of the optimized polymers; charge density difference for two example trajectories of PCPDT−BDT at 130 fs; Coulomb attractive energy for polymers PTB7 and PBB3; explanation of the NA-AIMD initial condition generation; and table with the NA-AIMD conditions (PDF)

AUTHOR INFORMATION

Corresponding Author

Stefan Schumacher − *Department of Physics and Center for Optoelectronics and Photonics Paderborn (CeOPP), Paderborn University, 33098 Paderborn, Germany; Wyant College of Optical Sciences, University of Arizona, Tucson, Arizona 85721, United States;* orcid.org/0000-0003-4042-4951; Email: stefan.schumacher@uni-paderborn.de

Authors

Fabian Bauch − *Department of Physics and Center for Optoelectronics and Photonics Paderborn (CeOPP), Paderborn University, 33098 Paderborn, Germany;* orcid.org/0009-0008-6279-077X

Chuan-Ding Dong − *Department of Physics and Center for Optoelectronics and Photonics Paderborn (CeOPP), Paderborn University, 33098 Paderborn, Germany;* orcid.org/0000-0001-8438-4416

Complete contact information is available at: https://pubs.acs.org/10.1021/acs.jpcc.3c07513

Notes

The authors declare no competing financial interest.

ACKNOWLEDGMENTS

We acknowledge funding from the Deutsche Forschungsgemeinschaft through project SCHU 1980/13. A grant for computing time at the Paderborn Center for Parallel Computing (PC^2) is gratefully acknowledged.

REFERENCES

(1) Clarke, T. M.; Durrant, J. R. Charge Photogeneration in Organic Solar Cells. *Chem. Rev.* **2010**, *110*, 6736−6767.

(2) Krebs, F. C.; Espinosa, N.; Hösel, M.; Søndergaard, R. R.; Jørgensen, M. 25th Anniversary Article: Rise to Power - OPV-Based Solar Parks. *Adv. Mater.* **2014**, *26*, 29−39.

(3) Yan, C.; Barlow, S.; Wang, Z.; Yan, H.; Jen, A. K.-Y.; Marder, S. R.; Zhan, X. Non-fullerene acceptors for organic solar cells. *Nat. Rev. Mater.* **2018**, *3*, 18003.

(4) Li, Y. Molecular Design of Photovoltaic Materials for Polymer Solar Cells: Toward Suitable Electronic Energy Levels and Broad Absorption. *Acc. Chem. Res.* **2012**, *45*, 723−733.

(5) Brabec, C. J.; Sariciftci, N. S.; Hummelen, J. C. Plastic Solar Cells. *Adv. Funct. Mater.* **2001**, *11*, 15−26.

(6) Brédas, J. L.; Norton, J. E.; Cornil, J.; Coropceanu, V. Molecular Understanding of Organic Solar Cells: The Challenges. *Acc. Chem. Res.* **2009**, *42*, 1691−1699.

(7) Deibel, C.; Dyakonov, V. Polymer-fullerene bulk heterojunction solar cells. *Rep. Prog. Phys.* **2010**, *73*, 096401.

(8) Grancini, G.; Maiuri, M.; Fazzi, D.; Petrozza, A.; Egelhaaf, H. J.; Brida, D.; Cerullo, G.; Lanzani, G. Hot exciton dissociation in polymer solar cells. *Nat. Mater.* **2013**, *12*, 29−33.
(9) Cai, Y.; Li, Y.; Wang, R.; Wu, H.; Chen, Z.; Zhang, J.; Ma, Z.; Hao, X.; Zhao, Y.; Zhang, C.; et al. A Well-Mixed Phase Formed by Two Compatible Non-Fullerene Acceptors Enables Ternary Organic Solar Cells with Efficiency over 18.6%. *Adv. Mater.* **2021**, *33*, 2101733.
(10) Fazzi, D.; Barbatti, M.; Thiel, W. Modeling ultrafast exciton deactivation in oligotiophenes *via* nonadiabatic dynamics. *Phys. Chem. Chem. Phys.* **2015**, *17*, 7787−7799.
(11) Akimov, A. V.; Prezhdo, O. V. Nonadiabatic Dynamics of Charge Transfer and Singlet Fission at the Pentacene/C_{60} Interface. *J. Am. Chem. Soc.* **2014**, *136*, 1599−1608.
(12) Jailaubekov, A. E.; Willard, A. P.; Tritsch, J. R.; Chan, W. L.; Sai, N.; Gearba, R.; Kaake, L. G.; Williams, K. J.; Leung, K.; Rossky, P. J.; et al. Hot charge-transfer excitons set the time limit for charge separation at donor/acceptor interfaces in organic photovoltaics. *Nat. Mater.* **2013**, *12*, 66−73.
(13) Fazzi, D.; Barbatti, M.; Thiel, W. Unveiling the Role of *Hot* Charge-Transfer States in Molecular Aggregates via Nonadiabatic Dynamics. *J. Am. Chem. Soc.* **2016**, *138*, 4502−4511.
(14) Sheng, C. X.; Tong, M.; Singh, S.; Vardeny, Z. V. Experimental determination of the charge/neutral branching ratio η in the photoexcitation of π-conjugated polymers by broadband ultrafast spectroscopy. *Phys. Rev. B* **2007**, *75*, 085206.
(15) Zhou, G.; Zhang, M.; Xu, J.; Yang, Y.; Hao, T.; Zhu, L.; Zhou, L.; Zhu, H.; Zou, Y.; Wei, G.; et al. Spontaneous carrier generation and low recombination in high-efficiency non-fullerene solar cells. *Energy Environ. Sci.* **2022**, *15*, 3483−3493.
(16) Wang, R.; Zhang, C.; Li, Q.; Zhang, Z.; Wang, X.; Xiao, M. Charge Separation from an Intra-Moiety Intermediate State in the High-Performance PM6:Y6 Organic Photovoltaic Blend. *J. Am. Chem. Soc.* **2020**, *142*, 12751−12759.
(17) Wang, T.; Chen, Z.-H.; Qiao, J.-W.; Qin, W.; Liu, J.-Q.; Wang, X.-Z.; Pu, Y.-J.; Yin, H.; Hao, X.-T. Correlating Charge Transfer Dynamics with Interfacial Trap States in High-Efficiency Organic Solar Cells. *ACS Appl. Mater. Interfaces* **2023**, *15*, 12109−12118.
(18) Chung, H. Y.; Park, J.-H.; Cui, J.; Kim, S.-Y.; Oh, J.; Kim, D.; Park, S. Y. Influence of Intramolecular Charge-Transfer Characteristics of Excitons on Polaron Generation at the Donor/Acceptor Interface in Polymer Solar Cells. *J. Phys. Chem. C* **2021**, *125*, 18352−18361.
(19) Jiao, Z.; Jiang, T.; Zhou, Z.; Qin, C.; Long, J.; Liu, Y.; Jiang, Y. Identification of a bridge-specific intramolecular exciton dissociation pathway in donor−π−acceptor alternating conjugated polymers. *Nanoscale Res. Lett.* **2021**, *16*, 51.
(20) Rolczynski, B. S.; Szarko, J. M.; Son, H. J.; Liang, Y.; Yu, L.; Chen, L. X. Ultrafast Intramolecular Exciton Splitting Dynamics in Isolated Low-Band-Gap Polymers and Their Implications in Photovoltaic Materials Design. *J. Am. Chem. Soc.* **2012**, *134*, 4142−4152.
(21) Tautz, R.; Da Como, E.; Wiebeler, C.; Soavi, G.; Dumsch, I.; Fröhlich, N.; Grancini, G.; Allard, S.; Scherf, U.; Cerullo, G.; et al. Charge Photogeneration in Donor−Acceptor Conjugated Materials: Influence of Excess Excitation Energy and Chain Length. *J. Am. Chem. Soc.* **2013**, *135*, 4282−4290.
(22) Zhao, N.; Zhang, R.; Zou, X.; Su, X.; Dang, F.; Wen, G.; Zhang, W.; Zheng, K.; Chen, H.; Wu, K. Photoinduced Polaron Formation in a Polymerized Electron-Acceptor Semiconductor. *J. Phys. Chem. Lett.* **2022**, *13*, 5143−5150.
(23) Cho, S.; Rolczynski, B. S.; Xu, T.; Yu, L.; Chen, L. X. Solution Phase Exciton Diffusion Dynamics of a Charge-Transfer Copolymer PTB7 and a Homopolymer P3HT. *J. Phys. Chem. B* **2015**, *119*, 7447−7456.
(24) Carsten, B.; Szarko, J. M.; Son, H. J.; Wang, W.; Lu, L.; He, F.; Rolczynski, B. S.; Lou, S. J.; Chen, L. X.; Yu, L. Examining the Effect of the Dipole Moment on Charge Separation in Donor−Acceptor Polymers for Organic Photovoltaic Applications. *J. Am. Chem. Soc.* **2011**, *133*, 20468−20475.
(25) Gélinas, S.; Paré-Labrosse, O.; Brosseau, C.-N.; Albert-Seifried, S.; McNeill, C. R.; Kirov, K. R.; Howard, I. A.; Leonelli, R.; Friend, R. H.; Silva, C. The Binding Energy of Charge-Transfer Excitons Localized at Polymeric Semiconductor Heterojunctions. *J. Phys. Chem. C* **2011**, *115*, 7114−7119.
(26) Collado-Fregoso, E.; Boufflet, P.; Fei, Z.; Gann, E.; Ashraf, S.; Li, Z.; McNeill, C. R.; Durrant, J. R.; Heeney, M. Increased Exciton Dipole Moment Translates into Charge-Transfer Excitons in Thiophene-Fluorinated Low-Bandgap Polymers for Organic Photovoltaic Applications. *Chem. Mater.* **2015**, *27*, 7934−7944.
(27) Havinga, E. E.; ten Hoeve, W.; Wynberg, H. A new class of small band gap organic polymer conductors. *Polym. Bull.* **1992**, *29*, 119−126.
(28) Jespersen, K. G.; Beenken, W. J. D.; Zaushitsyn, Y.; Yartsev, A.; Andersson, M.; Pullerits, T.; Sundström, V. The electronic states of polyfluorene copolymers with alternating donor-acceptor units. *J. Chem. Phys.* **2004**, *121*, 12613−12617.
(29) Tautz, R.; Da Como, E.; Limmer, T.; Feldmann, J.; Egelhaaf, H.-J.; von Hauff, E.; Lemaur, V.; Beljonne, D.; Yilmaz, S.; Dumsch, I.; et al. Structural correlations in the generation of polaron pairs in low-bandgap polymers for photovoltaics. *Nat. Commun.* **2012**, *3*, 970.
(30) Frisch, M. J.; Trucks, G. W.; Schlegel, H. B.; Scuseria, G. E.; Robb, M. A.; Cheeseman, J. R.; Scalmani, G.; Barone, V.; Petersson, G. A.; Nakatsuji, H. et al. *Gaussian 16*. Revision C.01; Gaussian Inc.: Wallingford CT, 2016.
(31) Dong, C.-D.; Schumacher, S. Microscopic Insights into Charge Formation and Energetics in n-doped Organic Semiconductors. *J. Phys. Chem. C* **2021**, *125*, 21824−21830.
(32) Dong, C.-D.; Schumacher, S. Molecular Doping of PCPDT-BT Copolymers: Comparison of Molecular Complexes with and without Integer Charge Transfer. *J. Phys. Chem. C* **2019**, *123*, 30863−30870.
(33) Dong, C.-D.; Schumacher, S. Molecular Doping in Few-Molecule Polymer-Dopant Complexes Shows Reduced Coulomb Binding. *J. Mater. Chem. C* **2020**, *8*, 11929−11935.
(34) Di Nuzzo, D.; Fontanesi, C.; Jones, R.; Allard, S.; Dumsch, I.; Scherf, U.; von Hauff, E.; Schumacher, S.; Da Como, E. How intermolecular geometrical disorder affects the molecular doping of donor−acceptor copolymers. *Nat. Commun.* **2015**, *6*, 6460.
(35) Fauvell, T. J.; Zheng, T.; Jackson, N. E.; Ratner, M. A.; Yu, L.; Chen, L. X. Photophysical and Morphological Implications of Single-StrandConjugated Polymer Folding in Solution. *Chem. Mater.* **2016**, *28*, 2814−2822.
(36) Crespo-Otero, R.; Barbatti, M. Spectrum simulation and decomposition with nuclear ensemble: formal derivation and application to benzene, furan and 2-phenylfuran. *Theor. Chem. Acc.* **2012**, *131*, 1237.
(37) Barbatti, M.; Ruckenbauer, M.; Plasser, F.; Pittner, J.; Granucci, G.; Persico, M.; Lischka, H. Newton-X: a surface-hopping program for nonadiabatic molecular dynamics. *Wiley Interdiscip. Rev.: Comput. Mol. Sci.* **2014**, *4*, 26−33.
(38) Tully, J. C. Molecular Dynamics with electronic transitions. *J. Chem. Phys.* **1990**, *93*, 1061−1071.
(39) Hammes-Schiffer, S.; Tully, J. C. Proton transfer in solution: Molecular dynamics with quantum-transitions. *J. Chem. Phys.* **1994**, *101*, 4657−4667.
(40) Domcke, W.; Yarkony, D. R.; Köppel, H. *Conical Intersections: Theory, Computation and Experiment*; World Scientific, 2011.
(41) Granucci, G.; Persico, M. Critical appraisal of the fewest switches algorithm for surface hopping. *J. Chem. Phys.* **2007**, *126*, 134114.
(42) Lu, T.; Chen, F. Multiwfn: a Multifunctional Wavefunction Analyzer. *J. Comput. Chem.* **2012**, *33*, 580−592.
(43) Liu, Z.; Lu, T.; Chen, Q. An sp-hybridized all-carboatomic ring, cyclo[18]carbon: Electronic structure, electronic spectrum, and optical nonlinearity. *Carbon* **2020**, *165*, 461−467.
(44) Roy, P.; Jha, A.; Yasarapudi, V. B.; Ram, T.; Puttaraju, B.; Patil, S.; Dasgupta, J. Ultrafast bridge planarization in donor-π-acceptor copolymers drives intramolecular charge transfer. *Nat. Commun.* **2017**, *8*, 1716.

https://doi.org/10.1021/acs.jpcc.3c07513
J. Phys. Chem. C 2024, 128, 3525−3532

(45) Paquin, F.; Latini, G.; Sakowicz, M.; Karsenti, P.-L.; Wang, L.; Beljonne, D.; Stingelin, N.; Silva, C. Charge Separation in Semicrystalline Polymeric Semiconductors by Photoexcitation: Is the Mechanism Intrinsic or Extrinsic? *Phys. Rev. Lett.* **2011**, *106*, 197401.
(46) Chen, Z.; Chen, X.; Qiu, B.; Zhou, G.; Jia, Z.; Tao, W.; Li, Y.; Yang, Y. M.; Zhu, H. Ultrafast Hole Transfer and Carrier Transport Controlled by Nanoscale-Phase Morphology in Nonfullerene Organic Solar Cells. *J. Phys. Chem. Lett.* **2020**, *11*, 3226−3233.
(47) Fazzi, D.; Barbatti, M.; Thiel, W. Hot and Cold Charge-Transfer Mechanisms in Organic Photovoltaics: Insights into the Excited States of Donor/Acceptor Interfaces. *J. Phys. Chem. Lett.* **2017**, *8*, 4727−4734.

https://doi.org/10.1021/acs.jpcc.3c07513
J. Phys. Chem. C 2024, 128, 3525−3532

Conclusion and Outlook 9

9.1 Conclusion

Opto-electronic devices based on organic semiconductors have successfully entered commercial markets. Organic light-emitting diodes (OLEDs) are indispensable components of state-of-the-art electronic devices, whereas the commercial implementation of organic semiconductors in photovoltaics remains comparatively limited. However, substantial progress over recent decades have culminating in power conversion efficiencies exceeding 21% [42], highlighting the potential use in everyday life.

The fundamental mechanisms governing charge-carrier generation and transport, as well as exciton formation and dissociation in organic photovoltaic devices, are largely understood. However, clarifying the complex interplay between chemical design, structural ordering, intrinsic electronic properties, electronic disorder, exciton dissociation, transport processes, and overall device performance remains a major challenge. A comprehensive understanding of these relationships is essential for the rational design and further optimization of high-performance organic photovoltaic systems.

This thesis employs electronic-structure methods to investigate the electronic properties and underlying mechanisms of organic semiconductors, with the objective of advancing the understanding of charge-carrier generation, charge-carrier transport, and device functionality in organic photovoltaic applications.

The generation of charge carriers through molecular dopants is a widely employed strategy to increase the charge-carrier density. More recently, Lewis acids and superbases have emerged as effective alternatives to conventional molecular dopants for p-type and n-type doping, respectively, demonstrating improved doping efficiency, better miscibility with organic semiconductors, and enhanced thermal stability. In one contribution included in this thesis [51], the superbase-doping mechanism was investigated in detail by analyzing the nucleophilic attack pathway and the associated intra- and intermolecular electron-transfer processes, as well as their connection to intermolecular complex formation. The findings reveal that, in the absence of carbon-carbon bond formation, a metastable electronic configuration characterized by a singly occupied orbital is formed, enabling efficient transfer

of the excess electron to a neighboring organic semiconductor. In contrast, when bond formation occurs intra- or intermolecularly, paired and spatially localized electronic states are generated. These results provide valuable mechanistic insight and contribute to a clearer understanding and further advancement of doping strategies reported in the literature.

A comprehensive understanding of charge transport in organic semiconductors is essential for the rational design of higher-performance devices. In one contribution [50], charge-transport mechanisms in organic semiconductor dimers were investigated using *ab initio* molecular dynamics simulations. Charge-transfer events were systematically correlated with polaron energy levels, and key vibrational modes facilitating charge transfer were identified through ground-state calculations. These results establish a foundation for the development of large-scale transport models that aim to predict charge mobility using physically meaningful charge-transport descriptors.

The excited-state manifold and its dynamics play a decisive role in organic photovoltaics, as they govern exciton dissociation pathways and recombination losses. These aspects are examined in depth through three key contributions presented in this thesis.

Using non-adiabatic *ab initio* molecular dynamics simulations, the time-dependent behavior of *hot* excitons is analyzed across four distinct donor-acceptor polymer architectures, yielding detailed insight into the evolution of their dipole moments and Coulomb interactions in the excited states [52]. These quantities are correlated with experimentally proposed polaron-pair formation mechanisms, further solidifying their relevance as descriptors of charge separation and clarifying how polymer architecture influences the underlying separation dynamics.

Furthermore, simulations of the PM6:Y_2CF_3 blend and the neat Y_2CF_3 film of the novel trifluoromethyl-substituted acceptor Y_2CF_3, combined with subsequent quantum-chemical calculations, provide detailed insight into the electronic manifolds of both systems [54]. In particular, correlations between exciton dissociation and molecular packing, as well as between charge transfer (electron and hole transfer) and molecular packing, are examined, revealing highly efficient exciton dissociation, as well as efficient electron-transfer pathways within the acceptor domain. The investigated trifluoromethyl-substituted acceptor has experimentally demonstrated superior performance compared to the state-of-the-art acceptor Y6, attributed to its favorable molecular packing and enhanced charge-carrier mobility [245]. Overall, this contribution delivers a comprehensive analysis of the electronic structure and fundamental mechanisms responsible for the improved performance of this novel acceptor material.

Finally, to further disentangle the relationship between chemical design and interfacial exciton dissociation, a series of molecular donor architectures is systematically screened [53]. The strength of electron-withdrawing terminal groups and the length of the π-bridge are correlated with exciton dissociation efficiency at the interface with Y6, providing additional insights into structure-property relationships governing interfacial charge separation.

9.2 Outlook

The findings generated throughout this thesis and the associated publications provide valuable insights and foundational work that can be expanded upon through multiscale simulations aimed at developing a deeper understanding of charge generation and transport in organic semiconductor devices on a larger scale.

For instance, kinetic Monte Carlo simulations represent a promising approach to further evaluate the suitability of the polaron energy level as a descriptor for charge transfer. By enabling a direct comparison between simulated charge carrier mobilities and experimental measurements, such simulations could provide deeper insight into the predictive power of this descriptor. In addition, extending the present study to include a statistical analysis over a large ensemble of propagated trajectories may yield statistically resolved rate constants, which can subsequently be validated against experimental data.

Building on the screened small-molecule donors, molecular dynamics simulations constitute a logical next step toward modeling realistic donor:acceptor interfaces. This would enable a systematic investigation of how the proposed molecular design principles influence intermolecular packing motifs and energetic disorder, thereby affecting charge transport and exciton dissociation properties.

Furthermore, for the novel trifluoromethyl-substituted acceptor Y_2CF_3, the role of the processing solvent on molecular packing, electronic properties, and ultimately device performance can be investigation in detail. Similarly, examining the effect of substituent positioning may uncover distinct morphological characteristics induced by the trifluoromethyl-side chain and provide additional guidelines for rational material design.

Appendix

A.1 Chemical Species

This section lists the chemical species that are abbreviated throughout the thesis. The chemical species investigated in the presented papers are not emphasized here, as they are shown in the respective papers.

- PCPDT–BT: Poly[2,6-(4,4-bis-(2-ethylhexyl)-4H-cyclopenta [2,1-b;3,4-b′] dithiophene)-alt-4,7(2,1,3-benzothiadiazole)]
- F_4TCNQ: 2,3,5,6-tetrafluoro-7,7,8,8-tetracyanoquinodimethane
- F_6TCNNQ: 1,3,4,5,7,8-hexafluorotetracyanonaphthoquinodimethane
- CN6–CP: Hexacyano-trimethylene-cyclopropane
- N–DMBI: 4-(1,3-dimethyl-2,3-dihydro-1H-benzoimidazol-2-yl)phenyl) dimethylamine
- BCF: Tris(pentafluorophenyl)borane
- TrTPFB: Trityl tetrakis(pentafluorophenyl)borate
- P2–t–Bu: 1-tert-butyl-2,2,4,4,4-pentakis(dimethylamino)-2λ5,4λ5-catenadi (phosphazene)
- P4–t–Bu: 1-tert-butyl-4,4,4-tris(dimethylamino)-2,2bis[tris(dimethylamino) phosphoranylidenamino]-2λ5,4λ5-catenadiphosphazen
- PC_{61}BM: [6,6] phenyl-C61-butyric acid methyl ester
- N2200: Poly[N,N'-bis(2-octyldodecyl)naphthalene-1,4,5,8-bis(dicarboximide) -2,6-diyl]-alt-5,5'-(2,2'-bithiophene)
- P3HT: Poly(3-hexylthiophene-2,5-diyl)

- PM6: Poly[(2,6-(4,8-bis(5-(2-ethylhexyl)-4-fluorothiophen-2-yl)-benzo[1,2-b:4,5-b’] dithiophene))-alt-(5,5-(1’,3’-di-2-thienyl-5’,7’-bis(2-ethylhexyl) benzo[1’,2’-c:4’,5’-c’]dithiophene-4,8-dione))]
- Y_2CF_3: 2,2’-[12,13-bis(2-ethylhexyl)-6-(3,3,3-trifluoropropyl)-3,9-diundecyl-12,13-dihydro-6H-thieno[2’,3’:4,5]thieno[3,2-b]thieno[2”,3”:4’,5’]thieno[2’,3’:4,5] pyrrolo[3,2-g][1,2,3]triazolo[4,5-e]indole-2,10-diyl]bis[methanylylidene (5,6-difluoro-3-oxo-1H-indene-2,1(3H)-diylidene)]dipropanedinitrile

A.2 Analytic Foundations

This section provides concise derivations of the physical mechanisms underlying the phenomena investigated in this thesis. Specifically, it covers the generalized Mulliken-Hush electronic coupling for excited-state transitions, spin-orbit coupling in singlet-triplet excited-state transitions, excited-state oscillator strengths and radiative decay processes, the thermal vibration correlation function associated with non-radiative decay, and the nuclear ensemble approach.

A.2.1 Electronic Coupling: Generalized Mulliken Hush Method

The electronic coupling $\mathcal{H}_{\mathrm{ab}}^{\mathrm{dia}}$ in a *two-state model* is equal to the off-diagonal term of the Hamiltonian matrix in the diabatic basis. Electronic structure calculations directly provide adiabatic quantities; therefore, the goal is to compute the electronic coupling from these adiabatic quantities. The Hamiltonian matrix $\mathcal{H}$ and dipole matrix elements $\boldsymbol{\mu}$ in both the diabatic and adiabatic representations are given by:

$$\mathcal{H}^{\mathrm{dia}} = \begin{pmatrix} \mathcal{H}_{\mathrm{aa}} & \mathcal{H}_{\mathrm{ab}} \\ \mathcal{H}_{\mathrm{ab}} & \mathcal{H}_{\mathrm{bb}} \end{pmatrix} \qquad \mathcal{H}^{\mathrm{adia}} = \begin{pmatrix} \mathcal{H}_{11} & 0 \\ 0 & \mathcal{H}_{22} \end{pmatrix} \tag{A.1}$$

$$\boldsymbol{\mu}^{\mathrm{dia}} = \begin{pmatrix} \boldsymbol{\mu}_{\mathrm{aa}} & \boldsymbol{\mu}_{\mathrm{ab}} \\ \boldsymbol{\mu}_{\mathrm{ab}} & \boldsymbol{\mu}_{\mathrm{bb}} \end{pmatrix} \qquad \boldsymbol{\mu}^{\mathrm{adia}} = \begin{pmatrix} \boldsymbol{\mu}_{11} & \boldsymbol{\mu}_{12} \\ \boldsymbol{\mu}_{12} & \boldsymbol{\mu}_{22} \end{pmatrix} \tag{A.2}$$

In the nomenclature, letters correspond to the diabatic basis and numbers to the adiabatic basis. The diabatic wave functions Ψ_a and Ψ_b of states a and b are expressed as linear combinations of the orthonormal (and real) adiabatic wave functions Ψ_1 and Ψ_2 (switching in bra-ket notation) [116, 117]:

$$|\Psi_a\rangle = c_a^1 |\Psi_1\rangle + c_a^2 |\Psi_2\rangle\,; \quad |\Psi_b\rangle = c_b^1 |\Psi_1\rangle + c_b^2 |\Psi_2\rangle\,; \quad c_a^1,\ c_a^2,\ c_b^1,\ c_b^2 \in \mathbb{R}\,. \tag{A.3}$$

Inserting the diabatic wave functions into the off-diagonal term of the Hamiltonian and using orthonormal conditions of $|\Psi_1\rangle$ and $|\Psi_2\rangle$ leads to the following expression for the electronic coupling in adiabatic quantities:

$$\mathcal{H}_{\mathrm{ab}}^{\mathrm{dia}} = \mathcal{H}_{11}^{\mathrm{adia}} c_a^1 c_b^1 + \mathcal{H}_{22}^{\mathrm{adia}} c_a^2 c_b^2\,, \tag{A.4}$$

where $\mathcal{H}_{11}^{\text{adia}}$ and $\mathcal{H}_{22}^{\text{adia}}$ are the eigenvalues E_1 and E_2, respectively; $E_2 > E_1$ in this representation. A commonly used orthogonal rotation [246] is chosen to represent the linear combination via

$$c_a^1 = \cos(\theta) \ , \quad c_a^2 = \sin(\theta) \ , \quad c_b^1 = -\sin(\theta) \ , \quad c_b^2 = \cos(\theta) \ , \tag{A.5}$$

where θ corresponds to a rotation. Inserting the rotation and using algebraic transformations, the electronic coupling reads

$$\mathcal{H}_{\text{ab}}^{\text{dia}} = \frac{1}{2}(\underbrace{E_2 - E_1}_{\Delta E_{12}}) \sin(2\theta) \ . \tag{A.6}$$

The dipole operator is projected onto the direction of the adiabatic dipole difference $\Delta\boldsymbol{\mu}_{12} = \boldsymbol{\mu}_{11} - \boldsymbol{\mu}_{22}$,

$$\mu_{ij} = \hat{\mathbf{e}} \cdot \boldsymbol{\mu}_{ij} \ , \text{ with } \hat{\mathbf{e}} = \frac{\Delta\boldsymbol{\mu}_{12}}{|\Delta\boldsymbol{\mu}_{12}|} \ . \tag{A.7}$$

The rotation angle θ is chosen so that the off-diagonal term of the dipole matrix element in the diabatic basis vanishes: $\mu_{\text{ab}} = 0$. Evaluating the matrix element then yields

$$\tan(2\theta) = \frac{2\mu_{12}}{\Delta\mu_{12}} \ , \tag{A.8}$$

with $\Delta\mu_{12} = \mu_{11} - \mu_{22}$ the difference in dipole moments of the adiabatic states. Algebraic transformations yield the final expression for the electronic coupling from adiabatic quantities:

$$\mathcal{H}_{\text{ab}}^{\text{dia}} = \frac{\mu_{12}\Delta E_{12}}{\sqrt{(\Delta\mu_{12})^2 + 4(\mu_{12})^2}} \ . \tag{A.9}$$

A.2.2 Spin-Orbit Coupling

To evaluate the spin-orbit coupling between the $I-$th singlet excited state and the $J-$th triplet excited state with corresponding electronic wave functions $\Psi_I^{\text{S}} \equiv |\text{S}_I\rangle$ and $\Psi_J^{\text{T}} \equiv \left|\text{T}_J\right\rangle_{s,m}$ with spin angular momentum s and magnetic quantum number m, respectively, the perturbation Hamiltonian in Fermi's golden rule (Equation 5.2) takes the form of the

relativistic *one-electron spin-orbit* Breit-Pauli Hamiltonian [118, 122]:

$$\hat{\mathcal{H}}^{\mathrm{SO}} = \frac{\alpha_0^2}{2} \sum_i^{N_{\mathrm{el}}} \sum_A^{N_A} \frac{Z_A}{r_{iA}^3} (\mathbf{r}_{iA} \times \hat{\mathbf{p}}_i) \cdot \hat{\mathbf{s}}_i \equiv \sum_i^{N_{\mathrm{el}}} \zeta(\mathbf{r}_i) \hat{\mathbf{l}}_i \cdot \hat{\mathbf{s}}_i \,, \tag{A.10}$$

with $\zeta(\mathbf{r}_i) = \sum_A^{N_A} \frac{\alpha_0^2}{2} \frac{Z_A}{r_{\mathrm{iA}}^3}$; $\hat{\mathbf{l}}_i = \mathbf{r}_{iA} \times \hat{\mathbf{p}}_i$ is the orbital angular momentum operator and $\hat{\mathbf{s}}_i$ the spin angular momentum operator of electron i; Z_A is the bare positive charge on nucleus A; α_0 is the fine-structure constant. The sum extends over all electrons i and nuclei A. For completeness, it should be noted that the Breit-Pauli operator is composed of more complex terms, e.g., spin-other-orbit contributions; however, these are neglected in the formalism. The spin-orbit coupling $V_{\mathrm{ST}_{s,m}}^{\mathrm{SOC}}$ reads:

$$\hat{V}_{\mathrm{ST}_{s,m}}^{\mathrm{SOC}} = \langle \mathrm{S}_I | \, \mathcal{H}^{\mathrm{SO}} \, | \mathrm{T}_J \rangle_{s,m} \,. \tag{A.11}$$

To evaluate the spin-orbit coupling, the second quantization notation is used [120], in which Slater determinants build from orthonormal spin-orbitals ϕ_r can be expressed of fermionic creation ($\hat{a}^\dagger$) and annihilation ($\hat{a}$) operators acting on the vacuum-state to represent the wave function:

$$\frac{1}{\sqrt{N!}} \det |\phi_t \dots \phi_s \phi_r| \leftrightarrow \hat{r}^\dagger \hat{s}^\dagger \dots \hat{t}^\dagger \, |\mathrm{vac}\rangle \,. \tag{A.12}$$

Moreover, any first-quantized one-electron operator $f(r)$ can be expressed in one-to-one correspondence via:

$$\sum_{i=1}^{N} f(r) \leftrightarrow \sum_{j,k} \langle \phi_j | \, f \, | \phi_k \rangle \, \hat{j}^\dagger \hat{k} \,. \tag{A.13}$$

The operators are subject to the anticommutator relation $\left[\hat{r}, \hat{t}^\dagger\right]_+ = \delta_{\mathrm{rt}}$ through Fermi statistics. Following this representation, Equation A.10 is expressed as [247]:

$$\hat{\mathcal{H}}_{\mathrm{so}} = \sum_{p,q} \sum_{\sigma,\sigma'} \langle \phi_{p\sigma} | \, \zeta(\mathbf{r}) \left(\hat{l}_x \hat{s}_x + \hat{l}_y \hat{s}_y + \hat{l}_z \hat{s}_z \right) \, | \phi_{q\sigma'} \rangle \, \hat{a}_{p\sigma}^\dagger \hat{a}_{q\sigma'} \,. \tag{A.14}$$

Here, $|\phi_{p\sigma}\rangle = |\phi_p\rangle \otimes \sigma$ is the spinor consisting of a spatial $|\phi_p\rangle$ part and the spin $\sigma \in \{\alpha, \beta\}$ (spin-up and spin-down); in the context of density functional theory formalism, $|\phi_p\rangle$ are Kohn-Sham orbitals. The sums p and q run over all orthonormal Kohn-Sham orbitals.

Evaluating Equation A.14 using the Pauli spin matrices leads to the following equations:

$$\begin{aligned}
\hat{\mathcal{H}}^x_{\mathrm{so}} &= \frac{1}{2}\sum_{p,q} h^x_{pq}\left(\hat{a}^\dagger_{p\alpha}\hat{a}_{q\beta} + \hat{a}^\dagger_{p\beta}\hat{a}_{q\alpha}\right) , \\
\hat{\mathcal{H}}^y_{\mathrm{so}} &= \frac{1}{2\mathrm{i}}\sum_{p,q} h^y_{pq}\left(\hat{a}^\dagger_{p\alpha}\hat{a}_{q\beta} - \hat{a}^\dagger_{p\beta}\hat{a}_{q\alpha}\right) , \\
\hat{\mathcal{H}}^z_{\mathrm{so}} &= \frac{1}{2}\sum_{p,q} h^z_{pq}\left(\hat{a}^\dagger_{p\alpha}\hat{a}_{q\alpha} - \hat{a}^\dagger_{p\beta}\hat{a}_{q\beta}\right) ,
\end{aligned} \tag{A.15}$$

where i is the imaginary unit. The factors $h^d_{pq} = \langle\phi_p|\,\zeta(\mathbf{r})\hat{l}_d\,|\phi_q\rangle$ with $d \in \{x, y, z\}$ are integrals between the Kohn-Sham orbitals p and q. Using Casida's formalism [121] for the singly-excited configuration within time-dependent density functional theory under *Tamm-Dancoff approximation* (TDA), the wave function of the $I-$th singlet excited state can be expressed via:

$$|\Psi^{\mathrm{exc}}_I\rangle = \sum_{i,a,\sigma} c^{ia\sigma}_I \hat{a}^\dagger_{a\sigma}\hat{a}_{i\sigma}\,|\Psi_0\rangle \ . \tag{A.16}$$

Here, $|\Psi_0\rangle$ is the ground state wave function composed of Kohn-Sham orbitals via the Slater determinant representation; the sum runs over both spins ($\sigma \in \{\alpha, \beta\}$), index a denotes virtual (unoccupied) orbitals and index i represents occupied orbitals; $c^{ia\sigma}_I$ is the excitation coefficient for the respective $i \rightarrow a$ contribution. See Section A.4.2 for a brief introduction of TDA. In particular, the resulting excited state wave function for the $I-$th singlet excited state and $J-$th triplet excited state reads [247]:

$$\begin{aligned}
|\mathrm{S}_I\rangle &= \sum_{i,a} s^{ia}_I\left(\hat{a}^\dagger_{a\alpha}\hat{a}_{i\alpha} + \hat{a}^\dagger_{a\beta}\hat{a}_{i\beta}\right)|\Psi_0\rangle\,, \\
|\mathrm{T}_J\rangle_{1,0} &= \sum_{i,a} t^{ia}_J\left(\hat{a}^\dagger_{a\alpha}\hat{a}_{i\alpha} - \hat{a}^\dagger_{a\beta}\hat{a}_{i\beta}\right)|\Psi_0\rangle\,, \\
|\mathrm{T}_J\rangle_{1,1} &= \sqrt{2}\sum_{i,a} t^{ia}_J\hat{a}^\dagger_{a\alpha}\hat{a}_{i\beta}\,|\Psi_0\rangle\,, \\
|\mathrm{T}_J\rangle_{1,-1} &= \sqrt{2}\sum_{i,a} t^{ia}_J\hat{a}^\dagger_{a\beta}\hat{a}_{i\alpha}\,|\Psi_0\rangle\,,
\end{aligned} \tag{A.17}$$

where the singlet s^{ia}_I and triplet t^{ia}_J excitation coefficients rely the normalization $\sum_{i,a}(t^{ia}_J)^2 = \sum_{i,a}(s^{ia}_I)^2 = \frac{1}{2}$. Inserting the excited state wave function expansion (Equation A.17) and the second-quantized spin-orbit operator (Equation A.15) into Equation A.11, and evaluating the annihilation and creating operators yields the following equations for the spin-orbit

coupling between singlet and triplet excited states:

$$\begin{aligned}
\langle \mathrm{S}_I | \hat{\mathcal{H}}_{so} | \mathrm{T}_J \rangle_{1,0} &= \frac{1}{2} \left(- \sum_{i,j,a} \left(s_I^{ia} \right)^* t_J^{ja} h_{ji}^z + \sum_{i,a,b} \left(s_I^{ia} \right)^* t_J^{ib} h_{ab}^z \right) , \\
\langle \mathrm{S}_I | \hat{\mathcal{H}}_{so} | \mathrm{T}_J \rangle_{1,1} &= \frac{1}{2\sqrt{2}} \left(\sum_{i,j,a} \left(s_I^{ia} \right)^* t_J^{ja} \left(h_{ji}^x + \mathrm{i} h_{ji}^y \right) - \sum_{i,a,b} \left(s_I^{ia} \right)^* t_J^{ib} \left(h_{ab}^x + \mathrm{i} h_{ab}^y \right) \right) , \\
\langle \mathrm{S}_I | \hat{\mathcal{H}}_{so} | \mathrm{T}_J \rangle_{1,-1} &= - \left(\langle \mathrm{S}_I | \hat{\mathcal{H}}_{so} | \mathrm{T}_J \rangle_{1,1} \right)^* .
\end{aligned} \tag{A.18}$$

Here, a, b denote virtual (unoccupied) Kohn-Sham orbitals and i, j occupied Kohn-Sham orbitals. Note that in Equation A.18, i is used as an index and i as imaginary unit; the resulting spin-orbit couplings are complex values. The total spin-orbit coupling to triplet excited state $|T_J\rangle$ is evaluated as summation over the magnetic quantum number m:

$$V^{\mathrm{SOC}} = \sqrt{\left| \langle \mathrm{S}_I | \hat{\mathcal{H}}_{so} | \mathrm{T}_J \rangle_{1,0} \right|^2 + \left| \langle \mathrm{S}_I | \hat{\mathcal{H}}_{so} | \mathrm{T}_J \rangle_{1,1} \right|^2 + \left| \langle \mathrm{S}_I | \hat{\mathcal{H}}_{so} | \mathrm{T}_J \rangle_{1,-1} \right|^2} . \tag{A.19}$$

A.2.3 Oscillator Strength and Radiative Decay Rates from the Einstein Coefficient Relation

After excitation from state i to j (approximated as harmonic oscillator), spontaneous emission of radiation may occur, i.e., a transition from state j to i accompanied by emission of a photon. The total energy W of a classical harmonic oscillator in free space as a function of time is given by [248]:

$$W(t) = W_0 \mathrm{e}^{-\gamma_{\mathrm{cl}} t} , \tag{A.20}$$

where the energy decay rate is

$$\gamma_{\mathrm{cl}} = \frac{e^2 \omega^2}{6\pi\varepsilon_0 m_e c^3} , \tag{A.21}$$

and ω is the angular frequency of the oscillation. As usual, ε_0 denotes the permittivity of free space, c the speed of light, m_e the electron mass, and e the elementary charge. Within this classical description, the excited state is associated and scaled with a characteristic radiative decay rate given by γ_{cl}.

Following Hilborn [84], the Einstein coefficient for spontaneous emission A_{ji} can be defined

via the oscillator strength for emission f_{ji} and the γ_{cl} of the classical harmonic oscillator as:

$$A_{ji} = -3 f_{ji} \gamma_{\mathrm{cl}} \, . \tag{A.22}$$

Correlating the absorption oscillator strength f_{ij} to the emission oscillator strength f_{ji}:

$$g_i f_{ij} = -g_j f_{ji} = g f \, . \tag{A.23}$$

For non-degenerate singlet states (spin multiplicity 1), one has $g_i = g_j = 1$.

Reordering Equation A.22 and inserting the relation leads to the spontaneous emission rate constant:

$$A_{ji} = \frac{\omega_{ji}^2 e^2}{2\pi\varepsilon_0 m_e c^3} f_{ij} \, . \tag{A.24}$$

Formulating the angular frequency into wave numbers $\tilde{\nu}$ in cm^{-1} ($\omega = 2\pi\tilde{\nu}c$) and evaluating the constants yields (almost exactly)

$$A_{ji} \approx \frac{2}{3} \tilde{\nu}_{ji}^2 f_{ij} \, . \tag{A.25}$$

Here, $\tilde{\nu}_{ji}$ is expressed in cm^{-1} and A_{ji} is obtained in s^{-1}.

Bridging to a quantum mechanical treatment of transition rates, the radiative decay rate can be also derived from Fermi's golden rule (Equation 5.1) under electronic dipole perturbation, i.e., an oscillating dipole coupled to a local electric field at the emitting chromophore [84, 249]. The resulting transition rate reads:

$$A_{ji} = \frac{\omega_{ji}^3}{3\pi\varepsilon_0 \hbar c^3} |\boldsymbol{\mu}_{ji}|^2 \, , \tag{A.26}$$

where $\boldsymbol{\mu}_{ji}$ is the electric transition dipole moment between the states, and $\hbar$ is the reduced Planck constant. Comparing both expressions, one can relate a general expression for the oscillator strength for a given transition, e.g., spontaneous emission, to its electrical transition dipole moment via

$$f_{ij} = \frac{2 m_e \omega_{ij}}{3 e^2 \hbar} |\boldsymbol{\mu}_{ij}|^2 \, . \tag{A.27}$$

Thus, within the electric dipole approximation, the classical radiation damping picture

becomes formally consistent with the quantum mechanical spontaneous emission rate once the oscillator strength is introduced as the dimensionless measure of transition probability.

The spontaneous emission rate derived as done above or via Fermi's golden rule apply to molecules (or atoms) in free-space. But, in the context of molecules in a bulk dielectric medium whose polarization can in turn affect the spontaneous emission, a higher-order perturbation embedding the polarization of the medium is necessary. To model the influence of the polarizable medium, the local electric field can be expressed by the overall macroscopic electric field, in an isotropic medium the relationship can be expressed via an scalar factor f' as $\mathbf{E}^{\text{local}} = f' \times \mathbf{E}^{\text{macro}}$. The influence of a surrounding medium with refractive index n on the spontaneous emission rate can be mounted as [125]:

$$k_{\text{r}} = nf'(n)^2 A_{\text{ji}} \,, \tag{A.28}$$

The factor n arises from the modification of the photonic density of states in the dielectric medium, whereas $f'(n)^2$ accounts for the change of the local electric field amplitude at the position of the emitter.

The scalar factor $f'(n)$ is characterized by the refractive index n of the material. In this work, $f'(n)$ takes the following relationship derived by Lorentz, leading to the *virtual cavity* (Lorentz) model [124–126]:

$$f'(n) = \left(\frac{n^2 + 2}{3}\right) \,. \tag{A.29}$$

In the *virtual cavity* model, no physical cavity is introduced; instead, a hypothetical spherical region (Lorentz sphere) around the emitter is considered, which is assumed not to perturb the homogeneous polarization of the surrounding dielectric. The microscopic polarization within the Lorentz sphere is taken to be identical to the macroscopic polarization of the medium. Owing to symmetry, the average field produced by dipoles inside the Lorentz sphere vanishes at its center, so that only the surface polarization of the sphere contributes to the local field.

A.2.4 Thermal Vibration Correlation Function

To evaluate the non-radiative decay of excited states to the ground state, the non-adiabatic coupling model [127, 128] can be used in combination with the thermal vibration correlation

function [129–131], which is described in the following.

Starting from Fermi's golden rule in Equation 5.1, the perturbation Hamiltonian has the form of the non-adiabatic coupling between Born-Oppenheimer states; after applying the Condon approximation it reads:

$$\mathcal{H}'_{fi} = \sum_{l} \langle \phi_f | \hat{P}_{fl} | \phi_i \rangle \langle \chi_{f\nu_f} | \hat{P}_{fl} | \chi_{i\nu_i} \rangle \ . \tag{A.30}$$

Here, the indices i and f denote the initial and final state; $\phi_{i(f)}$ and $\chi_{i(f)}$ the corresponding electronic and nuclei wave functions; $\nu_{i(f)}$ denote the collection of quantum numbers of the harmonic oscillators of the vibrational modes of the respective states; and $\hat{P}_{fl} = -\mathrm{i}\hbar\frac{\partial}{\partial Q_{fl}}$ is the normal mode momentum operator along normal mode l of the final state. As usual, $\hbar$ is the reduced Planck constant, and i is the imaginary unit. Assuming that in the initial vibrational modes are thermally occupied following a Boltzmann distribution

$$P_{i,\nu_i}(T) = \frac{\mathrm{e}^{-\beta E^{\mathrm{vib}}_{i,\nu_i}}}{Z_i}, \quad \text{with } Z_i = \sum_{\nu_i=0}^{\infty} \mathrm{e}^{-\beta E^{\mathrm{vib}}_{i,\nu_i}} \ , \tag{A.31}$$

the internal conversion rate k_{IC} reads [129–131, 250]:

$$k_{\mathrm{IC}} = \frac{2\pi}{\hbar} \sum_{l,k} \mathcal{R}^f_{lk} \frac{1}{Z_i} \sum_{\nu_i,\nu_f} \mathrm{e}^{-\beta E^{\mathrm{vib}}_{i,\nu_i}} \mathcal{P}^f_{lk} \delta\left(E_{if} + E^{\mathrm{vib}}_{i,\nu_i} - E^{\mathrm{vib}}_{f,\nu_f}\right) \ , \tag{A.32}$$

with

$$\mathcal{R}^f_{lk} = \langle \phi_f | \hat{P}_{fl} | \phi_i \rangle \langle \phi_i | \hat{P}_{fk} | \phi_f \rangle , \tag{A.33}$$

$$\mathcal{P}^f_{lk} = \langle \chi_{f\nu_f} | \hat{P}_{fl} | \chi_{i\nu_i} \rangle \langle \chi_{i\nu_i} | \hat{P}_{fk} | \chi_{f\nu_f} \rangle \ , \tag{A.34}$$

where $\mathcal{R}^f_{lk}$ is the non-adiabatic electronic coupling term [127, 128]. The sums l and k run over all normal modes; the sums ν_i and ν_f run over all possible quantum numbers of the initial and final vibrational modes; $E^{\mathrm{vib}}_{i(j),\nu_{i(j)}}$ is the corresponding total vibrational energy of the molecule for the given quantum number (eigenvalues of the harmonic oscillators); E_{if} is the (adiabatic) energy difference between the electronic states; Z_i is the partition function of the Boltzmann distribution; $\beta = \frac{1}{k_B T}$; T is the temperature, and k_B is the Boltzmann constant. The superscript f denotes the derivatives to be taken with respect to the normal modes of the final states.

After applying a Fourier transformation to the Dirac-delta function, k_{IC} reads [130]:

$$k_{\mathrm{IC}} = \frac{1}{\hbar} \sum_{l,k} \mathcal{R}_{lk}^{f} \int_{-\infty}^{\infty} \mathrm{d}\tau \, \frac{1}{Z_i} \mathrm{e}^{\mathrm{i}E_{if}\tau} \underbrace{\sum_{v_i, v_f} \mathrm{e}^{-\beta E_{i,v_i}^{\mathrm{vib}}} \mathcal{P}_{lk}^{f} \mathrm{e}^{\mathrm{i}\left(E_{i,v_i}^{\mathrm{vib}} - E_{f,v_f}^{\mathrm{vib}}\right)\tau}}_{\rho_{lk}(\tau,T)} . \tag{A.35}$$

Here, $\rho_{lk}(\tau, T)$ is the thermal vibrational correlation function (TVCF), with $\tau = \frac{t}{\hbar}$; note that i in the exponential functions denotes the imaginary unit. The TVCF can be analytically expressed and solved [130].

A.2.5 Nuclear Ensemble Approach

In the nuclear ensemble approach, the absorption cross section is simulated based on Wigner-distributed nuclei positions on the vibronic ground state, which simultaneously generates initial conditions (position and momentum) used in molecular dynamics simulations [251, 252]. Starting from the absorption cross section $\sigma(E)$ within Born-Oppenheimer and electric dipole approximation [252]:

$$\sigma(E) = \frac{\pi}{3\hbar c \varepsilon_0 n_r E} \sum_{n,k} \int \left| \Delta E_{00,nk}(\mathbf{R}) \chi_{00}^{*}(\mathbf{R}) \boldsymbol{\mu}_{0,n}(\mathbf{R}) \chi_{nk}(\mathbf{R}) \right|^2 \delta\left(\Delta E_{00,nk}(\mathbf{R}) - E\right) \mathrm{d}^3 R \,, \tag{A.36}$$

where the sums run over all electronic states n and vibrational states k; χ represent the nuclear wave function; $\boldsymbol{\mu}_{0,n}$ is the electronic transition dipole moment between electronic ground and excited state; $\Delta E_{00,nk} = E_{nk} - E_{00} + \Delta E_{0,n}$ with vibrational energies E_{00} (E_{nk}) of the ground (excited) state and vertical excitation energy $\Delta E_{0,n}$; n_r is the refractive index. As usual, ε_0 denotes the permittivity of free space, c the speed of light, and $\hbar$ the reduced Planck constant.

The ultimate target is to compute the overlap function of the vibrational ground and excited state.

Transforming Equation A.36 into time domain while assuming the vibronic ground state at $t = 0$, applying an approximation for the vertical excitation energy ($\Delta E_{0,n} \approx \langle \Delta E_{00,nk} \rangle_k$) and approximating the overlap as

$$\chi_{00}^{*}(\mathbf{R}) \chi_n(\mathbf{R}, t) \approx |\chi_{00}(\mathbf{R})|^2 \exp\left[-\frac{\delta_n}{2\hbar} |t| - \frac{i}{\hbar} \Delta E_{0,n}(\mathbf{R}) t - \frac{i}{\hbar} E_{00}(\mathbf{R}) t \right] , \tag{A.37}$$

the cross section reads [251, 252]:

$$\sigma(E) = \frac{\pi\hbar e^2}{2m_e c\varepsilon_0 n_r E} \sum_n \int |\chi_{00}(\mathbf{R})|^2 \, \Delta E_{0,n}(\mathbf{R}) f_{0,n}(\mathbf{R}) \times g_{\text{lorentz}}\left(E - \Delta E_{0,n}(\mathbf{R}), \delta_n\right) \mathrm{d}^3R \, . \tag{A.38}$$

Here, m_e is the electron mass and e the elementary charge, and $f_{0,n}$ is the oscillator strength between the states. The parameter δ_n is associated with the lifetime of excited state n, which yields the finite sharpness of the g_{lorentz} function, which is a Lorentzian line shape defined by

$$g_{\text{lorentz}}(E - \Delta E_{0,n}, \delta_n) = \frac{1}{\pi} \frac{\delta_n/2}{\left(E - \Delta E_{0,n}(\mathbf{R})\right)^2 + (\delta_n/2)^2} \, . \tag{A.39}$$

Note that different approximations for the overlap can be defined, leading to different shapes of g.

At the heart of the nuclear-ensemble approach lies the estimation of the integral over the nuclei coordinates $\mathbf{R}$, which is done via a Monte Carlo approach sampling and ensemble of N_p random distributions of nuclear coordinates $\mathbf{R}_l$ (more specific, the normal coordinates $\mathbf{Q}_l$) and an independent sampled ensemble of momentum $\mathbf{P}_l$ [252]. Finally, the cross section reads

$$\sigma(E) = \frac{\pi\hbar e^2}{2m_e c\varepsilon_0 n_r E} \sum_n^{N_{\text{fin}}^{\text{el}}} \frac{1}{N_p} \sum_l^{N_p} \Delta E_{0,n}(\mathbf{R}_l) f_{0,n}(\mathbf{R}_l) \times g_{\text{lorentz}}\left(E - \Delta E_{0,n}(\mathbf{R}_l), \delta_n\right) \, , \tag{A.40}$$

where the electronic sum runs over finite electronic states $N_{\text{fin}}^{\text{el}}$. The acceptance of the sampled normal modes and momentum are evaluated via a Wigner distribution in phase space $\mathcal{P}_{\text{W}}(\mathbf{Q}, \mathbf{P})$, which is valid in the harmonic oscillator approximation of the ground state [251]:

$$\mathcal{P}_{\text{W}}(\mathbf{Q}, \mathbf{P}) = \prod_{j=1}^{3N_A-6} \frac{\alpha_j(T)}{\pi\hbar} \exp\left(-\frac{\alpha_j(T)\mu_j\omega_j\Delta Q_j^2}{\hbar}\right) \exp\left(-\frac{\alpha_j(T)P_j^2}{\mu_j\omega_j\hbar}\right) \, , \tag{A.41}$$

where ΔQ_j is the normal mode displacement relative to its equilibrium position. The temperature-dependent factor is defined as $\alpha_j(T) = \tanh(\hbar\omega_j/2k_BT)$, where T is the absolute temperature and k_B is the Boltzmann constant; μ_j and ω_j are the reduced mass and frequency of the harmonic normal mode. Both the absorption cross section and the Wigner distribution can, in principle, account for finite-temperature effects through the α_j

factor; however, such corrections are not considered in the present work, and all sampling procedures are performed in the $T = 0$ limit.

A.3 Reorganization Energy

This section summarizes the reorganization energy frameworks used throughout this thesis, with emphasis on the four-point method and the evaluation of reorganization energies associated with vibrational modes.

A.3.1 Reorganization Energy via the Four-Point Method

To evaluate the inner reorganization energy relevant for electron-transfer processes within the Marcus framework, the so-called four-point method is commonly employed [106]. This approach is based on the potential energy surfaces (PESs) of the reactant ($\mathcal{R}$) and product ($\mathcal{P}$) states and is defined as

$$\lambda = \underbrace{\big(E_{\mathcal{R}}(R_{\mathcal{P}}) - E_{\mathcal{R}}(R_{\mathcal{R}})\big)}_{\lambda_1} + \underbrace{\big(E_{\mathcal{P}}(R_{\mathcal{R}}) - E_{\mathcal{P}}(R_{\mathcal{P}})\big)}_{\lambda_2}, \tag{A.42}$$

where R denotes the nuclear coordinates at the equilibrium geometry of the respective electronic state, and E is the corresponding electronic energy evaluated on the specified PES.

Within the four-point method, λ_1 corresponds to the energy required to distort the reactant potential energy surface from its equilibrium geometry to the product geometry, while λ_2 represents the analogous distortion of the product surface to the reactant geometry. Together, these contributions quantify the overall geometric mismatch between the minima of the two PESs.

In Marcus theory, however, electron transfer is described along a one-dimensional reaction coordinate, and both PESs are harmonic with identical curvature along the reaction coordinate. Under these assumptions, the two distortion contributions become equal, i.e., $\lambda_1 = \lambda_2$, and the Marcus reorganization energy corresponds to either contribution, $\lambda^{\text{Marcus}} = \lambda_1 = \lambda_2$.

If the PESs deviate from perfect symmetry, which is typically the case in realistic systems, it is common practice to approximate the Marcus reorganization energy by averaging both contributions,

$$\lambda^{\text{Marcus}} = \frac{\lambda_1 + \lambda_2}{2}. \tag{A.43}$$

For large and complex systems consisting of two molecular units, such as donor:acceptor complexes, it is often computationally advantageous to evaluate the reactant and product states as combinations of isolated molecules. For instance, an electron-transfer process of the form $D_+A \longrightarrow DA_+$, where the subscript + indicates the location of the charge, can be approximated as $D_+ + A \longrightarrow D + A_+$ using separated donor and acceptor fragments. This approximation enables the calculation of reorganization energies for systems in which full geometry optimizations of the combined complex would be prohibitively expensive.

It should be noted, however, that this approach neglects certain reorganization effects, most notably changes in intermolecular degrees of freedom such as donor:acceptor distances and orientations, which may contribute significantly to the total inner reorganization energy.

A.3.2 Reorganization Energy Evaluation from Vibrational Mode Analysis

To evaluate the mode-resolved reorganization energies λ_m and Huang-Rhys factors S_m, the structural relaxation between two electronic states (reactant $\mathcal{R}$ and product $\mathcal{P}$) is projected onto a chosen set of vibrational normal modes. Within the harmonic approximation, the Huang-Rhys factor associated with vibrational mode m is given by [78]

$$S_m = \frac{1}{2}\omega_m \frac{\Delta Q_m^2}{\hbar} \,, \tag{A.44}$$

where ω_m is the angular frequency of mode m, and ΔQ_m denotes the mass-weighted displacement along the corresponding normal coordinate between the two equilibrium geometries.

The mass-weighted Cartesian displacement between the equilibrium structures of the two states is defined as

$$\Delta \mathbf{x} = \underline{\underline{\mathrm{M}}}^{1/2}\left(\mathbf{R}_{\mathcal{P}} - \mathbf{R}_{\mathcal{R}}\right) \,, \tag{A.45}$$

with diagonal mass matrix $\underline{\underline{\mathrm{M}}}$, which contains the atomic masses repeated for the three Cartesian directions. $\mathbf{R}_{\mathcal{P}}$ and $\mathbf{R}_{\mathcal{R}}$ are the sets of $3N$ Cartesian coordinates of the product and reactant states, respectively, where N is the number of atoms.

The displacement along vibrational mode m is obtained by projecting $\Delta\mathbf{x}$ onto the normal-mode eigenvector $\mathbf{l}_m$:

$$\Delta Q_m = \mathbf{l}_m^{\mathrm{T}} \Delta \mathbf{x} \,, \tag{A.46}$$

where $\mathbf{l}_m$ is the eigenvector associated with mode m in the chosen normal-mode basis. The choice of projection basis depends on the direction of the electronic transition; in practice, the normal modes of the final electronic state are commonly used.

From the Huang-Rhys factors, the contribution of each vibrational mode to the reorganization energy is given by

$$\lambda_m = \hbar\omega_m S_m \,, \tag{A.47}$$

and the total inner reorganization energy is obtained as [78]

$$\lambda = \sum_m \lambda_m = \sum_m \hbar\,\omega_m\, S_m \,. \tag{A.48}$$

When the normal modes of the two electronic states differ, the quantities ΔQ_m obtained by projection onto the respective mode sets correspond to different normal-coordinate bases. They represent projections of the same Cartesian displacement onto different vibrational subspaces and are therefore not interchangeable on a mode-by-mode level, although the total quadratic form defining the reorganization energy remains invariant within a given harmonic representation. If vibrational overlap integrals (Franck-Condon factors) are to be evaluated explicitly, the relationship between the two sets of normal modes must be taken into account, which can be achieved using the Duschinsky rotation and translation formalism [78].

A.4 Electronic-Structure Methods

A.4.1 Density Functional Theory

In this chapter, a concise overview of density functional theory (DFT) is provided for describing the electronic ground-state structure. Since DFT is a well-established and extensively documented framework, only its fundamental concepts and key approximations are highlighted here. For a comprehensive treatment, the reader is referred, for instance, to References [253–256].

The description of the electronic system starts from the time-independent Schrödinger equation under *Born-Oppenheimer approximation*. The corresponding eigenvalue problem for the electronic state $\phi_i(\mathbf{r}, \mathbf{R})$ is given by (cf. Equation 3.5):

$$\mathcal{H}_e(\mathbf{r}, \mathbf{R})\phi_i(\mathbf{r}, \mathbf{R}) = E_i(\mathbf{R})\phi_i(\mathbf{r}, \mathbf{R}) \,, \quad \text{with} \tag{A.49}$$

$$\mathcal{H}_e(\mathbf{r}, \mathbf{R}) = \underbrace{\sum_{i=1}^{N_\mathrm{el}} \frac{-\hbar^2 \nabla_{\mathbf{r}_i}^2}{2m_e}}_{\mathcal{T}^\mathrm{el}} + \underbrace{\sum_{i,j=1;i<j}^{N_\mathrm{el}} \frac{e^2}{|\mathbf{r}_i - \mathbf{r}_j|}}_{\mathcal{U}^\mathrm{el\text{-}el}} + \underbrace{\sum_{i=1}^{N_\mathrm{el}} \sum_{K=1}^{N_A} \frac{-Z_K e^2}{|\mathbf{R}_K - \mathbf{r}_i|}}_{\mathcal{V}^\mathrm{ext}} \,. \tag{A.50}$$

In this Hamiltonian, $\mathcal{T}^\mathrm{el}$ is the electronic kinetic energy of the N_el electrons; $\mathcal{U}^\mathrm{el\text{-}el}$ is the electron-electron electrostatic Coulomb interaction; $\mathcal{V}^\mathrm{ext}$ is the external potential arising from attractive Coulomb interaction between the electrons and the static N_A nuclei. Here, m_e and e are the electron mass and charge, respectively, and $\hbar$ is the reduced Planck constant. The nuclear-nuclear repulsion term is not included in the electronic Hamiltonian; within the Born-Oppenheimer approximation it represents a constant energy contribution for fixed nuclear geometry and is therefore added separately after solving the electronic problem.

A significant reduction of the problem complexity was achieved by Hohenberg and Kohn in 1964 through their *Hohenberg-Kohn theorem* [257], which establishes a unique one-to-one correspondence between the ground-state electron density $\rho_0(\mathbf{r})$ and the external potential $\mathcal{V}^\mathrm{ext}$ (up to an additive constant). This result allows the total energy to be reformulated as a functional of the electron density:

$$E_v[\rho] = \underbrace{\mathcal{T}^\mathrm{el}[\rho] + \mathcal{U}^\mathrm{el\text{-}el}[\rho]}_{:=\mathcal{F}[\rho]} + \underbrace{\mathcal{V}^\mathrm{ext}[\rho]}_{=\int \mathrm{d}^3\mathbf{r}\rho(\mathbf{r})\,v(\mathbf{r})} \,. \tag{A.51}$$

According to the variational principle, this energy functional $E_v[\rho]$ attains its minimum at the exact ground-state density ρ_0. The universal functional $\mathcal{F}[\rho]$ comprises the electronic kinetic energy and electron-electron interactions. However, its exact analytical form is unknown, necessitating suitable and reasonable approximations.

To address this limitation, Kohn and Sham introduced their approach in 1965, in which the interacting many-electron system is mapped onto an auxiliary system of non-interacting particles described by spin orbitals, referred to as *Kohn-Sham orbitals*, $\varphi_{i,\sigma}^{\mathrm{KS}}$. All unknown many-body effects are incorporated into the exchange-correlation functional and its associated exchange-correlation potential, $v_{xc,\sigma}$. The exchange-correlation functional accounts for the difference between the true interacting kinetic energy and that of the non-interacting reference system, as well as for non-classical electron-electron interaction effects. This leads to the self-consistent Kohn-Sham equations in atomic units for the orbitals and their associated eigenvalues $\varepsilon_{i,\sigma}$ [253–255]:

$$\left[-\frac{\nabla^2}{2} + v(\mathbf{r}) + \int \frac{\rho(\mathbf{r}')}{|\mathbf{r}-\mathbf{r}'|}\mathrm{d}^3r' + v_{xc,\sigma}(\mathbf{r})\right]\varphi_{i,\sigma}^{\mathrm{KS}}(\mathbf{r}) = \varepsilon_{i,\sigma}\varphi_{i,\sigma}^{\mathrm{KS}}(\mathbf{r})\ . \tag{A.52}$$

Within this framework, the Kohn-Sham electron density is defined as

$$\rho^{\mathrm{KS}}(\mathbf{r}) = \sum_{\substack{\sigma\in\{\alpha,\beta\}\\ i=1}}^{N_{\mathrm{el},\sigma}} |\varphi_{i,\sigma}^{\mathrm{KS}}(\mathbf{r})|^2 = \rho_\alpha^{\mathrm{KS}}(\mathbf{r}) + \rho_\beta^{\mathrm{KS}}(\mathbf{r}) \tag{A.53}$$

and, within the exact Kohn-Sham formalism, coincides with the exact interacting ground-state electron density. The spin-dependent exchange-correlation potential is obtained as

$$v_{xc,\sigma}(\mathbf{r}) = \frac{\delta E_{xc}[\rho_\alpha,\rho_\beta]}{\delta\rho_\sigma(\mathbf{r})}\ . \tag{A.54}$$

The ground-state wave function of the auxiliary Kohn-Sham system, ϕ_0, is constructed as a *Slater determinant* of the Kohn-Sham orbitals representing the non-interacting reference system. This form guarantees antisymmetry of the wave function and thus ensures compliance with the Pauli exclusion principle.

A.4.2 Time-Dependent Density Functional Theory

As DFT is formulated to describe ground-state electronic properties, the calculation of excited-state properties requires a time-dependent extension, namely time-dependent den-

sity functional theory (TD-DFT). TD-DFT is a well-established and extensively documented theoretical framework; therefore, only its essential concepts and key approximations are summarized here. For a comprehensive discussion, the reader is referred, for example, to References [121, 258–262].

The excitation of a molecular system can be described as the action of a time-dependent external electric field, treated as a perturbation in time t. Within the linear-response regime, this perturbation is commonly expressed as $v_t(\mathbf{r})f(t)$. The resulting external potential is then given by

$$v(\mathbf{r}, t) = v_{\text{static}}(\mathbf{r}) + v_t(\mathbf{r})f(t) \,, \tag{A.55}$$

where $v_{\text{static}}(\mathbf{r})$ denotes the static potential generated by the nuclei.

In analogy to the Hohenberg-Kohn theorem for DFT, the Runge-Gross theorem [263] establishes a one-to-one correspondence between the time-dependent electron density $\rho(\mathbf{r}, t)$, the time-dependent external potential (up to a purely time-dependent constant), and the time-dependent many-body wave function. Introducing a system of non-interacting particles within the Kohn-Sham formalism leads to the time-dependent Kohn-Sham equations for the spin-orbitals $\varphi_{i,\sigma}(\mathbf{r}, t)$:

$$\left[-\frac{\nabla^2}{2} + v(\mathbf{r}, t) + \int \frac{\rho(\mathbf{r}', t)}{|\mathbf{r} - \mathbf{r}'|} \mathrm{d}^3 r' + v_{xc,\sigma}(\mathbf{r}, t)\right] \varphi_{i,\sigma}(\mathbf{r}, t) = i\frac{\partial}{\partial t}\varphi_{i,\sigma}(\mathbf{r}, t) \,. \tag{A.56}$$

For simplicity, the superscript “KS” for the spin-orbitals is omitted.

Within the adiabatic approximation, the time-dependent exchange-correlation (xc) potential is assumed to be local in time. Consequently, it is approximated by the ground-state exchange-correlation functional evaluated at the instantaneous electron density:

$$v_{xc,\sigma}(\mathbf{r}, t) \approx \left.\frac{\delta E_{xc}^{\text{gs}}[\rho_\alpha, \rho_\beta]}{\delta \rho_\sigma(\mathbf{r})}\right|_{\rho(\mathbf{r})=\rho(\mathbf{r},t)} \,. \tag{A.57}$$

Next, considering a weak time-dependent perturbation of the ground state within linear response theory, the linear response of the electron density $\rho^{(1)}(\mathbf{r}, t)$ can be described via the linear-response kernel $\chi^{\text{KS}}_{\sigma,\sigma'}(t, t', \mathbf{r}, \mathbf{r}')$ of the non-interacting Kohn-Sham particles. This leads to a self-consistent formulation of the linear density response. After Fourier transformation to the frequency domain, the response equation for each spin component

becomes [258]

$$\rho_\sigma^{(1)}(\mathbf{r},\omega) = \sum_{\sigma'} \int \mathrm{d}^3 r'\ \chi^{\mathrm{KS}}_{\sigma,\sigma'}(\omega,\mathbf{r},\mathbf{r}') \Bigg[v_t(\mathbf{r}') f(\omega) + \sum_{\sigma''} \int \mathrm{d}^3 r'' \Bigg(\frac{1}{|\mathbf{r}'-\mathbf{r}''|} + \frac{\delta^2 E_{xc}}{\delta\rho_{\sigma'}(\mathbf{r}')\delta\rho_{\sigma''}(\mathbf{r}'')} \Bigg) \rho^{(1)}_{\sigma''}(\mathbf{r}'',\omega) \Bigg], \tag{A.58}$$

where the linear Kohn-Sham response kernel is given by

$$\chi^{\mathrm{KS}}_{\sigma,\sigma'}(\omega,\mathbf{r},\mathbf{r}') = \delta_{\sigma,\sigma'} \sum_{i,a} \Bigg(\frac{\varphi^*_{i\sigma}(\mathbf{r})\varphi_{a\sigma}(\mathbf{r})\varphi_{i\sigma}(\mathbf{r}')\varphi^*_{a\sigma}(\mathbf{r}')}{\omega - (\varepsilon_{a\sigma} - \varepsilon_{i\sigma}) + \mathrm{i}\eta} - \frac{\varphi_{i\sigma}(\mathbf{r})\varphi^*_{a\sigma}(\mathbf{r})\varphi^*_{i\sigma}(\mathbf{r}')\varphi_{a\sigma}(\mathbf{r}')}{\omega + (\varepsilon_{a\sigma} - \varepsilon_{i\sigma}) - \mathrm{i}\eta} \Bigg). \tag{A.59}$$

Here, $f(\omega)$ is the Fourier-transform of $f(t)$. Similar to above, index a denotes virtual (unoccupied) orbitals and index i denotes occupied orbitals. The limit $\eta \longrightarrow 0^+$ is understood, and i is the imaginary unit.

The self-consistent solution for the first-order density response can be written as

$$\rho^{(1)}(\mathbf{r},\omega) = \sum_{i,a,\sigma} \Big(X_{i,a,\sigma}(\omega)\varphi^*_{a\sigma}(\mathbf{r})\varphi_{i\sigma}(\mathbf{r}) + Y_{i,a,\sigma}(\omega)\varphi_{a\sigma}(\mathbf{r})\varphi^*_{i\sigma}(\mathbf{r}) \Big), \tag{A.60}$$

where $X_{i,a,\sigma}(\omega)$ and $Y_{i,a,\sigma}(\omega)$ denote the excitation and de-excitation amplitudes, respectively.

Adopting a matrix formalism and introducing the coupling-matrix $K_{pq\sigma,p'q'\sigma'}$ (with p, q general indices for orbitals) leads to the so-called *Casida-Equations* [121, 259, 262]:

$$\begin{pmatrix} \underline{\underline{\mathrm{A}}} & \underline{\underline{\mathrm{B}}} \\ \underline{\underline{\mathrm{B}}}^* & \underline{\underline{\mathrm{A}}}^* \end{pmatrix} \begin{pmatrix} \mathbf{X} \\ \mathbf{Y} \end{pmatrix} = \omega \begin{pmatrix} 1 & 0 \\ 0 & -1 \end{pmatrix} \begin{pmatrix} \mathbf{X} \\ \mathbf{Y} \end{pmatrix}. \tag{A.61}$$

Here, the matrix elements are defined as

$$A_{ia\sigma,i'a'\sigma'} = \delta_{\sigma\sigma'}\delta_{ii'}\delta_{aa'}(\varepsilon_{a\sigma} - \varepsilon_{i\sigma}) + K_{ia\sigma,i'a'\sigma'} \,, \tag{A.62}$$

$$B_{ia\sigma,i'a'\sigma'} = K_{ia\sigma,a'i'\sigma'} \,, \tag{A.63}$$

$$K_{pq\sigma,p'q'\sigma'} = \iint \mathrm{d}^3r\, \mathrm{d}^3r' \varphi^*_{p\sigma}(\mathbf{r})\varphi_{q\sigma}(\mathbf{r})\left(\frac{1}{|\mathbf{r}-\mathbf{r}'|} + \frac{\delta^2 E_{xc}}{\delta\rho_\sigma(\mathbf{r})\delta\rho_{\sigma'}(\mathbf{r}')}\right)\varphi^*_{p'\sigma'}(\mathbf{r}')\varphi_{q'\sigma'}(\mathbf{r}') \,. \tag{A.64}$$

Solving this eigenvalue problem yields excitation energies ω corresponding to transitions from the ground state to excited states.

At this point, two quantities of particular interest are the effective excited-state pseudo-wavefunction $|\phi_I^{\mathrm{exc}}\rangle$ and the associated ground-to-excited-state transition density. Within linear-response theory, the excitation and de-excitation amplitudes define an effective pseudo-wavefunction, which can be expressed in second quantization as a linear combination of single electron-hole excitations [121]:

$$|\phi_I^{\mathrm{exc}}\rangle = \sum_{i,a,\sigma}\left(X_{i,a,\sigma}\hat{a}^\dagger_{a,\sigma}\hat{a}_{i,\sigma} + Y_{i,a,\sigma}\hat{a}^\dagger_{i,\sigma}\hat{a}_{a,\sigma}\right)|\phi_0\rangle \,. \tag{A.65}$$

From here, the corresponding transition density is then given by:

$$\rho_{0I}(\mathbf{r}) = \langle\phi_0|\,\hat{\rho}\,|\phi_I^{\mathrm{exc}}\rangle = \sum_{i,a,\sigma}\left(X_{i,a,\sigma} + Y_{i,a,\sigma}\right)\varphi^*_{i,\sigma}(\mathbf{r})\varphi_{a,\sigma}(\mathbf{r}) \,. \tag{A.66}$$

This transition density, in turn, determines the transition dipole moment and thus oscillator strength of the electronic transition. Note, that the amplitudes are typically normalized.

Within the *Tamm-Dancoff approximation* (TDA) [264], the matrix $\underline{\underline{\mathrm{B}}}$ is neglected, which leads to vanishing de-excitation amplitudes. While this approximation typically has little impact on singlet excitation energies, it often improves the description of triplet excitations. However, both TDA and full linear-response TD-DFT remain inadequate in strongly correlated situations, such as conical intersections, due to the adiabatic approximation and the lack of double excitations, although inclusion of the $\underline{\underline{\mathrm{B}}}$ matrix can improve the formal consistency of the response equations.

A.4.3 Computational Methods

This section provides a brief overview of the methods used for electronic-structure calculations based on DFT and its TD variant, including the basis set and exchange-correlation functional employed throughout this thesis. In addition, complementary approaches that extend the standard (TD-)DFT framework are outlined: dispersion correction schemes, implicit solvation models, gap-tuning approach, and the broken-symmetry DFT method.

Basis Set

To numerically solve the Kohn-Sham equations within DFT or its TD variant, a finite basis set is introduced to represent the molecular orbitals $\varphi_i^{\mathrm{KS}}(\mathbf{r})$ (the spin index is omitted for clarity). Different numerical representations exist for this purpose, including plane waves and localized atomic orbitals. In Gaussian-based quantum chemistry implementations of DFT, the molecular orbitals are expanded in a linear combination of atomic orbitals (LCAO), in which the atomic orbitals are expressed as contracted gaussian-type functions (CGTFs), G_μ^{CGTF}, which themselves are linear combinations of gaussian-type functions (GTFs), g_ν [66].

A Kohn-Sham orbital is thus written as

$$\varphi_i^{\mathrm{KS}}(\mathbf{r}) = \sum_{\mu}^{N_\mu} c_{\mu i} G_\mu^{\mathrm{CGTF}} = \sum_{\mu}^{N_\mu} c_{\mu i} \left[\sum_{\nu}^{N_\nu} d_{\mu\nu} g_\nu(\mathbf{r}) \right] , \quad \text{with} \tag{A.67}$$

$$g_\nu(\mathbf{r}) = A_\nu (x - x_A)^m (y - y_A)^n (z - z_A)^o \exp\left(-\alpha_\nu |\mathbf{r} - \mathbf{r}_A|^2\right) . \tag{A.68}$$

Here, $c_{\mu i}$ are the molecular orbital expansion coefficients and $d_{\mu\nu}$ are the contraction coefficients defining each CGTF; N_μ and N_ν are the total number of CGTFs and the number of primitive Gaussians per contraction, respectively; α_ν and A_ν are the Gaussian exponent and normalization constant, respectively; x, y, z are Cartesian coordinates with its origin at the nucleus $\mathbf{r}_A$ (x_A, y_A, z_A), and $l = m + n + o$ defines the total angular momentum of the Cartesian Gaussian.

In most basis sets, a distinction is made between core and valence electrons. Core orbitals are typically represented by a single contracted basis function, while valence orbitals are often split into multiple contracted functions, giving rise to so-called split-valence basis sets, which provide enhanced radial flexibility.

A widely used family of CGTF basis sets is the Pople-type family [265], in which the core orbitals are represented by X primitive Gaussians and the valence orbitals by multiple contracted sets consisting of Y, Z, ...primitive Gaussians. Here, Y and Z, ...correspond to separate contractions for valence orbitals. These basis sets are commonly denoted as X-YZ...G.

To allow for directional distortion of the electron density, which is essential for an accurate description of chemical bonding, polarization functions may be added, denoted as X-YZ...G(polarization). This is realized by addition of CGTFs with angular momentum higher than the highest occupied atomic orbital of the free atom, for example, *d*-type functions for atoms with valence *p* orbitals.

Moreover, to properly describe weakly bound or spatially extended electron density, such as in anionic systems, diffuse functions can be incorporated into the basis set. These are additional CGTFs characterized by small Gaussian exponents α_ν, leading to increased radial extent of the basis functions. They are typically denoted as X-YZ...++G(polarization), where + denotes diffuse functions on heavy atoms, and ++ denotes diffuse functions on both heavy atoms and hydrogen.

The choice of basis set depends on the system under investigation. For medium-sized organic systems, the Pople-type 6-31G(d,p) basis set [265] is commonly employed, as it offers a reasonable balance between computational cost and accuracy.

Dispersion Correction

Dispersion, or van der Waals interaction, plays a crucial role in accurately describing intermolecular interactions as well as intramolecular interactions in large molecular systems. These interactions arise from correlated instantaneous fluctuations of the electron density and are not properly captured by conventional semi-local density functional approximations. Typically, the dispersion is incorporated as an additive energy correction term, E_{disp}, to the Kohn-Sham DFT energy, $E_{\text{KS-DFT}}$, written as

$$E_{\text{DFT-D}} = E_{\text{KS-DFT}} + E_{\text{disp}} \, . \tag{A.69}$$

It is common practice to employ an atom-pairwise formalism, in which the dispersion energy is expressed in terms of interatomic distance-dependent contributions. It can be

generalized to

$$E_{\text{disp}} = -\frac{1}{2} \sum_{A \neq B} \sum_{n=6,8,10,\ldots} s_n \frac{C_n^{\text{AB}}}{R_{\text{AB}}^n} f_{\text{damp},n}(R_{\text{AB}}) \,, \tag{A.70}$$

where the sum runs over all atom pairs AB, R_{AB} denotes the internuclear distance between atom A and B, s_n are global scaling factors, C_n^{AB} are the dispersion coefficients of pair AB, and f_{damp} is a damping function preventing divergence of the expression.

Widely used empirical dispersion corrections include Grimme's D2 method [266], which includes only the $6th$ order, and more advanced Grimme's D3 method [267], which accounts for the $6th$ and $8th$ orders. These approaches differ in their evaluation of the dispersion coefficients, inclusion of higher-order terms, and in the choice of damping function, which are given by

$$f_{\text{damp},n}^{\text{D2}}(R_{\text{AB}}) = \frac{1}{1 + \exp\left[-d\left(\frac{R_{\text{AB}}}{s_{R,n} R_{0,\text{AB}}^{\text{D2}}} - 1 \right) \right]} \,, \tag{A.71}$$

$$f_{\text{damp},n}^{\text{D3}} = \frac{1}{1 + 6\left(\frac{R_{\text{AB}}}{s_{R,n} R_{0,\text{AB}}^{\text{D3}}} \right)^{-\gamma_n}} \,, \tag{A.72}$$

or by the damping function introduced by Becke and Johnson (BJ) [268–270] of the form

$$f_{\text{damp},n}^{\text{BJ}}(R_{\text{AB}}) = \frac{R_{\text{AB}}^n}{R_{\text{AB}}^n + \left(\alpha_1 R_{0,\text{AB}}^{\text{BJ}} + \alpha_2 \right)^n} \,. \tag{A.73}$$

The parameters s_n, $s_{R,n}$, α_1, and α_2 depend on the specific choice of exchange-correlation functional employed. In the D2 method, the parameter $d = 20$ defines the steepness of the damping, whereas for D3 method, the parameters $\gamma_6 = 14$ and $\gamma_8 = 16$ govern short-range behavior.

In Grimme's D2 method, the cutoff-radius $R_{0,\text{AB}}$ is defined from the van der Waals atomic radii of the atoms A and B. In contrast, for Grimme's D3 dispersion method with and without the BJ damping function [271], the cutoff-radius is defined from the dispersion coefficients as

$$R_{0,\text{AB}}^{\text{D3(BJ)}} = \sqrt{\frac{C_8^{\text{AB}}}{C_6^{\text{AB}}}} \,. \tag{A.74}$$

Although the numerical values of the dispersion coefficients differ between the schemes,

they are generally associated with different orders of multipole interactions: C_6 predominantly reflects dipole-dipole dispersion, whereas C_8 is mainly dominated by dipole-quadrupole contributions.

Exchange-Correlation Functional

The central quantity governing the reliability of DFT and TD-DFT is the exchange-correlation (xc) functional. Typically these are parameterized against thermochemical datasets and/or high-level ab initio reference data, sometimes in combination with experimental measurements. Depending on the aim of the investigated system, appropriate functionals have to be chosen to reliably reflect the properties under investigation. In the simplest approximation, these rely on the local electron density and its gradient. Hybrid functionals incorporating a fraction of Hartree–Fock exchange have proven particularly successful in describing small organic semiconductors, such as the B3LYP functional. These can be further adjusted into hybrid functionals that separate the exact exchange contributions to short- and long-range contributions. Increasing the fraction of long-range exact exchange has been shown to provide a more accurate description of the excited-state character of organic semiconductors, particularly due to their pronounced charge-transfer nature. Commonly used methods include the Coulomb-attenuating method (CAM)-B3LYP, or the ωB97X-D functional; the latter also includes dispersion corrections by design.

B3LYP

This functional combines Becke's exchange functional [272], E_x^{B3}, consisting of the local spin-density approximation (LSDA) exchange, (E_x^{LSDA}), augmented by a gradient correction [273], ($\Delta E_x^{\mathrm{B88}}$), with a global fraction of exact Hartree-Fock exchange, (E_x^{HF}). The correlation energy is constructed by mixing the gradient-corrected correlation functional of Lee, Yang, and Parr [274], (E_c^{LYP}), with the local correlation functional of Vosko, Wilk, and Nusair [275], (E_c^{VWN}). The VWN variant may differ in different implementations of the functional.

The resulting exchange-correlation functional is given by

$$E_{xc}^{\mathrm{B3LYP}} = aE_x^{\mathrm{HF}} + (1-a)E_x^{\mathrm{LSDA}} + c\Delta E_x^{\mathrm{B88}} + bE_c^{\mathrm{LYP}} + (1-b)E_c^{\mathrm{VWN}}\,, \tag{A.75}$$

where the parameters $a = 0.2$, $b = 0.81$, and $c = 0.72$ are empirically fitted.

CAM-B3LYP

To resolve the problem that the exchange potential decays incorrectly in the B3LYP functional, the exchange component is separated into a short-range (SR) and long-range (LR)

component, leading to improved asymptotic behavior of the exchange potential. This is achieved by splitting the Coulomb-operator into [276]

$$\frac{1}{r_{12}} = \underbrace{\frac{\mathrm{erfc}(\omega r_{12})}{r_{12}}}_{\mathrm{SR}} + \underbrace{\frac{\mathrm{erf}(\omega r_{12})}{r_{12}}}_{\mathrm{LR}} \,. \tag{A.76}$$

Applying this range separation to the B3LYP functional yields the Coulomb-attenuated CAM-B3LYP functional [277]

$$\begin{aligned} E_{xc}^{\text{CAM-B3LYP}} &= \alpha E_x^{\mathrm{HF,SR}}(\omega) + (\alpha+\beta) E_x^{\mathrm{HF,LR}}(\omega) && \text{(A.77)} \\ &+ (1-\alpha) E_x^{\mathrm{LSDA,SR}}(\omega) + (1-\alpha-\beta) E_x^{\mathrm{LSDA,LR}}(\omega) && \text{(A.78)} \\ &+ c\left(\Delta E_x^{\mathrm{B88,SR}}(\omega) + \Delta E_x^{\mathrm{B88,LR}}(\omega)\right) && \text{(A.79)} \\ &+ b E_c^{\mathrm{LYP}} + (1-b) E_c^{\mathrm{VWN}} \,. && \text{(A.80)} \end{aligned}$$

The parameters $b = 0.81$, $c = 0.72$ are unchanged from B3LYP, while $\alpha = 0.19$ and $\beta = 0.46$ replace the global HF exchange parameter a in B3LYP. Here, α determines the fraction of exact HF exchange component at short range, while $\alpha + \beta$ determines its long-range contribution. The range-separation parameter is set to $\omega = 0.33$ bohr^{-1}. All values are empirically determined under physical constraints.

ωB97X-D

This functional is also a long-range corrected (LC) hybrid functional that combines the ωB97X functional with an empirical dispersion correction term. The KS-DFT exchange-correlation term combines exact HF exchange (SR and LR contributions), a modified SR-variant of Becke's E_x^{B97} exchange functional (denoted $E_x^{\mathrm{B97,SR}}$), as well as Becke's E_c^{B97} correlation [278]. The Becke's E_c^{B97} correlation is further decomposed into same-spin and opposite-spin components. The resulting ωB97X functional reads [279]

$$E_{xc}^{\omega\mathrm{B97X}} = E_x^{\mathrm{HF,LR}} + c_x E_x^{\mathrm{HF,SR}} + E_x^{\mathrm{B97,SR}} + E_c^{\mathrm{B97}} \,. \tag{A.81}$$

Dispersion interactions are accounted for via a correction similar to the D2-type empirical dispersion model, including only the $6th$-order term. The associated damping function is a zero-damping form that forces the dispersion correction to vanish at short interatomic

distances, it is given by [280]:

$$f_{\text{damp},n}^{\omega\text{B97X-D}} = \frac{1}{1 + a\left(\frac{R_{\text{AB}}}{R_{0,\text{AB}}}\right)^{-12}} , \tag{A.82}$$

with parameters specifically optimized for this functional. The cutoff-radius $R_{0,\text{AB}}$ is defined from the van der Waals atomic radii of the atoms A and B. This combination yields the final functional denoted ωB97X-D [280].

The range-separation parameter that defines the SR and LR exchange contributions is set to $\omega = 0.2$ bohr^{-1}. The fraction of SR-HF exchange is set to $c_x = 0.222036$. Note that the E_c^{B97} correlation comprises 15 parameters due to the spin-resolved formulation. All values are empirically determined under physical constraints.

Gap-Tuning Approach

To enhance the reliability of DFT calculations for the description of opto-electronic properties of organic semiconductors, the employed exchange-correlation functional can be systematically tuned to satisfy explicit physical constraints. In exact Kohn–Sham DFT, the HOMO energy equals the negative ionization potential (IP) as a consequence of Janak's theorem and the piecewise linearity of the total energy with respect to particle number [45, 281]. Approximate functionals violate this condition, and range-separated hybrids can be tuned to restore it. This concept is commonly extended to the anionic system, where the HOMO energy is constrained to reproduce the electron affinity (EA).

Within range-separated hybrid functionals, the range-separation parameter ω can be optimized such that these conditions are fulfilled. By enforcing agreement between orbital energies and the corresponding IP and EA, the resulting opto-electronic properties (including excitation energies, IPs, and EAs) show significantly improved agreement with experimental observations [45]. Since the IP and EA define the fundamental-gap of the system, this procedure is commonly referred to as gap-tuning approach.

The tuning procedure is carried out by minimizing the target function $J(\omega)$, which depends on the range-separation parameter ω:

$$J(\omega) = J_{\text{IP}}(\omega) + J_{\text{EA}} = \left|E_+(\omega) - E_0(\omega) + \varepsilon_0^{\text{H}}\right| + \left|E_0(\omega) - E_-(\omega) + \varepsilon_-^{\text{H}}\right| , \tag{A.83}$$

where E_0, E_+, and E_- denote the energy of the neutral, cationic, and anionic system, respectively. $\varepsilon_0^{\mathrm{H}}$ and $\varepsilon_-^{\mathrm{H}}$ denote the HOMO energy of the neutral and anionic system, respectively. Note that while alternative formulations of the target function $J(\omega)$ exist in the literature, all implementations are designed to enforce the same underlying physical constraints [45].

Polarizable Continuum Model

As explicit inclusion of a large number of solvent molecules is computationally expensive, an implicit solvation model is commonly employed to capture interactions between solvent and solute that strongly affect the solute's opto-electronic properties. Among these, widely used methods are based on the polarizable continuum model (PCM) [282, 283], in which the solvent is represented as a polarizable dielectric continuum surrounding a cavity that encloses the solute. The electrostatic potential generated by the solute polarizes the surrounding medium, and induces a reaction potential at the cavity surface that acts back on the solute.

Various methods exist to model the solvent cavity around the solute, which is usually based on a union of overlapping atom-centered spheres and subsequently processed into a smooth, discretized surface. Common cavity models include the scaled van der Waals surfaces, the Solvent Accessible Surface (SAS), and the Solvent Excluded Surface (SES). The cavity surface is divided into small surface elements, called tesserae. Inside the solvent cavity, the dielectric constant is set to $\varepsilon = 1$, whereas outside the cavity ε takes a finite value characteristic of the solvent, thus defining a dielectric boundary between the two regions.

The solute-solvent interaction is governed by polarization effects induced by the solute's electrostatic potential $V_{\mathrm{M}}(\mathbf{r})$, creating a reaction potential of the solvent, $V_{\mathrm{R}}(\mathbf{r})$. This interaction is described by the Poisson equation as

$$-\nabla\left[\varepsilon(\mathbf{r})\nabla V(\mathbf{r})\right] = 4\pi\rho_{\mathrm{M}}(\mathbf{r})\,, \tag{A.84}$$

where $\rho_{\mathrm{M}}(\mathbf{r})$ is the solute's charge distribution (including both nuclear and electronic contributions), and

$$V(\mathbf{r}) = V_{\mathrm{M}}(\mathbf{r}) + V_{\mathrm{R}}(\mathbf{r})\,. \tag{A.85}$$

By applying appropriate boundary conditions at the cavity surface, the reaction potential can be expressed in terms of so-called apparent surface charges (ASC), $\sigma(\mathbf{s})$, distributed over the cavity surface Γ. The reaction potential reads

$$V_{\mathrm{R}}(\mathbf{r}) = V_{\sigma}(\mathbf{r}) = \int_{\Gamma} \frac{\sigma(\mathbf{s})}{|\mathbf{r}-\mathbf{s}|} \mathrm{d}^2 s \ . \tag{A.86}$$

By using an integral equation formalism variant of PCM (IEFPCM) [284–286], the apparent surface charges are obtained by solving the following equation:

$$\mathbf{A}(\varepsilon)\boldsymbol{\sigma} = -\mathbf{g}(\rho_M) \ . \tag{A.87}$$

Here, the matrix notation is used to represent the discrete tesserae within this formalism. The matrix $\mathbf{A}(\varepsilon)$ accounts for the electrostatic interaction between tesserae across the dielectric boundary, and $\mathbf{g}(\rho_M)$ accounts for the interaction between the solute's charge density and the cavity surface. The surface charges are determined self-consistently within the self-consistent field (SCF) procedure in (TD-)DFT.

In conductor-like screening models, such as in C-PCM [287], the dielectric constant is taken to the limit $\varepsilon \to \infty$, eliminating the explicit ε-dependence of $\mathbf{A}$ and yielding computationally more efficient unscreened surface charges $\boldsymbol{\sigma}'$. The finite ε is introduced subsequently as a scaling factor $f(\varepsilon)$:

$$\boldsymbol{\sigma} = f(\varepsilon)\boldsymbol{\sigma}' \ . \tag{A.88}$$

The default solvation models and their implementations vary among different electronic-structure software packages, such as Gaussian 16 [147], Q-Chem 5.4 [123], or ORCA 6.0 [135]. The reader is referred to the respective documentation for details.

Broken-Symmetry

The approximate single-determinant Kohn-Sham implementations become inadequate when a multiconfigurational description of the wave function is required in certain situations for organic semiconductors. For example, a charge transfer character leading to odd electron populations on the molecular fragments of donor:acceptor complexes, $\mathrm{DA} \rightarrow \mathrm{D}_{+}\mathrm{A}_{-}$, or a (bi-)polaronic state of an organic semiconductor. In such situations, the spin-symmetric orbitals are insufficient to describe the electronic structure of the states. Here, spin-unrestricted formulation therefore constitutes the natural starting point, in

which the α- and β-orbitals are treated separately, allowing for different spatial distribution of the spin-polarized channels.

Within spin-unrestricted DFT, the broken-symmetry (BS) approach enables the formation of spin-polarized solutions by breaking spin symmetry, such that the resulting single-determinant wave function is no longer an eigenfunction of the total spin operator. In practice, this is often achieved by mixing near-degenerate frontier orbitals, which in simple cases corresponds to HOMO-LUMO mixing with opposite phase in the spin channels, generating spatially asymmetric orbitals [288, 289]. In this way, multiconfigurational effects can be mimicked within the single-determinant DFT framework, in accordance with schemes widely used in the literature to mimic the multiconfigurational character [290–292]. This procedure is usually applied in the initial formation of the orbitals, which subsequently serve as the starting point for the SCF procedure in DFT. However, the SCF procedure may converge back to a spin-symmetric solution if such a state is energetically favored.

While this procedure can yield meaningful charge distributions and energetics, spin-dependent properties derived from the resulting spin densities must be interpreted with caution. The BS wave function is affected by spin contamination, i.e. the admixture of higher-spin states inherent to the BS determinant, which leads to artificial spin densities. This spin contamination is an intrinsic feature of the broken-symmetry approach within a single-determinant framework and must be considered when interpreting results.

Bibliography

B

[1] H. Shirakawa, E. J. Louis, A. G. MacDiarmid, C. K. Chiang, and A. J. Heeger, Synthesis of electrically conducting organic polymers: halogen derivatives of polyacetylene, $(CH)_X$, Journal of the Chemical Society, Chemical Communications, 578–580 (1977).

[2] C. W. Tang, Two-layer organic photovoltaic cell, Applied Physics Letters **48**, 183–185 (1986).

[3] N. S. Sariciftci, L. Smilowitz, A. J. Heeger, and F. Wudl, Photoinduced electron transfer from a conducting polymer to buckminsterfullerene, Science **258**, 1474–1476 (1992).

[4] G. Yu and A. J. Heeger, Charge separation and photovoltaic conversion in polymer composites with internal donor/acceptor heterojunctions, Journal of Applied Physics **78**, 4510–4515 (1995).

[5] G. Yu, J. Gao, J. C. Hummelen, F. Wudl, and A. J. Heeger, Polymer photovoltaic cells: enhanced efficiencies via a network of internal donor-acceptor heterojunctions, Science **270**, 1789–1791 (1995).

[6] C. J. Brabec, N. S. Sariciftci, and J. C. Hummelen, Plastic solar cells, Advanced Functional Materials **11**, 15–26 (2001).

[7] L. Lu, T. Zheng, Q. Wu, A. M. Schneider, D. Zhao, and L. Yu, Recent advances in bulk heterojunction polymer solar cells, Chemical Reviews **115**, 12666–12731 (2015).

[8] J. Yi, G. Zhang, H. Yu, and H. Yan, Advantages, challenges and molecular design of different material types used in organic solar cells, Nature Reviews Materials **9**, 46–62 (2024).

[9] Z. Wang, D. Zhang, L. Yang, O. Allam, Y. Gao, Y. Su, M. Xu, S. Mo, Q. Wu, Z. Wang, J. Liu, J. He, R. Li, X. Jia, Z. Li, L. Yang, M. D. Weber, Y. Yu, X. Zhang, T. J. Marks, N. Stingelin, J. Kacher, S. S. Jang, A. Facchetti, and M. Shao, Mechanically robust and stretchable organic solar cells plasticized by small-molecule acceptors, Science **387**, 381–387 (2025).

[10] C. W. Tang and S. A. VanSlyke, Organic electroluminescent diodes, Applied Physics Letters **51**, 913–915 (1987).

[11] J. H. Burroughes, D. D. C. Bradley, A. R. Brown, R. N. Marks, K. Mackay, R. H. Friend, P. L. Burns, and A. B. Holmes, Light-emitting diodes based on conjugated polymers, Nature **347**, 539–541 (1990).

[12] M. Y. Wong and E. Zysman-Colman, Purely organic thermally activated delayed fluorescence materials for organic light-emitting diodes, Advanced Materials **29**, 1605444 (2017).

[13] H. Uoyama, K. Goushi, K. Shizu, H. Nomura, and C. Adachi, Highly efficient organic light-emitting diodes from delayed fluorescence, Nature **492**, 234–238 (2012).

[14] Y. Liu, C. Li, Z. Ren, S. Yan, and M. R. Bryce, All-organic thermally activated delayed fluorescence materials for organic light-emitting diodes, Nature Reviews Materials **3**, 18020 (2018).

[15] J. M. Dos Santos et al., The golden age of thermally activated delayed fluorescence materials: design and exploitation, Chemical Reviews **124**, 13736–14110 (2024).

[16] S. Banerjee, P. Singh, P. Purkayastha, and S. Kumar Ghosh, Evolution of organic light emitting diode (OLED) materials and their impact on display technology, Chemistry - An Asian Journal **20**, e202401291 (2025).

[17] A. Tsumura, H. Koezuka, and T. Ando, Macromolecular electronic device: field-effect transistor with a polythiophene thin film, Applied Physics Letters **49**, 1210–1212 (1986).

[18] G. Horowitz, Organic field-effect transistors, Advanced Materials **10**, 365–377 (1998).

[19] H. Sirringhaus, 25th anniversary article: organic field-effect transistors: the path beyond amorphous silicon, Advanced Materials **26**, 1319–1335 (2014).

[20] B. Lüssem, C.-M. Keum, D. Kasemann, B. Naab, Z. Bao, and K. Leo, Doped organic transistors, Chemical Reviews **116**, 13714–13751 (2016).

[21] J. Borges-González, C. J. Kousseff, and C. B. Nielsen, Organic semiconductors for biological sensing, Journal of Materials Chemistry C **7**, 1111–1130 (2019).

[22] H. Li, W. Shi, J. Song, H.-J. Jang, J. Dailey, J. Yu, and H. E. Katz, Chemical and biomolecule sensing with organic field-effect transistors, Chemical Reviews **119**, 3–35 (2019).

[23] M. E. Gemayel, K. Börjesson, M. Herder, D. T. Duong, J. A. Hutchison, C. Ruzié, G. Schweicher, A. Salleo, Y. Geerts, S. Hecht, E. Orgiu, and P. Samorì, Optically switchable transistors by simple incorporation of photochromic systems into small-molecule semiconducting matrices, Nature Communications **6**, 6330 (2015).

[24] J. Zou, J. Liao, Y. He, T. Zhang, Y. Xiao, H. Wang, M. Shen, T. Yu, and W. Huang, Recent development of photochromic polymer systems: mechanism, materials, and applications, Research **7**, 0392 (2024).

[25] V. Coropceanu, J. Cornil, D. A. da Silva Filho, Y. Olivier, R. Silbey, and J.-L. Brédas, Charge transport in organic semiconductors, Chemical Reviews **107**, 926–952 (2007).

[26] K. Walzer, B. Maennig, M. Pfeiffer, and K. Leo, Highly efficient organic devices based on electrically doped transport layers, Chemical Reviews **107**, 1233–1271 (2007).

[27] O. Ostroverkhova, Organic optoelectronic materials: mechanisms and applications, Chemical Reviews **116**, 13279–13412 (2016).

[28] O. V. Mikhnenko, P. W. M. Blom, and T.-Q. Nguyen, Exciton diffusion in organic semiconductors, Energy Environmental Science **8**, 1867–1888 (2015).

[29] J. Benduhn, K. Tvingstedt, F. Piersimoni, S. Ullbrich, Y. Fan, M. Tropiano, K. A. McGarry, O. Zeika, M. K. Riede, C. J. Douglas, S. Barlow, S. R. Marder, D. Neher, D. Spoltore, and K. Vandewal, Intrinsic non-radiative voltage losses in fullerene-based organic solar cells, Nature Energy **2**, 17053 (2017).

[30] D. Qian, Z. Zheng, H. Yao, W. Tress, T. R. Hopper, S. Chen, S. Li, J. Liu, S. Chen, J. Zhang, X.-K. Liu, B. Gao, L. Ouyang, Y. Jin, G. Pozina, I. A. Buyanova, W. M. Chen, O. Inganäs, V. Coropceanu, J.-L. Bredas, H. Yan, J. Hou, F. Zhang, A. A. Bakulin, and F. Gao, Design rules for minimizing voltage losses in high-efficiency organic solar cells, Nature Materials **17**, 703–709 (2018).

[31] S. Xie, Y. Xia, Z. Zheng, X. Zhang, J. Yuan, H. Zhou, and Y. Zhang, Effects of nonradiative losses at charge transfer states and energetic disorder on the open-circuit voltage in nonfullerene organic solar cells, Advanced Functional Materials **28**, 1705659 (2018).

[32] H. F. Haneef, A. M. Zeidell, and O. D. Jurchescu, Charge carrier traps in organic semiconductors: a review on the underlying physics and impact on electronic devices, Journal of Materials Chemistry C **8**, 759–787 (2020).

[33] T. Fukuhara, Y. Tamai, and H. Ohkita, Nongeminate charge recombination in organic photovoltaics, Sustainable Energy Fuels **4**, 4321–4351 (2020).

[34] S. Fratini, M. Nikolka, A. Salleo, G. Schweicher, and H. Sirringhaus, Charge transport in high-mobility conjugated polymers and molecular semiconductors, Nature Materials **19**, 491–502 (2020).

[35] P. Cheng and X. Zhan, Stability of organic solar cells: challenges and strategies, Chemical Society Reviews **45**, 2544–2582 (2016).

[36] N. Ahmad, J. Yuan, and Y. Zou, One more step towards better stability of non-fullerene organic solar cells: advances, challenges, future perspectives, and the era of artificial intelligence, Energy Environmental Science **8**, 5093–5158 (2025).

[37] C. Müller, On the glass transition of polymer semiconductors and its impact on polymer solar cell stability, Chemistry of Materials **27**, 2740–2754 (2015).

[38] H. Bronstein, C. B. Nielsen, B. C. Schroeder, and I. McCulloch, The role of chemical design in the performance of organic semiconductors, Nature Reviews Chemistry **4**, 66–77 (2020).

[39] T. Wang, G. Kupgan, and J.-L. Brédas, Organic photovoltaics: relating chemical structure, local morphology, and electronic properties, Trends in Chemistry **2**, 535–554 (2020).

[40] A. Khasbaatar, Z. Xu, J.-H. Lee, G. Campillo-Alvarado, C. Hwang, B. N. Onusaitis, and Y. Diao, From solution to thin film: molecular assembly of π-conjugated systems and impact on (opto)electronic properties, Chemical Reviews **123**, 8395–8487 (2023).

[41] G. Zhang, F. R. Lin, F. Qi, T. Heumüller, A. Distler, H.-J. Egelhaaf, N. Li, P. C. Y. Chow, C. J. Brabec, A. K.-Y. Jen, and H.-L. Yip, Renewed prospects for organic photovoltaics, Chemical Reviews **122**, 14180–14274 (2022).

[42] J. Fu, H. Li, H. Liu, P. Huang, H. Chen, P. W. K. Fong, T. A. Dela Peña, M. Li, X. Lu, P. Cheng, Z. Xiao, S. Lu, and G. Li, Two-step crystallization modulated through acenaphthene enabling 21% binary organic solar cells and 83.2% fill factor, Nature Energy **10**, 1251–1261 (2025).

[43] V. Rühle, A. Lukyanov, F. May, M. Schrader, T. Vehoff, J. Kirkpatrick, B. Baumeier, and D. Andrienko, Microscopic simulations of charge transport in disordered organic semiconductors, Journal of Chemical Theory and Computation **7**, 3335–3345 (2011).

[44] P. Friederich, V. Meded, F. Symalla, M. Elstner, and W. Wenzel, QM/QM approach to model energy disorder in amorphous organic semiconductors, Journal of Chemical Theory and Computation **11**, 560–567 (2015).

[45] V. Coropceanu, X.-K. Chen, T. Wang, Z. Zheng, and J.-L. Brédas, Charge-transfer electronic states in organic solar cells, Nature Reviews Materials **4**, 689–707 (2019).

[46] N. R. Tummala, Z. Zheng, S. G. Aziz, V. Coropceanu, and J.-L. Brédas, Static and dynamic energetic disorders in the C_{60}, $PC_{61}BM$, C_{70}, and $PC_{71}BM$ fullerenes, The Journal of Physical Chemistry Letters **6**, 3657–3662 (2015).

[47] N. E. Jackson, K. L. Kohlstedt, B. M. Savoie, M. Olvera de la Cruz, G. C. Schatz, L. X. Chen, and M. A. Ratner, Conformational order in aggregates of conjugated polymers, Journal of the American Chemical Society **137**, 6254–6262 (2015).

[48] S. M. Gali, G. D'Avino, P. Aurel, G. Han, Y. Yi, T. A. Papadopoulos, V. Coropceanu, J.-L. Brédas, G. Hadziioannou, C. Zannoni, and L. Muccioli, Energetic fluctuations in amorphous semiconducting polymers: impact on charge-carrier mobility, The Journal of Chemical Physics **147**, 134904 (2017).

[49] M. K. Sørensen, A. S. Gertsen, R. P. Fornari, B. Zhou, X. Zhang, P. U. Jepsen, E. Stanzani, S. Yun, M. Fernández Castro, M. Schwartzkopf, A. Koutsioubas, P. de Silva, M. Espindola-Rodriguez, L. T. Kuhn, and J. W. Andreasen, Manipulating organic semiconductor morphology with visible light, Advanced Functional Materials **33**, 2212835 (2023).

[50] F. Bauch, C.-D. Dong, and S. Schumacher, Dynamics-induced charge transfer in semiconducting conjugated polymers, Journal of Mateials Chemistry C **11**, 12992–12998 (2023).

[51] C.-D. Dong, F. Bauch, Y. Hu, and S. Schumacher, Charge transfer in superbase n-type doping of pcbm induced by deprotonation, Physical Chemistry Chemical Physics **26**, 4194–4199 (2024).

[52] F. Bauch, C.-D. Dong, and S. Schumacher, Dynamics of electron–hole coulomb attractive energy and dipole moment of hot excitons in donor–acceptor polymers, The Journal of Physical Chemistry C **128**, 3525–3532 (2024).

[53] F. Bauch, C.-D. Dong, and S. Schumacher, Designing high performance organic donor molecules for photovoltaics, Advanced Theory and Simulations, e01560 (2025).

[54] F. Bauch, X. Ni, S. M. Pratik, S. Nanayakkara, T. Wang, J.-L. Brédas, S. Schumacher, and V. Coropceanu, Electronic properties of organic solar cells based on CF_3-functionalized non-fullerene acceptors, ACS Applied Materials & Interfaces **18**, 2200–2211 (2026).

[55] R. Peierls, *Quantum theory of solids*, International series of monographs on physics (Clarendon Press, 1955).

[56] W. Brütting and C. Adachi, *Physics of organic semiconductors*, 2nd completely new revised edition (Wiley-VCH, Weinheim, 2012).

[57] A. Köhler and H. Bässler, *Electronic processes in organic semiconductors: an introduction* (Wiley-VCH, Weinheim, 2015).

[58] L. Alcácer, *Electronic structure of organic semiconductors*, 2053-2571 (Morgan & Claypool Publishers, 2018).

[59] T.-H. Le and H. Yoon, "Fundamentals of conjugated polymer nanostructures", in *Conjugated polymer nanostructures for energy conversion and storage applications* (John Wiley & Sons, Ltd, 2021) Chap. 1, pp. 1–42.

[60] L. Ding, Z.-D. Yu, X.-Y. Wang, Z.-F. Yao, Y. Lu, C.-Y. Yang, J.-Y. Wang, and J. Pei, Polymer semiconductors: synthesis, processing, and applications, Chemical Reviews **123**, 7421–7497 (2023).

[61] Z.-G. Zhang and J. Wang, Structures and properties of conjugated donor-acceptor copolymers for solar cell applications, Journal of Materials Chemistry **22**, 4178–4187 (2012).

[62] A. Casey, S. D. Dimitrov, P. Shakya-Tuladhar, Z. Fei, M. Nguyen, Y. Han, T. D. Anthopoulos, J. R. Durrant, and M. Heeney, Effect of systematically tuning conjugated donor polymer lowest unoccupied molecular orbital levels via cyano substitution on organic photovoltaic device performance, Chemistry of Materials **28**, 5110–5120 (2016).

[63] N. Luo, P. Ren, Y. Feng, X. Shao, H.-L. Zhang, and Z. Liu, Side-chain engineering of conjugated polymers for high-performance organic field-effect transistors, The Journal of Physical Chemistry Letters **13**, 1131–1146 (2022).

[64] M. Schwarze, K. S. Schellhammer, K. Ortstein, J. Benduhn, C. Gaul, A. Hinderhofer, L. Perdigón Toro, R. Scholz, J. Kublitski, S. Roland, M. Lau, C. Poelking, D. Andrienko, G. Cuniberti, F. Schreiber, D. Neher, K. Vandewal, F. Ortmann, and K. Leo, Impact of molecular quadrupole moments on the energy levels at organic heterojunctions, Nature Communications **10**, 2466 (2019).

[65] T. Dai, Y. Meng, Z. Wang, J. Lu, Z. Zheng, M. Du, Q. Guo, and E. Zhou, Modulation of molecular quadrupole moments by phenyl side-chain fluorination for high-voltage and high-performance organic solar cells, Journal of the American Chemical Society **147**, 4631–4642 (2025).

[66] A. Szabo and N. Ostlund, *Modern quantum chemistry: introduction to advanced electronic structure theory*, Dover Books on Chemistry (Dover Publications, 1996).

[67] F. Jensen, *Introduction to computational chemistry*, 2nd ed. (John Wiley & Sons, Chichester, England, 2007).

[68] M. Born and K. Huang, *Dynamical theory of crystal lattices* (Oxford University Press, Oxford, 1998).

[69] W. Domcke, D. Yarkony, and H. Köppel, *Conical intersections: electronic structure, dynamics & spectroscopy*, Advanced series in physical chemistry (World Scientific, 2004).

[70] B. F. E. Curchod and T. J. Martínez, Ab initio nonadiabatic quantum molecular dynamics, Chemical Reviews **118**, 3305–3336 (2018).

[71] A. W. Jasper, C. Zhu, S. Nangia, and D. G. Truhlar, Introductory lecture: nonadiabatic effects in chemical dynamics, Faraday Discussions **127**, 1–22 (2004).

[72] M. Born and R. Oppenheimer, Zur Quantentheorie der Molekeln, Annalen der Physik **389**, 457–484 (1927).

[73] W. Domcke, D. R. Yarkony, and H. Köppel, eds., *Conical intersections: theory, computation and experiment*, Vol. 17, Advanced Series in Physical Chemistry (World Scientific, Singapore, 2011).

[74] J. Franck and E. G. Dymond, Elementary processes of photochemical reactions, Transactions of the Faraday Society **21**, 536–542 (1926).

[75] E. Condon, A theory of intensity distribution in band systems, Physical Review **28**, 1182–1201 (1926).

[76] E. U. Condon, Nuclear motions associated with electron transitions in diatomic molecules, Physical Review **32**, 858–872 (1928).

[77] V. Balzani, ed., *Electron transfer in chemistry* (Wiley-VCH, Weinheim, 2001).

[78] J.-L. Brédas, D. Beljonne, V. Coropceanu, and J. Cornil, Charge-transfer and energy-transfer processes in π-conjugated oligomers and polymers: a molecular picture, Chemical Reviews **104**, 4971–5004 (2004).

[79] E. B. Wilson, J. C. Decius, and P. C. Cross, *Molecular vibrations: the theory of infrared and raman vibrational spectra* (McGraw-Hill Book Company, Inc, New York, 1955).

[80] L. D. Landau and E. M. Lifshitz, *Mechanics*, Third, Vol. 1, Course of Theoretical Physics, Translation of *Mekhanika*, third edition, by J. B. Sykes and J. S. Bell, Izdatelstvo Nauka, Moscow, 1993. First English edition published by Pergamon Press Ltd., 1960. Eleventh printing, 1996. (Butterworth-Heinemann, Oxford, 1976).

[81] M. Born and K. Huang, *Dynamical theory of crystal lattices*, Repr, The International Series of Monographs on Physics (Oxford : Clarendon, 1985).

[82] E. J. Mele and M. J. Rice, Vibrational excitations of charged solitons in polyacetylene, Physical Review Letters **45**, 926–929 (1980).

[83] M. Anderson, C. Ramanan, C. Fontanesi, A. Frick, S. Surana, D. Cheyns, M. Furno, T. Keller, S. Allard, U. Scherf, D. Beljonne, G. D'Avino, E. von Hauff, and E. Da Como, Displacement of polarons by vibrational modes in doped conjugated polymers, Physical Review Materials **1**, 055604 (2017).

[84] R. C. Hilborn, Einstein coefficients, cross sections, f values, dipole moments, and all that, American Journal of Physics **50**, 982–986 (1982).

[85] A. Sugie, K. Nakano, K. Tajima, I. Osaka, and H. Yoshida, Dependence of exciton binding energy on bandgap of organic semiconductors, The Journal of Physical Chemistry Letters **14**, 11412–11420 (2023).

[86] C. Wiebeler, R. Tautz, J. Feldmann, E. von Hauff, E. Da Como, and S. Schumacher, Spectral signatures of polarons in conjugated co-polymers, The Journal of Physical Chemistry B **117**, 4454–4460 (2013).

[87] R. L. Martin, Natural transition orbitals, The Journal of Chemical Physics **118**, 4775–4777 (2003).

[88] W. L. Jorgensen and J. Tirado-Rives, The OPLS [optimized potentials for liquid simulations] potential functions for proteins, energy minimizations for crystals of cyclic peptides and crambin, Journal of the American Chemical Society **110**, 1657–1666 (1988).

[89] W. L. Jorgensen, D. S. Maxwell, and J. Tirado-Rives, Development and testing of the OPLS all-atom force field on conformational energetics and properties of organic liquids, Journal of the American Chemical Society **118**, 11225–11236 (1996).

[90] Z. Zheng, N. R. Tummala, T. Wang, V. Coropceanu, and J.-L. Brédas, Charge-transfer states at organic-organic interfaces: impact of static and dynamic disorders, Advanced Energy Materials **9**, 1803926 (2019).

[91] F.-J. Kahle, A. Rudnick, S. Wedler, R. Saxena, R. Ammenhäuser, U. Scherf, S. Bagnich, H. Bässler, and A. Köhler, Static and dynamic disorder of charge transfer states probed by optical spectroscopy, Advanced Energy Materials **12**, 2103063 (2022).

[92] T. Förster, Zwischenmolekulare Energiewanderung und Fluoreszenz, Annalen der Physik **437**, 55–75 (1948).

[93] D. L. Dexter, A theory of sensitized luminescence in solids, The Journal of Chemical Physics **21**, 836–850 (1953).

[94] R. A. Marcus, On the theory of oxidation-reduction reactions involving electron transfer. I, The Journal of Chemical Physics **24**, 966–978 (1956).

[95] R. A. Marcus, Electron transfer reactions in chemistry. theory and experiment, Reviews of Modern Physics **65**, 599–610 (1993).

[96] V. G. Levich and R. R. Dogonadze, Theory of radiationless electron transitions between ions in solution, Doklady Akademii Nauk SSSR **124**, 123 (1959).

[97] V. G. Levich and R. R. Dogonadze, Adiabatic theory for electron-transfer processes in solution, Doklady Akademii Nauk SSSR **133**, 159 (1960).

[98] V. G. Levich and R. R. Dogonadze, Adiabatic theory of electron-transfer processes in solution, Collection of Czechoslovak Chemical Communications **26**, 193 (1961).

[99] V. G. Levich, "Present state of the theory of oxidation–reduction in solution (bulk and electrode reactions)", in *Advances in electrochemistry and electrochemical engineering*, Vol. 4, edited by P. Delahay (Interscience Publishers, 1966), pp. 249–371.

[100] Nobel Prize Outreach, *The nobel prize in chemistry 1992*, https://www.nobelprize.org/prizes/chemistry/1992/summary/, Accessed: 2025-09-17, 2025.

[101] V. Balzani, *Adiabatic versus non-adiabatic electron transfer* (John Wiley & Sons, Ltd, 2001).

[102] J. Jortner, Temperature dependent activation energy for electron transfer between biological molecules, The Journal of Chemical Physics **64**, 4860–4867 (1976).

[103] J. Jortner, Dynamics of electron transfer in bacterial photosynthesis, Biochimica et Biophysica Acta (BBA) – Reviews on Bioenergetics **594**, 193–230 (1980).

[104] M. Bixon and J. Jortner, *Electron transfer–from isolated molecules to biomolecules* (John Wiley & Sons, Ltd, 1999).

[105] K. Huang and A. Rhys, Theory of light absorption and non-radiative transitions in *F*-centres, Proceedings of the Royal Society of London. Series A. Mathematical and Physical Sciences **204**, 406–423 (1950).

[106] V. Lemaur, M. Steel, D. Beljonne, J.-L. Brédas, and J. Cornil, Photoinduced charge generation and recombination dynamics in model donor/acceptor pairs for organic solar cell applications: a full quantum-chemical treatment, Journal of the American Chemical Society **127**, 6077–6086 (2005).

[107] S. Kera, H. Yamane, and N. Ueno, First-principles measurements of charge mobility in organic semiconductors: valence hole-vibration coupling in organic ultrathin films, Progress in Surface Science **84**, 135–154 (2009).

[108] G. D'Avino, L. Muccioli, Y. Olivier, and D. Beljonne, Charge separation and recombination at polymer-fullerene heterojunctions: delocalization and hybridization effects, The Journal of Physical Chemistry Letters **7**, 536–540 (2016).

[109] T. Wang and J.-L. Brédas, Nonfullerene small-molecule acceptors for organic photovoltaics: understanding the impact of methoxy substitution position on molecular packing and electron-transfer properties, Advanced Functional Materials **29**, 1806845 (2019).

[110] M. D. Newton, Quantum chemical probes of electron–transfer kinetics: the nature of donor–acceptor interactions, Chemical Reviews **91**, 767–792 (1991).

[111] J. Cornil, D. Beljonne, J.-P. Calbert, and J.-L. Brédas, Interchain interactions in organic π–conjugated materials: impact on electronic structure, optical response, and charge transport, Advanced Materials **13**, 1053–1067 (2001).

[112] J. L. Brédas, J. P. Calbert, D. A. da Silva Filho, and J. Cornil, Organic semiconductors: a theoretical characterization of the basic parameters governing charge transport, Proceedings of the National Academy of Sciences **99**, 5804–5809 (2002).

[113] K. Senthilkumar, F. C. Grozema, F. M. Bickelhaupt, and L. D. A. Siebbeles, Charge transport in columnar stacked triphenylenes: effects of conformational fluctuations on charge transfer integrals and site energies, The Journal of Chemical Physics **119**, 9809–9817 (2003).

[114] E. F. Valeev, V. Coropceanu, D. A. da Silva Filho, S. Salman, and J.-L. Brédas, Effect of electronic polarization on charge–transport parameters in molecular organic semiconductors, Journal of the American Chemical Society **128**, 9882–9886 (2006).

[115] P.-.-O. Löwdin, On the non--orthogonality problem connected with the use of atomic wave functions in the theory of molecules and crystals, The Journal of Chemical Physics **18**, 365–375 (1950).

[116] C. Creutz, M. D. Newton, and N. Sutin, Metal–ligand and metal–metal coupling elements, Journal of Photochemistry and Photobiology A: Chemistry **82**, 47–59 (1994).

[117] R. J. Cave and M. D. Newton, Generalization of the Mulliken–Hush treatment for the calculation of electron transfer matrix elements, Chemical Physics Letters **249**, 15–19 (1996).

[118] K. G. Dyall and K. Faegri, *Introduction to relativistic quantum chemistry*, eng, 1st ed. (Oxford University Press, New York, 2007).

[119] K. G. Dyall and K. Faegri, *Introduction to relativistic quantum chemistry* (Oxford University Press, Incorporated., 2007).

[120] P. Jɹrgensen and J. Simons, *Second quantization–based methods in quantum chemistry* (Academic Press: New York, USA, 1981).

[121] M. E. Casida, "Chapter 5: Time–dependent density functional response theory for molecules", in *Recent advances in density functional methods*, Vol. 1, edited by P. C. Delano (World Scientific: Singapore, 1995), pp. 155–192.

[122] X. Gao, S. Bai, D. Fazzi, T. Niehaus, M. Barbatti, and W. Thiel, Evaluation of spin–orbit couplings with linear–response time–dependent density functional methods, Journal of Chemical Theory and Computation **13**, 515–524 (2017).

[123] E. Epifanovsky et al., Software for the frontiers of quantum chemistry: an overview of developments in the Q-Chem 5 package, Journal of Chemical Physics **155**, 084801 (2021).

[124] S. M. Barnett, B. Huttner, and R. Loudon, Spontaneous emission in absorbing dielectric media, Physical Review Letters **68**, 3698–3701 (1992).

[125] D. Toptygin, Effects of the solvent refractive index and its dispersion on the radiative decay rate and extinction coefficient of a fluorescent solute, Journal of Fluorescence **13**, 201–219 (2003).

[126] C.-K. Duan, M. F. Reid, and Z. Wang, Local field effects on the radiative lifetime of emitters in surrounding media: virtual- or real-cavity model?, Physics Letters A **343**, 474–480 (2005).

[127] R. Send and F. Furche, First-order nonadiabatic couplings from time-dependent hybrid density functional response theory: consistent formalism, implementation, and performance, The Journal of Chemical Physics **132**, 044107 (2010).

[128] D. B. Lingerfelt, D. B. Williams-Young, A. Petrone, and X. Li, Direct ab initio (meta-)surface-hopping dynamics, Journal of Chemical Theory and Computation **12**, 935–945 (2016).

[129] Y. Niu, Q. Peng, C. Deng, X. Gao, and Z. Shuai, Theory of excited state decays and optical spectra: application to polyatomic molecules, The Journal of Physical Chemistry A **114**, 7817–7831 (2010).

[130] Q. Peng, Y. Niu, Q. Shi, X. Gao, and Z. Shuai, Correlation function formalism for triplet excited state decay: combined spin-orbit and nonadiabatic couplings, Journal of Chemical Theory and Computation **9**, 1132–1143 (2013).

[131] Z. Shuai and Q. Peng, Excited states structure and processes: understanding organic light-emitting diodes at the molecular level, Physics Reports **537**, 123–156 (2014).

[132] J. C. Tully, "Nonadiabatic dynamics", in *Modern methods for multidimensional dynamics computations in chemistry*, edited by D. L. Thompson (World Scientific, Singapore, 1998), pp. 34–72.

[133] W. C. Swope, H. C. Andersen, P. H. Berens, and K. R. Wilson, A computer simulation method for the calculation of equilibrium constants for the formation of physical clusters of molecules: application to small water clusters, The Journal of Chemical Physics **76**, 637–649 (1982).

[134] H. J. C. Berendsen, J. P. M. Postma, W. F. van Gunsteren, A. DiNola, and J. R. Haak, Molecular dynamics with coupling to an external bath, The Journal of Chemical Physics **81**, 3684–3690 (1984).

[135] F. Neese, Software update: the ORCA program system—version 6.0, WIREs Computational Molecular Science **15**, e70019 (2025).

[136] J. C. Tully, Molecular dynamics with electronic transitions, The Journal of Chemical Physics **93**, 1061–1071 (1990).

[137] J. C. Tully and R. K. Preston, Trajectory surface hopping approach to nonadiabatic molecular collisions: the reaction of H^+ with D_2, The Journal of Chemical Physics **55**, 562–572 (1971).

[138] M. Barbatti, Nonadiabatic dynamics with trajectory surface hopping method, WIREs Computational Molecular Science **1**, 620–633 (2011).

[139] R. Crespo-Otero and M. Barbatti, Recent advances and perspectives on nonadiabatic mixed quantum-classical dynamics, Chemical Reviews **118**, 7026–7068 (2018).

[140] S. Hammes-Schiffer and J. C. Tully, Proton transfer in solution: molecular dynamics with quantum transitions, The Journal of Chemical Physics **101**, 4657–4667 (1994).

[141] F. Plasser, R. Crespo-Otero, M. Pederzoli, J. Pittner, H. Lischka, and M. Barbatti, Surface hopping dynamics with correlated single-reference methods: 9H-Adenine as a case study, Journal of Chemical Theory and Computation **10**, 1395–1405 (2014).

[142] I. G. Ryabinkin, J. Nagesh, and A. F. Izmaylov, Fast numerical evaluation of time-derivative nonadiabatic couplings for mixed quantum-classical methods, The Journal of Physical Chemistry Letters **6**, 4200–4203 (2015).

[143] L. Stojanović, S. Bai, J. Nagesh, A. F. Izmaylov, R. Crespo-Otero, H. Lischka, and M. Barbatti, New insights into the state trapping of UV-excited thymine, Molecules **21**, 1603 (2016).

[144] G. Granucci and M. Persico, Critical appraisal of the fewest switches algorithm for surface hopping, The Journal of Chemical Physics **126**, 134114 (2007).

[145] H. C. Andersen, Molecular dynamics simulations at constant pressure and/or temperature, The Journal of Chemical Physics **72**, 2384–2393 (1980).

[146] M. Barbatti, M. Ruckenbauer, F. Plasser, J. Pittner, G. Granucci, M. Persico, and H. Lischka, Newton-X: a surface-hopping program for nonadiabatic molecular dynamics, WIREs Computational Molecular Science **4**, 26–33 (2014).

[147] M. J. Frisch et al., *Gaussian 16 Revision C.01*, Gaussian Inc. Wallingford CT, 2016.

[148] C.-D. Dong and S. Schumacher, Molecular doping of PCPDT-BT copolymers: comparison of molecular complexes with and without integer charge transfer, The Journal of Physical Chemistry C **123**, 30863–30870 (2019).

[149] I. E. Jacobs and A. J. Moulé, Controlling molecular doping in organic semiconductors, Advanced Materials **29**, 1703063 (2017).

[150] P. Pingel and D. Neher, Comprehensive picture of *p*-type doping of P3HT with the molecular acceptor F_4TCNQ, Physical Review B **87**, 115209 (2013).

[151] A. D. Scaccabarozzi, A. Basu, F. Aniés, J. Liu, O. Zapata-Arteaga, R. Warren, Y. Firdaus, M. I. Nugraha, Y. Lin, M. Campoy-Quiles, N. Koch, C. Müller, L. Tsetseris, M. Heeney, and T. D. Anthopoulos, Doping approaches for organic semiconductors, Chemical Reviews **122**, 4420–4492 (2022).

[152] S. Luo, Z. Xu, F. Zhong, H. Li, and L. Chen, Doping-induced charge transfer in conductive polymers, Chinese Chemical Letters **35**, 109014 (2024).

[153] I. Salzmann, G. Heimel, M. Oehzelt, S. Winkler, and N. Koch, Molecular electrical doping of organic semiconductors: fundamental mechanisms and emerging dopant design rules, Accounts of Chemical Research **49**, 370–378 (2016).

[154] E. F. Aziz, A. Vollmer, S. Eisebitt, W. Eberhardt, P. Pingel, D. Neher, and N. Koch, Localized charge transfer in a molecularly doped conducting polymer, Advanced Materials **19**, 3257–3260 (2007).

[155] Y. Karpov, T. Erdmann, I. Raguzin, M. Al-Hussein, M. Binner, U. Lappan, M. Stamm, K. L. Gerasimov, T. Beryozkina, V. Bakulev, D. V. Anokhin, D. A. Ivanov, F. Günther, S. Gemming, G. Seifert, B. Voit, R. Di Pietro, and A. Kiriy, High conductivity in molecularly p-doped diketopyrrolopyrrole-based polymer: the impact of a high dopant strength and good structural order, Advanced Materials **28**, 6003–6010 (2016).

[156] Y. Liu, B. Nell, K. Ortstein, Z. Wu, Y. Karpov, T. Beryozkina, S. Lenk, A. Kiriy, K. Leo, and S. Reineke, High electron affinity molecular dopant CN6-CP for efficient organic light-emitting diodes, ACS Applied Materials & Interfaces **11**, 11660–11666 (2019).

[157] C.-Y. Yang, Y.-F. Ding, D. Huang, J. Wang, Z.-F. Yao, C.-X. Huang, Y. Lu, H.-I. Un, F.-D. Zhuang, J.-H. Dou, C.-a. Di, D. Zhu, J.-Y. Wang, T. Lei, and J. Pei, A thermally activated and highly miscible dopant for n-type organic thermoelectrics, Nature Communications **11**, 3292 (2020).

[158] C.-d. Dong and S. Schumacher, Molecular doping in few-molecule polymer-dopant complexes shows reduced coulomb binding, Journal of Materials Chemistry C **8**, 11929–11935 (2020).

[159] Y. Yamashita, J. Tsurumi, M. Ohno, R. Fujimoto, S. Kumagai, T. Kurosawa, T. Okamoto, J. Takeya, and S. Watanabe, Efficient molecular doping of polymeric semiconductors driven by anion exchange, Nature **572**, 634–638 (2019).

[160] Y. Yamashita, S. Kohno, E. Longhi, S. Jhulki, S. Kumagai, S. Barlow, S. R. Marder, J. Takeya, and S. Watanabe, N-type molecular doping of a semicrystalline conjugated polymer through cation exchange, Communications Materials **5**, 79 (2024).

[161] D. Kiefer, R. Kroon, A. I. Hofmann, H. Sun, X. Liu, A. Giovannitti, D. Stegerer, A. Cano, J. Hynynen, L. Yu, Y. Zhang, D. Nai, T. F. Harrelson, M. Sommer, A. J. Moulé, M. Kemerink, S. R. Marder, I. McCulloch, M. Fahlman, S. Fabiano, and C. Müller, Double doping of conjugated polymers with monomer molecular dopants, Nature Materials **18**, 149–155 (2019).

[162] T. Bathe, C.-D. Dong, and S. Schumacher, Microscopic study of molecular double doping, The Journal of Physical Chemistry A **126**, 2075–2081 (2022).

[163] J. Li, G. Zhang, D. M. Holm, I. E. Jacobs, B. Yin, P. Stroeve, M. Mascal, and A. J. Moulé, Introducing solubility control for improved organic p-type dopants, Chemistry of Materials **27**, 5765–5774 (2015).

[164] J. Liu, L. Qiu, R. Alessandri, X. Qiu, G. Portale, J. Dong, W. Talsma, G. Ye, A. A. Sengrian, P. C. T. Souza, M. A. Loi, R. C. Chiechi, S. J. Marrink, J. C. Hummelen, and L. J. A. Koster, Enhancing molecular n-type doping of donor-acceptor copolymers by tailoring side chains, Advanced Materials **30**, 1704630 (2018).

[165] P. Pingel, M. Arvind, L. Kölln, R. Steyrleuthner, F. Kraffert, J. Behrends, S. Janietz, and D. Neher, P-type doping of poly(3-hexylthiophene) with the strong Lewis acid tris(pentafluorophenyl)borane, Advanced Electronic Materials **2**, 1600204 (2016).

[166] J. Panidi, A. F. Paterson, D. Khim, Z. Fei, Y. Han, L. Tsetseris, G. Vourlias, P. A. Patsalas, M. Heeney, and T. D. Anthopoulos, Remarkable enhancement of the hole mobility in several organic small-molecules, polymers, and small-molecule:polymer blend transistors by simple admixing of the Lewis acid p-dopant $B(C_6F_5)_3$, Advanced Science **5**, 1700290 (2018).

[167] B. Yurash, D. X. Cao, V. V. Brus, D. Leifert, M. Wang, A. Dixon, M. Seifrid, A. E. Mansour, D. Lungwitz, T. Liu, P. J. Santiago, K. R. Graham, N. Koch, G. C. Bazan, and T.-Q. Nguyen, Towards understanding the doping mechanism of organic semiconductors by Lewis acids, Nature Materials **18**, 1327–1334 (2019).

[168] P. S. Marqués, G. Londi, B. Yurash, T.-Q. Nguyen, S. Barlow, S. R. Marder, and D. Beljonne, Understanding how Lewis acids dope organic semiconductors: a "complex" story, Chemical Science **12**, 7012–7022 (2021).

[169] J. Guo, Y. Liu, P.-A. Chen, X. Wang, Y. Wang, J. Guo, X. Qiu, Z. Zeng, L. Jiang, Y. Yi, S. Watanabe, L. Liao, Y. Bai, T.-Q. Nguyen, and Y. Hu, Revealing the electrophilic-attack doping mechanism for efficient and universal p-doping of organic semiconductors, Advanced Science **9**, 2203111 (2022).

[170] J. Guo, P.-A. Chen, S. Yang, H. Wei, Y. Liu, J. Xia, C. Chen, H. Chen, S. Wang, W. Li, and Y. Hu, Dopant-induced morphology of organic semiconductors resulting in high doping performance, Small Methods **9**, 2400084 (2025).

[171] F. Bauch, C.-D. Dong, and S. Schumacher, Protonation-induced charge transfer and polaron formation in organic semiconductors doped by Lewis acids, RSC Advances **12**, 13999–14006 (2022).

[172] H. Wei, Z. Cheng, T. Wu, Y. Liu, J. Guo, P.-A. Chen, J. Xia, H. Xie, X. Qiu, T. Liu, B. Zhang, J. Hui, Z. Zeng, Y. Bai, and Y. Hu, Novel organic superbase dopants for ultraefficient n-doping of organic semiconductors, Advanced Materials **35**, 2300084 (2023).

[173] H. Wei, P.-A. Chen, T. Wu, J. Xia, J. Ding, Y. Zhang, X. Zeng, Z. Gong, C. Peng, J. Xue, Z. Wan, W. Shi, L. Lan, Y. Bai, W. Yue, and Y. Hu, High-miscibility n-dopant for organic semiconductors enabling highly stable organic transistors, Advanced Functional Materials **35**, 2500631 (2025).

[174] H. Wei, J. Guo, H. Liu, T. Wu, P.-A. Chen, C. Dong, S.-J. Wang, S. Schumacher, Y. Bai, T. Lei, S. Wang, and Y. Hu, Novel phosphazenium tetrafluoroborate dopant enables efficient and thermally stable n-doped organic semiconductors, Advanced Electronic Materials, 2400767 (2024).

[175] H. Wei, T. Wu, C. Dong, C. Chen, Z. Gong, J. Xia, C. Peng, J. Ding, Y. Zhang, W. Shi, S. Schumacher, X. Zhang, Y. Bai, L. Jiang, L. Liao, T.-Q. Nguyen, and Y. Hu, Efficient n-doping of organic semiconductors via a broadly applicable nucleophilic-attack mechanism, Advanced Science, e20487 (2025).

[176] S. Giannini and J. Blumberger, Charge transport in organic semiconductors: the perspective from nonadiabatic molecular dynamics, Accounts of Chemical Research **55**, 819–830 (2022).

[177] H. Bässler and A. Köhler, "Charge transport in organic semiconductors", in *Unimolecular and supramolecular electronics i: chemistry and physics meet at metal-molecule interfaces*, edited by R. M. Metzger (Springer Berlin Heidelberg, Berlin, Heidelberg, 2012), pp. 1–65.

[178] T. Holstein, Studies of polaron motion: part i. the molecular-crystal model, Annals of Physics **8**, 325–342 (1959).

[179] T. Holstein, Studies of polaron motion: part ii. the "small" polaron, Annals of Physics **8**, 343–389 (1959).

[180] W. P. Su, J. R. Schrieffer, and A. J. Heeger, Solitons in polyacetylene, Phys. Rev. Lett. **42**, 1698–1701 (1979).

[181] W. Li, J. Ren, and Z. Shuai, A general charge transport picture for organic semiconductors with nonlocal electron-phonon couplings, Nature Communications **12**, 4260 (2021).

[182] Z. Shuai, H. Geng, W. Xu, Y. Liao, and J.-M. André, From charge transport parameters to charge mobility in organic semiconductors through multiscale simulation, Chemical Society Reviews **43**, 2662–2679 (2014).

[183] Y. Lu, J.-Y. Wang, and J. Pei, Strategies to enhance the conductivity of n-type polymer thermoelectric materials, Chemistry of Materials **31**, 6412–6423 (2019).

[184] N. Lu, L. Li, D. Geng, and M. Liu, A review for polaron dependent charge transport in organic semiconductor, Organic Electronics **61**, 223–234 (2018).

[185] H. Bässler, Charge transport in disordered organic photoconductors a Monte Carlo simulation study, physica status solidi (b) **175**, 15–56 (1993).

[186] Y. Olivier, V. Lemaur, J. L. Brédas, and J. Cornil, Charge hopping in organic semiconductors: influence of molecular parameters on macroscopic mobilities in model one-dimensional stacks, The Journal of Physical Chemistry A **110**, 6356–6364 (2006).

[187] V. Rühle, A. Lukyanov, F. May, M. Schrader, T. Vehoff, J. Kirkpatrick, B. Baumeier, and D. Andrienko, Microscopic simulations of charge transport in disordered organic semiconductors, Journal of Chemical Theory and Computation **7**, 3335–3345 (2011).

[188] C. Burke and A. Troisi, Models connecting microstructure and charge transport in disordered semiconducting polymers: from theories to digital design, Materials Horizons **12**, 9416–9431 (2025).

[189] J.-L. Brédas, J. E. Norton, J. Cornil, and V. Coropceanu, Molecular understanding of organic solar cells: the challenges, Accounts of Chemical Research **42**, 1691–1699 (2009).

[190] T. M. Clarke and J. R. Durrant, Charge photogeneration in organic solar cells, Chemical Reviews **110**, 6736–6767 (2010).

[191] J. Hou, O. Inganäs, R. H. Friend, and F. Gao, Organic solar cells based on non-fullerene acceptors, Nature Materials **17**, 119–128 (2018).

[192] J. J. M. Halls, C. A. Walsh, N. C. Greenham, E. A. Marseglia, R. H. Friend, S. C. Moratti, and A. B. Holmes, Efficient photodiodes from interpenetrating polymer networks, Nature **376**, 498–500 (1995).

[193] X. Wei, Z. V. Vardeny, N. S. Sariciftci, and A. J. Heeger, Absorption-detected magnetic-resonance studies of photoexcitations in conjugated-polymer/C_{60} composites, Physical Review B **53**, 2187–2190 (1996).

[194] C.-X. Sheng, M. Tong, S. Singh, and Z. V. Vardeny, Experimental determination of the charge/neutral branching ratio η in the photoexcitation of π-conjugated polymers by broadband ultrafast spectroscopy, Physical Review B **75**, 085206 (2007).

[195] G. Zhou, M. Zhang, J. Xu, Y. Yang, T. Hao, L. Zhu, L. Zhou, H. Zhu, Y. Zou, G. Wei, Y. Zhang, and F. Liu, Spontaneous carrier generation and low recombination in high-efficiency non-fullerene solar cells, Energy & Environmental Science **15**, 3483–3493 (2022).

[196] U. Rau, Reciprocity relation between photovoltaic quantum efficiency and electroluminescent emission of solar cells, Physical Review B **76**, 085303 (2007).

[197] J. Yuan, Y. Zhang, L. Zhou, G. Zhang, H.-L. Yip, T.-K. Lau, X. Lu, C. Zhu, H. Peng, P. A. Johnson, M. Leclerc, Y. Cao, J. Ulanski, Y. Li, and Y. Zou, Single-junction organic solar cell with over 15% efficiency using fused-ring acceptor with electron-deficient core, Joule **3**, 1140–1151 (2019).

[198] J. Yuan, T. Huang, P. Cheng, Y. Zou, H. Zhang, J. L. Yang, S.-Y. Chang, Z. Zhang, W. Huang, R. Wang, D. Meng, F. Gao, and Y. Yang, Enabling low voltage losses and high photocurrent in fullerene-free organic photovoltaics, Nature Communications **10**, 570 (2019).

[199] S. Shoaee, H. M. Luong, J. Song, Y. Zou, T.-Q. Nguyen, and D. Neher, What we have learnt from PM6:Y6, Advanced Materials **36**, 2302005 (2024).

[200] C. Chen, L. Wang, W. Xia, K. Qiu, C. Guo, Z. Gan, J. Zhou, Y. Sun, D. Liu, W. Li, and T. Wang, Molecular interaction induced dual fibrils towards organic solar cells with certified efficiency over 20%, Nature Communications **15**, 6865 (2024).

[201] Y. Li, W. Huang, D. Zhao, L. Wang, Z. Jiao, Q. Huang, P. Wang, M. Sun, and G. Yuan, Recent progress in organic solar cells: a review on materials from acceptor to donor, Molecules **27**, 1800 (2022).

[202] H. Gao, Y. Sun, L. Meng, C. Han, X. Wan, and Y. Chen, Recent progress in all-small-molecule organic solar cells, Small **19**, 2205594 (2023).

[203] L. Zhu, M. Zhang, G. Zhou, Z. Wang, W. Zhong, J. Zhuang, Z. Zhou, X. Gao, L. Kan, B. Hao, F. Han, R. Zeng, X. Xue, S. Xu, H. Jing, B. Xiao, H. Zhu, Y. Zhang, and F. Liu, Achieving 20.8% organic solar cells via additive-assisted layer-by-layer fabrication with bulk p-i-n structure and improved optical management, Joule **8**, 3153–3168 (2024).

[204] Y. Jiang, K. Liu, F. Liu, G. Ran, M. Wang, T. Zhang, R. Xu, H. Liu, W. Zhang, Z. Wei, Y. Cui, X. Lu, J. Hou, and X. Zhu, 20.6% efficiency organic solar cells enabled by incorporating a lower bandgap guest nonfullerene acceptor without open-circuit voltage loss, Advanced Materials **37**, 2500282 (2025).

[205] Y. Zhou, T. Kurosawa, W. Ma, Y. Guo, L. Fang, K. Vandewal, Y. Diao, C. Wang, Q. Yan, J. Reinspach, J. Mei, A. L. Appleton, G. I. Koleilat, Y. Gao, S. C. B. Mannsfeld, A. Salleo, H. Ade, D. Zhao, and Z. Bao, High performance all-polymer solar cell via polymer side-chain engineering, Advanced Materials **26**, 3767–3772 (2014).

[206] L. Lu, T. Zheng, Q. Wu, A. M. Schneider, D. Zhao, and L. Yu, Recent advances in bulk heterojunction polymer solar cells, Chemical Reviews **115**, 12666–12731 (2015).

[207] G. Zhang, F. R. Lin, F. Qi, T. Heumüller, A. Distler, H.-J. Egelhaaf, N. Li, P. C. Y. Chow, C. J. Brabec, A. K.-Y. Jen, and H.-L. Yip, Renewed prospects for organic photovoltaics, Chemical Reviews **122**, 14180–14274 (2022).

[208] Z. Luo, T. Xu, C. Zhang, and C. Yang, Side-chain engineering of nonfullerene small-molecule acceptors for organic solar cells, Energy & Environmental Science **16**, 2732–2758 (2023).

[209] R. Zhang, H. Chen, T. Wang, L. Kobera, L. He, Y. Huang, J. Ding, B. Zhang, A. Khasbaatar, S. Nanayakkara, J. Zheng, W. Chen, Y. Diao, S. Abbrent, J. Brus, A. H. Coffey, C. Zhu, H. Liu, X. Lu, Q. Jiang, V. Coropceanu, J.-L. Brédas, Y. Li, Y. Li, and F. Gao, Equally high efficiencies of organic solar cells processed from different solvents reveal key factors for morphology control, Nature Energy **10**, 124–134 (2025).

[210] J. Wang, Y. Wang, P. Bi, Z. Chen, J. Qiao, J. Li, W. Wang, Z. Zheng, S. Zhang, X. Hao, and J. Hou, Binary organic solar cells with 19.2% efficiency enabled by solid additive, Advanced Materials **35**, 2301583 (2023).

[211] J. Hofinger, C. Putz, F. Mayr, K. Gugujonovic, D. Wielend, and M. C. Scharber, Understanding the low voltage losses in high-performance non-fullerene acceptor-based organic solar cells, Materials Advances **2**, 4291–4302 (2021).

[212] J. Yan, E. Rezasoltani, M. Azzouzi, F. Eisner, and J. Nelson, Influence of static disorder of charge transfer state on voltage loss in organic photovoltaics, Nature Communications **12**, 3642 (2021).

[213] C. Göhler and C. Deibel, The role of dynamic and static disorder for charge-transfer states in organic bulk heterojunction solar cells, ACS Energy Letters **7**, 2156–2164 (2022).

[214] L. Zhu, M. Zhang, J. Xu, C. Li, J. Yan, G. Zhou, W. Zhong, T. Hao, J. Song, X. Xue, Z. Zhou, R. Zeng, H. Zhu, C.-C. Chen, R. C. I. MacKenzie, Y. Zou, J. Nelson, Y. Zhang, Y. Sun, and F. Liu, Single-junction organic solar cells with over 19% efficiency enabled by a refined double-fibril network morphology, Nature Materials **21**, 656–663 (2022).

[215] B. Carsten, J. M. Szarko, H. J. Son, W. Wang, L. Lu, F. He, B. S. Rolczynski, S. J. Lou, L. X. Chen, and L. Yu, Examining the effect of the dipole moment on charge separation in donor-acceptor polymers for organic photovoltaic applications, Journal of the American Chemical Society **133**, 20468–20475 (2011).

[216] B. Carsten, J. M. Szarko, L. Lu, H. J. Son, F. He, Y. Y. Botros, L. X. Chen, and L. Yu, Mediating solar cell performance by controlling the internal dipole change in organic photovoltaic polymers, Macromolecules **45**, 6390–6395 (2012).

[217] E. Collado-Fregoso, P. Boufflet, Z. Fei, E. Gann, S. Ashraf, Z. Li, C. R. McNeill, J. R. Durrant, and M. Heeney, Increased exciton dipole moment translates into charge-transfer excitons in thiophene-fluorinated low-bandgap polymers for organic photovoltaic applications, Chemistry of Materials **27**, 7934–7944 (2015).

[218] M. Privado, P. de la Cruz, P. Malhotra, G. D. Sharma, and F. Langa, Influence of the dipole moment on the photovoltaic performance of polymer solar cells employing non-fullerene small molecule acceptor, Solar Energy **221**, 393–401 (2021).

[219] R. Wang, C. Zhang, Q. Li, Z. Zhang, X. Wang, and M. Xiao, Charge separation from an intra-moiety intermediate state in the high-performance PM6:Y6 organic photovoltaic blend, Journal of the American Chemical Society **142**, 12751–12759 (2020).

[220] T. Wang, Z.-H. Chen, J.-W. Qiao, W. Qin, J.-Q. Liu, X.-Z. Wang, Y.-J. Pu, H. Yin, and X.-T. Hao, Correlating charge transfer dynamics with interfacial trap states in high-efficiency organic solar cells, ACS Applied Materials & Interfaces **15**, 12109–12118 (2023).

[221] S. Mahadevan, T. Liu, S. M. Pratik, Y. Li, H. Y. Ho, S. Ouyang, X. Lu, H.-L. Yip, P. C. Y. Chow, J.-L. Brédas, V. Coropceanu, S. K. So, and S.-W. Tsang, Assessing intra- and inter-molecular charge transfer excitations in non-fullerene acceptors using electroabsorption spectroscopy, Nature Communications **15**, 2393 (2024).

[222] S. M. Pratik, G. Kupgan, J.-L. Brédas, and V. Coropceanu, Analysis of the charge generation and recombination processes in the PM6:Y6 organic solar cell, Energy & Environmental Science **18**, 841–852 (2025).

[223] Z. Zheng, N. R. Tummala, Y.-T. Fu, V. Coropceanu, and J.-L. Brédas, Charge-transfer states in organic solar cells: understanding the impact of polarization, delocalization, and disorder, ACS Applied Materials & Interfaces **9**, 18095–18102 (2017).

[224] J. Benduhn, K. Tvingstedt, F. Piersimoni, S. Ullbrich, Y. Fan, M. Tropiano, K. A. McGarry, O. Zeika, M. K. Riede, C. J. Douglas, S. Barlow, S. R. Marder, D. Neher, D. Spoltore, and K. Vandewal, Intrinsic non-radiative voltage losses in fullerene-based organic solar cells, Nature Energy **2**, 17053 (2017).

[225] J. Liu, S. Chen, D. Qian, B. Gautam, G. Yang, J. Zhao, J. Bergqvist, F. Zhang, W. Ma, H. Ade, O. Inganäs, K. Gundogdu, F. Gao, and H. Yan, Fast charge separation in a non-fullerene organic solar cell with a small driving force, Nature Energy **1**, 16089 (2016).

[226] F. D. Eisner, M. Azzouzi, Z. Fei, X. Hou, T. D. Anthopoulos, T. J. S. Dennis, M. Heeney, and J. Nelson, Hybridization of local exciton and charge-transfer states reduces nonradiative voltage losses in organic solar cells, Journal of the American Chemical Society **141**, 6362–6374 (2019).

[227] G. Han, T. Hu, and Y. Yi, Reducing the singlet–triplet energy gap by end-group π–π stacking toward high-efficiency organic photovoltaics, Advanced Materials **32**, 2000975 (2020).

[228] Y. Shi, Y. Chang, K. Lu, Z. Chen, J. Zhang, Y. Yan, D. Qiu, Y. Liu, M. A. Adil, W. Ma, X. Hao, L. Zhu, and Z. Wei, Small reorganization energy acceptors enable low energy losses in non-fullerene organic solar cells, Nature Communications **13**, 3256 (2022).

[229] K. Vandewal, Interfacial charge transfer states in condensed phase systems, Annual Review of Physical Chemistry **67**, 113–133 (2016).

[230] J. Lee, K. Vandewal, S. R. Yost, M. E. Bahlke, L. Goris, M. A. Baldo, J. V. Manca, and T. Van Voorhis, Charge transfer state versus hot exciton dissociation in polymer–fullerene blended solar cells, Journal of the American Chemical Society **132**, 11878–11880 (2010).

[231] K. Vandewal, Z. Ma, J. Bergqvist, Z. Tang, E. Wang, P. Henriksson, K. Tvingstedt, M. R. Andersson, F. Zhang, and O. Inganäs, Quantification of quantum efficiency and energy losses in low bandgap polymer:fullerene solar cells with high open-circuit voltage, Advanced Functional Materials **22**, 3480–3490 (2012).

[232] S. D. Dimitrov, A. A. Bakulin, C. B. Nielsen, B. C. Schroeder, J. Du, H. Bronstein, I. McCulloch, R. H. Friend, and J. R. Durrant, On the energetic dependence of charge separation in low-band-gap polymer/fullerene blends, Journal of the American Chemical Society **134**, 18189–18192 (2012).

[233] G. Grancini, M. Maiuri, D. Fazzi, A. Petrozza, H.-J. Egelhaaf, D. Brida, G. Cerullo, and G. Lanzani, Hot exciton dissociation in polymer solar cells, Nature Materials **12**, 29–33 (2013).

[234] A. E. Jailaubekov, A. P. Willard, J. R. Tritsch, W.-L. Chan, N. Sai, R. Gearba, L. G. Kaake, K. J. Williams, K. Leung, P. J. Rossky, and X.-Y. Zhu, Hot charge-transfer excitons set the time limit for charge separation at donor/acceptor interfaces in organic photovoltaics, Nature Materials **12**, 66–73 (2013).

[235] R. Tautz, E. Da Como, T. Limmer, J. Feldmann, H.-J. Egelhaaf, E. von Hauff, V. Lemaur, D. Beljonne, S. Yilmaz, I. Dumsch, S. Allard, and U. Scherf, Structural correlations in the generation of polaron pairs in low-bandgap polymers for photovoltaics, Nature Communications **3**, 970 (2012).

[236] B. S. Rolczynski, J. M. Szarko, H. J. Son, Y. Liang, L. Yu, and L. X. Chen, Ultrafast intramolecular exciton splitting dynamics in isolated low-band-gap polymers and their implications in photovoltaic materials design, Journal of the American Chemical Society **134**, 4142–4152 (2012).

[237] H. Y. Chung, J.-H. Park, J. Cui, S.-Y. Kim, J. Oh, D. Kim, and S. Y. Park, Influence of intramolecular charge-transfer characteristics of excitons on polaron generation at the donor/acceptor interface in polymer solar cells, The Journal of Physical Chemistry C **125**, 18352–18361 (2021).

[238] Z. Jiao, T. Jiang, Z. Zhou, C. Qin, J. Long, Y. Liu, and Y. Jiang, Identification of a bridge-specific intramolecular exciton dissociation pathway in donor–π–acceptor alternating conjugated polymers, Nanoscale Research Letters **16**, 51 (2021).

[239] R. Tautz, E. Da Como, C. Wiebeler, G. Soavi, I. Dumsch, N. Fröhlich, G. Grancini, S. Allard, U. Scherf, G. Cerullo, S. Schumacher, and J. Feldmann, Charge photogeneration in donor-acceptor conjugated materials: influence of excess excitation energy and chain length, Journal of the American Chemical Society **135**, 4282–4290 (2013).

[240] S. Cho, B. S. Rolczynski, T. Xu, L. Yu, and L. X. Chen, Solution phase exciton diffusion dynamics of a charge-transfer copolymer PTB7 and a homopolymer P3HT, The Journal of Physical Chemistry B **119**, 7447–7456 (2015).

[241] N. Zhao, R. Zhang, X. Zou, X. Su, F. Dang, G. Wen, W. Zhang, K. Zheng, H. Chen, and K. Wu, Photoinduced polaron formation in a polymerized electron-acceptor semiconductor, The Journal of Physical Chemistry Letters **13**, 5143–5150 (2022).

[242] P. Roy, A. Jha, V. B. Yasarapudi, T. Ram, B. Puttaraju, S. Patil, and J. Dasgupta, Ultrafast bridge planarization in donor-π-acceptor copolymers drives intramolecular charge transfer, Nature Communications **8**, 1716 (2017).

[243] D. Fazzi, M. Barbatti, and W. Thiel, Modeling ultrafast exciton deactivation in oligothiophenes via nonadiabatic dynamics, Physical Chemistry Chemical Physics **17**, 7787–7799 (2015).

[244] D. Fazzi, M. Barbatti, and W. Thiel, Unveiling the role of hot charge-transfer states in molecular aggregates via nonadiabatic dynamics, Journal of the American Chemical Society **138**, 4502–4511 (2016).

[245] Y. Cho, Z. Sun, G. Li, D. Zhang, S. Yang, T. J. Marks, C. Yang, and A. Facchetti, CF_3-functionalized side chains in nonfullerene acceptors promote electrostatic interactions for highly efficient organic solar cells, Journal of the American Chemical Society **147**, 758–769 (2025).

[246] H.-J. Werner and W. Meyer, MCSCF study of the avoided curve crossing of the two lowest $^1\sum^+$ states of LiF, The Journal of Chemical Physics **74**, 5802–5807 (1981).

[247] X. Gao, S. Bai, D. Fazzi, T. Niehaus, M. Barbatti, and W. Thiel, Evaluation of spin-orbit couplings with linear-response time-dependent density functional methods, Journal of Chemical Theory and Computation **13**, 515–524 (2017).

[248] A. Corney, "The spontaneous emission of radiation", in *Atomic and laser spectroscopy* (Oxford University Press, 2006).

[249] I. I. Sobelman, *Atomic spectra and radiative transitions*, 1st, Vol. 1, Springer Series in Chemical Physics (Springer Berlin Heidelberg, Berlin, Heidelberg, 1979).

[250] Q. Wu, Q. Peng, Y. Niu, X. Gao, and Z. Shuai, Theoretical insights into the aggregation-induced emission by hydrogen bonding: a qm/mm study, The Journal of Physical Chemistry A **116**, 3881–3888 (2012).

[251] M. Barbatti, A. J. A. Aquino, and H. Lischka, The uv absorption of nucleobases: semi-classical ab initio spectra simulations, Physical Chemistry Chemical Physics **12**, 4959–4967 (2010).

[252] R. Crespo-Otero and M. Barbatti, Spectrum simulation and decomposition with nuclear ensemble: formal derivation and application to benzene, furan and 2-phenylfuran, Theoretical Chemistry Accounts **131**, 1237 (2012).

[253] W. Koch and M. C. Holthausen, *A chemist's guide to density functional theory*, 2nd, Print (Wiley-VCH, Weinheim, Germany, 2001).

[254] P. Geerlings, F. De Proft, and W. Langenaeker, Conceptual density functional theory, Chemical Reviews **103**, 1793–1874 (2003).

[255] K. Capelle, A bird's-eye view of density-functional theory, Brazilian Journal of Physics **36**, 1318–1340 (2006).

[256] A. J. Cohen, P. Mori-Sánchez, and W. Yang, Challenges for density functional theory, Chemical Reviews **112**, 289–320 (2012).

[257] P. Hohenberg and W. Kohn, Inhomogeneous electron gas, Physical Review **136**, B864–B871 (1964).

[258] R. Bauernschmitt and R. Ahlrichs, Treatment of electronic excitations within the adiabatic approximation of time dependent density functional theory, Chemical Physics Letters **256**, 454–464 (1996).

[259] R. E. Stratmann, G. E. Scuseria, and M. J. Frisch, An efficient implementation of time-dependent density-functional theory for the calculation of excitation energies of large molecules, The Journal of Chemical Physics **109**, 8218–8224 (1998).

[260] A. Dreuw and M. Head-Gordon, Single-reference ab initio methods for the calculation of excited states of large molecules, Chemical Reviews **105**, 4009–4037 (2005).

[261] C. A. Ullrich, *Time-dependent density-functional theory: concepts and applications* (Oxford University Press, Incorporated, 2012).

[262] C. A. Ullrich and Z.-h. Yang, A brief compendium of time-dependent density functional theory, Brazilian Journal of Physics **44**, 154–188 (2014).

[263] E. Runge and E. K. U. Gross, Density-functional theory for time-dependent systems, Physical Review Letters **52**, 997–1000 (1984).

[264] S. Hirata and M. Head-Gordon, Time-dependent density functional theory within the tamm-dancoff approximation, Chemical Physics Letters **314**, 291–299 (1999).

[265] W. J. Hehre, R. Ditchfield, and J. A. Pople, Self—consistent molecular orbital methods. xii. further extensions of gaussian—type basis sets for use in molecular orbital studies of organic molecules, The Journal of Chemical Physics **56**, 2257–2261 (1972).

[266] S. Grimme, Semiempirical gga-type density functional constructed with a long-range dispersion correction, Journal of Computational Chemistry **27**, 1787–1799 (2006).

[267] S. Grimme, J. Antony, S. Ehrlich, and H. Krieg, A consistent and accurate ab initio parametrization of density functional dispersion correction (dft-d) for the 94 elements H-Pu, The Journal of Chemical Physics **132**, 154104 (2010).

[268] A. D. Becke and E. R. Johnson, A density-functional model of the dispersion interaction, The Journal of Chemical Physics **123**, 154101 (2005).

[269] E. R. Johnson and A. D. Becke, A post-hartree-fock model of intermolecular interactions, The Journal of Chemical Physics **123**, 024101 (2005).

[270] E. R. Johnson and A. D. Becke, A post-hartree-fock model of intermolecular interactions: inclusion of higher-order corrections, The Journal of Chemical Physics **124**, 174104 (2006).

[271] S. Grimme, S. Ehrlich, and L. Goerigk, Effect of the damping function in dispersion corrected density functional theory, Journal of Computational Chemistry **32**, 1456–1465 (2011).

[272] A. D. Becke, Density-functional thermochemistry. iii. the role of exact exchange, The Journal of Chemical Physics **98**, 5648–5652 (1993).

[273] A. D. Becke, Density-functional exchange-energy approximation with correct asymptotic behavior, Physical Review A **38**, 3098–3100 (1988).

[274] C. Lee, W. Yang, and R. G. Parr, Development of the colle-salvetti correlation-energy formula into a functional of the electron density, Physical Review B **37**, 785–789 (1988).

[275] S. H. Vosko, L. Wilk, and M. Nusair, Accurate spin-dependent electron liquid correlation energies for local spin density calculations: a critical analysis, Canadian Journal of Physics **58**, 1200–1211 (1980).

[276] Y. Tawada, T. Tsuneda, S. Yanagisawa, T. Yanai, and K. Hirao, A long-range-corrected time-dependent density functional theory, The Journal of Chemical Physics **120**, 8425–8433 (2004).

[277] T. Yanai, D. P. Tew, and N. C. Handy, A new hybrid exchange-correlation functional using the coulomb-attenuating method (cam-b3lyp), Chemical Physics Letters **393**, 51–57 (2004).

[278] A. D. Becke, Density-functional thermochemistry. v. systematic optimization of exchange-correlation functionals, The Journal of Chemical Physics **107**, 8554–8560 (1997).

[279] J.-D. Chai and M. Head-Gordon, Systematic optimization of long-range corrected hybrid density functionals, The Journal of Chemical Physics **128**, 084106 (2008).

[280] J.-D. Chai and M. Head-Gordon, Long-range corrected hybrid density functionals with damped atom-atom dispersion corrections, Physical Chemistry Chemical Physics **10**, 6615–6620 (2008).

[281] J. F. Janak, Proof that $\frac{\partial E}{\partial n_i} = \epsilon$ in density-functional theory, Physical Review B **18**, 7165–7168 (1978).

[282] J. Tomasi, B. Mennucci, and R. Cammi, Quantum mechanical continuum solvation models, Chemical Reviews **105**, 2999–3094 (2005).

[283] G. Scalmani and M. J. Frisch, Continuous surface charge polarizable continuum models of solvation. i. general formalism, The Journal of Chemical Physics **132**, 114110 (2010).

[284] B. Mennucci, E. Cancès, and J. Tomasi, Evaluation of solvent effects in isotropic and anisotropic dielectrics and in ionic solutions with a unified integral equation method: theoretical bases, computational implementation, and numerical applications, The Journal of Physical Chemistry B **101**, 10506–10517 (1997).

[285] E. Cancès, B. Mennucci, and J. Tomasi, A new integral equation formalism for the polarizable continuum model: theoretical background and applications to isotropic and anisotropic dielectrics, The Journal of Chemical Physics **107**, 3032–3041 (1997).

[286] E. Cancès and B. Mennucci, New applications of integral equations methods for solvation continuum models: ionic solutions and liquid crystals, Journal of Mathematical Chemistry **23**, 309–326 (1998).

[287] M. Cossi, N. Rega, G. Scalmani, and V. Barone, Energies, structures, and electronic properties of molecules in solution with the c-pcm solvation model, Journal of Computational Chemistry **24**, 669–681 (2003).

[288] D. Cremer, Density functional theory: coverage of dynamic and non-dynamic electron correlation effects, Molecular Physics **99**, 1899–1940 (2001).

[289] Y. Kitagawa, T. Saito, Y. Nakanishi, Y. Kataoka, T. Matsui, T. Kawakami, M. Okumura, and K. Yamaguchi, Spin contamination error in optimized geometry of singlet carbene ($^1A_1$) by broken-symmetry method, The Journal of Physical Chemistry A **113**, 15041–15046 (2009).

[290] L. Noodleman and J. Norman Joe G., The $X\alpha$ valence bond theory of weak electronic coupling. application to the low-lying states of $Mo_2Cl_8^{4-}$, The Journal of Chemical Physics **70**, 4903–4906 (1979).

[291] L. Noodleman, Valence bond description of antiferromagnetic coupling in transition metal dimers, The Journal of Chemical Physics **74**, 5737–5743 (1981).

[292] L. Noodleman and D. A. Case, "Density-functional theory of spin polarization and spin coupling in iron-sulfur clusters", in *Advances in inorganic chemistry*, Vol. 38 (Elsevier, 1992), pp. 423–458.

Acknowledgments

Now it is time to thank all the people who supported me during my doctoral studies.

First, I would like to thank my supervisor, Prof. Dr. Stefan Schumacher, for his support and advice during my research work and for giving me the opportunity to write my dissertation in his research group. I would also like to thank the other members of the examination committee, Prof. Dr. Martin Brehm, Jun. Prof. Dr. Nicholas Güsken, and Dr. Matthias Reichelt, for their time in evaluating my dissertation.

My sincere thanks go to Dr. Chuan-Ding Dong for his mentorship during my doctoral studies. Our close collaboration and fruitful discussions helped me from the beginning to the end of my doctoral studies.

I would like to thank Prof. Dr. Jean-Luc Brédas and Dr. Veaceslav Coropceanu for the opportunity to conduct research in their group. Many thanks to you and your entire group for your generous hospitality, warm welcome, and fruitful discussions. I would also like to thank Stefan for funding and facilitating this stay.

My deepest gratitude goes to my family and friends, who always encourage me, motivate me to keep going, and never let me down. *Vielen herzlichen Dank für alles!*

I would like to thank my colleagues for their support and the many pleasant coffee breaks, which created a wonderful working atmosphere.

Erklärung

Ich versichere hiermit, dass ich die vorliegende Arbeit selbstständig verfasst und keine anderen Quellen und Hilfsmittel als die angegebenen benutzt habe. Zu diesen Hilfsmitteln zählen auch text- oder bilderzeugende KI-Werkzeuge (wie ChatGPT). Die Stellen der Arbeit, die anderen Werken (auch text- oder bilderzeugenden KI-Werkzeugen) dem Wortlaut oder dem Sinn nach entnommen sind, habe ich in jedem einzelnen Fall unter Angabe der Quelle als Entlehnung kenntlich gemacht. Ich versichere ferner, dass die Arbeit in gleicher oder ähnlicher Form noch keiner anderen Prüfungsbehörde vorgelegen hat und nicht als Prüfungsleistung angenommen wurde.

Ort, Datum

Unterschrift